INVESTIGATION OF NON-LINEAR PHENOMENA IN ROTOR-DAMPER ASSEMBLIES

by

J. E. H. Sykes

Thesis submitted for the degree of

Doctor of Philosophy

University of Southampton

August 1990

(I) PREFACE

The research described in this dissertation was carried out at the Department of Mechanical Engineering, University of Southampton between July 1987 and July 1990. The author would like to express his gratitude to Professor R. Holmes for his consistent and valued supervision, advice and enthusiasm.

This research project has been supported financially by Rolls Royce plc, Bristol and the Science and Engineering Research Council to whom the author is indebted.

The author would also like to thank members of the academic, postgraduate and technical staff whose advice and assistance has been greatly appreciated. In particular, the author would like to acknowledge the practical advice and assistance given by Mr C. R. Peach and Mr P. G. Wheeler who produced many effective design solutions throughout the experimental work.

The author is very grateful to Mr M. C. Levesley for proof reading the draft thesis and for many useful suggestions and to Mr M. Hill for help in preparing the script.

UNIVERSITY OF SOUTHAMPTON

ABSTRACT

FACULTY OF ENGINEERING AND APPLIED SCIENCE

MECHANICAL ENGINEERING

Doctor of Philosophy

INVESTIGATION OF NON-LINEAR PHENOMENA IN ROTOR-DAMPER ASSEMBLIES

by John Edward Hugh Sykes

The research, sponsored by Rolls Royce plc and the SERC, has involved a three bearing rigid motor assembly incorporating flexible, spring supports and unsealed squeeze-film dampers. A range of practical assemblies involving, at first, one and then two squeeze-film dampers with different static misalignments were studied. Non-linear jump phenomena and subharmonic resonances have been demonstrated both experimentally and theoretically for a range of rotor unbalance. The effects of varying oil supply have been demonstrated.

Theoretical investigation has modelled the unsealed squeeze-film damper with the Short Bearing approximation, providing a variable film extent with, for the most part, an absolute zero cavitation level. The equations of motion were solved by applying a Runge-Kutta method and resulting discrete time series have been used for frequency analysis. The practical use of analytical linear approximation has been assessed.

Frequency analysis of the experimental and theoretical vibration signals has led to the construction of waterfall diagrams which present the variations in the spectral content of the vibration throughout the speed range. Spectral analysis has indicated the effects of misalignment on the nature and severity of subsynchronous resonances and jump phenomena. In particular, the development of strong subharmonic resonance due to the introduction of static eccentricity to a squeeze-film damper is demonstrated. Also, the distribution of rotor weight between squeeze-film dampers with differing supports has been shown to have a marked effect on the assembly's vibration response, particularly with respect to any jump phenomena that are excited.

The research has demonstrated that it is possible for the vibration signatures of similar rotor-bearing assemblies to be strongly contrasting due to different accumulations of tolerances during manufacture, fitting and operation. The practical implications are discussed.

Methods of linearisation are discussed so that the non-linear characteristics of the squeeze-film damper might be rapidly estimated with reasonable accuracy. Such techniques should prove to be valuable in extending the capabilities of existing design analysis software which is currently employed to predict the vibration characteristics of complex turbomachinery assemblies.

(III) CONTENTS

(IV) LIST OF FIGURES

(V) LIST OF PLATES

(V) LIST OF TABLES

(V) NOMENCLATURE

NOMEN.	DESCRIPTION	UNIT
A_o	DC Harmonic Balance Displacement Coefficient	m
A_j	j^{TH} Frequency Harmonic Balance Displacement Coefficient	m
$A_{1/2}$	Half Engine Order Displacement Coefficient	m
A_1	SFD1 Bearing Factor, $\pi.\mu.R_1(l_1/c_1)^3f^2/bf(k_2.I)$ also synchronous displacement coefficient	- m
A_2	SFD2 Bearing Factor, $\pi.\mu.R_2(l_2/c_2)^3b/f(k_2.I)$	-
a	Rig Dimension also Linearised Force Coefficient	m N
B	Linear Damping Coefficient	-
B_j	j^{TH} Frequency Harmonic Balance Displacement Coefficient	m
b	Rig Dimension also Linearised Force Coefficient also Film Force Cavitation Extent Parameter (Ref [42])	m N
c	SFD Radial Clearance also Synchronous Damping Harmonic Balance Coefficient	m Ns/m
C_J	SFD Journal Centre	
C_B	SFD Bearing Centre	
d	Rig Dimension	m
e	SFD Eccentricity	m
E_o	SFD Static Eccentricity Ratio	-
f	Rig Dimension or Force	m
G	SFD Groove Depth	m
G_w	SFD Groove Width	m
h	Duffing Equation Damping Coefficient	-
H	Harmonic Balance Iteration Function	-

NOMEN.	DESCRIPTION	UNIT
I	Rotor Moment of Inertia per land	$kg.m^2$
J	Number of Equally Spaced Frequencies	-
k	Flexible Bearing Support Stiffness per land	N/m
$\bar{k}_2$	Non-Dimensional Stiffness per land, $k_2.b^2/(I.w^2) = (w/w_n)^{-2}$	-
$\bar{k}_1$	Non-Dimensional Stiffness per land, $k_1.f^2/(I.w^2)$	-
l	SFD Land Width	m
m	Mass	kg
N	Number of Lands per SFD also Synchronous Coefficient Number in Fourier Series	- -
P	SFD Oil Pressure	N/m
$P1$	SFD Radial Film Force per land	N
$P2$	SFD Tangential Film Force per land	N
Pc	Rotor Mass Unbalance Force per land	N
$Psup$	SFD Oil Supply Pressure	N/m^2,psi
Qc_2	Non-Dimensional Unbalance Force, $Pc.a.b/(I.c_2.w^2)$	-
Qs	Non-Dimensional Static Force, $m.g.d.b/(I.c_2.w^2)$	-
R	SFD Mean Radius	m
r	Radial Coordinate	m
s	Tangential Coordinate	m
t	Time	s
W	Journal Weight	N
w	Rotor Rotational Speed	rad/s
w_n	Rotor-Bearing Assembly First Bounce Vibration Mode Frequency (Configurations 1a,b)	rad/s
x	Horizontal Coordinate	m

NOMEN.	DESCRIPTION	UNIT
y	Vertical Coordinate	m
Z	Dummy parameter	-
z	Axial Coordinate	m
α	SFD Journal Attitude Angle	rad
β	SFD Speed Dependent Parameter, $A.\bar{k}^{0.5}/\pi$	-
δ	SFD1 non-dimensional preload (gravity offset), {m.g.d./(b.k2)}.f/(b.c1) for Configurations 1a,b {[m.g.d./(b.k2)] + c2}.f/(b.c1) for Configs. 2a,b	-
δP	Incremental Film Force	N
ϵ	Eccentricity Ratio, e/c	-
μ	Oil Dynamic Viscosity	Ns/m^2
ϕ	Angular Co-ordinate	rad
τ	Groove Performance Parameter	-
Φ	Quadratic Stiffness Coefficient	N/m^2
θ	Angular Co-ordinate	rad
Ω	Stiffness Coefficient	N/m^2
$\partial/\partial\phi$	Partial derivative with respect to ϕ	
$\dot{}$	Derivative with respect to time, t	1/s
$'$	Derivative with respect to Non-Dimensional Time, w.t	1/rad

Superscripts

$\bar{}$	Non-Dimensional Quantity
^{L}	Denotes Simplified Linear Model Variable

Subscripts

$_1$	After a parameter denotes SFD1

2	After a parameter denotes SFD2
r	After a parameter denotes radial
θ	After a parameter denotes tangential
x	After a parameter denotes horizontal
y	After a parameter denotes vertical

(VI) ABBREVIATIONS

Abbreviation	Description
c/min	Cycles Per Minute
EO	Engine Order
DOF	Degree of Freedom
FFT	Fast Fourier Transform
Fig	Figure
Ref	Reference
RRG	Rotor Relative to Ground
SERC	Science & Engineering Research Council
SFD	Squeeze-Film Damper
UK	United Kingdom
USA	United States of America

Chapter 1 INTRODUCTION

1.1 The Squeeze-Film Damper (SFD)

Aero-engines exhibit low structural damping which is compensated for by the inclusion of fluid film dampers within the rotor-bearing assemblies. The squeeze-film damper, or SFD, is a fluid film bearing designed to attenuate resonant rotor vibrations in turbomachinery. The SFD (Fig 1.1) is similar in operation to a fluid film journal bearing except for the essential difference that the SFD journal does not rotate relative to the housing. The SFD fluid film forces are generated by the squeeze and wedge action of the non-rotating journal as it vibrates within the housing. The rotation of the shaft is taken up by a rolling element bearing between the SFD journal and the rotor.

The SFD, in practice, develops both damping and stiffness force contributions in response to rotor unbalance and rotational speed. If the SFD is considered to execute circular, centred eccentricity orbits then the theoretical analysis is simplified and, with atmospheric fluid supply pressure assumed, it is possible to identify separate damping and stiffness film forces analytically. Thus, within the SFD, the damping force, P2, (Fig 1.1) acts to dampen the motion between the journal and the bearing housing. When an uncavitated fluid completely occupies the SFD clearance a 2π Film is said to exist. This film produces a particular value of damping force, dependent on the eccentricity vector of the journal with respect to the bearing housing and its relative motion. This 2π film does not develop a stiffness force. In the

instance when the clearance is occupied by 180° of uncavitated fluid, the other 180° being fully cavitated, then the π film damping force (P2) is half the value of the equivalent 2π film damping force and a stiffness force (labelled P1, Fig 1.1) is also developed by the SFD at right angles to the damping force. These damping and stiffness forces are detailed in Table 1.1 (The tables are to be found between the Figures and Appendix sections).

Theoretical analyses using film models other than the 2π and π films or, for non-circular or uncentralised eccentricity orbits develop forces P1 and P2 (Fig 1.1) which each contain damping and stiffness contributions.

The influence of fluid inertia may be significant in cases where the Gap Reynolds Number, R_e is greater than unity and its value can be determined from the equation;

$R_e = w.c^2/v$, where w = rotational speed,
c = radial clearance,
and v = kinematic viscosity.

The Reynolds Number is the ratio of inertial to viscous forces and the effect of fluid inertia can be described as adding mass to the journal.

1.2 Current Rotor-Bearing Assembly Design

The rotor bearing assemblies of modern aero-engines exhibit complicated vibrations. The degree of mass unbalance in a rotor is a primary source of vibration. A degree of rotor unbalance, within prescribed tolerances,

is present in the assembly initially and this can vary during service with a resulting increase in vibration. To improve engine efficiency some modern designs comprise of upto three rotors, sharing the same rotational axis. A long rotor (carrying low pressure turbine and compressor blading) is housed, or nested, inside a shorter, hollow rotor for medium pressure application which, in turn, is similarly nested inside a shorter rotor carrying high pressure blading. These rotors can all rotate at different speeds and in differing directions.

An aero-engine gas turbine rotor is often designed with a three rolling-element bearing arrangement (providing one thrust and three transverse, or radial, locations). As well as the two end bearing locations a bearing location between these two ends, near to the compressor, is often required to raise the first flexural mode frequency of rotor-bearing vibration and to help react the gyroscopic forces generated by the intake fan.

1.3 The Squeeze-Film Damper Applied to Turbomachinery

Two schools of thought exist in the design of SFDs to attenuate rotor vibration. Prominent aero-engine manufacturers in the USA tend towards implementing the SFD in a parallel damper and spring vibration isolation device, attempting to tune the lower bounce modes. In this instance the aim is to maintain the SFD statically centralised.

UK counterparts have successfully applied designs simply interposing the SFD between the rotor and the existing

support pedestal stiffness and, in the absence of any bearing misalignment, the static SFD position is with the journal fully eccentric under the rotor weight. In this instance there is no intention to alter the design's natural frequencies but only to provide damping to the response.

Both of these design concepts suffer from the inability to control bearing alignments with three bearing assemblies. Such misalignments have been suggested as a possible exacerbation of certain non-linear phenomena arising during engine tests.

1.4 The Squeeze-Film Damper Response

The desirable response that a rotor assembly employing centralised SFDs is designed to exhibit over the required speed range is similar to the linear damped second order system response (see Fig 1.2). Most of the assembly's damping is provided by the SFDs. Thus as speed increases the vibration amplitude increases upto a maximum, close to the system's first natural frequency, and then decreases asymptotically to a value determined by the unbalance at higher speeds until the operating speed is attained. The phase response (the phase angle between the displacement and the unbalance force) of an uncavitated and centralized SFD exhibiting circular orbits varies between 0° and 180°. At low speeds the phase is close to 0° and the rotor displacement is almost in phase with the unbalance force. The phase passes through 90° at the natural frequency and the rotor continues to invert towards 180° (full inversion) at higher speeds.

This desirable second order response is not always displayed over the speed range by the assembly because of the presence of jump phenomena (see Fig 1.3) and other system non-linearities. Jump phenomena can occur in the vibration of rotor-bearing assemblies as very sudden or sharp changes in the level of vibration within the system. This jump may be up (an increase in vibration) or down (a decrease in vibration). The jump is possible because of the presence of cavitation which dictates two stable vibration levels at any rotor speed within a specific speed range. Within this bistable region, 'B' in Fig 1.3, jumps may take place between the two stable vibration levels.

The bistable speed range and the two possible levels of vibration are both of interest in this study. Theoretical research predicts the presence of the bistable region and it is of interest to note whether the experimentally observed jumps occur within this predicted range.

With the presence of jumps the phase response also deviates from a desired second order response by revealing a delayed rotor inversion beyond the natural frequency. A jump down can cause a phase jump (sudden inversion) as well as a drop in amplitude.

Chapter 2 LITERATURE REVIEW

2.1 Background

2.1.1 Hydrodynamic Lubrication

Osbourne Reynolds' classic paper of 1886 [1] heralded the birth of the subject of Hydrodynamic Lubrication. A good account of the history of tribology, marking the first centenary of Reynolds' paper [1], is given by Dowson [2]. Dowson [2] discussed early experimental work including studies of olive oil by Beauchamp Tower and described how Reynolds followed this with his own work and developed hydrodynamic theory from the Navier-Stokes equations of fluid motion. The Reynolds Equation was a result of this theoretical study and governs pressure generation in a fluid-film with neglect of inertial and gravitational effects and assuming an iso-viscous and incompressible fluid.

Dowson [2] mentioned squeeze-films and the need for continued analysis before the design of components utilising squeeze-film hydrodynamic effects can be optimised. Pinkus and Sternlicht [3] have provided the subject of Hydrodynamic Lubrication with a text referred to by numerous researchers in which the various types of squeeze-film effects and dynamic loading are studied.

Vance [4] provides the only text known to the author which deals comprehensively with the subject of rotor-bearing dynamics. Fluid film bearings are utilised extensively in modern assemblies. A good introduction to the hydrodynamics of journal bearings and SFD's is provided and the strong influence that fluid film

bearings have on practical rotordynamics is made clear. This relatively brief text is supported by extensive reference to technical publications arising from Vance's lengthy experience in the field of rotordynamics.

2.1.2 Non-Linear Vibration

Useful background to vibration of rotor-bearing assemblies incorporating SFDs exists in many Mechanical Vibration texts. Of particular note are those texts that begin to consider the non-linear properties of some vibration phenomena which can be related to the non-linear response of SFD's within assemblies.

Den Hartog [5] considered the amplitude response when variable elasticity is a system element. Jump phenomena (associated with a bistable region within the frequency response of a system) arising from non-linear elasticity, or stiffness, is introduced. Timoshenko, Young and Weaver [6] also discussed variable elasticity and indicated the theoretical possibility of two separate bistable regions. The theoretical and experimental presence of a second bistable region, or upper branch at higher frequency ratios in the response of SFDs has been noted within an assembly incorporating a SFD by Simandiri and Hahn [7].

Tse, Morse and Hinkle [8] and Magnus [9] introduce their readers to some traditional concepts and techniques involved with non-linear vibration as a progression from linear approximations of real systems. The phase plane trajectory presentation, jump phenomena and subharmonic resonances are embraced in each of the two texts.

Stoker [10] and Blaquiere [11] and many other workers have provided texts where the basic tools of non-linear

system mathematical analysis are presented.

A wealth of published papers exists on the subject of non-linear vibration, the majority of which involve mathematical solution of approximate models. Some of the mathematical treatments yield results which provide interesting comparisons with the non-linear phenomena exhibited by SFD's. Simple non-linear equations, such as Duffing's equation [11],

$$x'' + u.x' + \bar{x}^3 = F.\cos(w.t) \ ,$$

yield solutions exhibiting jump phenomena and subharmonic, ultraharmonic and subultra harmonic resonances. The presence of regions of chaos, determined by so-called strange attractors, were first reported by Ueda [12]. Since then much academic effort has been expended in mathematical identification of the chaotic behaviour in such systems. Szemplinska-Stupnicka [13] used the principle of harmonic balance to demonstrate that an unsymmetric non-linearity gives rise to period doubling bifurcation about a subharmonic resonance at half the forcing frequency. This lack of symmetry can be represented by the Duffing Equation, above, with the addition of a time invariant forcing term, Fo as shown below

$$x'' + u.x' + \bar{x}^3 = Fo + F.\cos(w.t) \ .$$

In comparison, it was shown [13] that symmetric non-linearity, represented by the Duffing Equation, led to similar bifurcation about a subharmonic resonance at one third the forcing frequency. For the same forcing frequency, the subharmonic resonance solutions are accompanied by the other bistable solutions exhibiting high amplitude synchronous components and lower amplitude

integer harmonics.

Nayfeh [14] identified limits on the excitation amplitude required to generate subharmonic resonances in the response of a system involving quadratic and cubic non-linearities. The equation studied was one resulting from modelling the subharmonic response of gas bubbles, immersed in liquids, to a harmonic acoustic field. It has been shown that cavitating liquids emit subharmonic peaks. For subharmonic resonance to be assured, the excitation amplitude must be above a certain threshold level. Subharmonic resonance is possible, but not assured, for excitation below this threshold level down to a lower excitation threshold, below which subharmonic resonance is impossible.

Plaut and Hsieh [15] studied the subharmonic, synchronous and superharmonic response of a single degree-of-freedom system with weak quadratic and cubic non-linearities, a time delay in damping and parametric excitation. In some instances, increases in the time delay parameter cause increases in regions of synchronous bistable response of such systems.

2.1.3 Spectral Analysis

Fast fourier transform, or FFT, spectral analysis of vibration response is very useful in rotor-bearing assembly investigations. The presence of non-linear phenomena such as subharmonic resonance, combination frequencies and jump phenomena can be detected within frequency spectra of assembly vibrations. Newland [16] presents a range of theoretical techniques and Randall [17] described how one might use Bruel and Kjaer

equipment in frequency analysis.

Tomlinson [18] gives an example of how spectral analysis has been used to study a non-linear system's response. The presence of a non-linear combination resonance or frequency in the response of a structural beam is clearly illustrated by both experimental and theoretical waterfall diagrams and contour plots.

2.1.4 The Application of Squeeze-Film Dampers

Oil film journal bearings contribute damping to a system and can help to attenuate rotor vibration. However, they exhibit a stability threshold dependent on the natural frequency of the assembly. Broadly speaking, if the rotor is rotating at about twice the system natural frequency, then a self excited fluid whirl can take place in the bearing. This 'half speed whirl', also known as 'oil whip' [4], is an instability which displays a subharmonic response which continues at approximately the same frequency as speed is increased further. This vibration is theoretically unstable, predicting metal-to-metal contact between journal and housing, and Mitchell, Holmes and Byrne [19] demonstrated experimentally that the orbit attains some finite size, probably due to supply pressure and groove effects. On the other hand, the squeeze-film damper, or SFD, has no theoretical stability limit because the SFD journal does not provide a force in the direction of rotor spin. This apparent absence of a maximum stable speed is one of the primary reasons for the popularity of the SFD, over the journal bearing, as a means of introducing damping into a rotor-bearing system with inherently low material damping.

Cooper [20] noted the ability of a SFD to attenuate

resonant rotor-bearing assembly vibration levels in preference to mechanical vibration restriction. The work presented was of a qualitative nature and centred around attenuation of resonant rotor orbits due to unbalance prior to inversion by means of mechanical stops, journal bearings or SFDs. If inversion at low speeds, during run-up, could be achieved successfully for large unbalances then relatively low vibration levels at the operating speed would still result. The effect of applying mechanical contact with the rotor inverted was to immediately change the phase angle between deflection and unbalance. Contact at speeds just higher than the inversion speed tended to return the rotor to the non-inverted state. Such behaviour was often random. When a hydrodynamic journal bearing was applied to the system then inversion was improved. However, smooth operation at higher speeds was limited by the onset of oil whirl. With a SFD fitted to the system, resonance peaks disappeared and rotor inversion took place at low speeds. Oil supply pressure dictated the inversion speed and bistable operation, with resonance sometimes continuing above the critical speed. Theoretical analysis, utilising the Reynolds Equation indicated that an oil supply pressure increase resulted in a fall in the radial SFD film force component and an increase in the tangential component. This had the effect of increasing the SFD damping capacity and increasing the phase angle, encouraging inversion.

Kulina, Mullen, Natesh and Saltzman [21] demonstrated the ability of a parallel SFD and squirrel cage combination applied to a rolling element bearing in a multistage compressor to eliminate a critical speed problem. Simple linear analysis demonstrated the benefits of tuning the first critical below the operating range and providing the optimum damping to remove resonance peaks. The

difficulty of determining the level of damping present within a practical assembly was noted. Experimental tests on a rig were used to design a combination providing slightly overdamped conditions. Non-dimensional scaling was used successfully to apply the desirable experimental conditions to a compressor design.

Holmes [22] discussed the application of a SFD and support spring in both a parallel and series combination, citing the example of an automobile gas turbine engine. The parallel SFD and spring support combination is useful as a vibration isolator where the first assembly natural frequency is designed as a rigid rotor bounce mode and the SFD is statically centralised. This encourages circular centred orbits within the damper which is useful at the design stage as the theory for such hydrodynamic conditions can be considerably simplified. If oil supply pressure to the SFD is high enough then the minimum oil film pressure can be maintained above that required for cavitation. The presence of oil film cavitation leads to undesirable non-linear phenomena which affects the vibration response. Jump phenomena (sudden changes in vibration amplitude at particular rotor speeds) and subsynchronous resonance (due to oil film non-linearity) can become undesirable response features. This arrangement can be used to tune a dominant rigid body bounce mode with a well damped resonance at a rotor speed safely lower than the operating speed. The assembly would then operate at running speed with the rotor response inverted relative to the unbalance force vector and with a transmissibility lower than unity provided jump phenomena had been avoided (or if a jump down had occurred on run up) and no strong subsynchronous resonance was excited.

The application of a SFD element in series with a spring

support constitutes a flexibly supported SFD housing. No attempt is made to reduce the natural frequencies in this instance. No centring exists in the SFD and the rotor load is subsequently carried by the oil film. Circular centred orbits might be assumed for speeds close to critical speeds (for a sufficiently high unbalance force with respect to the static rotor load) when simple theory could be applied to estimate resonant amplitudes. Also quasi-linear (amplitude or force dependent) coefficients might be employed to provide alternative predictions, as discussed by Holmes and Dogan [23]. Theory shows that an uncavitated, or 2π film has no static load carrying capability. Cavitation does occur in this SFD arrangement in practice and negative pressure spikes (when oil film pressure falls below absolute zero pressure for a very short time, prior to cavitation) can result in tensile film stresses. Large orbits should be avoided; also orbits with sudden changes in rotor motion lead to sudden changes in transmitted force.

Dede and Holmes [24] studied the experimental and theoretical performance of engine journal bearings and squeeze-film bearings. Numerical time marching methods such as Runge-Kutta and predictor-corrector were discussed for solution of the Reynolds' equation. Complex engine load cycles lead to complicated journal bearing orbit loci and transmitted force response. Further complication arises when the differences in effective individual masses acting at each bearing along the crank shaft are analysed. The dynamic film pressure variation and rotor centre displacement orbits within a squeeze-film bearing were also studied. Sensitivity of rotor centre orbit to assumed negative pressure curtailment was demonstrated theoretically.

SFD's have been successfully employed within design

modifications made to prototype rotordynamic equipment with the objective of reducing large vibrations to contractually acceptable levels. Malanoski [25] discussed nine case histories where subsynchronous and synchronous vibrations have been successfully attenuated with modifications incorporating custom designed damping assemblies. A large compressor exhibited strong subsynchronous response arising from aerodynamic forcing of a flexible shaft even though the shaft was supported by a tilting-pad bearing (selected because of the lack of cross coupling within its oil film therefore lending a degree of stability). Application of a parallel SFD and spring combination (as discussed by Holmes [22]) to the housing of the tilting-pad bearing successfully reduced the vibration.

Ehrich and Childs [26] discussed the increasing tendency for modern turbomachinery to exhibit instability within the design speed range. Modern plant is lighter, runs at higher speeds and higher energy and power density levels and employs tighter clearances for increased efficiency. Instability associated with forward (and, on occasion, reverse) subsynchronous rotor whirl generated from tangential forcing was discussed. The SFD was cited as a popular method of introducing additional damping to an unstable system with the aim of rendering the design speed range stable throughout.

The addition of damping to control turbomachinery vibrations requires a knowledge of the position of nodes for the range of modes of interest. Obviously, damping must be provided remote from rotor nodes. However, the addition of external damping will affect the mode shapes and the precise amount of damping supplied by a modification is not easy to identify, particularly with non-linear elements such as SFDs. Adaptive rotor

vibration control has been proposed on occasion. In the few instances where the economics and practical limitations would permit, such measures as adaptive electromagnetic bearings governed by a control law have been expounded. Firoozian and Stanway [27] discuss a possible application of state variable feedback control of rotor vibration for a limited number of modes. A clear limitation that was identified was the possible destabilizing influence of higher modes of vibration, not taken into account by the state variable controller, on the closed loop system. Although filtering of the higher modes is a possible stabilising measure, it is clear that such a system must be tailor made for each application.

Burrows, Sahinkaya and Turkay [28] demonstrated that the vibration performance of a SFD within a light flexible rotor-bearing system can be enhanced by adaptively controlling the SFD supply pressure. From a knowledge of the system frequency response over the operating speed range a form of adaptive supply pressure control (stepping between a low and a high pressure level) would be applied to attenuate vibration at resonant speeds. This represents a relatively cheap and simple means of bearing control and was considered best implemented if the adaptive SFD can be located at a dominant anti-node. The electromagnetic bearing would facilitate a more comprehensive control scheme but introduces greater cost and complexity.

SFD elements employed in aero-engines to dampen the vibration arising from unbalance forcing not only have to combat the consistent unbalance arising from production tolerances and assembly distortions developing during service but also face the possibility of an extreme unbalance condition in the event of a catastrophic

incident such as blade loss. SFD design performance directed towards minimizing the consistent effects of relatively low unbalance forcing would be degraded if the SFD were also designed to successfully react to a sudden, large increase in forcing (due to blade loss or a comparable event). Generally, the higher the maximum unbalance a SFD is designed to cope with the greater the radial clearance within the SFD. Fleming [29] suggested the use of a 'Dual Clearance' SFD to provide optimised damping for both normal and abnormal unbalance levels. The dual clearance SFD is comprised of two SFD elements in series. One clearance is designed to perform well under normal, consistent unbalance and the other, larger clearance is designed to cope with extreme unbalance for a relatively short period. The larger clearance is prevented from acting with normal unbalance conditions by a parallel shear pin arrangement. The shear pins fail when the loading reaches a predetermined level, thus allowing the squeeze-film action to take place. If the engine is successfully shut down the shear pins can be replaced during engine repairs.

This dual clearance design is quite attractive when the shear pin arrangement prevents the larger clearance from acting at all while still efficiently activating it in the event of a predetermined overload.

2.2 The Theoretical Study of Squeeze-Film Dampers & Experimental Comparisons

The Navier Stokes equations are the starting point for the study of the fluid pressure distribution within the SFD. The Reynolds equation, derived from the Navier

Stokes equations, makes assumptions about the dominant forces (as already described in 2.1). White [30] discussed squeeze film hydrodynamics, reducing the Navier Stokes Equations to the Reynolds Equation. The analysis clearly demonstrated the application of the equation to squeeze film effects rather than to contemporary journal bearing applications. For circular centred orbits the instability of the intermediate solution of the three solutions available in so called bistable operation was demonstrated using the Routh Hurwitz Stability Criterion.

Pinkus and Sternlicht [3] have provided a widely used text covering the basic differential equations and a thorough range of the various analyses which lead to practical bearing designs. Squeeze film effects are discussed alongside dynamic loading and the emphasis of the text is directed towards bearings with rotation between journal and housing.

The Reynolds Equation has been and continues to be regularly applied to studying the hydrodynamic performance of the SFD. Booker [31] provided a table of the journal bearing integral arising from the Reynolds Equation in order that workers may be spared the task of repeating such evaluations.

Inertial effects within SFD elements are neglected in many instances, particularly with a journal carrying substantial rotor weight. Ramli, Ellis and Roberts [32] suggest that inertial forces are significant due to a general increase in the bearing or gap Reynolds Number over recent years. The Reynolds Number, being the ratio of fluid inertia forces to fluid viscous forces, indicates the relative significance of inertial effects when it has a value in excess of unity. The paper discusses the prediction of inertial coefficients for

SFDs of particular land width to diameter, (l/D) ratios using a perturbation technique. Smith [33] published a general pressure differential equation for the inertial effects, similar to the two dimensional Reynolds Equation, which Ramli et al [32] solved using an iteration employing a finite difference approximation for the differentials. Results for inertial coefficients for short bearings and long bearings are given for different methods of solution and compared with the asymptotic results for (l/D) tending to zero (the Short Bearing Approximation) and to infinity (the Long Bearing Approximation). It was concluded that a simple solution for inertial coefficients, which required little computation was possible.

Roberts, Holmes and Mason [34] incorporated inertial forces within a theoretical linearized theory by introducing 'acceleration' coefficients associated with a 'hydrodynamic mass'. A least squares parametric identification technique was applied to discrete experimental time series. The resulting SFD damping and stiffness coefficient estimates converged after sufficient iteration and, correspondingly, the predicted state variable variation with time coincided with experimentally measured response. If coefficient iteration is limited to the damping term then convergence is degraded over a similar number of iterations. Limitations with this technique include the assumption of linear independence between the velocity and acceleration and the absence of 'memory' effects (which typically arise in cavitated films). Experimental free-decay tests with full film conditions for a range of parallel spring (beam) stiffness, static eccentricity and initial displacement provided data from which, with a knowledge of undamped natural frequencies and effective masses the various parameters could be identified. The Short Bearing

theoretical radial and transverse damping coefficients were generally lower than those identified from experiment. Experimental damping coefficient variation with static eccentricity was however similar to Short Bearing results. Experimentally determined inertial coefficients were generally an order of magnitude higher than those predicted by the theory.

The Short Bearing Approximation has been popularly applied to those unsealed SFDs employed in aero-engine rotor-bearing assemblies which have a small (l/D) ratio. The approximation assumes fluid flow within the SFD to be dominant in the axial direction and Mohan and Hahn [35] assumed this to be valid for $(l/D) < 0.25$ referring to [3] and others for justification of this figure. Mohan and Hahn indicated that at that time (1974) there was a lack of design data for SFDs. Dowson [2] made a similar suggestion about squeeze-film elements as a whole in 1986.

The paper [35] indicated the pitfall that improper SFD design can lead to transmissibilities rising above unity in some instances. Mohan and Hahn examined a two bearing SFD arrangement with a centrally preloaded rotor and employed the Capriz [36] expressions for a π, or 180° film. Distinction was made between three modes of response, namely inverted, whirl and chaotic vibrations. The effects and interaction of bearing geometry, fluid viscosity and rotor unbalance were discussed with reference to the effects on transmissibility and, in turn, on the implications on rolling element bearing life. The region of SFD operation within which linear theory may be usefully applied was identified. A design example was presented using the theory discussed.

Gunter, Barrett and Allaire [37] applied the Short

Bearing Approximation to the Reynolds Equation in their theoretical analysis. Using polar coordinates, they integrated the pressure expression in closed form assuming circular centred orbits. This assumption leads to a tangential force due to damping and a radial force due to stiffness within the fluid film. The effect of reducing these forces by a factor of four when a circular central supply groove is introduced was outlined. The desirable aspects of including a parallel retaining spring and undesirable cavitation effects were discussed. Practical application of this theory was developed for a two-spool jet engine. When cavitation occurs, it was demonstrated that SFD stiffness increases at a greater rate than damping as eccentricity increases. A non-linear transient analysis produced a rotor orbit time history and the effects of unbalance on maximum film pressures, transmissibility and the possibility of nonsynchronous whirl were indicated. Indications of SFD overload due to experimental observation of jump phenomena were presented. A range of conclusions was given including the possibilities for valid application of linearized coefficients (which are relatively constant for eccentricities below 0.4), for desirable phase between eccentricity and unbalance at operating speed and for the identification of bifurcation.

Feder, Bansal and Blanco [38] also studied the SFD forces resulting from circular centred orbits but used the Long Bearing Approximation to simulate the effect of end seals on discharge pressure. Variation of fluid extent was studied between the π film and the 2π film. Linear superposition of inlet and cavitation pressures was assumed theoretically. A circular centred orbit size and speed was stipulated in experimental tests. The radial (or stiffness) and tangential (or damping) force coefficients (known as Tondl coefficients) were evaluated

and compared with the test values derived from a digital test data reduction procedure. The coefficient normalization and pressure superposition were justified by the agreement between theoretical and experimental results. It was also demonstrated experimentally that radial force decreased (indicated by increasing eccentricity) as inlet pressure was increased upto the point where a full, 2π film was achieved.

The theoretical analysis of more general SFD theory often takes the form of a numerical integration of the film pressures to obtain SFD forces which are in turn involved in equations of motion whose solution is solved over some defined period of time by a powerful numerical method such as the Runge-Kutta method. Numerous texts covering numerical methods exist. Carnahan, Luther and Wilkes [39] presented an extensive range of numerical methods applicable to the solution of practical dynamic systems. Bert and Stricklin [40] compared the ability of six different numerical integration methods to generate the transient solutions to linear damped, non-linear conservative and non-linear non-conservative equations of motion for one degree of freedom. Two explicit methods, namely the central difference and Runge-Kutta methods and four implicit methods, namely the Houbolt, Newmark, Wilson Theta and Harmonic Acceleration methods were analysed. Comparing the accuracy of the peak values alone the explicit methods were the most efficient algorithms, with the the central difference method the best overall. High order methods with variable step and sometimes variable order have been successfully applied to SFD research.

Holmes [41] investigated the load-carrying capability of SFDs employing the Runge-Kutta-Merson method to perform the time history solution of the dynamic equations. The

SFD was shown to be unable to support a static force alone in the absence of an additional dynamic force. Dynamic force capacity arising from tangential and, or radial velocities was demonstrated. Chaotic solution of the equations of motion was shown to result when the SFD parameter, β was too low, where

$$\beta = \mu.R.l^3/(m.w.c^3) \quad ,$$

μ = oil viscosity,
R = mean radius,
l = land width,
m = rotor mass per land,
c = radial clearance and
w = rotational frequency.

The onset of chaotic behaviour of the SFD is relevant to the relatively recent studies into the occurrence of chaos in non-linear systems [12].

Humes and Holmes [42] employed the Runge-Kutta-Merson method to solve the same dynamic equations as presented in a preceding paper [41], but used the Booker integral table [31] to evaluate the π and 2π film SFD forces and introduced a parameter, "b" which determined the extent of subatmospheric film pressures. Adjustment of "b" allowed film force variation between a π and a 2π film, ie;

$$P = P_{\pi} + b(P_{2\pi} - P_{\pi})$$

where P = resultant film force,
P_{π} = π film force and
$P_{2\pi}$ = 2π film force.

Craven and Holmes [43] discussed the numerical solution

of the equations of motion of a reciprocating engine crankshaft utilising a Short Bearing approximation for bearing forces. A fast numerical method involving the trapezium rule and Newton iteration proved to be between five and ten times faster than the Runge-Kutta method. This was primarily due to the complex bearing load cycles requiring very small Runge-Kutta time steps for adequate accuracy. In comparison the unbalance excitation experienced by SFDs in turbomachinery is very simple and the time step size is primarily affected by the squeeze-film force non-linearities.

Guilhen, Berthier and Ferraris [44] employed the Runge-Kutta-Gill, Adams-Moulton and Newmark methods to study the instability of second order rotor-bearing systems whose matrices are non-symmetric due to gyroscopic effects and hydrodynamic bearing properties. All three methods provided satisfactory numerical convergence. The Newmark method was also used to produce the steady state response. Low damping caused lengthy transients which sometimes required prohibitive computation times before a steady state solution was reached.

Greenhill and Nelson [45] presented a secant root finding algorithm for application to rigid or flexible rotor, multiple SFD assemblies modelled with closed form SFD stiffness and damping expressions arising from the assumption of circular centred orbits. The algorithm iterated using a functional relationship between a proposed eccentricity ratio and the calculated unbalance response and it was sensitive to the increase in non-linear behaviour at higher eccentricity ratios. Applications of this method which were presented include a rigid rotor, single centralised, π film SFD system whose bistable response at sufficiently high unbalance factors was clearly demonstrated by the results from the

algorithm. Also flexible rotor, multiple SFD analysis was presented, culminating in a twenty element model with nine discrete masses, three SFDs and a total of eighty four degrees of freedom. Convergence problems were discussed and practical explanation for such shortcomings was provided.

Taylor and Kumar [46] also used the assumption of circular, centred and synchronous SFD orbits. The Short Bearing (Ocvirk) solution employing standard integrals [31] was applied to a rigid rotor, single parallel SFD and spring combination. The steady state theoretical solutions from a non-iterative technique were presented. The bistable amplitude, transmissibility and power dissipation characteristics of the response were produced for a range of unbalance and different SFD parameters. The power dissipation arising from the tangential film force components and its sensitivity to increases in unbalance was demonstrated. Such information would be useful in designing oil cooling equipment and studying the power requirements for starting up the machine. The discussion of this paper [46], by Hahn highlights the advantage of transient studies in studying solution stability.

The forces generated by SFD elements are non-linear for all but highly idealised situations. However, the SFD is often part of a practical assembly which can be modelled successfully employing linear theory which demands relatively small amounts of computation. If a non-linear SFD model is incorporated into a large linear model of the whole assembly then the effort required to achieve a solution becomes computationally exhaustive. The techniques applied to the linearization of journal bearing film force predictions can be readily adapted to the SFD application. Much research has been directed

towards achieving a satisfactory linear model for the SFD in order to maintain overall computational efficiency.

Holmes [47] extended the earlier work carried out by himself and other workers investigating the linear modelling of SFD film forces. A range of linear, quasi-linear and non-linear models employing the Short Bearing Approximation were examined. In this instance the SFD formed part of a vibration isolator, with a parallel retaining spring exhibiting a range of static eccentricity. Linear damping was studied by observing the effect of small perturbations of the journal centre (about a static equilibrium position) on the uncavitated film forces. Linear damping coefficients were then developed which depended on a static eccentricity determined from a knowledge of the rotor weight and the parallel spring stiffness. Displacement dependent, or quasi-linear coefficients were developed whose effect was adjusted at each step of a dynamic analysis. A feature of a linear analysis had been the inability of the coefficients to curb journal displacements to the degree exhibited by the more accurate quasi-linear analysis.

Holmes and Sykes [48] rapidly estimated the sizes and dispositions of large vibrations resulting from the combined action of rotating and static forces in rotor assemblies incorporating oil-film journal bearings and SFDs. Correspondence between the velocity and displacement coefficients for journal centre perturbation from a static equilibrium position and from a steady state orbit was demonstrated.

Holmes and Dogan [23] applied quasi-linear coefficients to a model comprising a flexible pedestal in series with a SFD supporting a rigid rotor. The effective damping and stiffness coefficients were derived from tabulated data

for a range of dynamic force. A mean static journal position and synchronous amplitudes in the horizontal and vertical directions were evaluated for each set of SFD governing parameters. Comparisons between the SFD displacement orbits of a number of quasi-linear and non-linear computations indicated the potential of such a method to improve the modelling of SFD operation in rotor-bearing assemblies by using computationally efficient linear analysis techniques.

Burrows, Sahinkaya and Kucuk [49] modelled SFD oil-film forces using estimated linear coefficients derived from application of a least-squares optimisation technique to the Reynolds Equation. The paper discussed the ability of analytical bearing coefficients to provide adequate linearized approximations of SFD film forces. The arrangement studied was a parallel SFD and retainer spring assembly exhibiting varying degrees of static eccentricity and attitude. It was concluded that linear coefficients provide adequate predictions only when running at low speeds with a small unbalance, whereas the least-squares estimates are applicable to a range of operating conditions, such as resonant conditions.

Stanway, Burrows and Holmes [50] carried out discrete-time modelling of the SFD. For a parallel SFD and retaining spring combination experimental PRBS (pseudo-random binary sequence) perturbation was applied to the SFD journal within its static housing for a range of static journal eccentricities. The input PRBS was provided by an electromagnetic shaker and measured together with the journal amplitude response. From these the frequency characteristics of the assembly were derived. The oil pressure was maintained at a level capable of providing a full film. The damping coefficients only were sought and results from experiment

were compared with those from the Short Bearing theory. With PRBS displacements less than ten per cent of the clearance, the linearization technique was appropriate. The introduction of cavitation leads to cross coupling effects and subsequent research has examined this in detail.

Stanway, Firoozian and Mottershead [51] applied a time domain filtering algorithm to the displacement response to single frequency excitation. A similar arrangement was employed as in previous research [50] with an unsealed SFD. Direct and cross damping coefficients for a π film SFD model were compared with experimental estimates for the uncoupled and coupled cases. The damping coefficients estimated from experiment were generally lower than those predicted by the π film. The frequency response functions from identified models and FFT analysis of experimental data were also compared with results from the π film theory.

Szeri, Raimondi and Giron-Duarte [52] derived linear force coefficients for SFDs. Analysis used the full Navier-Stokes equations and simplified the complicated expressions by an order of magnitude analysis. The inertial contributions to the film forces were discussed. With a 2π film the magnitude of the inertial coefficients varied linearly with the Reynolds Number. Conclusions drawn include the importance of inertial effects in SFDs with large clearance, high speed and low viscosity, that is when the gap Reynolds Number, R_e is greater than unity.

Chen and Xu [53] employed harmonic balance to estimate equivalent Fourier displacement coefficients for a rotor supported in a SFD without centralisation. SFD orbits demonstrating subharmonic rotor motion were derived from

synchronous and non-synchronous Fourier coefficients and compared with the response obtained from Runge-Kutta solutions. Two cases were presented with only light static loading with respect to the dynamic unbalance force. Xu [54] applied harmonic balance to the synchronous response of simple rigid and flexible rotor assemblies. Again the harmonic balance results compared well with Runge-Kutta solutions for the limited results presented. Simple analysis of bistable operation was presented but no results around natural frequencies were discussed.

Feng and Hahn [55] compared theoretical results from incompressible lubricant models (cavitation at absolute zero pressure and at ambient pressure) and from homogeneous compressible film models with experimental results from a vertical axis SFD and parallel spring assembly. The compressible film model of Hayward [56] gave a higher viscosity for a cavitated film than for an uncavitated film whereas the Isbin model [57] gave the reverse. Thus the Hayward model compared quite well with the zero cut-off incompressible model and the Isbin with the π film model. Application of the Routh stability criterion revealed that, in agreement with incompressible models, the compressible models only predict instability for the intermediate of the three solutions at each speed within the bistable region. Over the narrow range of bearing parameter, the Hayward model compared best with experimental results and the zero pressure cut-off was shown to give nearly as good a comparison.

Feng and Hahn [58] provide so-called jump maps indicating the regions of bistable operation for ranges of SFD bearing parameter, speed and unbalance. The effect of increased inlet pressure in suppressing jumps was also

noted. The test rig used was an idealised vertical axis, single SFD configuration with a parallel retaining spring. Experiment and theory lacked correlation throughout and it is considered that little confidence can be placed in the use of the jump maps for design. Quantitative data regarding SFD bistable operation should only be applied when similarity between SFD designs is maintained and the configuration of the SFD within rotor-bearing assembly is also comparable.

Nikolajsen and Holmes [59] demonstrated experimentally the effectiveness of SFDs as vibration isolators within a flexible rotor-bearing system involving gyroscopic effects from rotor mounted discs. Oil film journal bearings were in series with the SFDs. The use of Belleville washers as linear springs enabled easy variation of support stiffness which is not possible with a squirrel-cage arrangement. Linear theory was utilised and response predictions, when compared with experimental responses proved to be reasonable. Larger values of SFD damping resulted in well defined instability threshold speeds both theoretically and experimentally. Lower damping produced stable responses with the onset of non-synchronous whirling at speeds between two and three times the first critical speed. A second whirl region would appear at higher speeds. With increasing oil viscosity firstly the second and then the first whirl regions would be eliminated. Such non-linear vibrations clearly impair the system performance.

Dyer and Reason [60] investigated experimentally the generation of tensile stresses in a journal bearing oil film. A maximum tensile stress of 740 kN/m^2 was recorded. Generation of tensile stresses was shown to be prevalent but sporadic in nature over a number of journal cycles when, if tensile stresses were not developed then the

minimum pressure would be similar to the oil vapour pressure over a finite angular region. Factors inhibiting tensile stress development by encouraging cavitation include bearing surface finish, the presence of dissolved gas, successive fluid tensioning, fluid particulate content and fluid viscosity. The generation of tensile stress can be greatly enhanced by squeeze film effects, as in SFDs, and is dependent on the rate of divergence between the bearing surfaces, such that no tensile stress is developed above a critical eccentricity ratio,

$$\epsilon_{(CRIT)} = D / c ,$$

where 'D' is the critical rate of bearing surface divergence (in m/rad). It was also noted that bearing surface damage could be caused by tensile stress in addition to well recognised cavitation effects.

Walton, Walowit, Zorzi and Schrand [61] presented experimental photographic evidence demonstrating the development and behaviour of cavitation within SFDs with groove feed/drain and hole feed/drain facilities. Typical aircraft gas turbine SFD designs were employed with speeds upto 20 000 rpm. The grooved SFD provided evidence supporting the popular assumption that fluid flow is predominantly axial. Also an increase in the oil supply pressure was shown to increase the minimum speed at which cavitation begins. However, contrary to popular assumption was the observation that significant flow reversal and evidence of cavitation within the groove takes place. Cavitation within a grooved SFD was stable and repetitive whereas, the hole feed/drain SFD demonstrated a less repeatable cavitation pattern and indicated the need for comprehensive analysis. In general the need for the implementation of more complicated and more accurate boundary conditions within analyses is

required if progress is to be made with the application of existing methods.

Zeidan and Vance [62] studied the cavitation taking place in a controlled orbit SFD with high speed motion pictures and piezoelectric pressure transducers. Five regimes of SFD operation were identified through a speed range upto 5 000 rpm and with an eccentricity of 0.45. The inadequacy of the popular π film approximation was illustrated. Air ingress through serrated piston rings, sealing the SFD, reduced the negative pressure amplitude and inhibited vapour cavitation. Although detrimental to damping, the air bubbles can reduce the potential of bearing surface damage due to vapour cavitation. Pressure generation within the supply groove was identified due to axial flow from the SFD land into the groove.

Botman and Samaha [63] studied experimentally the behaviour of supercritical rotors mounted vertically within a bearing arrangement incorporating SFDs. Rotor speeds of upto 55 000 c/min were achieved by applying a multiplane, multispeed balancing technique employing the least squares method. Rotor response was, generally, dominated by a bistable region around the first critical speed with subharmonic resonance featuring at higher speeds still. The effect of reducing the SFD clearance, without increasing the oil supply pressure, was to degrade the response by introducing rotor instability at very high speeds. A higher supply pressure, with the smaller clearance, eliminated the instability. It was concluded that bistable operation is more important than subharmonic resonance, although both are deleterious to rotor operation. The critical speeds showed some dependence on rotor unbalance and linear transfer matrix (critical speed) and unbalance response results were compared with experiment.

Cookson, Feng and Kossa [64] studied the effect of journal misalignment on SFD film forces. The oil film pressure profile is affected by axial and angular misaligning couples. SFD film force analysis was carried out employing the Simpson integration of the SFD film pressures with 72 circumferential and 20 axial divisions per land and was considered accurate for pressure resolution. It was concluded that significant increases in transmissibility can arise from journal misalignment and, for the case presented, a maximum misalignment slope of 0.0005 radians was required for such effects to be negligible.

Holmes and Dede [65] demonstrated the nonlinear characteristics of rotor response resulting from the complicated unbalance generated by two rotors. (Practical aero-engine assemblies comprise upto three nested rotors mounted in SFD bearing arrangements.) One rotor was coupled to the SFD housing and the other was coupled to the journal. The rotors could rotate at differing speeds and in the same or different directions. The SFD experimental response illustrated bistable operation and subharmonic resonance. Spectral analysis demonstrated the subharmonic frequencies and also indicated the presence of combination frequencies. Combination frequencies resulted from both the addition and subtraction of the rotor speeds. The non-linear characteristics borne out in experimental results were demonstrated by theoretical analysis. Nayfeh [66] demonstrated that a single degree-of-freedom system involving quadratic and cubic non-linearities, when excited by two frequencies, produced a response containing combination tones very similar to those demonstrated by Holmes and Dede [65].

Sideband frequencies may also be present in the rotor-

bearing response. Neilson and Barr [67] demonstrated the sideband generation using a bearing support with a discontinuous stiffness characteristic. A squirrel cage support acted alone upto a particular radial displacement after which housing contact with a snubber ring caused a second, stiffer squirrel cage to provide additional bearing housing support through the snubber ring. The radial clearance between the bearing housing and the snubber ring was of similar dimensions to an aero-engine SFD. It was found that the sideband spectral spacing corresponded to the frequency of contact between the housing and snubber. Thus the sidebands are combination frequencies. Jumps down with increasing speed were generated as the speed passed through and beyond the two dominant natural frequencies. Earlier studies by Black [68] on the effect of contact between a whirling rotor and a stator had also demonstrated various jump phenomena for conditions of synchronous rotor whirl. Also counterwhirl with rolling or slip at the contact was studied. It was concluded that, dependent upon the rotor and stator damping, there is a minimum angle of friction below which counterwhirl is impossible.

2.3 Assessment of Previous Work and Direction for Current Research

Although published work generally shows an appreciation of the significance of SFD nonlinear phenomena it has not pursued the analysis of phenomena observed in the responses of practical rotor-bearing assemblies to assess the influence of pertinent rotordynamic elements such as SFD misalignment and support conditions. Rather, previous research has tended to simplify the problem. This has led

to a good understanding of the response of the single, centralised, π film SFD configuration in particular. Deviations from this design have received very little attention, considering the extent to which practical considerations deprive the assembly of accurate SFD alignment.

The results from research published to date into the non-linear phenomena associated with SFDs have all been directed to idealised test facilities for ease of modelling. The range of phenomena reported has been limited. Simandiri and Hahn [7] present one occurrence of jump phenomena in a range of experimental studies supporting their theoretical modelling [69] in which a range of jump phenomena are presented and a comprehensive range of 'design' data is discussed. The range of validity [7] is discussed quite well except that the experimental SFD sealing conditions are not detailed.

Quantitative results should only be applied to SFDs with similar geometries, including the supply groove depth and discharge paths. Similar criticism can be levelled at the range of validity of the 'design' data presented by Feng and Hahn [58]. All of the results are for the idealisation of statically centralised SFDs. The validity of this assumption, even though it may be a design aim of those companies employing such bearing assemblies, becomes less valid when the practical build up of manufacturing tolerances and in-service assembly distortions cause the static SFD set up to become eccentric.

White [30] provides an early and extensive study into SFDs which demonstrated jump phenomena with a vertically mounted rigid rotor. In practice, such a configuration is rarely found in turbomachinery. White was unable to draw

useful conclusions apart from the fact that jumps occurred at well defined speeds, dependent on the SFD parameters.

Gunter et al [37] provide very limited experimental evidence of jump phenomena and the idealised condition of a static central SFD is assumed, enabling simplified theoretical modelling. It is noted with interest that, where provided, the SFD sealing appears to be carried out by O-rings. It should be emphasised that the dynamic characteristics of O-rings vary non-linearly with a range of parameters and is particularly sensitive to temperature and amplitude variations as discussed by Smalley, Darlow and Mehta [70]. Xu [71] studies jump phenomena as part of the transient analysis of flexible rotor-bearing assemblies.

The published research generally presents a large amount of information regarding the ideal operation of SFDs and, in the pursuit of quantitative experimental correlation, test rigs have been designed to control such variables as SFD misalignment. When considering the practical application of SFDs it is necessary to appreciate such desirable ideal design configurations. However, the accurate control of SFD alignment within current aero-engine assemblies is not possible, particularly when the engine is of a modular build. Therefore, an understanding of how SFD misalignment and its interaction with other variables, such as SFD housing support flexibility, is also required at the design stage if the potential for non-linear phenomena is to be appreciated prior to commissioning. It is clear that useful research would involve a study of those SFD variables of practical significance which have not been appreciated by current published work.

No published research (known to the author) studies the effect of rotor-bearing alignments on the presence of jump phenomena and subharmonic resonance. The preloading of flexible bearing supports, such as squirrel cages, and the consequent SFD static eccentric conditions determine the severity of the non-linear response generated in practical situations. Simply, for a given unbalance and other dynamic variables, operation of a SFD, supported concentrically by a parallel squirrel-cage arrangement, may satisfactorily attenuate transmitted rotor forces. However, if the same arrangement had a static SFD eccentricity then the SFD forces generated would be significantly more non-linear and could well introduce undesirable non-linear phenomena into the running speed range.

A broad understanding of the qualitative effects of misalignment would be highly instructive at the design analysis stage. The influence of individual components within a full assembly would be very difficult to assess unless the assembly is built up in stages from a relatively simple assembly whose components can be assessed progressively.

Chapter 3 RESEARCH OBJECTIVES

The lack of previous research into the influence of manufacturing assembly tolerances and SFD support considerations on non-linear phenomena called for a broad investigation into these parameters. Broad objectives were proposed which, it was considered, could be achieved within the time limit of the Research Grant. The research objectives were as follows:

1 To reproduce non-linear phenomena within the experimental response of a rotor-bearing assembly test rig for a range of configurations (Table 3.1). Primary consideration was to be given to the experimental simulation of jump phenomena, as observed in actual aero-engine tests. Previous reported experimental occurrences were limited. The objective of the research forming this thesis was to establish, as far as possible, a comprehensive range of results demonstrating non-linear jumps.

Another primary engine vibration problem, namely subsynchronous resonance was also to be a significant non-linear response embraced by the investigation.

2 The configurations (Table 3.1) were chosen to promote a comprehensive illustration of the influence of individual rotordynamic components upon the overall response. Thus the configurations would initially comprise of a single SFD and proceed to involve two SFDs where each damper experienced a range of static set-up conditions.

The choice of configurations was made to enable the study of as wide a range of practical assemblies as the time allowed. The configuration chronology was designed to facilitate the appreciation of each dynamic element's contribution to the overall assembly response; the final assembly was to demonstrate the essential features of the sponsor's design concept.

Rig configuration 1a (Table 3.1) would involve one SFD, SFD1 part way along the rotor, its housing rigidly supported to ground, and flexible support, k_2 at the bearing further towards the free rotor end. This would permit two degrees of freedom (DOF), namely the horizontal and vertical displacement of the rotor relative to ground. SFD1 would be centrally positioned with no static eccentricity. Configuration 1b would introduce static eccentricity to SFD1 thus increasing the effective rotor weight that SFD1 carried.

Rig Configuration 2a would introduce the action of SFD2 between the flexibility, k_2 and the rotor. There would now be four DOF, namely the horizontal and vertical rotor and SFD2 housing displacements relative to ground. Configuration 2a would maintain SFD1 in a statically centralised condition and the SFD2 journal would carry the rotor weight so that it was fully eccentric, E_{o2} equal to 1.0, due to gravity in the static condition. The effect of introducing a static eccentricity to SFD1 would then be studied. By further increasing this static eccentricity, E_{o1} to 1.0 and centralising SFD2, configuration 2b would be achieved.

By introducing the flexible support, k_1 between the SFD1 housing and ground the rig would now exhibit six DOF, that is the horizontal and vertical rotor, SFD2 housing and SFD1 housing displacements relative to ground. With all three bearings statically aligned, the rotor weight would dictate configuration 3a, with both E_{o1} and E_{o2} equal to 1.0. Then configuration 3b could be achieved from configuration 3a by centralising SFD1, illustrating off-loading of SFD1 due to misalignment of its housing.

3 The rotor-bearing assemblies were to be modelled theoretically to assess the capability of numerical predictions to reproduce non-linear phenomena. A general model of the SFD, allowing variations in cavitation and supply pressures, was to be applied to the rig model and analysed using numerical integration. Simpler analysis of models using analytical non-linear SFD film forces and linear damping approximations was to be used to provide additional information.

4 Theoretical and experimental results were to be analysed and presented, for the most part as rotor centre orbits, frequency response graphs and waterfall diagrams. These popular forms are in keeping with general rotordynamic practice.

5 The physical mechanisms which promote non-linear phenomena in practical assemblies were to be sought. Broad guidelines for improving the vibration response of subsequent rotor-bearing assembly designs arising from the results were to be identified, if possible.

Chapter 4 THEORETICAL ANALYSIS OF ROTOR-BEARING ASSEMBLIES

The non-linear analysis assumed the following;

1. The Reynolds Equation and the Short Bearing approximation applied.
2. The rotor remained rigid.
3. The flexible SFD housing support bars contributed a constant, linear radial stiffness to the system.
4. Rotor gyroscopic forces were relatively insignificant.

The first assumption implied that the Gap Reynolds number was less than unity and that the SFD land length to mean radius ratio, (l/R) was small.

4.1 Squeeze-Film Damper Film Forces

The Short Bearing Approximation to the Reynolds Equation was applied to the SFD models as the axial lengths were short in comparison with the SFD radii, see Appendix 1.

The dynamic pressure generated at any point in a SFD can be derived as discussed in Appendix 2 and is given by;

$$\bar{P}(\phi,\bar{z}) = \frac{6(1/R)^2(\epsilon'.\cos\phi + \epsilon.\alpha'.\sin\phi)(\bar{z}^2 - 0.25)}{(1 + \epsilon.\cos\phi)^3} + \bar{P}sup(0.5 - \bar{z}) \quad \ldots\ldots\{4.1\}$$

where $\bar{z} = 0$ at the mid-land position,
$\bar{z} = -0.5$ at the land supply edge and
$\bar{z} = 0.5$ at the land discharge edge.

Now, referring to Fig 1.1, the forces are derived by integration of the pressure equation,

$$P1 = - \mu.w(c/R)^2.R.1 \int_{\phi_2}^{\phi_1} \int_{-½}^{½} \bar{P}(\phi,\bar{z}).\cos\phi.d\bar{z}.d\phi$$

$$P2 = - \mu.w(c/R)^2.R.1 \int_{\phi_2}^{\phi_1} \int_{-½}^{½} \bar{P}(\phi,\bar{z}).\sin\phi.d\bar{z}.d\phi \quad \ldots\ldots\{4.2\}$$

The effect of cavitation on the force is realised by assigning the pressure, $P(\phi,z)$ to the cavitation pressure if the value of $P(\phi,z)$ falls below the cavitation pressure.

4.2 Equations of Motion

The rotor-bearing assembly with two SFDs can be modelled as a dynamic system with the following equations, by taking moments about the pivot bearing. Referring to diagrams of the mathematical models of the experimental rig configurations in Figs 4.1, 4.2 and 4.3 (shown schematically in Table 3.1) the equations of motion are;

Configurations 1a,b

$$\ddot{y}_2(I/b) = a.Pc.\sin(w.t) - b(k_2(b/f)\epsilon_1.c_1.\sin(\alpha_1)) - f(P1_1.\sin(\alpha_1) + P2_1.\cos(\alpha_1)) - m.g.d$$

$$\ddot{x}_2(I/b) = a.Pc.\cos(w.t) - b(k_2(b/f)\epsilon_1.c_1.\cos(\alpha_1)) - f(P1_1.\cos(\alpha_1) - P2_1.\sin(\alpha_1))$$

.....{4.3}

Configurations 2a,b and 3a,b

$$\ddot{y}_2(I/b) = a.Pc.\sin(w.t) - b(P1_2.\sin(\alpha_2) + P2_2.\cos(\alpha_2)) - f(P1_1.\sin(\alpha_1) + P2_1.\cos(\alpha_1)) - m.g.d$$

$$\ddot{x}_2(I/b) = a.Pc.\cos(w.t) - b(P1_2.\cos(\alpha_2) - P2_2.\sin(\alpha_2)) - f(P1_1.\cos(\alpha_1) - P2_1.\sin(\alpha_1))$$

.....{4.4}

These equations describe the rotor motion at the SFD2 journal in a cartesian (x,y) coordinate system. A comprehensive form of these equations of motion can be

written, non-dimensionally, as

Configurations 1a,b

$$y_2'' = Qc_2.\sin(w.t) - (\bar{k}_2.\epsilon_1.\sin(\alpha_1))(c_1/c_2)(b/f)$$

$$- (c_1/c_2)(b/f)(\bar{P}1_1.\sin(\alpha_1) + \bar{P}2_1.\cos(\alpha_1)) - Qs$$

$$x_2'' = Qc_2.\cos(w.t) - (\bar{k}_2.\epsilon_1.\cos(\alpha_1))(c_1/c_2)(b/f)$$

$$- (c_1/c_2)(b/f)(\bar{P}1_1.\cos(\alpha_1) - \bar{P}2_1.\sin(\alpha_1))$$

.....{4.5}

Configurations 2a,b and 3a,b

$$y_2'' = Qc_2.\sin(w.t) - (\bar{P}1_2.\sin(\alpha_2) + \bar{P}2_2.\cos(\alpha_2))$$

$$- (c_1/c_2)(b/f)(\bar{P}1_1.\sin(\alpha_1) + \bar{P}2_1.\cos(\alpha_1)) - Qs$$

$$x_2'' = Qc_2.\cos(w.t) - (\bar{P}1_2.\cos(\alpha_2) - \bar{P}2_2.\sin(\alpha_2))$$

$$- (c_1/c_2)(b/f)(\bar{P}1_1.\cos(\alpha_1) - \bar{P}2_1.\sin(\alpha_1))$$

.....{4.6}

where $\bar{P}1,2_2 = P1,2_2.b^2/(I.c_2.w^2)$

$$\bar{P}1,2_1 = P1,2_1.f^2/(I.c_1.w^2)$$

and $y_2'',x_2'' = \ddot{y}_2,\ddot{x}_2/(c_2.w^2)$

Variation in the SFD static misalignment conditions is

achieved by employing the term δ. Thus, converting the cartesian rotor motion at SFD2 relative to ground to the SFD1 polar motion for configurations 2a,b;

$$\epsilon_{y1} = Z.\bar{y}_2 - E_{o1} + \delta \qquad \epsilon_{y1}' = Z.y_2'$$

$$\epsilon_{x1} = Z.\bar{x}_2 \qquad \epsilon_{x1}' = Z.x_2'$$

$$\epsilon_1 = (\epsilon_{x1}^2 + \epsilon_{y1}^2)^{1/2}$$

$$\alpha_1 = \tan^{-1}(\epsilon_{y1}/\epsilon_{x1})$$

$$\epsilon_1' = (\epsilon_{x1}.\epsilon_{x1}' + \epsilon_{y1}.\epsilon_{y1}') / \epsilon_1$$

$$\alpha_1' = (\epsilon_{x1}.\epsilon_{y1}' - \epsilon_{y1}.\epsilon_{x1}') / \epsilon_1^2$$

where $Z = (f.c_2/b.c_1)$

.....{4.7}

It has been shown [72] that the SFD housing mass of the test facility for a series SFD and spring configuration has little influence on the rotor dynamics. Thus, neglecting the SFD2 housing mass the force prevailing in the spring, k_2 must equal and oppose the resultant SFD2 film force. Therefore, we can conclude that for configurations 2a,b and 3a,b that the following equations apply

$$\bar{k}_2(\bar{y}_2 - \epsilon_2.\sin(\alpha_2)) = \bar{P}1_2.\sin(\alpha_2) + \bar{P}2_2.\cos(\alpha_2)$$

$$\bar{k}_2(\bar{x}_2 - \epsilon_2.\cos(\alpha_2)) = \bar{P}1_2.\cos(\alpha_2) - \bar{P}2_2.\sin(\alpha_2)$$

.....{4.8}

and, similarly, for Configurations 3a,b only

$$\bar{k}_1(\bar{y}_1 - \epsilon_1.\sin(\alpha_1)) = \bar{P}1_1.\sin(\alpha_1) + \bar{P}2_1.\cos(\alpha_1)$$

$$\bar{k}_1(\bar{x}_1 - \epsilon_1.\cos(\alpha_1)) = \bar{P}1_1.\cos(\alpha_1) - \bar{P}2_1.\sin(\alpha_1)$$

.....{4.9}

where $\bar{x}_1 = \bar{x}_2(c_2/c_1)(f/b)$

$\bar{y}_1 = \bar{y}_2(c_2/c_1)(f/b)$.

4.3 The 2π Film and π Film Squeeze-Film Damper Models

The 2π or full squeeze-film is uncavitated. The π or half squeeze-film model consists of a 180° cavitation zone of full damper land width with the rest of the clearance full of fluid. Where atmospheric pressure is considered as a zero gauge pressure datum, both of these solutions assume zero supply pressure and zero outlet pressure. The 2π film implies significant tensile stress whereas the π film solution assumes cavitation occurring where the fluid pressure falls below atmospheric pressure (14.7 psi absolute).

The purpose of assuming either a 2π film or π film is that these two simplified solutions of the Short Bearing Approximation give simple expressions for the stiffness and damping forces P1, P2 generated by the squeeze-film, see Table 1.1 and Appendix 3. When these two forces are substituted into the equations of motion ({4.3}), equations {4.9} are derived by non-dimensionalising. Equations {4.10} are expressions for the phase between the unbalance force and the attitude of the journal, $(w.t - \alpha_1)$, Fig 4.1.

2π Film; $Q_{c1}^2(w/w_n)^4(1 - \epsilon^2)^3/\epsilon^2 = (1 - \epsilon^2)^3\{1 - (w/w_n)^2\}^2 + A_1^2.(w/w_n)^2$

.....{4.9a}

π Film; $Q_{c1}^2(w/w_n)^4(1 - \epsilon^2)^3/\epsilon^2 = (1 - \epsilon^2)^3\{1 - (w/w_n)^2\}^2 + A_1^2(w/w_n)^2\{1/4 + 4.\epsilon^2/(\pi(1 - \epsilon^2))\} + 4.\epsilon(1 - \epsilon^2)A_1(w/w_n)\{1 - (w/w_n)^2\}/\pi$

.....{4.9b}

2π Film; $\tan(w.t - \alpha_1) = A_1.\bar{k}_1^{0.5}/\{(\bar{k}_1 - 1)(1 - \epsilon^2)^{1.5}\}$

.....{4.10a}

π Film; $\tan(w.t - \alpha 1) = A_1.\bar{k}_1^{0.5}/[2\{2.A_1.\bar{k}_1^{0.5}.\epsilon/((1 - \epsilon^2)^2) + (\bar{k}_1 - 1)(1 - \epsilon^2)^{1.5}\}]$

.....{4.10b}

Where $\bar{k}_1 = (w_n/w)^2$.

4.4 Computation Techniques

Computation was carried out using the Fortran 77 high level programming language, compiled and executed by Version 3 of VS Fortran implemented on the University of Southampton Computing Service's IBM 3090 mainframe computer. Vectorisation of the code was employed during compilation in order to optimise the computational speed where applicable.

Two different numerical techniques were required to solve the system behaviour using the simple 2π or π film models and the general Short Bearing model, as described below.

4.4.1 2π Film and π Film Computation

The 2π and π film equations {4.9} were solved for eccentricity ratio, ϵ, and phase, $(w.t - \alpha)$, (the other parameters being known) using a relatively simple iteration technique.

4.4.2 General Short Bearing Solution Computation

The computation employed to obtain predictions using the general Short Bearing solution involves the use of two numerical methods, Simpson's Integration for the SFD pressure field and a Runge-Kutta method applied to the system's differential equations.

The computation technique took the form of the generation of the system's response to an initial set of parameters, the unbalance, rotor speed and SFD pressure conditions having been stipulated.

Each degree of freedom (DOF) within the model had three associated variables, namely displacement, velocity and acceleration. The initial set of system displacement and velocity values were used to calculate the mesh, or array, of SFD pressures. Integration of these pressures, over the clearance area, using Simpson's method yielded an estimate of the film forces developed by the SFD. An acceptable pressure resolution was obtained with eleven points along the land width and thirty seven points around the damper circumference and these dimensions were used as the pressure array dimensions. The Reynold's equation assumes that, because the film thickness is very small, there is a negligible pressure variation over the film thickness. This meant that the forces experienced by the journal and housing were assumed to be identical.

The film force estimates were incorporated in the equations of motion and the system's acceleration vectors were calculated. Acceleration and velocity vectors were used by the Runge-Kutta-Merson algorithm to predict the velocity and displacement vectors, respectively, forward in time. The results were checked against an acceptable error band. If the error was very small then the time step was increased and if the error was large then the time step was reduced. When the results had a calculated error within the band then these results were accepted. In this way the time history developed through the transient response and the steady state response was determined. The variable time step helped the numerical method to traverse the required non-dimensional time

range efficiently.

Rig configuration 1a, involving two DOFs, used initial eccentricity values of the smallest eccentricity ratio solution from the π film model. Also, the value of ϵ_1' was set to 0.1 and α_1' was set to the rotor speed. The steady state solution was evaluated for a non-dimensional time of upto 250 radians (over 40 rotor revolutions).

The initial values for configuration 1b were experienced guesses. If no steady state orbit solution was forthcoming after a non-dimensional time of 150 radians then the last calculated displacement and velocity values were submitted as a new set of initial values. Configurations 2a,b each constituted a four degree of freedom (DOF) model and initial values were estimated from an understanding of the static conditions and after some preliminary computation. Where there was doubt whether the transient had decayed, the integration was continued to 250 radians.

The results of prime interest, to date, have been the displacement orbit size and the phase between unbalance force and displacement. These were compared with the experimentally observed rig behaviour.

4.4.3 Frequency Analysis

To carry out a theoretical frequency content study of the assembly vibration response a discrete vibration time series had to be generated. The discrete time series was derived from numerical time history results using the Runge-Kutta-Merson method. The sampled time interval, in seconds, had to be set at a constant value, depending on

the FFT requirements. For comparison with the experimental results, this time series had to be generated after the transient response had decayed, leaving a steady-state response.

A Radix-2 Fast Fourier Transform (FFT) algorithm, as discussed in [16], was programmed, initially, to manipulate a 2048 or 2052 element discrete time series into a single or averaged 1024 element positive frequency spectrum, respectively. This method allowed the frequency content of the experimental results to be compared with the frequency content of the theoretical results by means of individual spectra and by constructing equivalent waterfall diagrams using GINO graphical plotting routines.

Initially the discrete time series was obtained from the Runge-Kutta-Merson by stepping non-dimensional time (w.t) by the series time interval. If the error was such that the time step had to be reduced, then the time step was halved. If the error was still too large then the time step was halved again, and so on. When the error dictated that the time step be increased then the time step was doubled until it was equal to the time series interval. In this way the time step was always some integer proportion of the series interval. This first method was used to obtain spectra with a 0.2 Hz resolution, directly comparable with the experimental results. However, the storage required (even for the spectra of one SFD) and the CPU time required to generate discrete time series in excess of five seconds duration was prohibitive.

A more efficient means of deriving the spectral content of time histories was developed which did not interfere with the original Runge-Kutta-Merson algorithm. During the integration a check was kept on the time so that, if

the time became greater than the next time value required in the series, then the Runge-Kutta time and step size were stored and the time was set to the value required by the series. The values of the dynamic parameters were then calculated at that time. Then the stored time and step size were reinstituted and the Runge-Kutta-Merson was allowed to proceed normally again until the subsequent series time value was exceeded. In this way an accurate discrete time series was obtained without degrading the efficiency of the numerical integration. Five frequency resolutions were programmed (0.2, 0.25, 0.5, 1.0 and 7.0 Hz), still maintaining a simple FFT application.

Results employing a 1.0 Hz resolution (requiring a 512 element discrete time series) sufficed and typically 45 minutes to one hour of CPU time was required to generate the spectra for a waterfall diagram, compared with about four hours for 0.2 Hz resolution.

Chapter 5 THEORETICAL RESULTS

In order to appreciate the theoretical prediction of non-linear jump phenomena and subsynchronous resonances the following provides some simplified analysis. To demonstrate the development of jump phenomena in the response of a system with a non-linear spring characteristic consider the undamped equation of motion,

$$m.\ddot{x} + f(x) = P_c\cos(wt) \qquad \ldots\ldots\{5.1\}$$

where $f(x)$ is a non-linear hardening spring force given by the force versus maximum displacement curve of Fig 5.1. If it is assumed for the purposes of this illustration that the response, $x(t)$ is sinusoidal and synchronous and of the form

$$x(t) = x_o\cos(wt) \qquad \ldots\ldots\{5.2\}$$

then, at the point of maximum displacement, it can be shown that

$$f(x_o) = P_c + mw^2x_o \qquad \ldots\ldots\{5.3\}$$

The amplitude of the forced vibration, x_o can be found using Fig 5.1. The point of intersection of the spring characteristic curve, $f(x_o)$ with the straight line of ordinate intercept, P_c and gradient $\tan^{-1}(mw^2)$ gives the maximum amplitude, x_o at the particular frequency, w and this straight line represents the right hand side of

equation {5.3}. For simplification, assuming that the forcing, P_c is independent of frequency then the straight line ($P_c + mw^2$) intersects the ordinate at the same point, P_o for any frequency. The corresponding response curve can be constructed, Fig 5.2.

The points marked A_1, A_2, etc in Fig 5.2 correspond to the similarly labelled points in Fig 5.1. Thus the minimum jump frequency corresponds to points A_3, B_3 and C_3 where B_3 and C_3 are coincident. In this undamped case the upper branch, points A and C, continues indefinitely. This demonstration of a hardening response is considered more fully by Den Hartog [5].

The forcing due to unbalance increases with speed and the non-linear response with damping is of the form of Fig 1.3. In this instance the amplitude is zero when the rotor is stationary and tends to an asymptote at high speeds. The response could be constructed from Fig 5.1 by observing the variation of unbalance, P_c with rotor speed.

The theoretical possibility of half engine orders, 1/2 EO, can be simply assessed by considering a non-linear stiffness ($k + \Phi x$) and that the system satisfies the differential equation;

$$m.\ddot{x} + (k + \Phi.x)x = P_s + P_c.\cos(wt) \qquad \ldots\ldots\{5.4\}$$

Assuming that a possible solution is of the form

$$x = A.\cos(wt/2),$$

then

$$A(k - mw^2/4)\cos(wt/2) + \Phi A^2/2 + \{\Phi A^2\cos(wt)\}/2$$

$$= P_s + P_c\cos(wt)$$

and this equation is satisfied for

$$A = \sqrt{(2P_s/\Phi)} \quad ,$$

$$A = \sqrt{(2P_c/\Phi)} \quad \text{and}$$

$$w = 2\sqrt{(k/m)} \quad .$$

....{5.5}

The first two conditions of equations {5.5} imply $P_s = P_c$, which happens to be conducive to rattle within a SFD since the static force, P_s is just neutralised by the dynamic force, P_c. The third condition indicates that a response, x at the system natural frequency is possible if the rotor speed is twice that natural frequency. Furthermore, if the non-linear stiffness is considered to have the form $(k + \Phi_1 x + \Phi_2 x^2)$ then the theoretical possibility of response at both 1/2 EO and 3/2 EO can be shown.

5.1 The 2π Film and π Film Model Predictions

The amplitude and phase using the 2π and π film solutions for configuration 1a, say depend only upon the values of w/w_n, A_1 and Q_{c2}. The value attributed to the SFD1 "A" parameter, A_1 can be debated. The traditional algebraic expression for A_1, given in the nomenclature, is for the two land SFD where the lands are assumed to be completely uncoupled by the circular circumferential oil supply groove and the oil within the groove is considered to

generate negligible film forces of its own. If the lands are considered fully coupled then the net effect is that A_1 takes on a value four times that given by the traditional two land expression. This is because A_1 is proportional to land width cubed and inversely proportional to the square root of the product of the mass and stiffness. When compared with the traditional two land model, the single land of double length carries twice the rotor weight and experiences twice the support stiffness per land.

In practice, it is expected that, although the SFD design traditionally implies the two land assumption, the effective A_1 will lie between the two extremes. For this reason two values of A_1, namely 0.02132 and 0.08528 were studied as these two extremes.

Firstly with the assumption of two uncoupled SFD lands, the predictions of the 2π film solutions in Fig 5.3 indicate responses which resemble that of a second order system. As the frequency ratio, w/w_n increases from zero, the eccentricity ratio increases until it is a maximum at approximately the first natural frequency, that is w/w_n equals 1.0, after which it falls off asymptotically. With increasing unbalance factor, Q_{c2}, amplitude rises.

The 2π film phase solution passes through 90°, that is rotor inversion takes place, at a w/w_n value of about 1.0 from zero at low speeds towards a 180° asymptote at high speeds. The effect of increasing unbalance, Q_{c2}, is to reduce the gradient that the phase takes through 90° degrees, indicating an increase in damping at high eccentricities.

Because the contribution from the SFD is only one of damping for a 2π film then, apart from the resonance

region around rotor inversion, the response is governed primarily by the stiffness, k_1. Then the only effect of increasing the SFD parameter, A_1, is to reduce the resonance peak and the phase inversion gradient, Fig 5.4. However, with a π film the SFD generates non-linear stiffness and damping forces.

The π film results in Fig 5.5 indicate the presence of a bistable region at speeds above a frequency ratio of one due to the nonlinear hardening effect of the increasing stiffness of the SFD with amplitude. For low unbalance, that is Q_{c2} equals 0.245 the bistable region extends between frequency ratios of about 1.12 and 1.33. As unbalance increases the minimum jump frequency increases. The higher unbalance ratios shown have bistable behaviour extending past frequency ratios of 2.5. The eccentricity ratios are similar to the 2π film solutions apart from the bistable, or jump regions.

The π film phase response shows that, in order to produce an inverted mode of operation, a jump down in amplitude with increasing speed is required above the natural frequency. After inversion the π film solutions are very similar to the corresponding 2π film solutions because, with the smaller orbit, the SFD stiffness is much smaller and, with the phase inverted, the stiffness, k_1 dominates the response.

If the lands are now assumed coupled, with A_1 set at 0.08528, Fig 5.6 shows that the π film results indicate a rise in the minimum jump frequency and a reduction in the maximum jump frequency. Thus the bistable region is reduced and if the value of A_1 is increased still further, then for the lowest value of Q_{c2} studied here (0.245, Fig 5.6), a bistable region may not be predicted. The π film minimum jump frequency does not vary

significantly with the unbalance factor, Q_{c2} and SFD1 damping parameter, A_1 for the range of parameters pertinent to this research, Fig 5.7. Only when Q_{c2} is above about 1.0 does the increase in minimum jump frequency with increasing values of A_1 become significant.

5.2 General Short Bearing Model Predictions

The general short bearing model SFD parameters were identical to those of the π film model apart from the stipulation of a cavitation pressure and a positive oil supply pressure.

The theoretical rotor centre orbits which will be presented in this research represent the steady state responses at SFD1 and/or SFD2 (accomplished after a minimum of twenty four and a maximum of forty rotor revolutions from similar initial conditions) for exactly two rotor revolutions.

It was often difficult, particularly with configuration 2b to obtain both stable solutions where bistable regions are encountered. In some cases, experienced attempts with different transients and reductions in the permissible error did not yield both bistable solutions. This was because, for the two possible solutions, the initial dynamic conditions which would lead to the 'evasive' solution were not straight forward and attempted guesses were unsuccessful. Although experience might lead to the belief that a second stable solution was present, the lack of success in achieving the second solution might question such faith. However, the results to date

provide a reasonable complement of bistable solutions.

The waterfall diagrams presented consist of linear, vertical (y) amplitude FFT spectra for comparison with the experimental spectral data. Practical constraints on computing time governed the extent of the study. Attention was given to the case with unbalance, Q_{c2} equal to 0.611 as this unbalance illustrated most non-linear phenomena.

5.2.1 Configuration 1a

The π and 2π film models (equations {4.9} and {4.10}) assume that the rotor weight can be excluded from the model because the rotor is supported centrally within the SFD by the parallel linear stiffness. However, this assumption is not valid when a non-linear element is in parallel with the linear support stiffness. This assumption is strictly valid when the rotor axis is vertical and then, with the parallel support undeflected, all bearing housings are aligned. In practice the weight of the horizontal rotor deflects the support stiffness and to centralise the SFD, the SFD housing is offset from its aligned condition in the direction of gravity.

The rotor centre orbits when unbalance, Q_{c2} is 0.733 were produced with both the rotor weight omitted and included (the static centralisation of SFD1 being maintained), Fig 5.8. In this instance, it is clear that there is very little difference between these two sets of orbits. The combined unbalance and rotor weight forcing vectors in conjunction with the non-linearities generated by the centralised SFD1 still give rise to a relatively simple response. The orbits indicate that a jump occurred

between frequency ratios, w/w_n of 1.02 and 1.57. All subsequent computation was carried out with the rotor weight effect included.

The response curves, Figs 5.9, 5.10 display similarities with the π film responses, Fig 5.5. Bistable regions are indicated by a jump at the minimum jump frequency for all but the lowest unbalance, Q_{c2} at 0.245. At the lowest unbalance the response is similar to that of a 2π film, Fig 5.3. The effect of the supply pressure, Psup variations, in the range 2 to 24 psi, on model response is very small, Figs 5.9 and 5.10, respectively. The minimum jump frequency ratio ranges from 1.26 to 1.56 for Q_{c2} values from 0.490 to 0.733, respectively.

Increasing the damper factor, A_1 from 0.02132 (Fig 5.9) to 0.08528 (Fig 5.11) has the effect of eliminating the bistable regions which give rise to the jump phenomena. These results are similar to the 2π film results, Fig 5.4.

The waterfall diagram, Fig 5.12 shows the dominant synchronous activity and the presence of a low amplitude subsynchronous response at the natural frequency, w_n. A jump is clearly demonstrated in the synchronous response between 37 Hz and 41 Hz rotor speeds (1.14 and 1.27 w/w_n).

The simple π film and 2π film model responses compare favourably with the general Short Bearing model responses with and without the jump phenomena, respectively. This is due to the relatively simple nature of configuration 1a, where the static centralisation of SFD1 employing a linear spring, k_2 in parallel encourages circular centred orbits which lead to a hardening response around the first rigid body mode at high unbalance, introducing

bistable operation.

Subsequent model configurations, employing the general Short Bearing Approximation do not retain the features of the π and 2π film assumptions due to static eccentricities within the dampers. It will therefore be instructive to observe whether such static eccentricities encourage or discourage jump phenomena.

5.2.2 Configuration 1b

Eccentricity Ratio, E_{o1} = 0.8

Fig 5.13 gives the rotor centre orbits with a static eccentricity, E_{o1} of 0.8 which restricts the orbit position to the lower part of the clearance. A jump down is clearly indicated between rotor speeds of 45 Hz and 51 Hz. A strong nonsynchronous component is indicated in the non-circular orbit at 73 Hz rotor speed.

The response curves, Fig 5.14 demonstrate the effect of static eccentricity further dampening the resonance due to the increase in the film forces generated by non-concentric journal motion. Here, the interaction between the squeeze-film, with respect to cavitation, and the resultant forcing arising from the rotor weight and unbalance gives rise to undesirable non-linear phenomena. The rise in amplitude, after jump down on run up, above frequency ratios, w/w_n of about 1.80 for the two intermediate unablances (Q_{c2} of 0.611 and 0.490) is due to the subsynchronous activity noted in the orbits, Fig 5.13.

Fig 5.14 shows that jump phenomena are predicted for all

but the lowest unbalance (Q_{c2} of 0.245). Bistable operation is detected for the highest unbalance, Q_{c2} equal to 0.733, but the eccentricity ratio, ϵ_1 persists at a value of about 0.95 for all speeds above w/w_n of 1.0.

The waterfall diagram, Fig 5.15, highlights the spectral activity with Q_{c2} equal to 0.611 and indicates that the subsynchronous response at high speed prevails as a half engine order (1/2 EO). The effect of static eccentricity is to enable the apparent natural frequency to increase in proportion to the rotor speed. Therefore, a strong response results at a 1/2 EO, degrading the vibration response within the operating speed range in addition to the jump phenomena. The split into two apparent natural frequencies around 1/2 EO may be due to the asymmetry in SFD1. Higher engine orders will also be noted.

Eccentricity Ratio, E_{o1} = 0.4

The response with E_{o1} reduced to 0.4, Fig 5.16, is slightly less severe than with E_{o1} set to 0.8. This is because the rise in amplitude of the lower of the bistable solutions was restricted to higher unbalances. With Q_{c2} at 0.490 the amplitude of the lower of the bistable solutions falls gradually with increasing speed, which suggests that subsynchronous activity does not develop at high speeds in this instance.

5.2.3 Configuration 2a With SFD1 Statically Concentric

Rotor centre orbits for a Q_{c2} of 0.611 and Psup of 2 psi are given for SFD1 and SFD2 in Figs 5.17a,b, respectively. At the lowest speed studied, w/w_n equal to

0.46, there is a large vertical supersynchronous oscillation in the SFD1 orbit, Fig 5.17a. A jump down between 39 Hz and 51 Hz is clear. At higher speeds still, some double loops develop, indicating the presence of subsynchronous response.

The SFD2 orbits, Fig 5.17b are strongly restricted to the lower part of the SFD clearance, under the influence of the rotor weight. The jump, described above in Fig 5.17a, is also clear in the SFD2 orbits although the nonsynchronous activities at high speed are less discernible due to the small orbit size.

The response obtained over the unbalance range studied for SFD1 and SFD2 with Psup again set to 2 psi is given in Figs 5.18a and 5.18b, respectively. Bistable regions are predicted for all but the smallest unbalance, Q_{c2} equal to 0.245. The jump characteristics are similar to those predicted for configuration 1a. The SFD2 phase varies significantly throughout the vibration orbits and is not presented. Figs 5.19a and 5.19b present the response for SFD1 and SFD2, respectively with Psup set to 15 psi. Bistable operation is also indicated for unbalances, Q_{c2} of 0.490 and higher.

Fig 5.20 gives the waterfall diagrams for SFD1 and SFD2. A jump down between a high amplitude at 41 Hz and a low amplitude at 45 Hz is clear in both SFDs. The synchronous, 1EO response is dominant throughout apart from one exception in SFD1 at 17 Hz where the small synchronous response was overshadowed by a strong 2EO resonance close to the first bounce frequency of 32.4 Hz. SFD1 exhibits some response at higher integer engine orders but not as much as is shown by SFD2.

Subsynchronous resonance develops at speeds above 49 Hz

and remains close to the first bounce frequency as speed increases. This subsynchronous response, whilst clear in the response of SFD1, is of a very low amplitude in SFD2, due to the low synchronous response.

5.2.4 Configuration 2a With SFD1 Statically Eccentric

The static eccentricity in SFD1, E_{o1} was set to a value of 0.5. Figs 5.21a,b present the rotor centre orbits within the clearance circle for SFD1 and SFD2, respectively with Q_{c2} equal to 0.611 and a Psup of 2 psi. Fig 5.21a indicates that the SFD1 orbit at low speeds (15 Hz or w/w_n equal to 0.463) is elliptical, with the major axis almost vertical indicating a supersynchronous oscillation at a frequency slightly greater than twice the running speed. This is similar to the result already discussed (Fig 5.17a) and the introduction of static eccentricity, E_{o1} reduces the vertical journal excursions (Fig 5.21a). Increasing in speed, Fig 5.21a also shows the strong synchronous resonance above the first bounce frequency (w/w_n equal to 1.20) and a smaller, inverted orbit after a jump down (when w/w_n is equal to 1.51). At rotor speeds of twice the first bounce frequency (w/w_n equal to 2.01) some subsynchronous resonance, 1/2 EO at the first bounce frequency is clear, superimposed on the dominant synchronous response. With w/w_n equal to 2.5 the orbit indicates a dominant 1/2 EO response.

Fig 5.21b indicates that throughout the speed range the SFD2 journal is restricted to orbits dominated by the static weight of the rotor, positioned low in the vertical plane. However, the jump down is still indicated as in Fig 5.21a, between 39 Hz and 49 Hz rotor speed (or w/w_n equal to 1.2 and 1.51).

Figs 5.22a,b give the predicted amplitude responses for SFD1 and SFD2, respectively, each with a Psup of 2 psi. There is little useful information in the varying phase for both SFDs and so the x and y direction orbit size eccentricity ratios are presented. Bistable operation is predicted for frequency ratios above about 1.5. The lower of the two bistable solutions increases significantly above a frequency ratio of 1.9, dropping again when w/w_n has a value of 2.5. This illustrates the development of subsynchronous vibration.

Fig 5.23 presents the waterfall diagrams for SFD1 and SFD2 with E_{o1} equal to 0.5. A jump between 53 Hz and 57 Hz is predicted in both SFD1 and SFD2. The jump is noticable in the synchronous 1EO and higher engine orders. At speeds above this jump, a 1/2 EO subharmonic resonance develops which dominates the synchronous component at speeds above 61 Hz.

It should be noted that the 73 Hz spectrum has no subsynchronous component but does have a strong synchronous component, Fig 5.23. This represents the non-inverted bistable solution at this speed. Attempts were made to obtain the inverted solution for 73 Hz by applying different initial conditions, but due to some numerical sensitivity the non-inverted orbit remained.

5.2.5 Configuration 2b

With SFD1 now supporting the rotor weight and SFD2 centralised in the static condition, rotor centre orbits for a Q_{c2} of 0.611 and Psup of 2 psi are given for SFD1 and SFD2 in Figs 5.24a,b, respectively. At all speeds except the highest, the SFD1 orbit, Fig 5.24a was

severely restricted to the bottom of the clearance circle. A jump up occurs between w/w_n equal to 2.01 and 2.50, when the SFD1 orbit was circular and encompassing about 98% of the clearance. It should be noted that no change in the cavitation pressure had been imposed.

The SFD2 orbits of Fig 5.24b are strongly influenced by the SFD1 orbit shapes and orientation. The jump, described above in Fig 5.24a, is also clear in the SFD2 orbits. Some horizontal 'figure-of-eight' motions are discernible which suggests a dominant horizontal forcing, [47].

The response obtained over the unbalance range studied for SFD1 and SFD2 with Psup set to 2 psi is given in Figs 5.25a,b, respectively. Bistable operation, with jumps up as speed is increased, is indicated for all but the lowest unbalance. A jump up from a low amplitude at w/wn equal to 1.64 to a high amplitude at w/w_n equal to 1.76 occurs for the highest unbalance, Q_{c2} equal to 0.733. The jump is clearest in the SFD1 response, Fig 5.25a, but also evident in the SFD2 response, Fig 5.25b. The x component of eccentricity ratio, or horizontal amplitude peaks close to the unity frequency ratio for all but the lowest unbalance, Q_{c2} equal to 0.245.

Figs 5.26a,b give the amplitude response for SFD1 and SFD2, respectively with Psup set to 15 psi. The results are similar to those for 2 psi, Figs 5.25a,b. A jump occurs between w/w_n equal to 1.76 and 1.88. Also the rise in the x component of eccentricity ratio for Q_{c2} equal to 0.611 above w/w_n equal to two is damped by the increase in Psup to 15 psi. Bistable operation with Q_{c2} as low as 0.611 is predicted.

Fig 5.27 gives the waterfall diagrams for SFD1 and SFD2

for Q_{c2} equal to 0.611 and indicates that most of the spectral activity is contained within the synchronous frequencies, 1EO and higher integer engine orders. A jump between rotor speeds of 77 and 81 Hz is clear in the SFD1 waterfall diagram but not in that of SFD2.

5.2.6 Configurations 3a and 3b

Extensive attempts were made to carry out the numerical integration required to achieve the steady state responses to unbalance. However the computation of solutions for configurations 3a and 3b proved to be impractical due to the excessive CPU time that it took to traverse transient responses.

Chapter 6. THE EXPERIMENTAL ROTOR-BEARING FACILITY

To create a realistic test rig a three-bearing rigid rotor assembly incorporating the essential vibrational features of a small aero-engine was developed and Plates 1 and 2 give two elevated views of the rig. The test rig, also shown in Fig 6.1 was used to investigate the operation of the SFDs, 1, at two of its three rolling-element bearings, 2. The self alignment capability of the bearing, 3, constituted a pivot about which an antisymmetric, or conical mode of vibration occurred when the rotor, 4, was acted upon by a force arising from rotation of the unbalance mass, 5. Flexible bars, 6, simulated pedestal flexibility and were mounted into heavy foundation blocks, 7, which represented ground, or the engine casing. Note that with the full assembly, Fig 6.1, the central SFD housing was not connected in any way to the foundation block on its right. Comparisons between different rig configurations (Table 3.1) allowed the influence of individual assembly components and in-service assembly misalignment conditions to be analysed. Relevant dimensions are given in Appendix 1.

6.1 Rig Configurations

As previously outlined in Chapter 3 and summarised in Table 3.1, the range of configurations to be studied were drawn up to cover as wide a range of practical assemblies as possible. The practical considerations in achieving these configurations are discussed below.

Rig configuration 1a involves one midspan damper, SFD1 with the four parallel housing bars forming a flexible bearing support, k_2 at the bearing further towards the free rotor end. (Note that the left hand block, Fig 6.1, and the bars, k_1, were not incorporated in the assembly until configuration 3a.) The two degrees of freedom (DOF) in this assembly are the horizontal and vertical displacement of the rotor relative to ground. SFD1 is centrally positioned with no static eccentricity, which encourages circular, centred vibration orbits. To achieve configuration 1a, the SFD1 housing is centralised using shim and 'clock gauges' to measure the journal position relative to the housing whilst ensuring that the bars, k_2 remain deflected under the rotor weight. When centralised, the SFD1 housing is bolted directly to the foundation block to the right of SFD1, Fig 6.1, which also houses the bars, k_2. Configuration 1b involves unbolting the SFD1 housing from the foundation block and raising it vertically so that the effect of a static eccentricity is introduced before re-fastening it to the block. The static eccentricity increases the effective rotor weight carried by the squeeze-film of SFD1.

Rig Configuration 2a introduces the action of SFD2 between the parallel bars, k_2 and the rotor. The corresponding four DOF of the rig are now the horizontal and vertical rotor and SFD2 housing displacements relative to ground. Configuration 2a maintains SFD1 in a statically centralised condition, by aligning the housing using the same method as for configuration 1a except that now the SFD2 journal carries the rotor weight so that it is fully eccentric due to gravity in the static condition. Some eccentricity in SFD1, namely E_{o1} equal to 0.5, was also studied. As with configuration 1b, this was achieved by raising the SFD1 housing. By raising the SFD1

housing further still the rotor weight was taken up by SFD1 and the bars, k_2, were relieved. The SFD1 housing was raised until SFD2 was statically centralised before SFD1 was bolted to the block, constituting configuration 2b.

Introducing the bars, k_1 to support the SFD1 housing flexibly to ground, via the left hand foundation block, Fig 6.1, increases the assembly complexity further. The rig now exhibits six DOF with the horizontal and vertical rotor, SFD2 housing and SFD1 housing displacements relative to ground. With the rotor supported centrally in the SFD2 housing by a jack, the SFD1 housing is aligned centrally by adjusting the thickness of the shim between the foundation block supporting the bars, k_1 and its baseplate. In this way all three bearings are aligned. Then the rotor is lowered so that it is fully eccentric in SFD2 and finally it is fully eccentric in SFD1. Rotor weight is thus carried by the housings of both SFD1 and SFD2. This assembly constitutes configuration 3a. Configuration 3b is achieved from configuration 3a by lowering the SFD1 housing until the rotor is centralised within SFD1. This is done by reducing the thickness of the shim from between the foundation block supporting the bars, k_1 and its baseplate.

6.2 Squeeze-Film Damper Geometry

Constant SFD1 and SFD2 geometries were employed throughout the study. The SFDs consisted of two similar unsealed lands separated by a central circumferential supply groove in the housings which promoted an even circumferential supply reservoir, as illustrated in Fig

6.2. The grooves were supplied by three equispaced ports with pressurised oil. Geometry details include number of lands, damper radial clearance, c, ratio of land width to radial clearance, (l/c), and ratio of land width to mean damper radius, (l/R). Reference should be made to Appendix 1 for these parameter values.

The depth of the oil supply groove, which is positioned mid-way between the two lands is of interest. A shallow groove can contribute some damping to the system itself. On the other hand, a deep groove, although its reservoir action may contribute very little in the way of damping, may introduce some undesirable turbulent oil flow conditions.

The initial groove depth was 0.5 mm in each SFD. These grooves were deepened to 2.0 mm to observe some change in the effective damping upon the response to unbalance by further encouraging jump phenomena. It is considered that this groove modification did not significantly change the character of the oil entering the damper clearance.

Results for configuration 1a are for SFD1 with both a 0.5 mm or a 2mm deep oil supply groove. In this way, comparisons are afforded using the two groove depths. Results for configurations 2 and 3 are for 2.0 mm deep grooves in both SFD1 and SFD2.

6.3 Instrumentation and its Calibration

A variety of instrumentation was utilised to demonstrate the experimental rig behaviour (see Fig 6.3 and Plate 3) and details of the equipment are given in Appendix 4.

The instrumentation provided electrical signals from which the rotor-bearing response to unbalance could be analysed. These signals were recorded on half inch magnetic tape using a seven channel tape recorder. The parameters of interest are as listed below.

Rotor Displacement

The position of the rigid rotor, relative to ground, was detected using two capacitance transducers positioned to observe the horizontal, x, and vertical, y, displacements. A power amplifier system was used to power the transducers and to amplify their output signals. Configurations 2a,b required the rotor position relative to SFD2 housing to be measured for which a second pair of transducers was used. Plate 4 shows the free (right hand, Fig 6.1) end of the rotor with the probes mounted to ground and the SFD2 housing. A third pair of transducers were mounted to ground to measure the SFD1 housing displacements relative to ground for configurations 3a and 3b and the probes can be seen in Plate 1.

The transducers detect the rotor vibration from the variations in the size of the gap between a polished portion of the rotor surface (close to the free rotor end) and the transducer faces. This gap variation results in capacitance fluctuations and an electrical vibration signal is produced.

The capacitance transducers were calibrated remote from the rig using static displacements (from slip gauges and a purpose built screw gauge micrometer calibration jig) over the range of gaps that would be experienced on the rig. A linear relationship between gap size (and, hence, rotor displacement) and the transducer amplified output

voltage was observed. Fig 6.4 gives the calibration for the six transducers used on the rig.

In order to maintain a constant dielectric constant, the capacitance gaps between the probe heads and the target surface, such as the rotor, had to be kept free from oil. This was achieved, during the experiment, by employing oil thrower discs on the rotor and various sealing devices. In addition, it was found necessary during configurations 2a (and subsequently) to employ small jets of air to blow between the probe head and the rotor to remove traces of oil that had leaked into the probe area from the SFD2 discharge.

Rotor Speed

The rotor speed was measured using a photoelectric diode which admitted light from an area on the rotor of which one half, or 180° was black and the other was white. As the rotor rotated the diode detected an approximately square wave light fluctuation of the same frequency as the rotor speed, converted this into an electrical output which was displayed as a speed reading (Hz) upon input to a counter. The counter provided an amplified square wave (TTL) speed output for recording. Rotor speed was indicated to the nearest whole Hertz (to maintain a rapid speed update) and this was verified by the synchronous vibration component identified during spectral analysis.

Phase

The phase angle between the unbalance force and the rotor displacement was detected using the amplified square wave speed signal (which was in phase with the unbalance mass placed on the rotor) and the amplified rotor y displacement signal. These two signals were input to a

phase meter to obtain the phase angle. The maximum phase error, neglecting electronic inaccuracies, was estimated at ± 1.0°.

SFD Oil Supply Pressure

The static pressure of the oil supplied to the SFDs was monitored using a dial gauge on each of the three oil supply lines (120° equispaced around the housings). Pressure could be read quite easily to within ± 0.25 psi and the gauges were found to be accurate within this tolerance when compared with a calibrated air supply pressure.

A minor shortcoming arose when the rig was modified from configuration 1b to configuration 2a in that the maximum oil supply pressure that the existing pump and motor arrangement could deliver fell from 24 psi to 15 psi. This was due to the addition of SFD2 which effectively doubled the oil flow demand. However it was considered that this did not affect the ability to provide a full 2π film of oil in each SFD, when required.

The supply pressure available was determined by the maximum flowrate afforded by the existing supply pump and motor configuration. It is interesting that the theoretical maximum flow through SFD1 alone with a 24 psi supply pressure is almost identical to the flow through SFD1 and SFD2 together with a 15 psi supply pressure. This is discussed in Appendix 5.

Frequency Analysis

A spectrum analyser was employed to carry out a spectral analysis of the experimental vibration signals. This allowed jump phenomena, combination frequencies and

subharmonic resonances to be observed within the frequency range analysed by studying individual spectra and by the compilation of spectra as waterfall diagrams.

SFD Oil Viscosity Calibration

The oil used in the rig was Shell Calibration Fluid 'C'. Samples of this oil were taken from the rig's oil tank and the viscosity was determined for a number of temperatures covering the range of temperatures measured before and after experimental data recording. A Brookfield viscometer was used and Fig 6.5 shows the calibration.

An alcohol thermometer was used before and after recording experimental data to measure the temperature of the oil being discharged from the SFD. It was estimated that during the experiment the oil had an average dynamic viscosity of 6.0 cP.

6.4 Static Natural Frequencies

The static natural frequencies of the rig were determined by carrying out an impulse test with the rotor stationary. The impulse was provided by a soft hammer which smartly struck the flexibly mounted bearing housing a number of times. The spectrum analyser captured the transient responses from the amplified displacement probe signals, generating the spectra from which the natural frequencies were determined.

The essential elements determining the static natural frequencies for configurations 1a through to 2b were the

rotor and the flexible bars, k_2. The SFD2 clearance was packed with shim to lock it and this assembly demonstrated a lowest natural frequency at 32.4 Hz, in both the horizontal (x) and the vertical (y) directions, Fig 6.6a. This lowest natural frequency is for a bounce mode with the rotor rigid. Higher natural frequencies were 200 Hz or more.

Configurations 3a and 3b involved both sets of flexible bars, k_1 and k_2, supporting the rotor. The clearances of SFD1 and SFD2 were packed with shim and the transient responses indicated a first bounce mode frequency in the horizontal, x direction of 34.8 Hz and in the vertical, y direction of 36.8 Hz, Fig 6.6b. This indicated a degree of anisotropy.

The natural frequencies of the SFD housings alone on their flexible support bars were determined. A response at 64.0 Hz, with some harmonics, was recorded with the SFD1 housing supported by the flexible bars, k_1, Fig 6.7a. The natural frequency of the SFD2 housing with its support, k_2 was observed at 89.2 Hz, with some harmonics, Fig 6.7b.

6.5 Rig Motor & Pump Frequency Contributions

The rotor-bearing assembly was serviced by a drive motor and two motor-pump units to supply and retrieve oil. These units had their own vibration characteristics which the rotor-bearing assembly response was guarded against by appropriate precautionary measures. However, these measures (a very solid assembly foundation and flexible drive coupling) still allowed some vibration from the auxiliary equipment to be transmitted into the rotor-

bearing assembly.

To identify this auxiliary equipment rig vibration contamination tests were carried out with the auxiliary equipment running and the rotor stationary. The rotor vibration developed by the oil motor-pump units alone (Fig 6.8a) and with the drive motor (on standby) in addition (Fig 6.8b) show that low levels of vibration at 25 Hz (and harmonics, probably due to electrical mains) and at 32.4 Hz (rig first bounce mode) are present along with other noise.

6.6 Experimental Investigations

The experimental test rig was used to record and examine the responses of the range of configurations of the three bearing assembly (Table 3.1) to mass unbalance. Non-linear phenomena were sought over a range of rotor speed (w/w_n = 0.46 to 2.5), mass unbalance (Q_{c2} = 0.25 to 0.73), oil supply pressure (Psup = 2.0 to 24.0 psi) and appropriate static eccentricities (E_{o1} and E_{o2} = 0.0 to 1.0). These parameter ranges were established following an initial theoretical study of the π and 2π Film solutions and after commissioning of the experimental rig revealed the presence of jump phenomena.

Up to four mass unbalances were used to excite the rig response:

25 gram. equivalent to Q_{c2} = 0.245 ,
50 gram. equivalent to Q_{c2} = 0.490 ,
62.5 gram. equivalent to Q_{c2} = 0.611 and
75 gram. equivalent to Q_{c2} = 0.733 .

The recording of experimental signals was carried out

with the rotor speed constant. Thus the steady state response of the system at each particular speed was recorded. This was to eliminate any rotor acceleration effects and enable accurate construction of waterfall diagrams from experimental vibration frequency spectra. To study the range of configurations for various unbalances and supply pressures, in excess of 1400 steady state responses were recorded from a total of 59 runs (averaging 24 speeds per run).

The tests were analysed by studying the SFD orbit magnitudes and the phase angles between SFD eccentricity vectors and the unbalance. The rotor speed was represented as a frequency ratio, by dividing by the first bounce mode frequency of configuration 1a, namely 32.4 Hz. Rotor displacements relative to ground and relative to the SFD2 housing were sampled by a spectrum analyser, utilising the Hanning time window.

Chapter 7. EXPERIMENTAL RESULTS & THEIR COMPARISON WITH THEORETICAL PREDICTIONS

Experiments were carried out to determine whether or not jump phenomena, as predicted by the theoretical π film and general Short Bearing approximations, could be reproduced experimentally. In particular, the nature of the jump phenomena and the occurrence of the subsynchronous resonances demonstrated theoretically are to be compared with the experimental observations of such non-linear phenomena.

7.1 Rig Configuration 1a

7.1.1 Shallow Oil Supply Groove

With the SFD1 journal statically centred in the bearing housing the resulting vibration orbits were almost circular about the housing centre. For the highest unbalance, Q_{c2} equal to 0.733, supply pressure, Psup set at 2 psi and at a rotor speed of 55 Hz (w/w_n = 1.70), SFD1 exhibited a circular orbit encompassing about 40% of the clearance and the orbit size rose gradually for decreasing speeds down to 45 Hz, Fig 7.1. The orbit suddenly jumped up in size whilst running down between rotor speeds of 45 Hz and 43 Hz. The large orbit at 43 Hz displayed a 'three-lobe' profile which was traced back to a 0.04mm three jaw chuck machining distortion of the SFD1 journal. Large orbits persisted through the first bounce mode frequency, 32.4 Hz, and fell off as speed was

further decreased, encompassing only about one tenth of the clearance at 17 Hz.

Fig 7.2 gives the amplitude and phase responses of SFD1 to a range of unbalance for the 'shallow' groove, 0.5 mm deep, again with supply pressure, Psup equal to 2 psi. The jump is clear with the highest unbalance, Q_{c2} equal to 0.733. The lower unbalances demonstrated 'smooth' amplitude responses, peaking around the first bounce mode, ($w/w_n = 1$).

The jump was observed with the highest unbalance mass ($Q_{c2} = 0.733$) only. The jump occurred at frequency ratios, w/w_n equal to 1.36, 1.30 and 1.33 with oil supply pressures, Psup of 2, 4 and 6 psi, respectively. The jump down with Psup set at 6 psi, Fig 7.3 was observed from recordings made with increasing rotor speed. Lower values of Psup required the rotor to be accelerated quickly from a low speed and vibration level past the minimum jump frequency, to a low stable vibration (at w/w_n of about 1.6). Then, starting with a low vibration level at high speed it was possible to observe a jump up as speed was decreased. This jump up occurred at the lowest speed of the bistable region, the minimum jump frequency. (A slow acceleration at the lower oil pressures had resulted in the vibration rising to very high levels above 32.4 Hz, ie w/w_n equal to unity, which persisted at high speeds without a jump down.)

The phase between the rotor displacement and the unbalance force (Fig 7.3) shows that the rotor inverted in a way similar to that of a second order system for low unbalance factors ($Q_{c2} = 0.245$ & 0.490). The highest unbalance used ($Q_{c2} = 0.733$), producing jumps in rotor displacement, or eccentricity, gave a phase response which indicated that the rotor did not follow a smooth or

continuous inversion path. As the oil supply pressure was increased from 2 psi, Fig 7.2, to 6 psi, Fig 7.3, the size of the phase jump decreased for unbalance, Q_{c2} of 0.733 (see also Table 7.1).

It is of interest to note that with a Psup of 6 psi and a Q_{c2} of 0.733 (Fig 7.3) the phase is greater than 90° between w/w_n values of 1.02 and 1.20 (being a maximum of 108° when w/w_n is 1.14). This higher pressure encourages inversion but this trend reverses at higher speed, reducing the phase until sudden inversion, or jump occurs when w/w_n is 1.33. The most likely cause of this is that an increase in supply pressure would tend to increase the speed at which cavitation becomes significant. With sufficient cavitation the hardening response raises the effective natural frequency which causes the phase to remain below 90°, delaying inversion.

Increasing oil supply pressure to SFD1 from 2 to 6 psi had the effect of reducing the dynamic eccentricity ratios for any particular unbalance. Also, at high speed and a Q_{c2} of 0.733, the phase increased with decreasing oil pressure, indicating a more complete inversion. It is clear that the damping in the system was increased with increasing oil supply pressure. As rotor speed was increased and with a Q_{c2} of 0.733, a high amplitude response persisted above a frequency ratio of unity even when the oil supply pressure, Psup was raised to 25 psi.

The experimental orbits, Fig 7.1, with a shallow groove in SFD1, compare well in general shape and disposition with the theoretical results, Fig 5.8. The orbits are fairly circular and concentric. At this unbalance, Q_{c2} equal to 0.733, an experimental jump up on run down was demonstrated between frequency ratios, w/w_n of 1.39 and 1.33, Fig 7.2, compared with a theoretical jump at the

minimum jump frequency at a w/w_n of about 1.51 in the theoretical results, Fig 5.9. The experimental orbits demonstrated slightly more system damping than was implied in the predictions, but all the essential features were reproduced.

7.1.2 Deep Oil Supply Groove

The SFD oil supply groove depth was increased from 0.5 mm to 2.0 mm. Fig 7.4 gives the experimental responses for the deep-grooved SFD using two different supply pressures. An intermediate unbalance, namely Q_{c2} equal to 0.611 was also employed in order to further investigate the possibility of jump phenomena. A jump was demonstrated with Q_{c2} as low as 0.490, when Psup was 2 psi. Therefore, at this level of unbalance, a reduction in damping due to deepening the supply groove was evident from the increase in resonant amplitude and the introduction of a jump in the response.

After the SFD1 groove depth was increased experiments with rig configuration 1a indicated that, even with the lowest SFD1 oil supply pressure studied, 2 psi, bistable operation was only achieved for unbalances, Q_{c2} of 0.490 and above, Fig 7.4. The minimum jump frequencies observed in the experimental and theoretical results are summarised in Table 7.4. The predicted jump frequencies from the general solution of the short bearing approximation were, on average, 15 % higher than the experimental frequencies. The minimum jump frequencies predicted by the half, or π film model, although still higher than the experimental minimum jump frequencies, were closer to them, being, on average 10 % higher. This is possibly due to variation in the experimental minimum film pressure below the value of absolute zero adopted by

the model. Film tension spikes of short duration have been noted experimentally [72].

The π film theory (Figs 5.5 and 5.6) suggests that a bistable region existed for the full range of unbalance studied (Q_{c2} values from 0.245 to 0.733), whereas the 2π film theory (Figs 5.3 and 5.4) indicates no bistable regions for the same set of parameters. The unsimplified Short Bearing predictions, modelling film extent between the 2π and π film models, indicates bistable regions for unbalance factors, Q_{c2} above and including 0.490 with A_1 set to 0.02132, Figs 5.9 and 5.10. With A_1 increased to 0.08528 no bistable regions existed, Fig 5.11. The extent of the experimental bistable operation was observed with Q_{c2} as low as 0.490 with the deep supply groove but only at the highest unbalance, Q_{c2} equal to 0.733, with the shallow supply groove. This suggests that the effective experimental A_1 value was between 0.02132 and 0.08528, namely the two land and one land assumption, respectively. With the deep supply groove and the highest unbalance, Q_{c2} equal to 0.733, inversion was not possible, even with a high rotor speed acceleration and so the minimum jump frequency in this instance was not observed.

Predicted responses indicate that a supply pressure variation from 2 to 6 psi had a negligible effect on the vibration amplitude, Figs 5.9 and 5.10. Increases in the experimental pressure caused the apparent damping in the responses to increase slightly, Figs 7.2 and 7.3. The effect of varying supply pressure on the film forces developed by the unsimplified Short Bearing model are illustrated in Table 7.7. It is clear that the effect of increasing supply pressure whilst keeping cavitation constant is to reduce the radial force component, P1 and increase the tangential component, P2. Therefore, the

model behaves as expected, reducing the extent of film cavitation either by an increase in supply pressure or by a decrease in the cavitation pressure, although an increase in supply pressure does not noticeably effect the predicted frequency response.

Employing a supply pressure of 2 psi, the experimental waterfall diagrams, with linear, voltage amplitude, show that a jump was detectable in the synchronous or first engine order, 1EO, and second engine order, 2EO, Fig 7.5. The logarithmic scale (lower diagram) highlighted the lower amplitude activity. When a jump up was imminent on run down there was a rise in the amplitude of a broad band of frequencies at the point when the jump occurred. Also, subsynchronous activity was low and generally independent of speed, around the 32.4 Hz natural frequency, w_n.

The theoretical waterfall diagram, Fig 5.12, compares well with the experimental. The response is dominated in both the experimental and theoretical cases by the synchronous response. The theoretical waterfall diagram indicates a very low amplitude harmonic response at 2EO, whereas the experimental has a slightly higher 2EO response, Fig 7.5. This is probably attributable to practical tolerances within the test rig, that is, slight misalignment and geometric tolerances might contribute to exciting the low amplitude harmonic components observed in the experimental diagram. The subsynchronous activity is of low amplitude in both the theoretical and experimental responses, occurring at about 32.4 Hz (w_n) and remaining constant with increasing speed.

The experiments and predictions for configuration 1a have both demonstrated how jump phenomena can develop due to the non-linear stiffening properties of the SFD when the

rotor unbalance is suitably high. The effect of deepening the oil supply groove was to reduce the level of unbalance at which jump phenomena become a feature. The occurrence of experimental jump phenomena indicates that, from comparisons with predictions, the value of the bearing parameter, A_1 lies between the two (or separate) land assumption (A_1 = 0.02132) and the single (or coupled) land assumption (A_1 = 0.08528). The nonsynchronous response of both the experiment and theory agreed, predicting low level subsynchronous resonance at the first bounce mode frequency.

Since the purpose of the research was to investigate non-linear phenomena and jumps were more easily promoted by the deep-grove SFD, this was retained for the rest of the experiments.

7.2 Rig Configuration 1b

Static eccentricity was introduced in the negative y direction to the journal, that is in the same direction as gravity and this encouraged uncentralised non-circular orbits. The static eccentricity did not restrict the occurrence of jump phenomena. Experiments showed that high dynamic eccentricities and non-inverted response arising from an unbalance factor, Q_{c2}, of 0.733 were still significant features with static eccentricities, E_{o1}, of 0.4 and 0.8. The orbit magnitude in the y direction was employed as it illustrates bistable operation well.

Static Eccentricity, E_{o1} = 0.8

Fig 7.6 shows the experimental rotor centre orbits for the deep groove SFD1 with static eccentricity, E_{o1} set to 0.8, Q_{c2} equal to 0.490 and Psup set at 2 psi. A jump down on run up is clear between w/w_n of 1.27 and 1.33. A strong non-synchronous response is clear at w/w_n equal to 2.253. The frequency response, Fig 7.7 shows that, with Q_{c2} equal to 0.490 and Psup at 2 psi, the amplitude rose quite steeply through the bounce mode (w/w_n =1) until the jump down, as already observed in the orbits, took place.

The experimental rotor centre orbits, Fig 7.6, compare well with the theoretical predictions, Fig 5.13. A jump down is clear in both cases, occurring at w/w_n equal to about 1.30 experimentally (Fig 7.7) and 1.45 theoretically (Fig 5.14). A strong subsynchronous response, illustrated by a "double loop", is illustrated at high speeds both in the rig response and in the predictions.

Fig 7.7 demonstrates that for a higher unbalance, Q_{c2} equal to 0.611, an experimental jump up on run up occurred at w/w_n of about 1.05 followed by a steady increase in amplitude upto a w/w_n of 1.76, above which the vibration levels were considered potentially destructive. Even with a supply pressure, Psup of 20 psi, the experimental response at this level of unbalance would not invert to a lower level past the unity frequency ratio. No jumps or any other significant non-linear phenomena occurred with Q_{c2} below 0.490, the response simply displayed a well damped amplitude with inversion taking place around the natural frequency. The steep rise in experimental amplitude above the unity frequency ratio was not reproduced precisely in the

theoretical response where the amplitude rose to a high level before the unity frequency ratio.

Fig 7.8 shows a range of responses with various SFD parameters, A_1 where increasing the A_1 value clearly increases the effective damping. The precise value of A_1 is doubtful, as discussed earlier, and it is possible that in this instance the forms of the experimental results, as shown in Fig 7.7, are due to a steady reduction in the effective value of A_1 with increasing speed. It is possible that the value of A_1 is reduced by variations in the fluid such as cavitation bubbles being drawn into the positive pressure region. This would reduce the damping capacity of the SFD and could occur without the average cavitation pressure in the negative pressure region rising. Alternatively, variation of the stipulated theoretical cavitation pressure, Pmin, Fig 7.9 shows that the response is very similar for various values of Pmin, except that as Pmin is reduced the minimum jump frequency is reduced. Thus, it is probable that the form of the experimental responses was due to a variation in the effective A_1 value.

The experimental waterfall diagrams, Fig 7.10, with a Q_{c2} of 0.490 for the response of SFD1 show a strong jump down with increase in speed. Strong 1/2 EO subsynchronous resonance which dominated the synchronous amplitude, was also demonstrated, the orbit of which is presented in Fig 7.6 (w/w_n 2.253). The effect of SFD1 static eccentricity, E_{o1} equal to 0.8, on the experimental spectral response is to increase the harmonic content of the waterfall diagram, Fig 7.10, with 2 EO, 3 EO and 4 EO spectral components in evidence, particularly at a speed equal to the bounce mode frequency, 32.4 Hz. The theoretical waterfall diagram, Fig 5.15, also shows this effect with harmonics upto the 4 EO frequency at rotor

speeds around the first bounce mode frequency. Also, at higher rotor speeds, a 1/2 EO subsynchronus response is shown in both the theoretical and experimental waterfall diagrams, accompanied by a weak response at the 3/2 EO and 5/2 EO. The sharp increase in the subsynchronous resonance after about 69 Hz rotor speed is clear in both the theoretical and experimental diagrams. The theoretical 1/2 EO and 3/2 EO responses appear to bifurcate, or split at 77 Hz and 81 Hz rotor speed. This feature was not present in this experimental case but was observed in other cases.

Static Eccentricity, E_{o1} = 0.4

With static eccentricity, E_{o1} at 0.4, the SFD1 responses demonstrated jumps down on run up with Q_{c2} as low as 0.490, Fig 7.7, as they did with E_{o1} equal to 0.8. Also, an increase in amplitude at higher speeds indicates the onset of subsynchronous activity with this unbalance.

Even with supply pressure, Psup raised to 20 psi the effect of static eccentricity, E_{o1} was to prevent the inversion of the response for the higher unbalance, Q_{c2} equal to 0.611. The amplitude continued to rise with increasing speed until the vibration level was considered unsafe.

The comparison of the experimental results for E_{o1} equal to 0.4 with the theoretical predictions shows similar features as does the comparison for the larger static eccentricity, E_{o1} equal to 0.8. A jump up with run down, at a minimum jump frequency is predicted, Fig 5.16. However, as speed is reduced further, the high amplitude falls off more quickly in the experimental results than is predicted, again perhaps due to a change in the

effective value of A_1, as described above.

7.3 Rig Configuration 2a With SFD1 Statically Concentric

As can be seen from Table 3.1, configuration 2a incorporates two SFDs, each of which would have a likely effect on the overall response. The central preloading of SFD1, stipulating zero static eccentricity, encouraged circular journal orbits there. The experimental response to various unbalance factors indicated that the static load acting on SFD2 was large enough to prevent appreciable lift from its fully eccentric position. Thus the flexible bars (k_2) deflected appreciably to conform with the rotor vibration, as observed in the SFD1 orbit. Figs 7.11a,b show the journal centre orbits within the clearance circle (radius c) for SFD1 and SFD2, respectively during run down for a Q_{c2} of 0.611 and oil supply pressure, Psup of 2 psi. A jump up between rotor speeds of 41 Hz and 39 Hz (or w/w_n of 1.27 and 1.20, respectively) was recorded, although the latter only is shown as an orbit in Figs 7.11a,b.

Figs 7.12a,b give the amplitude and phase responses for SFD1 and SFD2 each with Psup set at 2 psi. Jumps up, at the minimum jump frequency, were clearly indicated during run down in both the amplitudes of SFD1 and SFD2 and in the phase of SFD1. The jump phenomenon was exhibited over a range of unbalance parameter, Q_{c2} from 0.490 to 0.733. The SFD2 phase vs speed relationship varied due to the highly non-linear effect of the damper and provided no useful information.

Figs 7.13a,b present the responses for SFD1 and SFD2, respectively, with Psup set at 15 psi. Only the highest unbalance, Q_{c2} equal to 0.733 resulted in a jump up during run down. Lower unbalances produced responses without bistable characteristics. Tables 7.2 and 7.3 summarise the experimentally observed jumps for SFD1 and SFD2, respectively.

Figs 7.14a,b present the waterfall diagrams for rotor (that is, SFD journal) displacements relative to SFD1 and SFD2 housings, respectively. As expected from the orbits and vibration amplitudes discussed above, a much lower frequency response is indicated within SFD2 than in SFD1. With a logarithmic scale it was clear that when a jump up was imminent on run down there was a clear rise in the amplitude of a broad band of frequencies at the point when the jump occurred and this has already been noted in configuration 1a. Fig 7.15 indicates the change in broad band frequency response with bistable operation (Q_{c2} equal to 0.733) and without bistable operation (Q_{c2} equal to 0.245) for SFD1. The frequency analysis of configuration 2a responses indicated that subsynchronous response at rotor speeds equal to and greater than about 65 Hz, that is twice the first natural frequency, was dominant in the first bounce mode, Fig 7.14a. This response was still overshadowed by large synchronous components, as is indicated from the shape of the rotor centre orbits of Fig 7.11a. At 65 Hz rotor speed the response at 32.4 Hz represented a 1/2 EO subharmonic.

A good qualitative agreement of non-linear characteristics exists between the prediction and experimental observation of bistable operation at low SFD supply pressure, Figs 5.18 and 7.12, respectively. At a higher SFD supply pressure then the experiment, Fig 7.13, indicates bistable operation for the highest unbalance

studied, Q_{c2} equal to 0.733, while the lower unbalances demonstrated a damped resonance. However, theoretical predictions for the higher supply pressure were similar to those for the lower pressure. The lack of influence of supply pressure on the predictions has already been noted in configuration 1a (refer to section 7.1.2). The experimental minimum jump frequencies and their theoretical counterparts are presented in Table 7.5. The theoretical minimum jump frequencies, as before (section 7.1), were predicted higher than those observed experimentally. It is possible that this was due to differences between the experimental and theoretical cavitation conditions. For example, as the rotor speed was reduced the effective experimental cavitation might have been less than predicted by the model's absolute zero (-14.7 psi gauge) cut-off thus delaying the jump up, in a similar way to that indicated in Fig 7.9.

The predicted orbits, Fig 5.17, compare well in general shape and disposition within the SFD1 and SFD2 clearances with the experimental orbits, Fig 7.11, except at the lowest speed of 15 Hz, or w/w_n equal to 0.463. The large vertical supersynchronous oscillation predicted at this speed was identified as a response at the bounce mode of 32.4 Hz in the waterfall diagram of Fig 5.20, along with a lower amplitude synchronous response. The experimental synchronous amplitude at this speed was similarly low, Fig 7.14a, and, although evident, the response at 32.4 Hz (w_n) was lower still, suggesting that the experimental system damping is higher than the theoretical.

At speeds below the first bounce mode it is possible to excite the bounce mode experimentally so that it overshadows the synchronous response if the system damping is sufficiently low, Fig 7.16. Another point worth noting is that the predicted response at w_n might

have been a persistent transient and might have died away if the numerical integration was continued further still. Fig 7.17 gives the predicted orbits at 15 Hz rotor speed when the single land assumption is applied, that is A_1 and A_2 are increased to 0.08528 and 0.16040, respectively. This increase in damping from the two land assumption reduces the supersynchronous response substantially.

A response at 32.4 Hz for a 15 Hz rotor speed approximates a second harmonic, 2EO. The large vertical response predicted in this instance is interesting because it is not predicted from theoretical considerations for configuration 1a, Fig 5.12, where the response is dominated by the synchronous response with only a low response at the first bounce frequency. In configuration 1a, the rotor at the SFD2 location experiences a restoring force from the support bars (k_2) which is in phase with the deflection. The only difference between the configurations 1a and 2a is that configuration 2a introduces SFD2 whose journal carries significant rotor weight so that, at low rotor speeds, little lift is apparent and the orbits are very small. However, SFD2 affects both the phase and amplitude of the force acting on the rotor and it is possible that, as a result of having both dampers active, the non-symmetric forcing in the vertical direction provided by the rotor weight and unbalance excites the first bounce mode, whereas the horizontal response, driven by the symmetric horizontal unbalance force vector, is less affected.

Over the rest of the speed range the predicted waterfall diagram revealed the presence of low amplitude subsynchronous resonance at the bounce mode frequency, w_n, and jumps in the harmonic components, similar to those present in the experimental results.

7.4 Rig Configuration 2a With SFD1 Statically Eccentric

The experimental response with SFD1 static eccentricity, E_{o1} equal to 0.5 was studied for an unbalance, Q_{c2} of 0.611 and with Psup set to 2 psi. Figs 7.18a,b and 7.19a,b give some rotor centre orbits and the amplitude response over the speed range for SFD1 and SFD2, respectively. When the responses are compared with those for E_{o1} equal to zero (Figs 7.11a,b and 7.12a,b) there is one significant difference, namely that the response of SFD1, Fig 7.18a indicates the presence of a strong subsynchronous response at high rotor speeds. As speed was decreased, a jump up occurred between frequency ratios, w/w_n of 1.57 and 1.51 (51 and 49 Hz, respectively), Fig 7.19a. The response of SFD2, Figs 7.18b and 7.19b, demonstrates the jump phenomenon clearly at the same speeds as for SFD2. However, the subsynchronous response at high speeds, although clear in the experimental SFD1 orbits is not as clear in the SFD2 orbits possibly due to the smaller orbit size.

The experimental and theoretical orbits, Figs 7.18 and 5.21, respectively, both illustrate strong nonsynchronous vibrations at w/w_n of 2.5 and the jump up on run down from a "double loop" SFD1 orbit to a very large centred SFD1 orbit. The general comparison of orbit size and disposition between experiment and predictions is good.

The theoretical response demonstrated bistable operation at all speeds above w/w_n of about 1.3, with the lower solution clearly rising above w/w_n of about 1.90 due to the increase in subsynchronous activity. A similar rise in the experimental results was less pronounced in the frequency response, Fig 7.19, but significant in the

orbits and waterfall diagrams (Fig 7.20). The experimental bistable region was indicated at speeds above w/w_n of about 1.5.

Thus, when static eccentricity, E_{o1} was introduced to configuration 2a then, at speeds between 65 and 81 Hz the subsynchronous response was of 1/2 EO. That is, the dominant subsynchronous component's frequency increased proportional to speed. Also, the experimental waterfall diagram, Fig 7.20, shows that at 81 Hz rotor speed (w/w_n = 2.5) this 1/2 EO had increased dramatically in amplitude and for SFD1 was comparable with the synchronous component. In SFD2 the 1/2 EO was dominant over the synchronous vibration. The 3/2 EO and 5/2 EO components were also significant in this situation.

The experimental spectral information clearly illustrates the jump up on run down in the synchronous and harmonic responses and a similar jump up on run down (at the minimum jump frequency) is clear in the synchronous and harmonic responses of the predicted waterfall diagram, Fig 5.23.

The predicted response indicates significant response at 2 EO at low speeds, coinciding with the first bounce mode (32.4 Hz). This is similar to the predictions for configuration 2a with SFD1 statically concentric, Fig 7.14, but with SFD1 statically eccentric this response at the first bounce mode is reduced in amplitude, probably due to the increase in damping of the uncentred journal motion in that instance. At higher speeds, before the jump up on run down, the theory and the experiment both indicate very strong 1/2 EO components, accompanied by 3/2 EO and 5/2 EO responses, particularly in the SFD2 response. It should be noted that at 73 Hz rotor speed (marked by an asterisk) the spectrum is for the non-

inverted solution, Fig 5.23. The inverted, lower amplitude solution was sought at all speeds above the minimum jump frequency. However, at 73 Hz rotor speed, numerical sensitivities prevented this solution from being marched out for long enough to obtain the full discrete time series required by the FFT algorithm. Initially the method would begin to converge to the lower solution, but then the numerical response would suddenly switch to converge to the larger solution and this feature was consistent for a range of initial conditions.

7.5 Rig Configuration 2b

Configuration 2b involved the raising of the SFD1 housing so that it took the rotor weight and unloaded the support, k_z and centralised SFD2.

The experimental response of the rig to various unbalance factors indicated that the static load acting on SFD1 restricted its journal movement to orbits close to its fully eccentric position at speeds upto a critical speed. During run up, a jump up in orbit size took place at the critical speed, when unbalance was sufficiently high. The central positioning of SFD2 to give zero static eccentricity, did not encourage circular journal orbits there; instead the SFD2 journal motion was heavily influenced by the shape of the SFD1 orbits. Figs 7.21a,b show the journal centre orbits within the clearance circle (radius c) for SFD1 and SFD2, respectively for a Q_{c2} of 0.611 and Psup set at 2 psi. A jump up between w/w_n of 1.57 and 2.01 (51 and 65 Hz, respectively) is clearly demonstrated.

Figs 7.22a,b give the amplitude responses over the rotor speed range for SFD1 and SFD2 with Psup set at 2 psi. Jump phenomena were exhibited over a range of Q_{c2} from 0.490 to 0.733. On run down a jump down would occur at a lower speed than that at which a jump up occurred on run up and this demonstrated a hysteresis of about 4 Hz rotor speed.

Figs 7.23a,b give the amplitude responses over the rotor speed range for SFD1 and SFD2 with Psup set at 15 psi. Jump phenomena were still exhibited over a range of Q_{c2} from 0.490 to 0.733 but with Q_{c2} equal to 0.490 a jump was only discernible in the 'y' eccentricity of SFD1. Hysteresis in the jump speeds between run up and run down was evident within these results, also.

The experimental and theoretical orbits, Figs 7.21 and 5.24, respectively, compare well, demonstrating a relatively low amplitude response on run up followed by a strong jump up at high speed. The experimental jump occurs earlier in the speed range than its predicted counterpart. For a low supply pressure, Psup equal to 2 psi and with Q_{c2} equal to 0.733 the experimental response, Fig 7.22 indicates a jump up at w/w_n of about 1.54, and the theory, Fig 5.25, predicts a jump up at w/w_n of about 1.70. With Q_{c2} equal to 0.490 the experimental jump up occurs at w/w_n of about 1.98 which compares with the corresponding prediction at w/w_n of about 2.07. These results are summarised in Table 7.6. The theory predicted maximum jump frequencies slightly higher than those observed experimentally by an average of about 5 % with respect to the experimental frequencies.

The experimental results demonstrated a clear hysteresis; jump up on run up took place at a higher speed than jump

down on run down. With Psup set at 2 psi, the rotor speed hysteresis was about 4 Hz and increased to about 6 Hz when Psup was set at 15 psi. Such hysteresis was not present in the theoretical results. The theoretical bistable regions above these maximum jump frequencies were observed to persist well above the speed range relevant to this study. The experimental hysteresis might be due to a change in the SFD parameters so that, with one particular set of parameters, a jump up on run up occurs at a specific speed and this might be accompanied by a change in one or more parameter values (such as cavitation pressure) which persists on run down causing the jump down to occur at a lower speed. This point will be given further consideration later.

The effect of increasing supply pressure in the experiment and theoretical predictions compares well; both indicated that with Psup at 15 psi the jump up would only occur for the two highest unbalances (Q_{c2} equal to 0.611 and 0.733) whereas with Psup equal to 2 psi the jump up would be possible for unbalances down to and including Q_{c2} equal to 0.490.

Fig 7.24 presents experimental waterfall diagrams for SFD1 and SFD2. A strong jump down with decreasing speed is present with Q_{c2} equal to 0.611, also shown in Figs 7.21 and 7.22. This is clear in the synchronous and higher integer engine orders. Some subsynchronous activity is also clear with this scaling.

Configuration 2b displayed some 1/2 EO, 3/2 EO and 5/2 EO nonsynchronous components in the experimental response, Fig 7.24. This became noticable at rotor speeds around the first bounce frequency. The amplitude of these half integer engine orders was never large enough to dominate the synchronous component. The theoretical waterfall

diagram, Fig 5.27, compares well with the experiment, predicting the jump up with increasing speed and the absence of any significant subsynchronous resonances.

7.6 Rig Configuration 3a

Configuration 3a involved the flexible supporting of both SFD1 and SFD2 with support bars, k_1 and k_2, respectively. Both SFDs were fully eccentric in the static case.

As expected, the inclusion of k_1, flexibly supporting SFD1's housing, had the effect of raising the static natural frequency of the assembled test rig (with SFD1 and SFD2 clearances shimmed) to an average of about 36 Hz (see section 6.5). However, the frequency ratio, w/w_n, was maintained with w_n equal to 32.4 Hz for ease of comparison.

For this configuration both SFDs were loaded statically to an eccentricity ratio of unity (refer to section 6.1). Figs 7.25a,b and c show the experimental orbits of SFD1, SFD2 and rotor relative to ground at SFD2 (RRG2) with Qc2 0.611 and Psup at 2 psi. The orbits of SFD1, Fig 7.25a, are generally restricted to the bottom of the clearance circle and the greatest orbit size, at w/w_n 0.957 after a jump up, was about half the clearance. After jump down, some non-synchronous activity was discernible at w/w_n equal to 1.142. For SFD2, Fig 7.25b demonstrates a similar response to SFD1 but exhibits larger orbits. RRG2 orbits also show the jump up and down and subharmonic resonance, Fig 7.25c.

The SFD1 orbit amplitudes were generally very low, as

shown in the amplitude ratios of Fig 7.26a, only rising above a value of about 0.1 around resonance. However, the SFD2 amplitudes were significantly larger, particularly around the peak amplitudes occurring around the jump up on run up, just above a w/w_n of about 0.9 for the two highest unbalances, Q_{c2} equal to 0.733 and 0.611. For the highest unbalance, Q_{c2} equal to 0.733, the vibration after the jump up was considered excessively high and rotor speeds were not increased further. The rotor amplitudes relative to ground at SFD2, RRG2, exceeded the range of the capacitance displacement transducer, at the peak amplitudes, rising above 2.0 mm (peak to peak), Fig 7.26c.

Raising the supply pressure, Psup to 14 psi (the maximum available for the configuration), restricted the jump phenomena to the highest unbalance, Q_{c2} equal to 0.733, Figs 7.27a,b and c. The maximum rotor displacement, RRG2 was about 1.7 mm.

The spectral contents of the SFD2 and RRG2 'y' direction signals are given in the waterfall diagrams of Figs 7.28a,b, respectively and clearly demonstrate the peak amplitudes in 1 EO, 2 EO, 3 EO and 4 EO at a rotor speed of about 31 Hz. Also, non-synchronous activity (1/2 EO, 3/2 EO, etc) around the first bounce mode static frequency of 36 Hz is significant when Q_{c2} is 0.490.

7.7 Rig Configuration 3b

Configuration 3b was similar to configuration 3a except that the journal of SFD1 was centralised in the static case. The response of configuration 3b was similar to

that of configuration 3a. Static centralisation of SFD1 generally increased the SFD1 orbit sizes and centralised them, Fig 7.29a. The effect on the SFD2 and RRG2 orbits was to eliminate the subsynchronous activity at w/w_n equal to 1.14, Figs 7.29b,c, respectively.

The amplitude responses demonstrated that the jump phenomena were still observable for an unbalance, Q_{c2} of 0.611 but not for Q_{c2} of 0.490, Figs 7.30a,b, and c. Fig 7.31 demonstrates the absence of significant subsynchronous activity in configuration 3b.

7.8 Discussion

The experimental and theoretical results demonstrated similar ranges of non-linear phenomena. The comparison of the occurrence of such phenomena for each configuration is good. The significant practical effects of misalignment and SFD support were comprehensively borne out in the theoretical results, giving an appreciation of the range of vibration characteristics that are to be expected from rigid rotor-damper assemblies. The range of non-linear phenomena observed in configurations 1a through to 3b are summarised in Table 7.8.

The quantitative discrepancy between the results of the general Short Bearing theory and experiment is generally related to two factors. Firstly, the experiment displayed a more damped response than does the traditional theoretical representation of the SFD having two independent lands, for the range of unbalance presented. Alternatively, if the lands are considered

coupled so that the SFD parameters, A_1 and A_2 are increased, the predictions exhibit a more damped response with a significant reduction in the occurrence of non-linear phenomena than observed from the experiments. The experiments thus lie between the two extremes.

Variations in the film conditions may alter the effective experimental SFD bearing parameters, A_1 and A_2. For instance, White [30] observed cavitation extending around the damper annulus (throughout the positive pressure region) and bubbles collecting at the mid land position. This cavitation effectively reduced the capacity of the SFD by creating two half width lands separated by a circumferential cavitation region, in the same way that a central groove can decouple two lands to a certain extent. It is clear that the effective damping capacity of the SFD is reduced if cavitation occurs in a positive pressure region. Therefore cavitation variations can cause the effective experimental 'A' values to change.

The only damping allowed for in the theoretical rig model was provided by the SFDs. The experimental rig itself might have experienced additional damping from sources other than the SFDs. Considering the experimental facility, internal material damping from the rotor would be negligible due to its rigidity over the operating speed range. Internal damping from the SFD housing support bars, which did deflect appreciably would be present. However, the analysis of the static natural frequencies of the support bars with and without the rotor assembled indicated very low damping following a soft hammer impulse. A typical logarithmic decrement of below about 0.07 indicated a maximum damping ratio, with respect to critical damping, of the order of 0.01. Rotor windage and other secondary effects were considered insignificant and so attention was directed to the

possibility of the two land SFD model underestimating the damping.

Secondly, although setting the cavitation pressure, Pmin to absolute zero has been shown to be generally applicable, there are instances when the experimental response can only be simulated by a change in the cavitation pressure.

The principal assumptions associated with the two land SFD model which can be questioned are:

- With the Short Bearing approximation applied, it was assumed that inertial effects were low. Calculations for the Gap Reynold Number, R_e associated with the range of operation of the test rig indicated that R_e varied between about 1.0 and 10.0. It would appear that such values may be significant. However, when the weight of the rotor is considered, it is clear that any added mass effects from the oil film, which weighs some twenty thousand times less than the rotor, would be negligible, even at high speeds.

- The dual land SFD was assumed to operate with the central circumferential oil supply groove decoupling the pressure distributions within each land and contributing negligible dynamic pressure itself.

  Experiments, although initially carried out using a circumferential supply groove depth, G equal to 0.5 mm, were continued using a deep supply groove, with G equal to 2.0 mm. Although the results with a deep grooved SFD did indicate a reduction in damping from the shallow groove results, the experimental rig still demonstrated more damping than the two land theory predicted.

As an alternative theoretical assumption to the two land SFD model, the circumferential supply groove was assumed to couple the dynamic pressure profile between the lands. Some predictions were obtained using the appropriately higher value of damper parameter, A_1 equal to 0.08528. Fig 5.11 shows the predictions for configuration 1a with a range of unbalance and supply pressure, Psup set at 2 psi. No bistable operation is indicated and the resulting response curves are similar to the 2π film predictions, Fig 5.3, although clearly less damped. Therefore the experimental results, Figs 7.2 and 7.4, indicate that the appropriate damping developed by SFD1 fell between the values indicated by the coupled and uncoupled land assumptions, A_1 equal to 0.08528 and 0.02132, respectively.

- The SFD model simulated the cavitation as a single rupture or bubble, when the dynamic pressure fell below an assumed minimum, or cut-off pressure. This introduced inaccuracies because the practical situation does not produce such a condition. Instead, the cavitation almost certainly consisted of a large number of vapour and gaseous cavitation bubbles of varying size, possibly concentrated around the region of minimum pressure with gaseous cavitation extending around the full clearance, throughout the positive pressure region (refer to [30], [61] and [62]). However, the added complication of a compressible film model has been shown to produce only marginal improvements in the comparison with experimental results, [55].

- It is possible that further improvement between the quantitative correlation of experimental and theoretical results will result if, at each speed, the approximate experimental cavitation pressure is

calculated from one or more pressure recordings made at the SFD housing surfaces. The approximate variation of cavitation pressure over the speed range for each case could then be used within the variable film extent model [72]. Thus, the resulting predictions may agree with the experiment more closely.

This technique is generally limited to laboratory conditions where the such pressure measurements are relatively easy. Identifying a specific cavitation pressure from a pressure signal displayed on an oscilloscope screen was hampered in the present work by instrumentation problems. The adoption of absolute zero as a reasonably applicable cavitation pressure has been successful in producing a good comparison with other models [58] and experimental recordings [72] indicate that it is the most appropriate average value to employ.

Chapter 8 PRACTICAL IMPLICATIONS ARISING FROM THE RESEARCH

Non-linear phenomena attract significant academic attention and a lot of research has been and continues to be carried out in the area of non-linear analysis. This attention is commendable since the practical consequences arising from the occurrence of some non-linear phenomena are severe. For instance, the dramatic destruction of the Tacoma Narrows suspension bridge was caused by non-linear aeroelastic excitation [73]. The occurrence of non-linear phenomena in aero-engine vibration responses can also have significant consequences, particularly during the development of a new or modified design.

The present research has demonstrated the ability of a range of rotor-bearing assemblies, incorporating unsealed SFDs, to exhibit a number of undesirable non-linear phenomena. Jump phenomena can lead to high transmitted forces and sudden changes in engine vibration. Non-synchronous response causes fluctuating rotor stresses in flexible shafts. It also leads to subharmonic resonances, sometimes larger than the resonances developed by unbalance.

It should be remembered when considering the difficulties which SFDs can introduce to the rotordynamics of an aero-engine, that, despite their drawbacks, SFDs have provided a very cost effective means of introducing damping to rotor assemblies, thus improving the vibration characteristics of modern assemblies for all but a relatively small number of troubled designs. It was the unpredictability and severity of jumps and subsynchronous

resonances which led to the sponsorship of the present research.

8.1 The Effect of Manufacturing Tolerances on Assembly Vibration Response

Aero-engine assemblies employ one or more SFDs per rotor, each within a bearing pedestal characterised by a certain stiffness. A degree of misalignment in three-bearing assemblies is inevitable due to the 'stack up' of tolerances, and the effects of high speed manoeuvres of military aircraft may serve to further affect the bearing alignments.

Most assemblies employ sealed SFDs to improve damping capacity and strong jump phenomena are not always a problem. However, there have been many reported instances and results emanating from this research indicate the physical mechanisms which promote such phenomena.

Holmes and Dogan's work [23] indicated that a jump up on run up can exist when a rotor is supported by a rigidly housed SFD and high vibration amplitudes can prevent higher speeds being attained. The same SFD, when mounted flexibly can respond without a jump up but non-synchronous rotor centre orbits can be introduced at speeds around the assembly's new natural frequency. Low vibration levels can, however, be achieved at speeds above this natural frequency.

Based on the present research, assemblies with a single SFD, centred by a flexible rotor support, are likely to exhibit jumps only when the unbalance is relatively high,

probably outside acceptable contractual limits. These jumps are analogous to the classical non-linear hardening spring response and arise from the stiffness property of a cavitated squeeze-film which increases with speed. On the other hand, the same assemblies with the SFD statically off-centred are likely to demonstrate that low unbalance, possibly within contractual limits, can excite jumps and strong subharmonic resonance.

Some assemblies incorporate two SFDs with very different housing supports, for example, one rigidly housed and the other flexibly housed. With the former statically centred and the latter carrying the rotor weight the response is likely to be governed by the former, the latter having little influence. Jump phenomena will occur around the first bounce mode frequency if unbalance is sufficiently large. At high speed, after jump down, satisfactory operation should be possible with low amplitude subsynchronous activity around the bounce mode frequency. Raising the housing of the rigidly-supported SFD is likely to result in subharmonic resonance possibly dominating the synchronous response and degrading the operating speed range.

By raising the rigidly mounted SFD housing further still, until it carries the static rotor weight and such that the flexibly supported SFD is centred, safe operation can only be guaranteed upto a certain speed, at which a strong jump up can be expected. On running down, the vibration will jump down at a lower speed. A static eccentricity applied to the flexibly-supported SFD may alleviate the jump or increase the speed at which it takes place due to some of the rotor weight being supported dynamically by this flexibly supported SFD.

The flexible supporting of both SFDs with similar support

stiffnesses should give rise to desirable operation for all but a small speed range around the first bounce mode. It may be that jumps and subharmonic resonance at these speeds could be eliminated by additional damping from SFD sealing without degrading the rest of the speed range. Centralising one of the SFDs has the effect of reducing the subharmonic resonance at speeds around the first bounce mode.

The presence of half engine order subharmonic resonance dominating the synchronous response at speeds well above the bounce frequency would suggest that one of the SFDs was not supported flexibly enough and was neither fully eccentric, nor concentric in its housing. If, in another case, strong jumps up on acceleration were encountered at speeds well above the bounce mode, then it might be caused by a SFD housing support being too rigid for it to safely carry the rotor weight. Improvements might be achieved by off-loading the 'rigidly' housed SFD, softening its support or both.

8.2 The Effect of Squeeze-Film Damper Support Flexibility on Assembly Vibration Response

Assembly vibration response depends jointly on the extent of misalignment and bearing housing support flexibility and these were discussed above. However, it is instructive to note from section 8.1 that the flexible supporting of a SFD in a two bearing assembly can alleviate a potential jump up which would occur at high speed, above the first bounce mode and probably within the operating range. It should be remembered that the

introduction of support flexibility may not be desirable due to the need to restrict rotating component displacements to ensure good blade tip and gland sealing to maintain efficiency, for example.

The vibration response of a three bearing assembly incorporating more than one SFD with contrasting support flexibilities is critically dependent upon the degree of misalignment within the assembly. Any rigidly supported SFDs should be statically centralised so as to exhibit circular centred orbits (refer to section 8.1). Even relatively small static eccentricities within rigidly supported SFDs can lead to strong subsynchronous resonance at high speed and with a rigidly supported SFD carrying substantial static load, jumps up at high speed are possible. If such an arrangement is employed then, if the clearance of the rigidly housed SFD were enlarged (with respect to traditional designs), the static centralisation with respect to the manufacturing tolerances could be improved and the nonlinearities leading to undesirable phenomena curtailed. The negative aspect of such an action would be the noticable reduction in damping provided by a SFD of similar width and diameter but increased clearance. On the other hand, this reduction in damping may not be detrimental if the original design provided more than the critical damping for the assembly. It should be noted that estimating the effective linear damping introduced by SFDs to an assembly is difficult, with the range of uncertainty possibly encompassing both under and over-critical situations. It is often difficult, therefore, to optimise the amount of damping introduced to the assembly.

It is quite clear from experimental results that with more than one SFD the flexible supporting of each SFD housing, although increasing the maximum rotor excursions

causes the vibration response above the first bounce mode to be of low amplitude. The vibration response is also less susceptible to changes in misalignment.

8.3 The Application of Squeeze-Film Damper Performance Parameters

In designing a SFD for vibration isolation within a rotor-bearing assembly, a quantitative assessment of the SFD damping capacity is required. Traditionally either the speed dependent parameter, 'β' or speed independent parameter, 'A' have been utilised. In general

$$\beta = \mu R(l/c)^3/mw$$

and $$A = \pi\beta/\bar{k}^{0.5} = \pi\mu R(l/c)^3/(km)^{0.5}$$

where $$\bar{k} = (w_n/w)^2$$

and where the mass, m is that assembly mass carried by the SFD, per land.

If we consider the radial clearance between the journal and the bottom of the circumferential oil supply groove, then an equivalent parameter can be attributed to the groove to consider the contribution of the groove to the overall SFD performance. This parameter, τ will be defined as;

$$\tau = 0.5\{(Gw/(G + c))/(l/c)\}^3$$

and gives a measure of the performance of the central circumferential groove compared to the performance of a

two land SFD.

With a 0.5 mm deep groove the theoretical groove contribution to the SFD1 capacity, τ equals 0.09% of the two land capacity. τ is reduced to 0.006% for a groove depth of 2.0 mm. Hence it is quite clear that the contribution of the groove to the overall capacity of the SFD1 is negligible. The situation is similar for SFD2.

The 'two land' approach considers that the two lands, separated by the supply groove, contribute independently to the damping capacity of the SFD and assumes that the groove decouples the lands' pressure distributions. Another approach is to consider a 'one land' assumption, ie that the groove might not be acting as a supply reservoir but provides coupling of the two lands' pressure distributions. If the SFD is considered as a single land then the values of A and β are quadrupled over the 'two land' assumption, as described previously (section 5.1).

The experimental effects of deepening the SFD supply groove have been demonstrated in configuration 1a to reduce the damping capacity of the SFD to some degree. The effect of groove depth on response has been shown to be significant, especially for particular unbalance values where the groove deepening has given rise to jump phenomena where previously the response was continuous over the speed range, being similar to that of a 2π film model. In general the response of the experimental test facility indicates that the effective A and β parameter values lie between the 'two land' and 'one land' assumptions.

In practice the value of parameter A, for instance can vary considerably due to changes in viscosity arising

from temperature fluctuations. Temperature rises of only 2°C were typical during a run-up and run-down of the test rig. Industrial units would experience significant temperature variation and so the need to assess the possible range of SFD performance parameters such as A and β is obvious.

The effective viscosity of a bubbly oil is different from that of the same oil when uncavitated. In practice the cavitation consists of a mass of bubbles whose number, size and distribution depend upon a range of parameters, such as rotor speed, viscosity and journal/housing surface roughness. Such cavitation has been approximated [55] by employing homogeneous compressible fluid models. Some suggest that cavitation reduces the effective dynamic viscosity [57] whereas others suggest the opposite [56].

Therefore, in practice the effective 'A' value can vary over the speed range. During the design of an assembly it is impractical to account for detailed variations in the 'A' or 'β' parameters, however an appreciation of the physical parameters which affect them should be assessed so that approximate ranges for the values of 'A' or 'β' can be established.

Chapter 9 NON-LINEAR PHENOMENA

The principal non-linear phenomena observed in the present research can be categorised as being jump phenomena and nonsynchronous response. Subharmonic resonance is a particular form of nonsynchronous response, occurring at a natural frequency of the system and excited by forcing occurring at an integer multiple of the natural frequency.

9.1 Jump Phenomena

The jump up with decreasing speed or jump down with increasing speed above the first bounce mode frequency corresponds to the classical non-linear 'hardening spring' response. The difference in the two speeds is the effective range of the bistable region, Fig 1.3. Equally, a jump up with increasing speed might be attributed to a non-linear 'softening spring' effect.

In terms of non-linear analysis, the synchronous jump phenomenon is a simple fold catastrophe. A good physical analogy is the jump characteristic of the load-deflection behaviour of a shallow tied arch as described by Thompson [73]. Consider the simple π film model of configuration 1a (a parallel SFD and spring combination); starting from rest (w/w_n at zero) then the system's response to unbalance can be described by a phase diagram which consists of one stable phase trajectory or periodic attractor with all numerical or physical transient

starting conditions being attracted to the single trajectory, Fig 9.1a (shown as a circle A on the unscaled phase diagram for simplicity). The arrowed lines approaching circle A indicate paths of attraction that a transient might undergo before reaching the periodic trajectory.

At the minimum jump frequency, as indicated in Fig 1.3, then two periodic attractors, one nested inside the other will appear, Fig 9.1b. The smaller of the attractors (labelled B in Fig 9.1b) represents the inverted solution whilst the larger trajectory represents the non-inverted solution. Any deviation away from the lower of the solutions will result in the system coming to rest at the higher solution. At higher rotor speeds, ie within the bistable region, the two stable solutions are accompanied by an unstable solution known as a separatrix, labelled S, Fig 9.1c. As its name implies, the separatrix separates the two nested periodic attractors and, depending upon the starting point of a numerical or practical transient, it will determine which of the two stable solutions are achieved. At the maximum speed within the bistable region, the separatrix will disappear and two stable trajectories exist, as at the minimum jump frequency. However, in this instance any deviation from the larger solution will result in inversion to the lower solution, Fig 9.1d. At speeds above the bistable region only one solution exists and the phase diagram will only consist of a single attractor, as in Fig 9.1a, but the attractor label would be B in this instance in keeping with the notation of Figs 9.1b,c and d.

The jump phenomenon between circular centred orbits is relatively simple to appreciate. Also, in statically loaded SFDs, the large 'non-inverted' orbit is not dissimilar to that occurring in the simple π film

hardening response. The smaller orbit can be of complicated shape and can contain significant non-synchronous components.

A jump up and subsequent jump down can occur when a SFD is aligned between the fully eccentric and concentric conditions. On run up a jump up is initiated and is probably due to a softening property of the oil film whereas the subsequent jump down relates to a hardening of the film properties. It is interesting to note that Reif [74] demonstrated that solutions of the Duffing equation including the effect of static deflection, of the form;

$$\ddot{y} + \bar{k}.\bar{y} + \bar{k}_3.\bar{y}^3 - Q_s = Q_c.\cos(wt) \ ,$$

where $\bar{k}_3$ is very much less than $\bar{k}$,

gave a harmonic response involving a jump up at frequency ratios above unity followed by a jump down with increasing speed. Reif [74] attributed this response to the presence of the static load, Q_s which is analogous to the misaligning of a SFD. Possible explanations for such a jump up on run up have been presented earlier (section 7.2), namely that the apparent softening characteristic could be induced by a change in the cavitation conditions of the SFDs, or a change in the effective SFD parameter, 'A'.

There is experimental evidence [72] that sudden venting of the SFD from atmosphere changes the effective cavitation conditions, and could promote the jump up with increasing speed. Oil-film pressure measurements taken for configuration 2b indicated that the minimum pressure rose after jump up on run up from about absolute zero pressure to about atmospheric pressure. A limited

hysteresis in the rotor speeds, of about 4 Hz at most, was noted between the jump up on run up and the jump down on run down.

9.2 The Influence of Cavitation Pressures on Jump Phenomena In Uncentralised Squeeze-Film Dampers

To study the 'softening spring' effect further, consider a rotor supported by one SFD which is rigidly supported, Fig 9.2. The rotor weight will guarantee fully eccentric static SFD conditions, similar to an arrangement previously studied, [72]. When unbalance forces are small the high squeeze-film forces produced around the fully eccentric condition, in conjunction with the rotor weight, successfully restrain the SFD journal motion. However, with increasing speed, the unbalance force might become large enough to cause the journal motion to execute the upper part of its orbit towards the clearance centre. This might reduce the restraint on the journal during its movement remote from the fully eccentric position to an extent that a sudden jump up in orbit size takes place.

Fig 9.3 gives two theoretical orbits for different cavitation pressures (Pmin of -14.7 and 0.0 psi), all other conditions being the same. A sudden change in cavitation pressure could arise from atmospheric venting and result in a jump in the orbit from a small non-circular response (-14.7 psi) to a large, full clearance orbit (0.0 psi). The amplitude responses for a range of Pmin from 0.0 psi (high cavitation extent) to -45.0 psi (low cavitation extent) is given in Fig 9.4. A consistent decrease in the jump speed with increasing cavitation

extent is illustrated. With cavitation occurring below atmospheric pressure, 0.0 psi there is no distinct jump as such but a sharp increase in the amplitude slope. Fig 9.5 shows the predicted response for conditions of film rupture at absolute zero pressure on run up followed by atmospheric cavitation after jump up. There is a distinct hysteresis between the jump up on run up and the jump down on run down. This response thus has the characteristics of a softening spring and mimics the response of configuration 2b. The indications are therefore that the stiffly supported SFD has a dominating influence on the response of the complete assembly.

9.3 The Development of Subharmonic Resonance

Significant subharmonic resonances of half engine order have been demonstrated both experimentally and theoretically during the research study. Non-synchronous activity at 3/2 EO, 5/2 EO and 7/2 EO accompanied these subharmonics.

A statically centred SFD in configurations 1a and 2a gave rise to weak subsynchronous resonance at the static natural frequency, Figs 5.12 and 5.20. Static eccentricity applied to the same SFD increased its non-linearity and excited strong half engine order subharmonics, this time corresponding to the dynamic natural frequency, determined by the stiffnesses of both the static components and the SFD's, Figs 5.15 and 5.23.

The development of subharmonic resonances within the responses of non-linear dynamic systems has been

researched extensively. The Duffing equation has been instrumental in explaining the period doubling bifurcation associated with the onset of subharmonic resonance. Stoker [10] states that subharmonic response is produced because of bifurcation from the harmonic component.

The excitation force for the rotor-bearing assembly consists of a rotating unbalance vector and a static rotor weight vector. This unsymmetric forcing is similar to the forcing applied to Duffing's Equation by Szemplinska-Stupnicka [13], namely

$$x'' + h.x' + \bar{x}^3 = Q_s + Q_c.\cos(w.t) \quad .$$

A consistent characteristic of the subharmonic resonances studied has been that, in comparison with the synchronous response (and other integer EO's), the subharmonics do not stand out as sharp amplitude spikes above the noise level of the autopower spectra. The peak subharmonic amplitudes are sandwiched between gradually decreasing spectral activity, as shown in Fig 9.6e and the experimental spectrum of Fig 9.7. This observation suggests that period doubling bifurcation between DC and rotor angular frequency (Fig 9.6a to e) is responsible for the gradual rise to the subharmonic peak of the 1/2 EO, as discussed in [13]. Thus, the full solution has the form;

$$x(t) = A_o + A_1.\cos(w.t) + A_{1/2}.\cos(w.t/2 + \phi).$$

Szemplinska-Stupnicka [13] identifies, in conjunction with such bifurcation, transitions to chaotic motion within small frequency regions. The chaotic motion takes the form of irregular fluctuation of the subharmonic prior to decay. Fluctuation of the vibration orbits

exhibiting 1/2 EO vibration components have been noted experimentally for specific speeds and are possibly practical examples of the existence of chaotic attractors within the rotor-bearing responses.

It would be interesting to note the harmonic order of subharmonic resonances observed in a vertical rotor assembly, when the rotor weight excitation is removed and the forcing is symmetric as in the equation;

$$x'' + h.x' + \bar{x}^3 = Qc.\cos(w.t) \quad .$$

From this equation the resulting subharmonic motion has been demonstrated at a 1/3 EO, [13].

It is also interesting to note that introducing the static eccentricity of SFD1 in configurations 1b and 2a gave rise to an increase in the strength of the 1/2 EO response so that, in some instances, it dominated the synchronous response. Fig 9.7 shows that not only does the response at 1/2 EO, 3/2 EO, etc accompany an increase in E_{o1} from zero to half, but that all 1/2 EO, 1 EO, 3/2 EO, 2 EO, etc show signs of period doubling bifurcation.

Chapter 10 THE ABILITY OF LINEAR ANALYSIS TO PREDICT EXPERIMENTAL RESULTS

A simple linear analysis of a system representing a two SFD rotor-bearing assembly is now presented to establish the usefulness of such approximate modelling in estimating the synchronous experimental responses.

10.1 Linear Analysis

Linear analysis requires a small fraction of the computational effort required for non-linear analysis. It is instructive to ascertain the extent to which linear analysis can predict the synchronous trends demonstrated by the experiment.

Analysis of the simple three DOF system, Fig 10.1 gives a linear response where the mass, m^L represents a rigid rotor. The linear dampers, b_1^L and b_2^L represent the damping contribution of two SFDs and the flexibilities, K_1^L and K_2^L can be representative of the stiffness contributions of two SFDs or can represent SFD centralising springs, or bearing housing supports.

Referring to Fig 10.1, omitting the superscript '^{L}' (for simplicity) and observing Newton's Second Law;

$$P_c.\sin(w.t) = m.\ddot{X} + K_1(X - x_1) + b_1(\dot{X} - \dot{x}_1) + K_2(X - x_2) + b_2(\dot{X} - \dot{x}_2) \quad \ldots\ldots\{10.1\}$$

$$K_1(X - x_1) + b_1(\dot{X} - \dot{x}_1) = k_1.x_1$$

....{10.2}

$$K_2(X - x_2) + b_2(\dot{X} - \dot{x}_2) = k_2.x_2$$

....{10.3}

Assume solutions of the form $X = X.\sin(w.t - \phi)$

$x_1 = x_1.\sin(w.t - \phi_1)$

$x_2 = x_2.\sin(w.t - \phi_2)$

....{10.4}

By differentiating {10.4} with respect to time and substituting into {10.1}, {10.2} and {10.3} then

If $\sin(w.t) = 1$ then $\cos(w.t) = 0$, therefore we can write

$$P_C = X[\{K_1 + K_2 - m.w^2\}\cos\phi + \{b_1 + b_2\}w.\sin\phi] - x_1[K_1.\cos\phi_1 + b_1.w.\sin\phi_1] - x_2[K_2.\cos\phi_2 + b_2.w.\sin\phi_2]$$

....{10.5}

$$k_1.x_1.\cos\phi_1 = K_1(X.\cos\phi - x_1.\cos\phi_1) + b_1.w(X.\sin\phi - x_1.\sin\phi_1)$$

....{10.6}

$$k_2.x_2.\cos\phi_2 = K_2(X.\cos\phi - x_2.\cos\phi_2) + b_2.w(X.\sin\phi - x_2.\sin\phi_2)$$

....{10.7}

Also, if $\sin(w.t) = 0$ then $\cos(w.t) = 1$, therefore we can write

$$0 = X[\{- K_1 - K_2 + m.w^2\}\sin\phi + \{b_1 + b_2\}w.\cos\phi] + x_1[K_1.\sin\phi_1 - b_1.w.\cos\phi_1] + x_2[K_2.\sin\phi_2 - b_2.w.\cos\phi_2] \quad \ldots\ldots\{10.8\}$$

$$- k_1.x_1.\sin\phi_1 = K_1(- X.\sin\phi + x_1.\sin\phi_1) + b_1.w(X.\cos\phi - x_1.\cos\phi_1) \quad \ldots\ldots\{10.9\}$$

$$- k_2.x_2.\sin\phi_2 = K_2(- X.\sin\phi + x_2.\sin\phi_2) + b_2.w(X.\cos\phi - x_2.\cos\phi_2) \quad \ldots\ldots\{10.10\}$$

Equations {10.5} through to {10.10} can be non-dimensionalised and written in matrix form;

$$[P_C] = [K].[X] \quad \ldots\ldots\{10.11\}$$

where $[P_C] = (\overline{P}_C \;\; 0 \;\; 0 \;\; 0 \;\; 0 \;\; 0)^T$

$$[X] = (\overline{X}.\cos\phi \;\; \overline{X}.\sin\phi \;\; \overline{x}_1.\cos\phi_1 \;\; \overline{x}_1.\sin\phi_1 \;\; \overline{x}_2.\cos\phi_2 \;\; \overline{x}_2.\sin\phi_2)^T$$

and

$$[K] = \begin{bmatrix} E1 & E2 & -E3 & -E4 & -E5 & -E6 \\ E2 & -E1 & -E4 & E3 & -E6 & E5 \\ E3 & E4 & -E7 & -E4 & 0 & 0 \\ E4 & -E3 & -E4 & E7 & 0 & 0 \\ E5 & E6 & 0 & 0 & -E8 & -E6 \\ E6 & -E5 & 0 & 0 & -E6 & E8 \end{bmatrix}$$

where $w_n = \sqrt{[(k_1 + k_2)/m]}$,

$E1 = (K_1 + K_2)/(k_1 + k_2) - (w/w_n)^2$,
$E2 = (b_1 + b_2)(w/w_n)/\sqrt{[m(k_1 + k_2)]}$,
$E3 = K_1/(k_1 + k_2)$
$E4 = b_1(w/w_n)/\sqrt{[m(k_1 + k_2)]}$,
$E5 = K_2/(k_1 + k_2)$,
$E6 = b_2(w/w_n)/\sqrt{[m(k_1 + k_2)]}$,
$E7 = (K_1 + k_1)/(k_1 + k_2)$ and
$E8 = (K_2 + k_2)/(k_1 + k_2)$.

Therefore, the matrix, [X] can be solved from

$$[X] = [K]^{-1}.[Pc] \qquad \ldots\ldots\{10.12\}$$

10.2 Rig Similarity

The response of the rig , Fig 10.2, can be derived from the simple model, Fig 10.1, by assigning appropriate dynamic parameters. Thus the following table dictates the similarity between the rig model of Fig 10.2 and the simplified model of Fig 10.1.

Fig 10.1	Fig 10.2
M^L	M
X^L	X(d/b)
x_1^L	x_1(d/f)
x_2^L	x_2(d/b)
P_C^L	P_C(a/d)
b_1^L	b_1(f/d)^2
b_2^L	b_2(b/d)^2
K_1^L	k_1(f/d)^2
K_2^L	k_2(b/d)^2

The range of rig configurations, Table 3.1, that were researched was reproduced by 'locking out' or 'removing' the appropriate stiffnesses and dampers by assigning appropriately large or small parameter values, respectively.

10.3 Linear Predictions

The parameter values indicated in the results, Figs 10.3 to 10.8 refer to the simple rig model of Fig 10.1. Fig

10.3 gives the linear responses for configuration 3a, that is b_1 and b_2 are assumed to be similar when both SFD1 and SFD2 are fully eccentric in the static condition. A resonance peak is observed only for over-critical damping and for all values of damping the amplitude in SFD2 was greater than that in SFD1.

To approximate configuration 3b the values of b_1 were set at 20% of the values of b_2 to represent the reduced damping by centring SFD1. Fig 10.4 gives the linear responses for configuration 3b and it can be seen that the amplitude of SFD1 is greater than that of SFD2 for over-critical damping.

The linear approximation to configuration 2a, Fig 10.5 with b_1 at 20% the value of b_2, indicates that the motion of SFD1 is greater than that of SFD2 for over-critical damping. The maximum SFD1 amplitude occurs for a high value of damping and takes the form of a distinct resonance peak close to w/w_n equal to one and when the damping factor B equals 3.464.

Fig 10.6 provides the linear response for configuration 2b with b_1 and b_2 set to the same value to simulate the horizontal situation. This is because, even with SFD1 fully eccentric in the static condition, the effective horizontal clearance is still about $0.99c_1$. Fig 10.7 approximates the vertical condition with b_2 set at 20% of b_1. There is no longer any distinct resonance peak around the natural frequency ($w/w_n = 1$). In Fig 10.6 the displacement of SFD1 is lower than that for SFD2 for all under-critical damping. With over-critical damping, B equal to 4.436, then the amplitude of SFD1 rises gradually with speed. The SFD2 amplitude also rises with speed but peaks at about w/w_n equal to 1.2. The horizontal response, Fig 10.6 is generally greater than

the vertical response, Fig 10.7 due to the static conditions with SFD1 fully eccentric (in the vertical direction). Fig 10.8 indicates the response for configurations 1a,b and demonstrates a distinct peak amplitude at the natural frequency for under-critical damping.

Considering the phase responses for configurations 3a and 3b, the rotor relative to ground (RRG2) response illustrates a second order response, whilst the SFD1 and SFD2 responses are third order. With configurations 2a and 2b, the SFD1 response is the rotor response relative to ground and is second order whilst the SFD2, still interposed between the rotor and a linear spring, maintains a third order response. Finally, configurations 1a and 1b illustrate a simple second order system.

10.4 Comparison Between Linear and Experimental Results

The linear analysis was carried out to observe how well a linear model would approximate the non-linear synchronous response of the experimental test rig with the exception of the non-linear jump phenomena. The simple rig model of Fig 10.1 generated the linear responses for configuration 3a. A resonance peak is observed only for over-critical linear damping and for all values of damping the amplitude in SFD2 was greater than that in SFD1, Fig 10.3, and this trend was observed experimentally, Figs 7.22 and 7.23.

Fig 10.4 gives the linear responses for configuration 3b

and it can be seen that the amplitude of SFD1 is greater than that of SFD2 for over-critical damping. Experiment, Fig 7.26, does show the SFD1 orbits to be larger than those of SFD2, except where non-linear jumps occur.

The linear approximation to configuration 2a indicates that the motion of SFD1 is greater than that of SFD2 for over-critical damping, Fig 10.5. It is interesting that the maximum SFD1 amplitude takes the form of a distinct resonance peak close to w/w_n equal to unity and when B equals 3.464. The experimental results, Figs 7.12 and 7.13, also indicate a resonance peak (accompanied by a jump, or non-linear hardening). The experiment also indicated that the SFD1 phase response passed through 90°, the point of inversion, at about w/w_n equal to 0.9 and this was the case for the linear analysis with B equal to 3.464, Fig 10.5.

Figs 10.6 and 10.7 provide linear responses for comparison with configuration 2b horizontal (x) and vertical (y) results, respectively, Figs 7.22 and 7.23. There is no longer any distinct resonance peak around the natural frequency (w/w_n equal to unity). The displacement of SFD1 is lower than that for SFD2 for all under-critical damping. With over-critical damping, B equal to 4.436, then the amplitude of SFD1 rises gradually with speed. The SFD2 amplitude also rises with speed but peaks at about w/w_n equal to 1.2. These trends for supercritical damping are similar to the experimental responses.

Fig 10.8 indicates the response for configurations 1a,b and demonstrates a distinct peak amplitude at the natural frequency for under-critical damping. If the increase in SFD1 static eccentricity is compared with an increase in damping then the linear effect of reducing the peak

amplitude is similar to the experimental responses, Figs 7.2, 7.3. 7.4 and 7.7.

The linear analysis has demonstrated that, with the exclusion of non-linear jumps and non-synchronous activity, the relative dynamic response of two SFDs can be observed. It can be concluded that the best agreement between the experimental and linear results occurs for damping ratios, B, of the order of 10^1 (between 1.0 and 10) for configurations 2 and 3. It is consistent with the experimental rig being over-critically damped, which indicates significant damping contributions provided by the two unsealed SFDs. In configurations 1a,b, with only SFD1 active, then the response appears under-critically damped.

Chapter 11 RAPID ESTIMATION OF THE SQUEEZE-FILM DAMPER NON-LINEAR RESPONSE

In order to be able to reproduce the non-linear SFD vibration characteristics afforded by the Short Bearing Approximation in a linear form and to improve the speed of computation of the response over the Runge-Kutta method, techniques for linearising the SFD response have to be reported in the literature.

Dogan [72] investigated a quasi-linear method which involved the use of stored stiffness and damping coefficients for a range of dynamic and static forces. The fundamental damping and stiffness coefficients were derived from a Fourier analysis of Runge-Kutta results. A tabulation of coefficients was required over a range of the dynamic force for each value of the static force to be considered . Then, using these SFD coefficients and a linear rotordynamic model, an iteration on the dynamic force was carried out to converge to a solution of the response. The most significant amount of computation was required to produce the stored coefficient tables.

Alternative methods of note include the secant root finding algorithm researched by Greenhill and Nelson [45] who assumed circular centred orbits. This iterative technique enabled analysis of intershaft SFDs and other complicated SFD applications with a linear model of flexible multi-shaft systems. In order to appreciate the application of the uncentralised SFD, with and without parallel support stiffness, the method of orbit perturbation was studied.

11.1 Orbit Perturbation

Orbit perturbation is a method where linearised coefficients are rapidly calculated from the perturbation of the squeeze-film damper (SFD) journal from a circular orbit. This technique has been applied by Holmes and Sykes, Appendix 6, to journal bearings and SFDs for large amplitude vibrations. The following is a summary of the application to the SFD.

To observe the perturbation of a journal from its circular orbit, it is convenient to work in a rotating coordinate system, 's' and 'r', Fig 11.1. Referring to Fig 11.1, the effect of a static load, W on the SFD journal can be analysed. $\delta P_r'$ and $\delta P_s'$ are the incremental oil-film forces, defined as

$$\delta P_r' = - a_{rr}.r - b_{rr}.\dot{r} - a_{rs}.s - b_{rs}.\dot{s}$$

$$\delta P_s' = - a_{ss}.s - b_{ss}.\dot{s} - a_{sr}.r - b_{sr}.\dot{r}$$

$$\ldots\ldots\{11.1\} ,$$

k is the parallel spring stiffness and ϵ_o is the eccentricity ratio determining the radius of the circular journal orbit within the clearance, c. From Fig 11.1,

$$m[\ \ddot{s} - s.w^2 + 2.\dot{r}.w\ ] = - (a_{ss} + k)s - b_{ss}.\dot{s} - a_{sr}.r - b_{sr}.\dot{r} - W.\cos(wt)$$

$$m[\ \ddot{r} - r.w^2 - 2.\dot{s}.w\ ] = -(a_{rr} + k)r - b_{rr}.\dot{r} - a_{rs}.s - b_{rs}.\dot{s} - W.\sin(wt)$$

.....{11.2}

Equations {11.2} can be solved for their particular integrals and substituting r = y.sin(wt) + x.cos(wt) gives the following

$$y = W\ (a_1.c_1 + b_1.w.d_1)/(a_1^2 + w^2.b_1^2)$$

$$x = W\ (a_1.d_1 - b_1.w.c_1)/(a_1^2 + w^2.b_1^2)$$

.....{11.3}

Where

$$a_1 = b_{rr}.b_{ss}.w^2 - (a_{ss} + k - 2.m.w^2)(a_{rr} + k - 2.m.w^2) - (b_{sr} + 2.m.w)(b_{rs} - 2.m.w)w^2 + a_{sr}.a_{rs}$$

$$b_1 = -b_{ss}(a_{rr} + k - 2.m.w^2) - b_{rr}(a_{ss} + k - 2.m.w^2) + a_{rs}(b_{sr} + 2.m.w) + a_{sr}(b_{rs} - 2.m.w)$$

$$c_1 = w.b_{rs} + a_{ss} + k - 4.m.w^2$$

$$d_1 = w.b_{ss} - a_{rs}$$

.....{11.4}

The values of x and y, equations {11.3}, locate the centre of the circular journal orbit within the clearance circle and can be non-dimensionalised so that

$$\bar{y} = y/c$$

$$\bar{x} = x/c.$$

The linear coefficients a_{rr}, b_{rr}, etc, equations {11.4}, are functions of ϵ_o and ϵ_o is a function of the dynamic force provided by unbalance and the SFD parameters.

Consider the response due to unbalance; Fig 11.2 represents the SFD journal within its housing with the unbalance force, P_c indicated. The orbit amplitude depends upon P_c, the film forces, P1 and P2 and the spring force, $k.c.\epsilon_o$. The equations of motion for concentric motion can be written as,

$$P_c.\cos(wt - \alpha) - P1 - k.c.\epsilon_o = - m.c.\epsilon_o.w^2$$

$$P_c.\sin(wt - \alpha) - P2 = 0$$

.....{11.5}

For a half cavitated, or π film, the forces P1 and P2 are given in Table 1.1 where, in this instance, ϵ in Table 1.1 is replaced by ϵ_o.

When the expressions for P1 and P2 are substituted into equation {11.5} then, after some manipulation, the π film response is given by

$$Q_c^2 = [\beta^2.\epsilon_o^2/(1 - \epsilon_o^2)^3][\pi^2/4 + 4.\epsilon_o^2/(1 - \epsilon_o^2)]$$

$$+ \epsilon_o^2(\bar{k} - 1)^2 + 4.\epsilon_o^3.\beta(\bar{k} - 1)/(1 - \epsilon_o^2)^2$$

.....{11.6}

where $\beta = A(\bar{k})^{0.5}/\pi$

It should be noted that equation {11.6} is similar to equation {4.9b} which was used to model the test rig response using a π film model for circular centred orbits.

Although the assumptions made concerning the cavitation zone, Appendix 6, are not generally applicable in practice, such film forces provide a demanding test of this linear treatment. Further still, if the case where k is assumed to be zero is analysed then the squeeze-film non-linearities will dominate the calculations. It has been shown, Appendix 6, that equations {11.4} can be reduced to give

$$a_1 = -(a_{ss} - 2.m.w^2)(a_{rr} + a_{ss})$$

$$b_1 = (a_{rs}/w)(a_{rr} + a_{ss})$$

$$c_1 = 2.a_{ss} - 4.m.w^2$$

$$d_1 = -2.a_{rs} \qquad \text{.....\{11.7\}}$$

where

$$a_{rr} = 2.m.w^2.\beta.\epsilon_o(1 + \epsilon_o^2)/(1 - \epsilon_o^2)^3$$

$$a_{ss} = m.w^2.\beta.\epsilon_o/(1 - \epsilon_o^2)^2$$

and $a_{rs} = -m.w^2.\beta.\pi/4(1 - \epsilon_o^2)^{1.5}$

Fig 11.3 gives the SFD journal centre orbits within the clearance circle obtained using the Runge-Kutta-Merson

method employing the full non-linear film forces and compares those orbits with ones obtained using the orbit perturbation method for a π film. The governing factors are $\bar{W}$, Qc and $\bar{W}/\beta$. Where the weight factor, $\bar{W}$ is large compared with the damper parameter, β then the comparison between the non-linear orbits and the linear estimations is good for higher unbalances, Qc.

Figs 11.3a,b provide the comparison between non-linear and linear orbits with $\bar{W}/\beta$ equal to 0.5 and β equal to 0.4. Good comparisons exist for all unbalance factors, Qc down to 0.4. When $\bar{W}/\beta$ is kept the same, but β is increased to 2.0, Figs 11.3c,d, then a good comparison is afforded only for unbalance factors, Qc as low as 1.5. This value of unbalance is also the lowest unbalance at which comparisons are good for β and $\bar{W}$ set to 1.0, Figs 11.3e,f. In general, if the orbit circumscribes the clearance centre then the comparison is good.

The limitations of the rapid linear estimation are that the solutions are generally valid above a certain unbalance. This unbalance is only low enough for practical design purposes when β is reasonably low and the ratio of $\bar{W}$ to β is low also. These limitations restrict the use of such a method to lightly loaded SFDs.

However, if the SFD design is to incorporate a parallel support spring, $\bar{k}$ then this will reduce the effect of the weight by supporting the journal within the clearance, rather than journal lift being completely relied upon from the film forces. In this instance, the rapid orbit perturbation method produces a good comparison with the non-linear orbits at low unbalances as well as at high unbalances. Figs 11.4a,b show the non-linear and linear orbits for the same parameter values as Figs 11.3e,f with the addition of a parallel support such that $\bar{k}$ is equal

to 2.0. That is the journal would take up a static vertical eccentricity ratio of one half. The comparisons are very good for a large range of unbalance.

In conclusion, this technique has significant limitations if it is to be applied to the design of SFDs without parallel spring supports. The relatively low levels of unbalance of interest in practice for smooth running would generally be lower than the unbalances which give a good linear estimation. Some unbalances, such as those associated with turbine blade loss, may be high enough to give a good estimation. The orbit perturbation method would be most useful where parallel support stiffness is applied and the applicability of the method could be assessed at the extremes of the governing parameter ranges.

An alternative method of linearisation, namely harmonic balance has been applied widely in non-linear analysis [75]. The method is introduced and its general features are discussed below.

11.2 The Harmonic Balance Method

This method enables a full non-linear SFD model to be approximated by linear Fourier coefficients. Applied generally the method is capable of deriving quasi-linear stiffness and damping coefficients for as full a Fourier Series as is required. Thus, as well as the synchronous response, the non-synchronous response of an assembly might be investigated.

The non-linear horizontal, or x displacement can be

written as a Fourier Series in the form:

$$x(t) = A_o + \sum_{(j=1)}^{J} (A_j.\cos(jwt/N) + B_j.\sin(jwt/N)) \qquad \text{.....\{11.8\}}$$

and similarly in the vertical, or y direction. J is the total number of equally spaced frequencies of interest and A_j and B_j are the linear Fourier displacement coefficients. N is an integer which is smaller than J and A_N and B_N are the synchronous components of the displacement response. The non-linear force can also be approximated using linear coefficients such that

$$fx(t) = fo + k.x + c.\dot{x} + \sum_{(j\neq N)}^{J} (a_j.\cos(jwt/N) + b_j.\sin(jwt/N)) \qquad \text{.....\{11.9\}}$$

where fo is a static force, k is a synchronous stiffness coefficient, c is a synchronous damping coefficient and a_j and b_j are nonsynchronous force coefficients.

Therefore, providing that a non-linear force function, fx can be described and integrated with respect to (w.t), a set of linear force coefficients can be derived from a set of initial amplitude coefficient estimates and an iteration process can be used to generate a revised set of amplitude coefficients. The iteration is repeated until convergence is achieved and the process is illustrated by the flow diagram of Fig 11.5. The method and, in particular the numerical convergence stability is discussed further in Appendix 7.

Chapter 12 CONCLUSIONS

The experimental facility has demonstrated a range of non-linear phenomena within its vibration responses associated with aero-engine assemblies. Both the results from experimental tests and the theoretical treatment have illustrated the dependence of the type and severity of the jump phenomena and the rotor speeds at which they occur upon the SFD misalignment and support conditions.

The following detailed conclusions are derived from the results of the research programme:

- Jump phenomena and strong subsynchronous resonances are the most dangerous vibration characteristics arising from the application of squeeze-film dampers, SFDs. Their occurrence, for any given assembly, depends upon the level of unbalance. As with any vibration problem, influencing the source of vibration, in this instance by reducing rotor unbalance, is the best remedy.

- The level of unbalance at which jump phenomena become a significant feature of the response depends primarily on the level of bearing misalignment.

- Where an assembly employs more than one SFD with contrasting housing support flexibilities, then the rotor weight should be distributed so that the more rigidly supported SFD carries as little weight as possible in order to avoid non-linear phenomena within the vibration response. The potential for severe occurrences of non-linear vibration phenomena in such an assembly is reduced by minimising the static

eccentricity of the more rigidly housed damper.

- The ability of an increased oil supply pressure (within a range typical of an aero-engine) to eliminate experimental non-linear phenomena displayed by an unsealed SFD is generally minimal. In a few instances increases in supply pressure did remove jump phenomena at a particular unbalance level.

- Theoretical application of the Short Bearing Approximation of the Reynolds Equation to squeeze-film dampers has demonstrated the ability to predict jump phenomena and non-synchronous resonances. The Short Bearing model allowed a variable film extent by virtue of the provision of specific cavitation pressures. A cavitation pressure of absolute zero (-14.7 psi gauge) was generally used throughout the modelling of the experimental rig response.

- Reservations concerning the modelling of the SFD's central circumferential oil supply groove as a constant pressure reservoir have been discussed. The true experimental value for SFD damping capacity appears to lie between the traditional assumption that the damper can be modelled as having two separate lands and the assumption that the damper acts as a single, double width land. The traditional assumption underestimates the damping demonstrated by the experimental responses.

- The application of the fourth order Runge-Kutta-Merson numerical integration method to the solution of the non-linear equations of motion was appropriate for the rig configurations involving two and four degrees of freedom (DOF). However, the integration was impractically slow for the more complex rig assemblies, involving six DOF.

- A good complement of bistable solutions from the non-linear equations was achieved after careful selection of initial conditions for the numerical integration. In a very small number of instances, at particular speeds, only one bistable solution was found, even after attempts with a range of initial conditions.

- The use of a constant cavitation pressure (namely absolute zero) during modelling allows a comprehensive range of phenomena to be reproduced. Some particular detailed aspects of the experimental responses require changes in the cavitation pressure. For example the hysteresis associated with a softening spring response has been modelled by referring to experimental pressure recordings to approximate sudden changes in the cavitation conditions.

- The experimentally observed jump phenomena and subsynchronous resonances and the corresponding non-linear theoretical predictions compared well, both being influenced by changes in the rig assembly configurations in a similar fashion.

- A simple linear analysis can illustrate the synchronous response of an assembly in the absence of non-linear phenomena. However, the potential for non-linear phenomena to occur within aero-engine assemblies incorporating SFDs degrades the usefulness of such analysis for design simulation purposes. In addition to a linear analysis of the whole assembly, a simplified model of the rotor-bearing assembly should be analysed experimentally and/or with non-linear theoretical techniques to observe the potential for significant non-linear phenomena.

The results have provided an insight into the mechanisms of SFD phenomena and the practical implications arising from these findings have been discussed. Bearing misalignments of a few hundredths of a millimetre and excessive weight carried by the more rigidly housed bearings can lead to sudden occurrences of jump phenomena and subharmonic resonance.

A linear analytical treatment of the theoretical rig model has indicated the experimental synchronous trends and suggested that the effective damping provided by the SFDs during experiment, in the absence of non-linear phenomena, was over-critical for configurations 2 and 3, but was under-critical for configuration 1.

The modelling of the non-linear SFD response is dominated by two conflicting factors; modelling accuracy and the speed of computation. On the one hand the full non-linear analysis is accurate but involves long computations. On the other hand a simplified linear analysis is very quick but provides reasonable results only for simple assemblies. Therefore, a method of linearising the SFD response which is able to mimic the non-linearities of the SFD would compromise these two conflicting parameters. The research into the orbit perturbation method indicates that accurate results are forthcoming for SFDs with parallel spring supports, or for lightly loaded SFDs. Other existing methods, such as harmonic balance and least squares methods, can be applied to the linearisation of the SFD response.

It is interesting that the jump phenomena and subsynchronous resonances demonstrated by a simple non-linear equation, the Duffing Equation, display the same characteristics as the experimental SFD response and corresponding short bearing predictions.

Chapter 13 RECOMMENDED FURTHER RESEARCH

It is possible to make a number of recommendations for future research. There are four areas where further research has the potential for providing significant results. The first three areas are immediately practical in their objectives, whereas the fourth area would be regarded as theoretical research which did not aim to satisfy any specific practical engineering application but might well lead to a better understanding of the modelling of the squeeze-film damper.

Firstly, bearing in mind that the presence of jump phenomena and strong subsynchronous resonances represent the two most undesirable vibration characteristics of SFDs, there is obvious scope for studying these phenomena further. It would be instructive to consider the effects of rotor flexibility on the occurrence of such phenomena. Although military gas turbine rotor-bearing assemblies involve relatively stiff rotors, that is they operate below the first flexural mode of vibration, civil assemblies operate with their rotors displaying a significant degree of flexibility. Both an experimental and theoretical approach would be required. However, difficulties in computing solutions for a multi-DOF flexible rotor model incorporating non-linear SFD modelling may be encountered. Numerical integration may be impractically slow. A technique such as the secant root finding algorithm adopted by Greenhill and Nelson [45] for flexible rotor models might be applied in this instance. However, modelling might be restricted by assumptions such as the approximation of circular centred orbits.

Secondly, the use of end seals with SFDs is widespread as this reduces the oil flow discharged from the ends of a SFD and raises the effective damping provided by the SFD. End seals were not studied in the present research because it was considered that end seals would discourage the occurrence of jumps and subsynchronous resonances if the SFD damping was too high. Following on from the present research, it would be useful to observe the effects of end seals on reducing the occurrence of non-linear phenomena. Preliminary work has been carried out [78] and the indications are that seals remove jumps from the response if supported by a high supply pressure.

Thirdly, the area which would benefit the design of rotor-bearing assemblies incorporating SFDs most significantly is the provision of the computer code for a SFD linearisation algorithm. Such an algorithm should be capable of providing reasonably accurate estimates of the non-linear response arising from the SFDs within a linear rotor-bearing model. The convergence of such a method should be relatively fast and accurate when compared with numerical integration of the full non-linear solution.

Harmonic balance is one method which might be instrumental in achieving a useful linearised SFD model. The numerical stability of this method is discussed in Appendix 7. It may be possible to develop a stable iteration algorithm which can be applied to rotor-bearing models with many degrees of freedom and incorporating more than one SFD. Once the stability of this technique is mastered and the accuracy assessed, it may be applied with an existing linear analysis suite. The benefit of the Harmonic Balance method over other methods includes the ability of the method to involve non-analytical SFD film force models and the method does not require either large stores of data or the non-linear computation

required to generate such data. Also, the Fourier analysis within the Harmonic Balance method can also be augmented to involve more than the synchronous response to search for the possibilities of subsynchronous resonance and other nonsynchronous activity.

The first three proposals have clear practical engineering objectives. Finally, considering the similarities between the non-linear phenomena illustrated by the Short Bearing model of the SFD and the Duffing equation, it would be illustrative to apply traditional mathematical non-linear analysis techniques to SFD modelling. Particularly for bistable operation, the use of the phase plane to map out the transient response from a numerical integration would illustrate how, depending upon initial conditions, the computation converges to one solution's trajectory. Use of Poincare sections would also be useful in studying regions of chaos occurring during modelling. Although the practical applications of the results of such studies are not as tangible as those arising from the first three areas of proposed further research, use of such analysis tools may produce results which allow a fuller appreciation of the non-linear modelling.

FIGURES

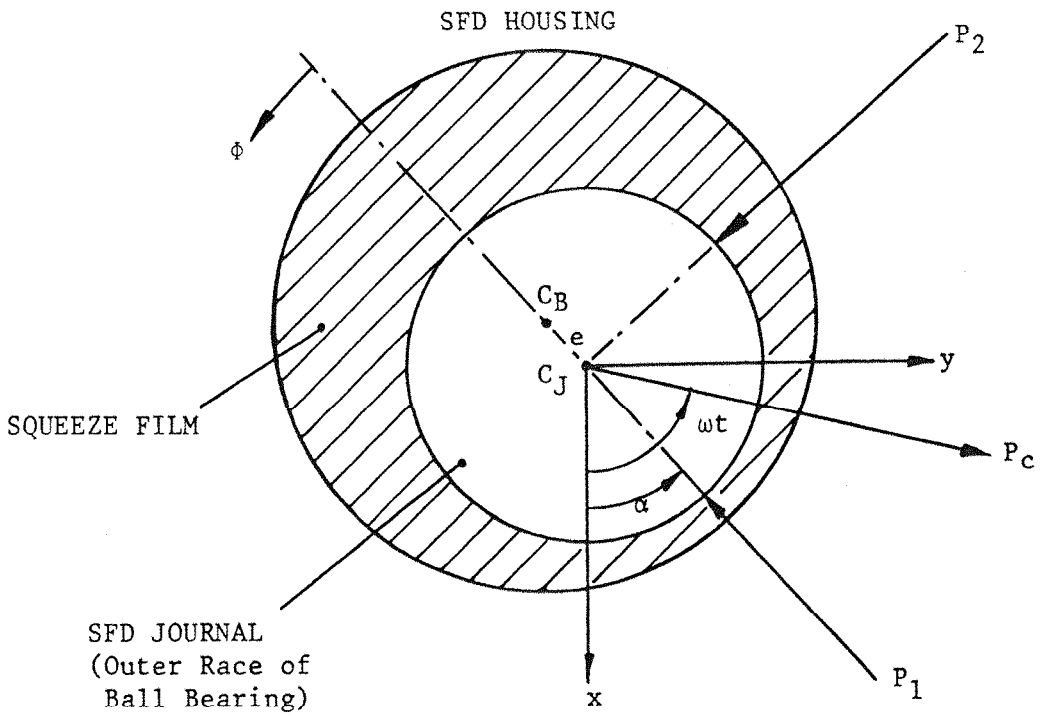

THE SQUEEZE-FILM DAMPER (SFD)

FIGURE 1.1

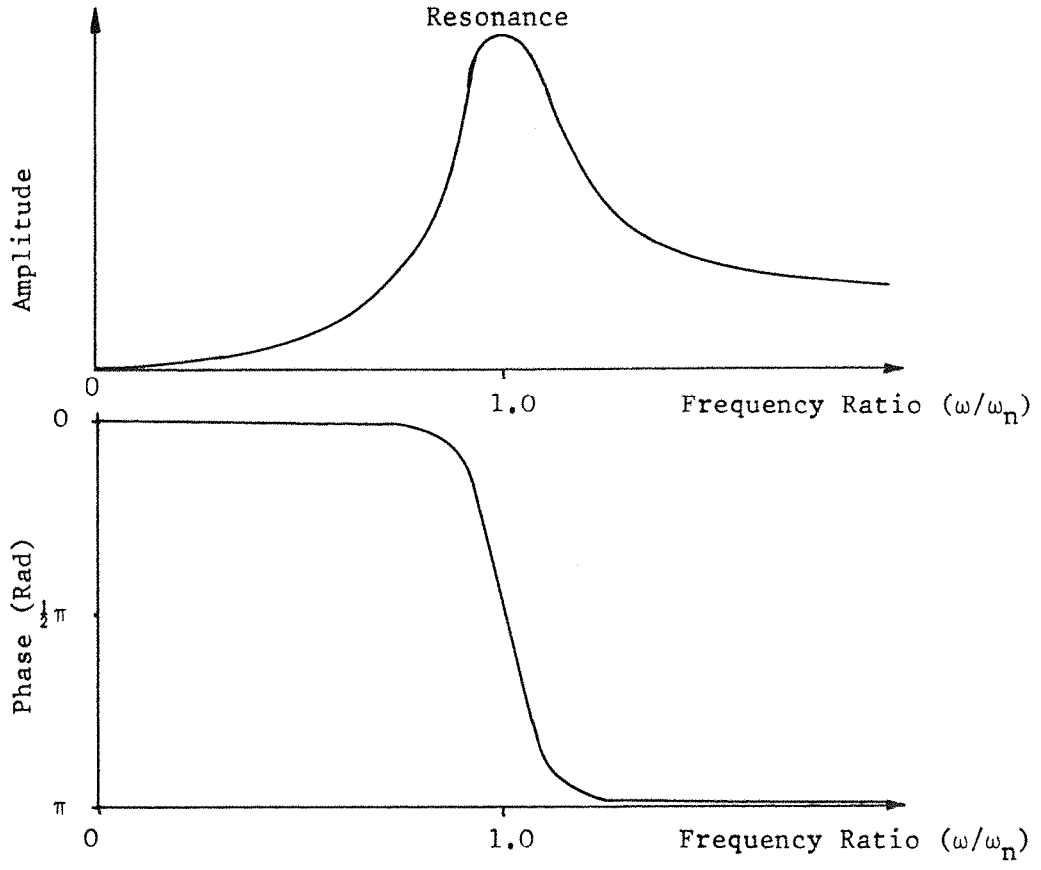

Fig. 1.2 SECOND ORDER RESPONSE

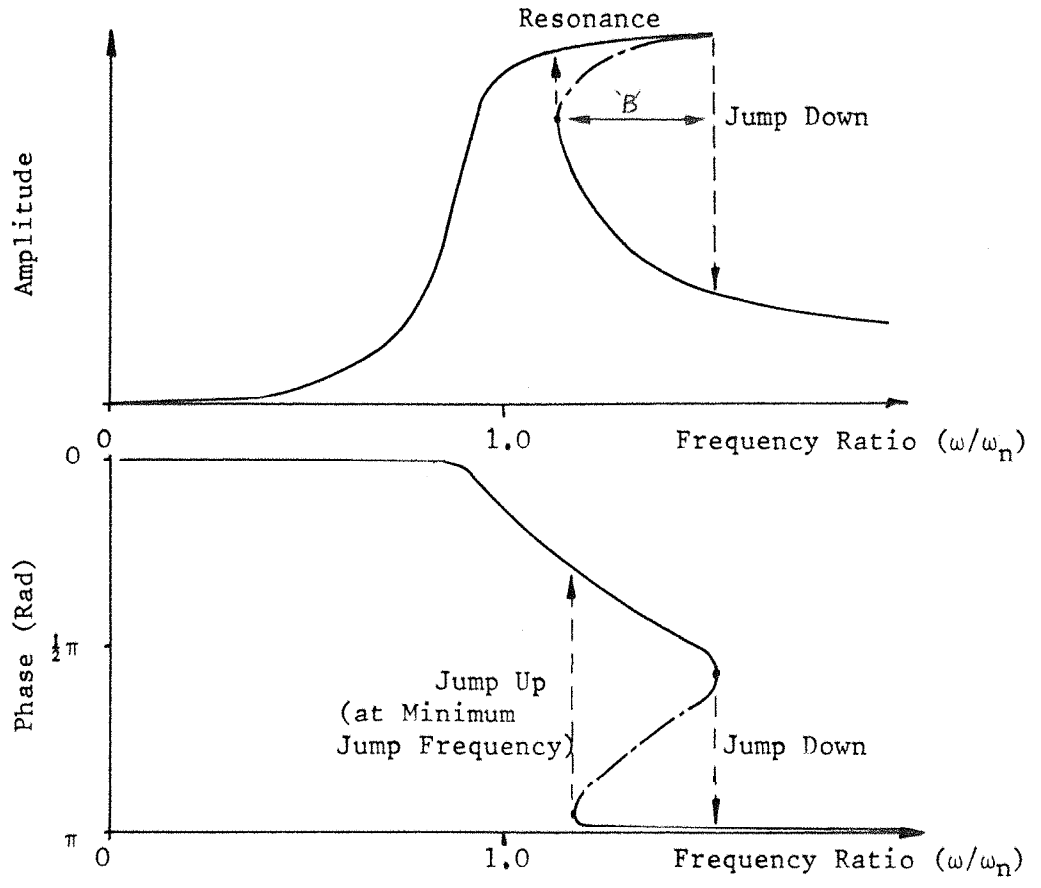

Fig. 1.3 NON-LINEAR 'HARDENING SPRING' RESPONSE

FIGURE 4.1

CONFIGURATIONS 1a,b RIG MODEL

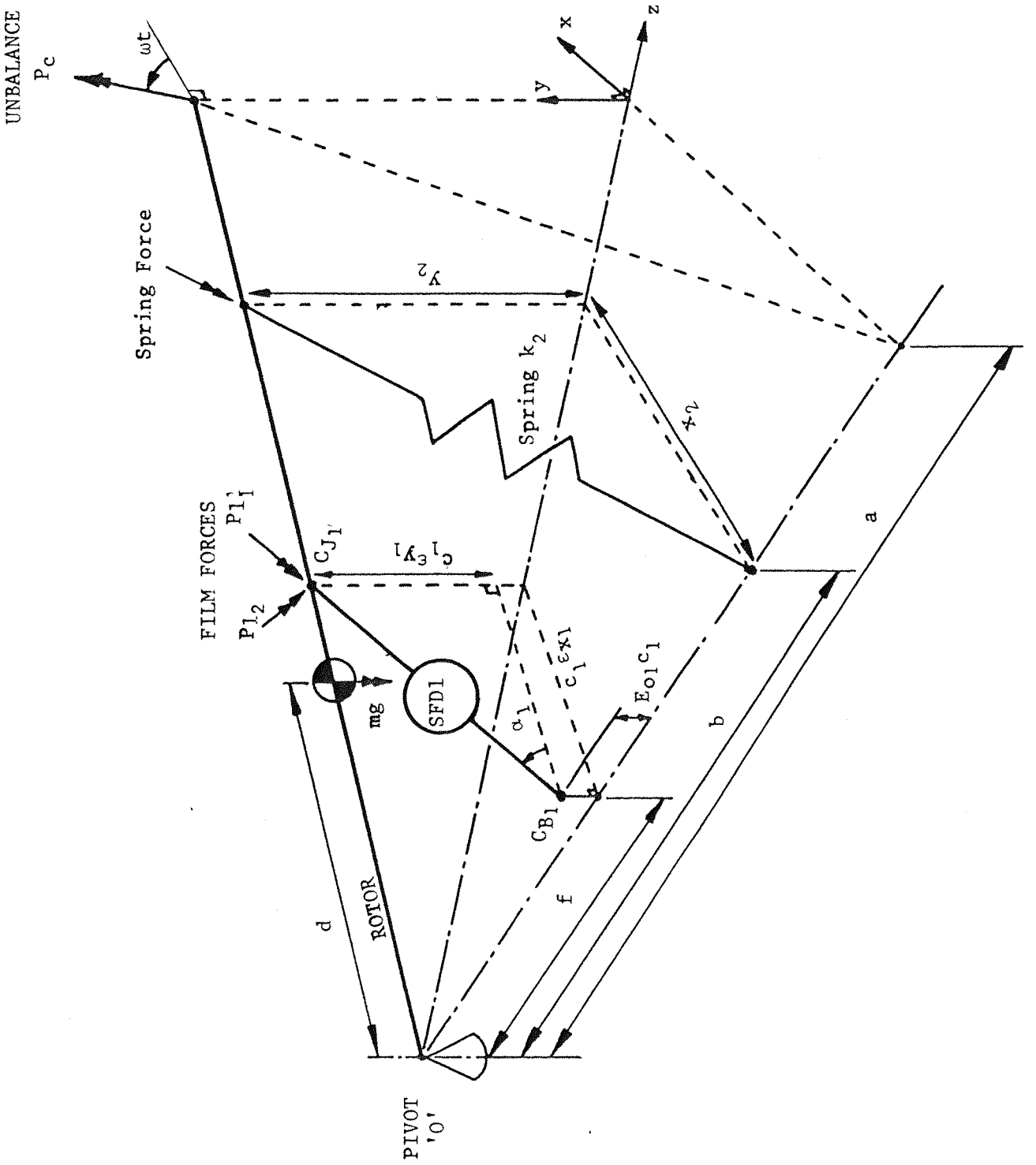

FIGURE 4.2

CONFIGURATIONS 2a,b RIG MODEL

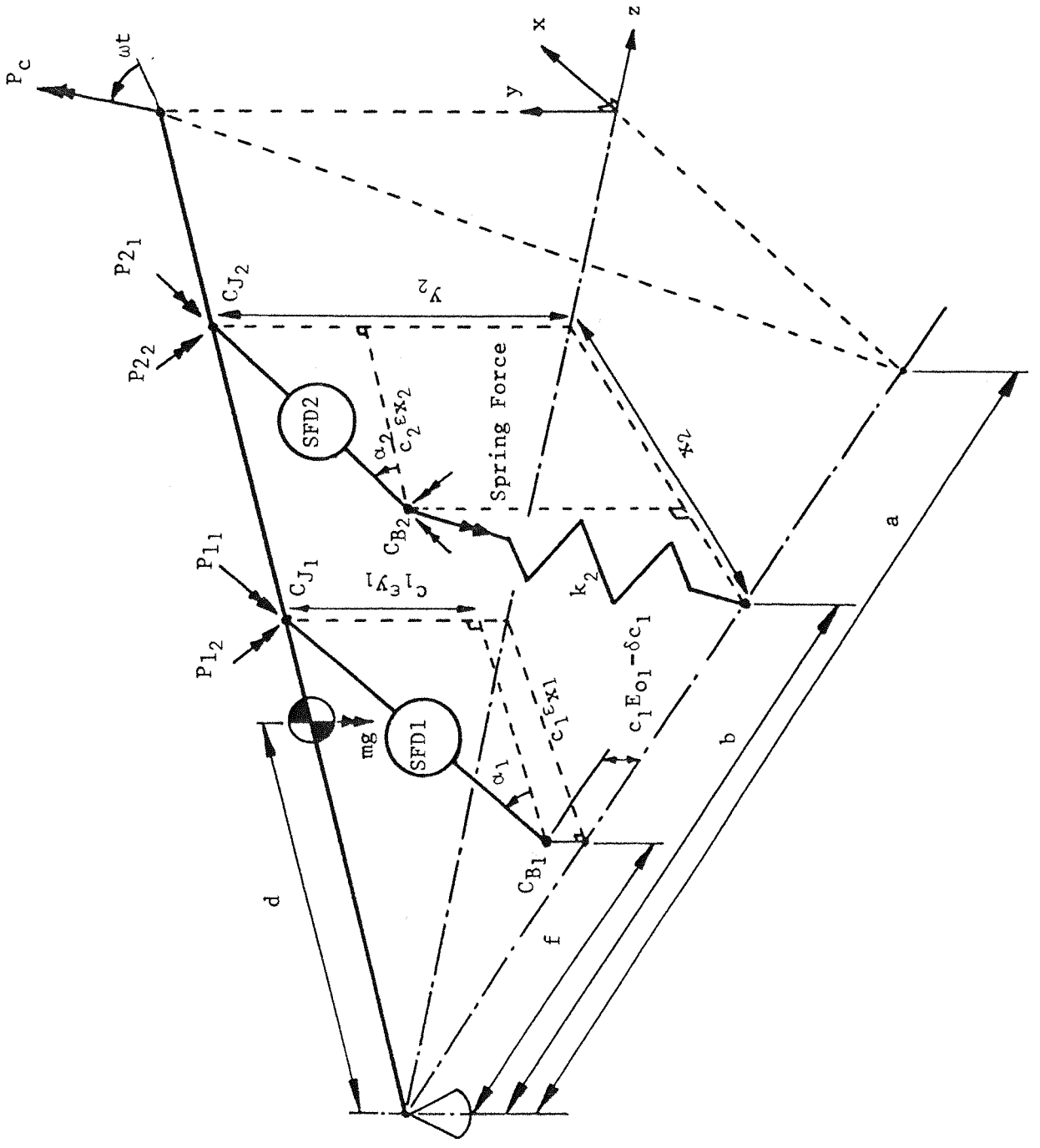

FIGURE 4.3
CONFIGURATIONS 3a,b RIG MODEL

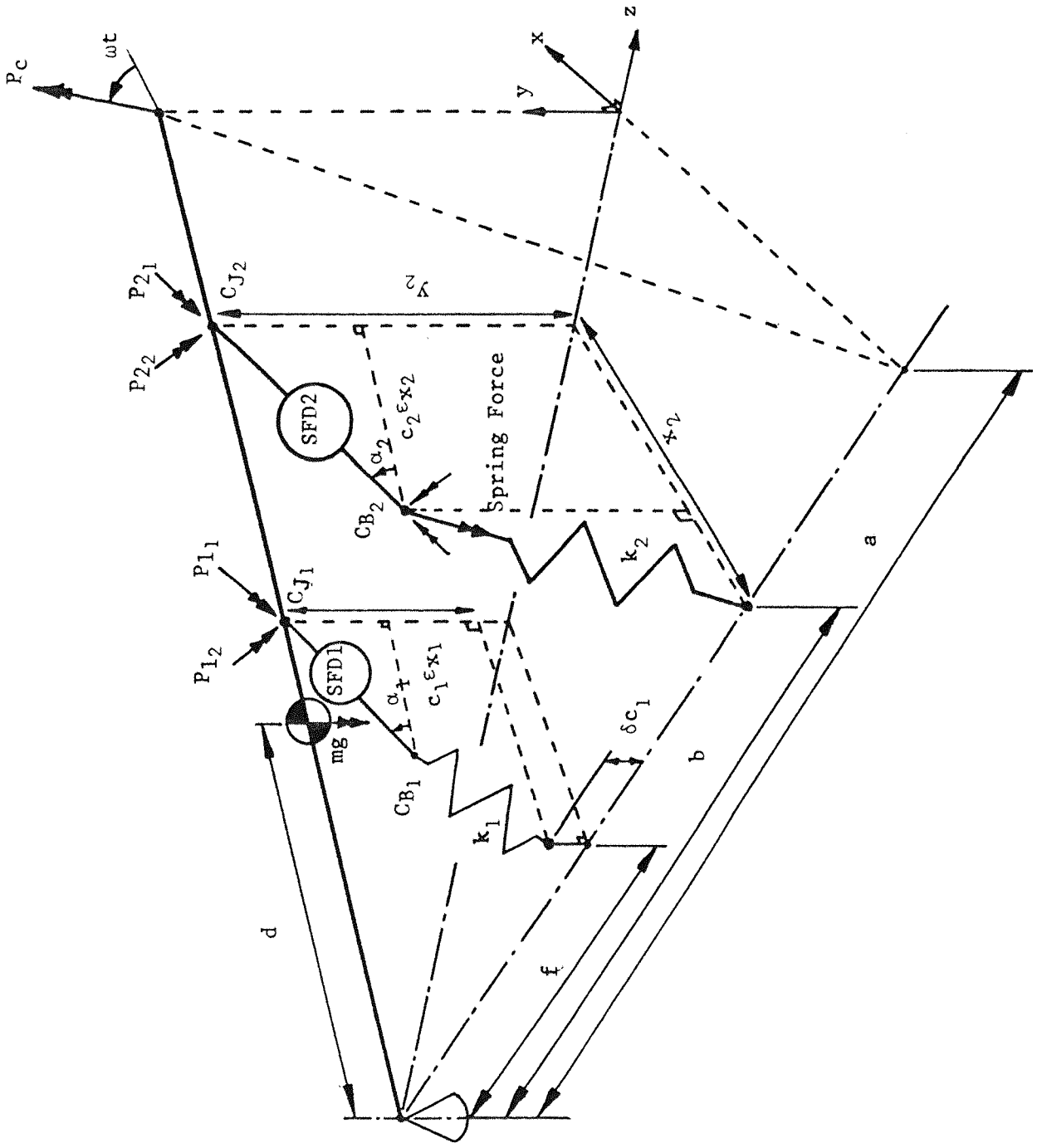

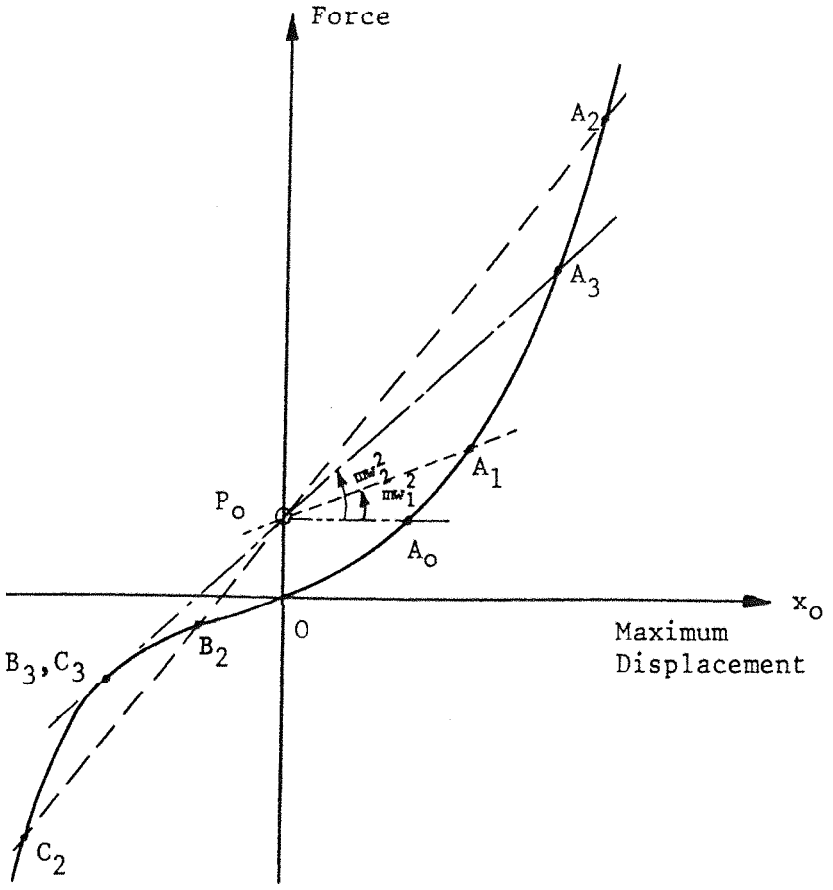

FIGURE 5.1 Hardening Spring Stiffness Curve

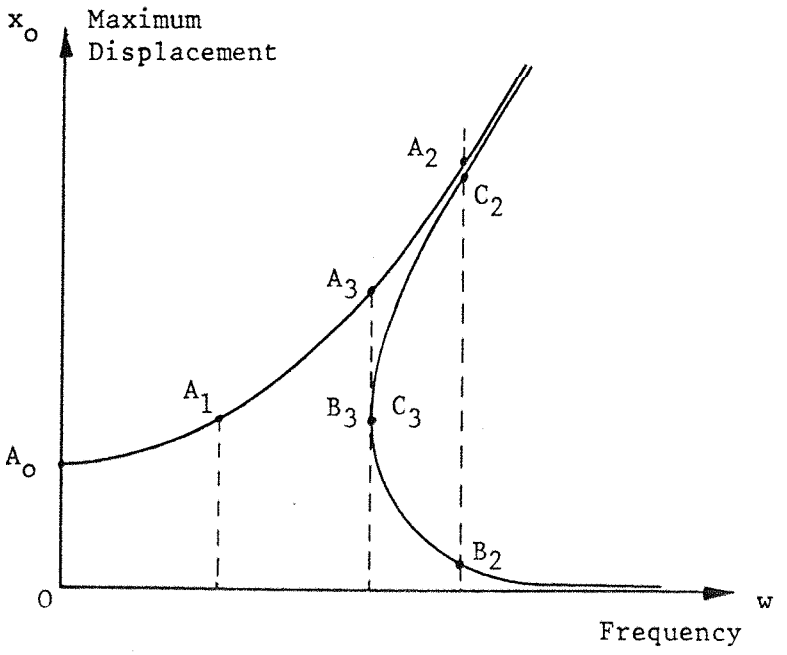

FIGURE 5.2 Hardening Spring Frequency Response

SQUEEZE-FILM DAMPER SFD1

THEORETICAL 2PI-FILM SOLUTION

A =	0.2132E -1	0.2132E -1	0.2132E -1
Qc2 =	0.7332E 0	0.4901E 0	0.2450E 0
Eo =	0.0000E 0	0.0000E 0	0.0000E 0
Psup=	0.0000E 0	0.0000E 0	0.0000E 0

(psi

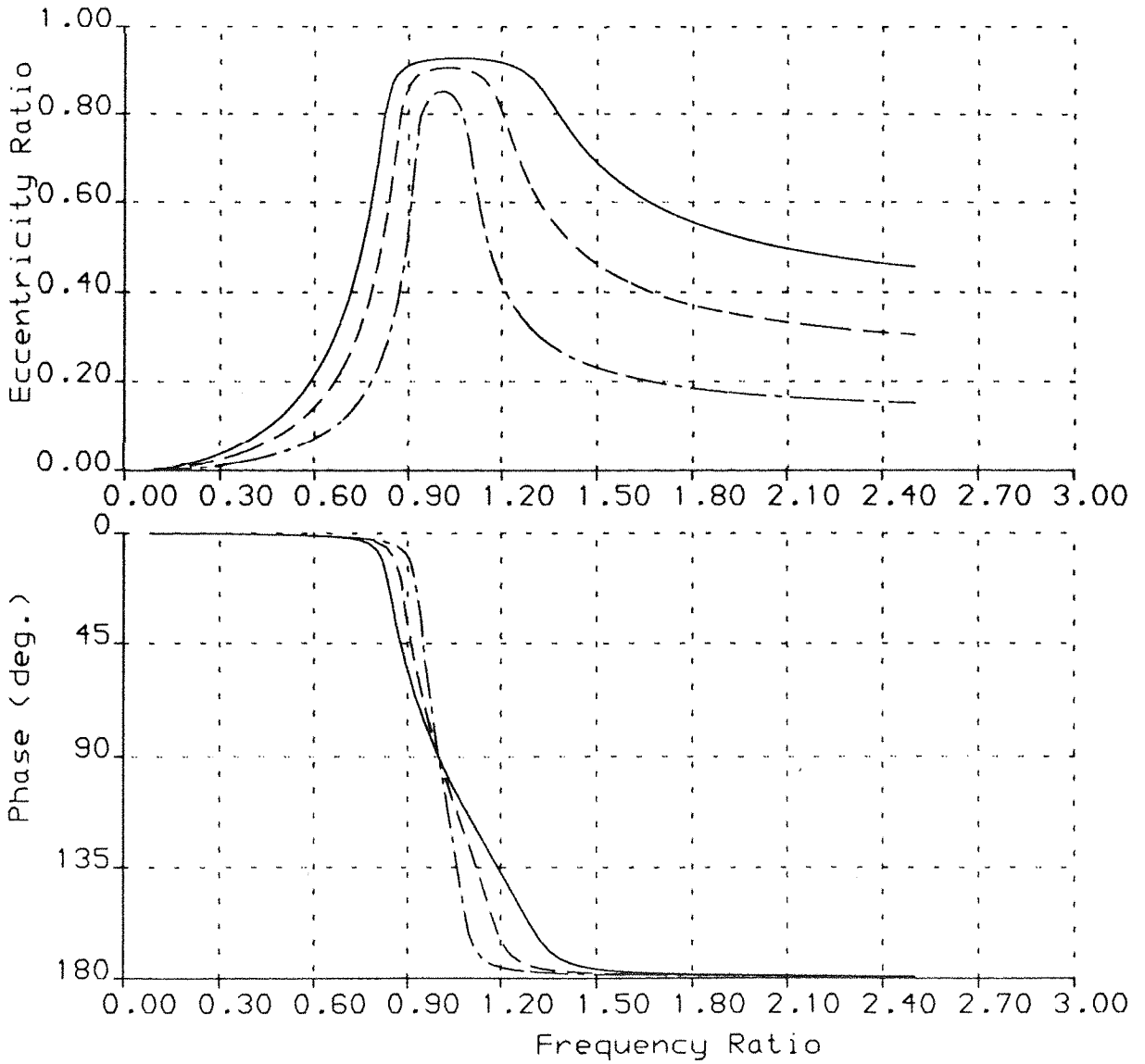

ROTOR-BEARING ASSEMBLY RESPONSE TO UNBALANCE
SQUEEZE-FILM DAMPER RESEARCH Rig Config. 1a

FIGURE 5.3

SQUEEZE-FILM DAMPER SFD1

THEORETICAL 2PI-FILM SOLUTION

A =	0.8528E -1	0.8528E -1	0.8528E -1
Qc2 =	0.7332E 0	0.4901E 0	0.2450E 0
Eo =	0.0000E 0	0.0000E 0	0.0000E 0
Psup=	0.0000E 0	0.0000E 0	0.0000E 0 (psi)

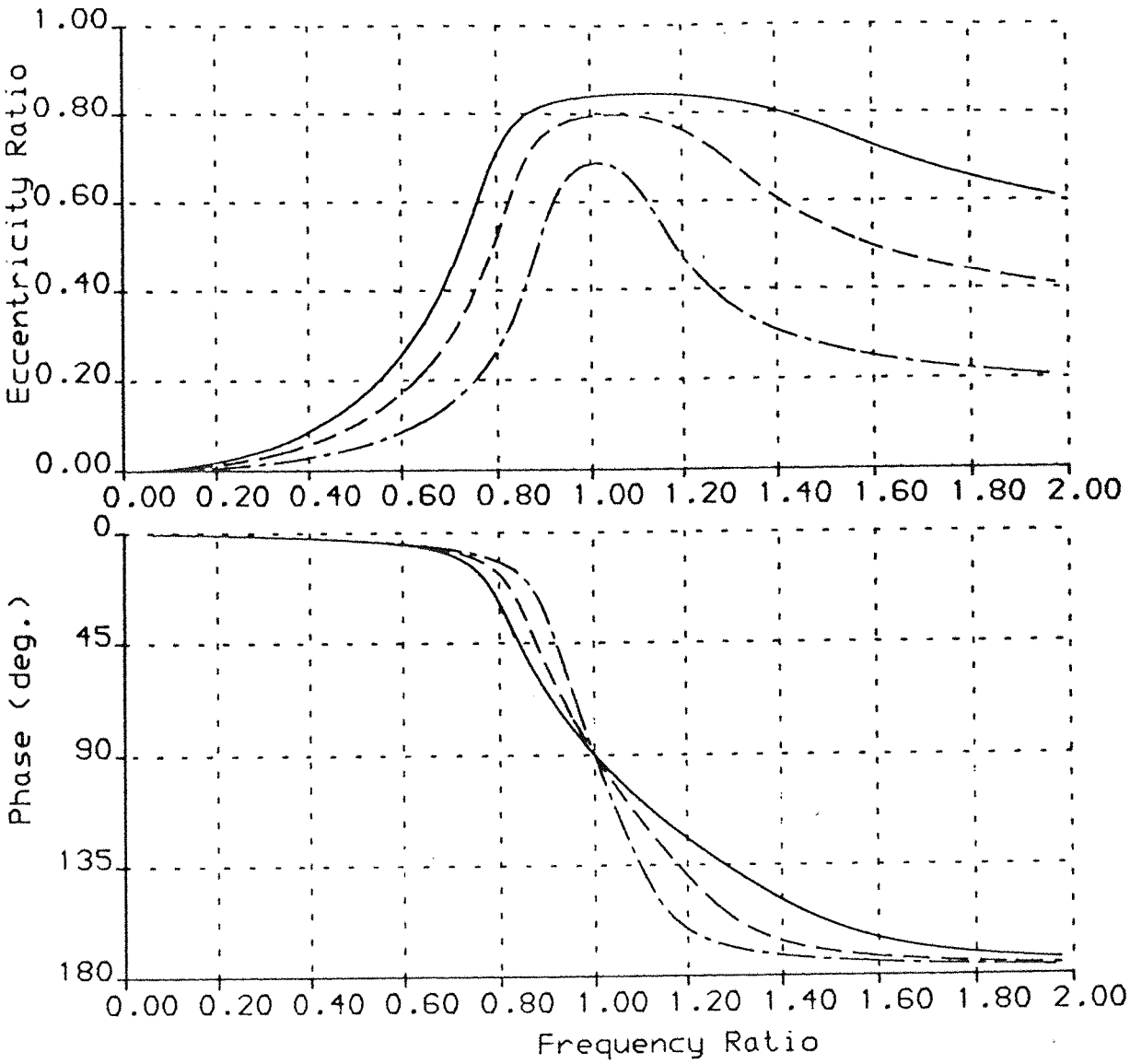

ROTOR-BEARING ASSEMBLY RESPONSE TO UNBALANCE
SQUEEZE-FILM DAMPER RESEARCH Rig ConFig. 1a

FIGURE 5.4

SQUEEZE-FILM DAMPER SFD1

THEORETICAL PI-FILM SOLUTION

A =	0.2132E -1	0.2132E -1	0.2132E -1
Qc2 =	0.7332E 0	0.4901E 0	0.2450E 0
Eo =	0.0000E 0	0.0000E 0	0.0000E 0
Psup=	0.0000E 0	0.0000E 0	0.0000E 0 (psi
Pmin=	0.0000E 0	0.0000E 0	0.0000E 0

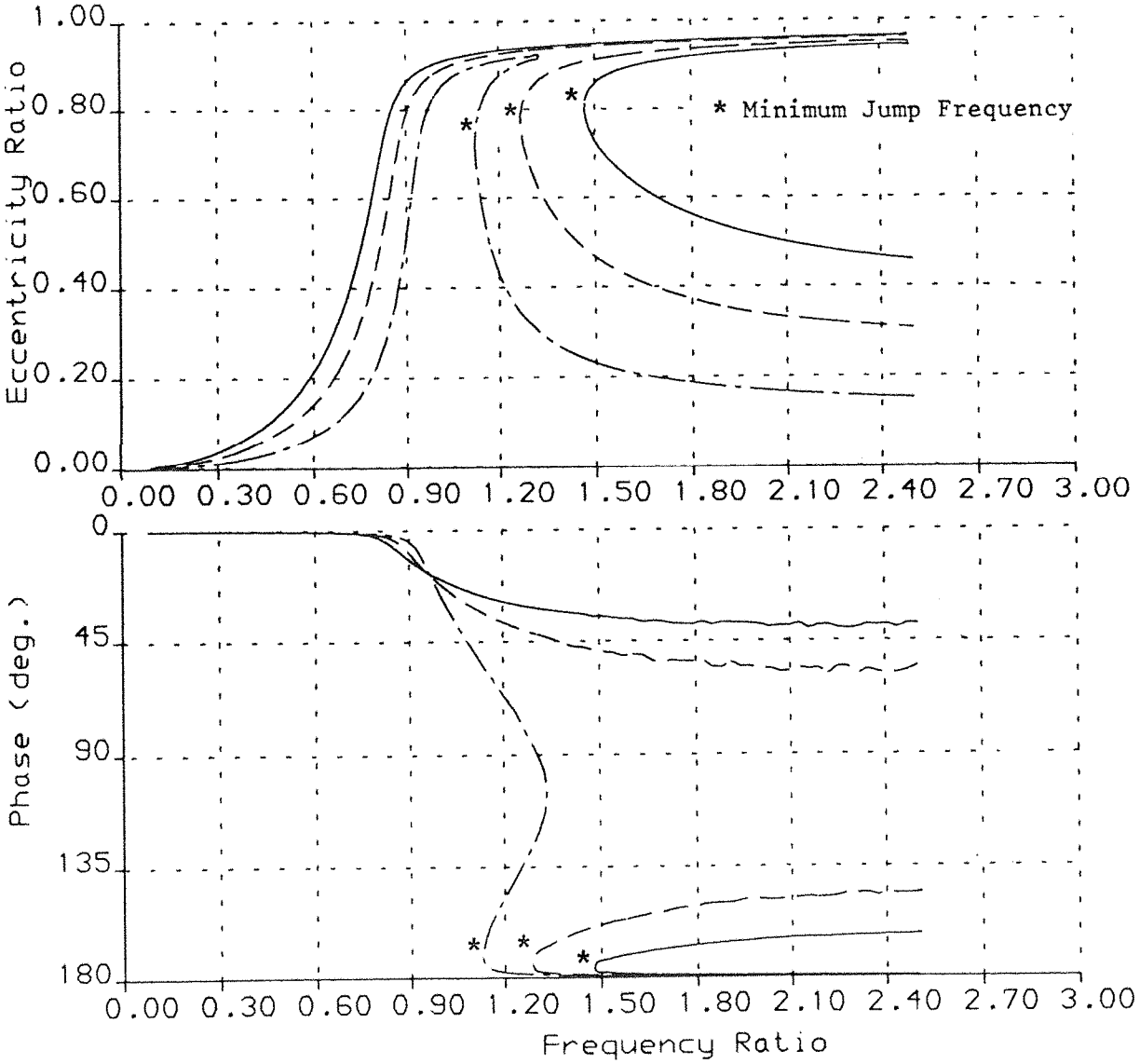

ROTOR-BEARING ASSEMBLY RESPONSE TO UNBALANCE
SQUEEZE-FILM DAMPER RESEARCH Rig Config. 1a

FIGURE 5.5

SQUEEZE-FILM DAMPER SFD1

THEORETICAL PI-FILM SOLUTION

A =	0.8528E -1	0.8528E -1	0.8528E -1
Qc2 =	0.7332E 0	0.4901E 0	0.2450E 0
Eo =	0.0000E 0	0.0000E 0	0.0000E 0
Psup=	0.0000E 0	0.0000E 0	0.0000E 0 (psi
Pmin=	0.0000E 0	0.0000E 0	0.0000E 0

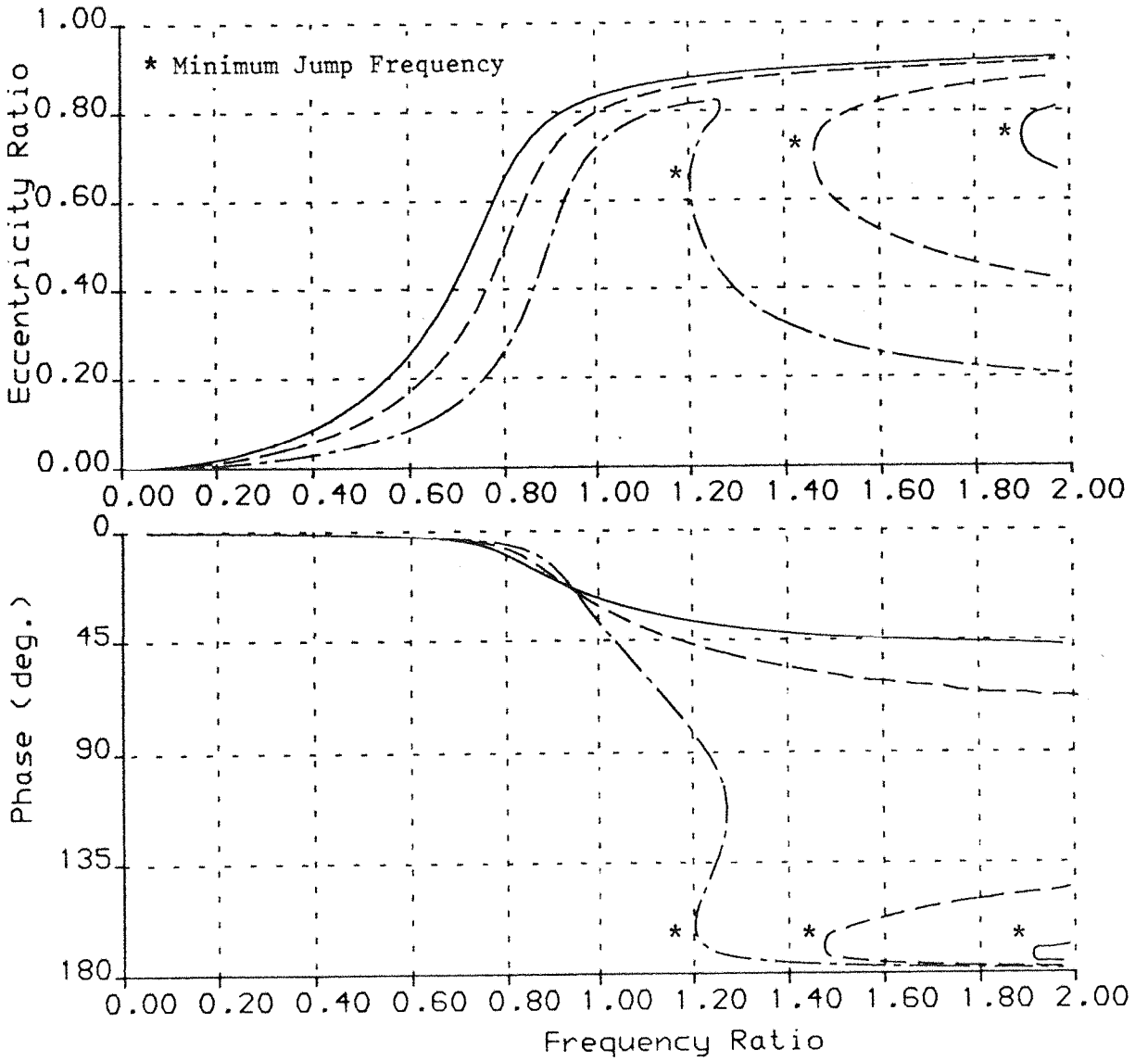

ROTOR-BEARING ASSEMBLY RESPONSE TO UNBALANCE

SQUEEZE-FILM DAMPER RESEARCH Rig Config. 1a

FIGURE 5.6

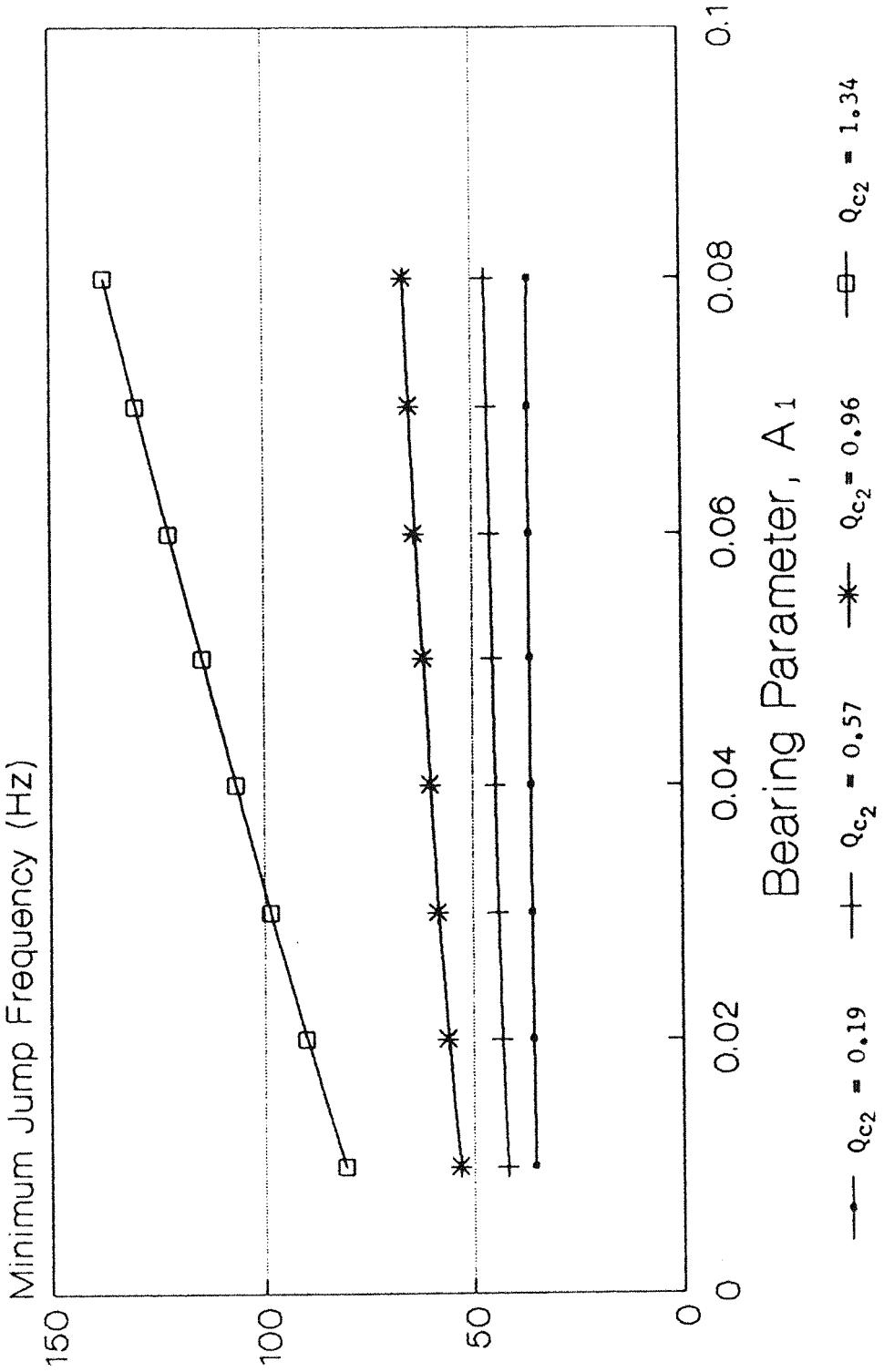

FIGURE 5.7

MINIMUM JUMP FREQUENCIES FOR π FILM SQUEEZE-FILM DAMPER MODEL

FIGURE 5.8

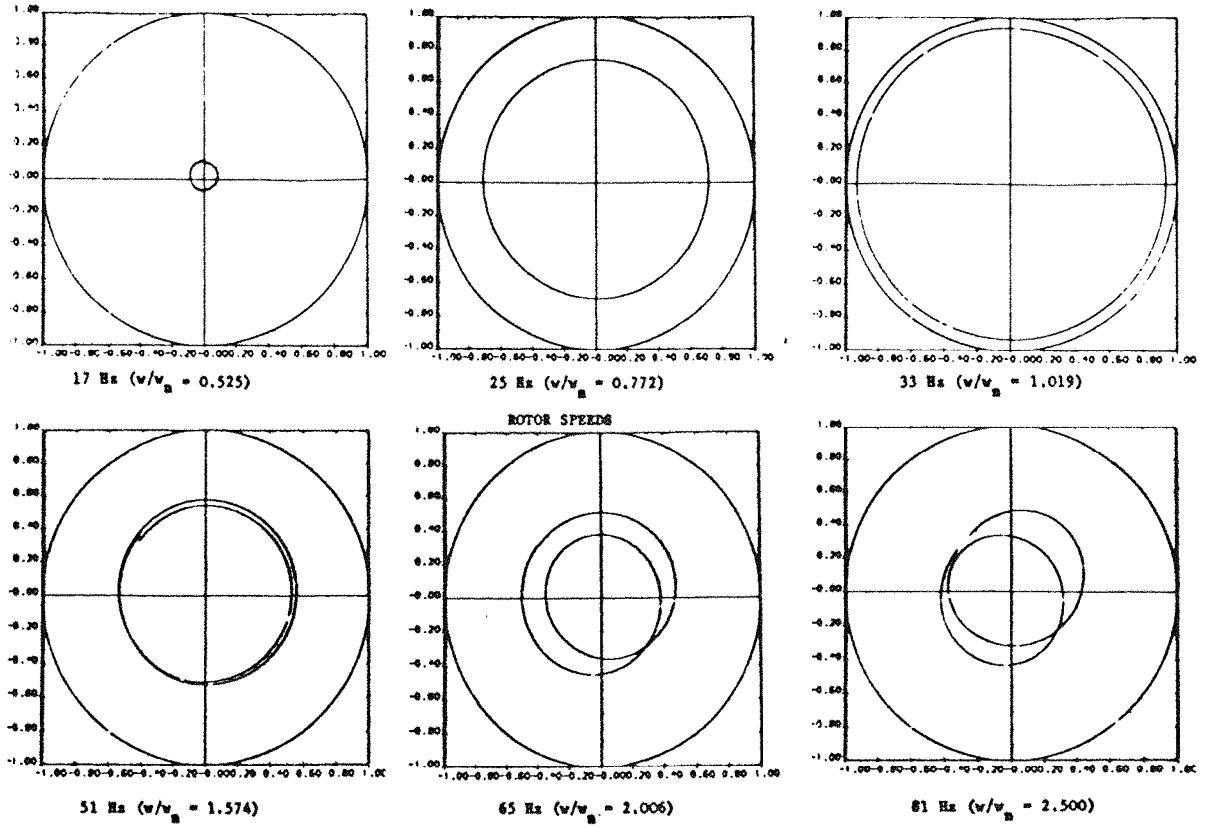

(a)

ROTOR WEIGHT EFFECT EXCLUDED

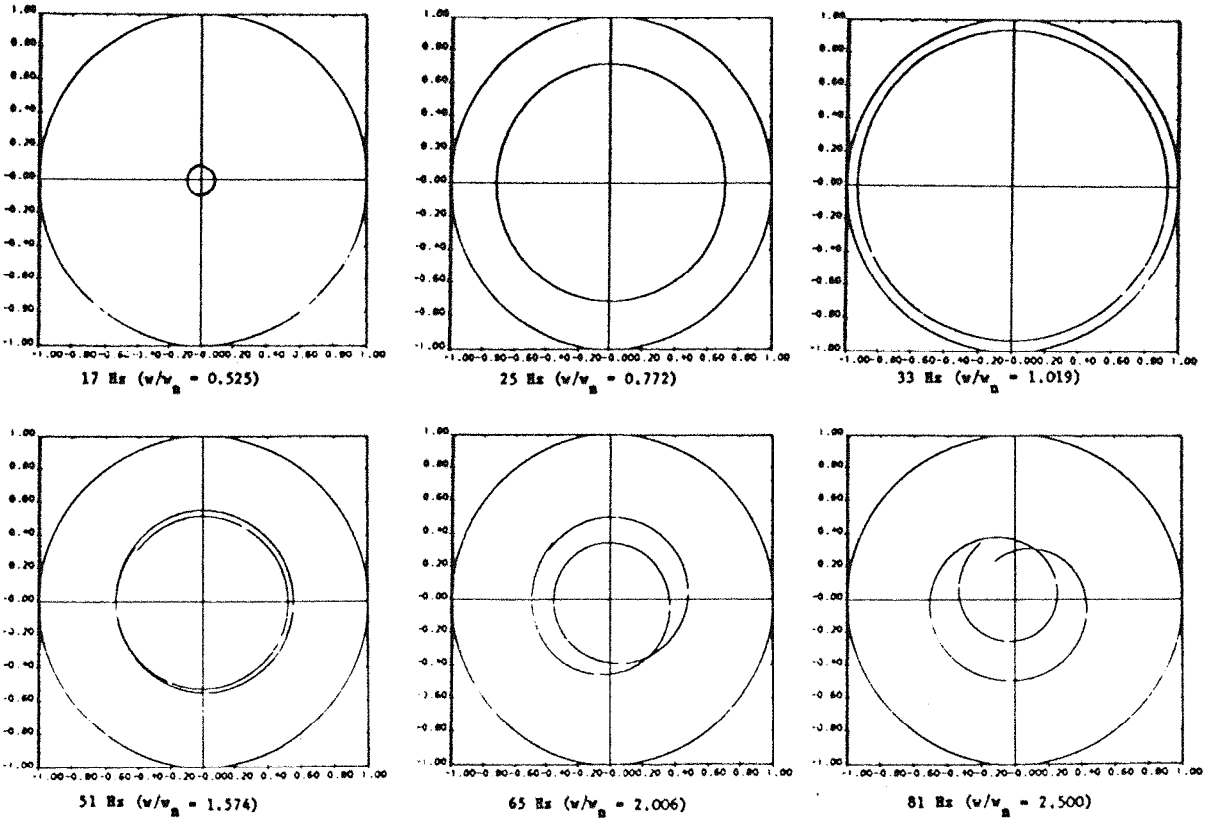

(b)

ROTOR WEIGHT EFFECT INCLUDED

SFD1 JOURNAL CENTRE ORBITS WITHIN CLEARANCE CIRCLE (Radius c_1)

CONFIGURATION 1a (Q_{c_2}=0.733, Psup=2psi)

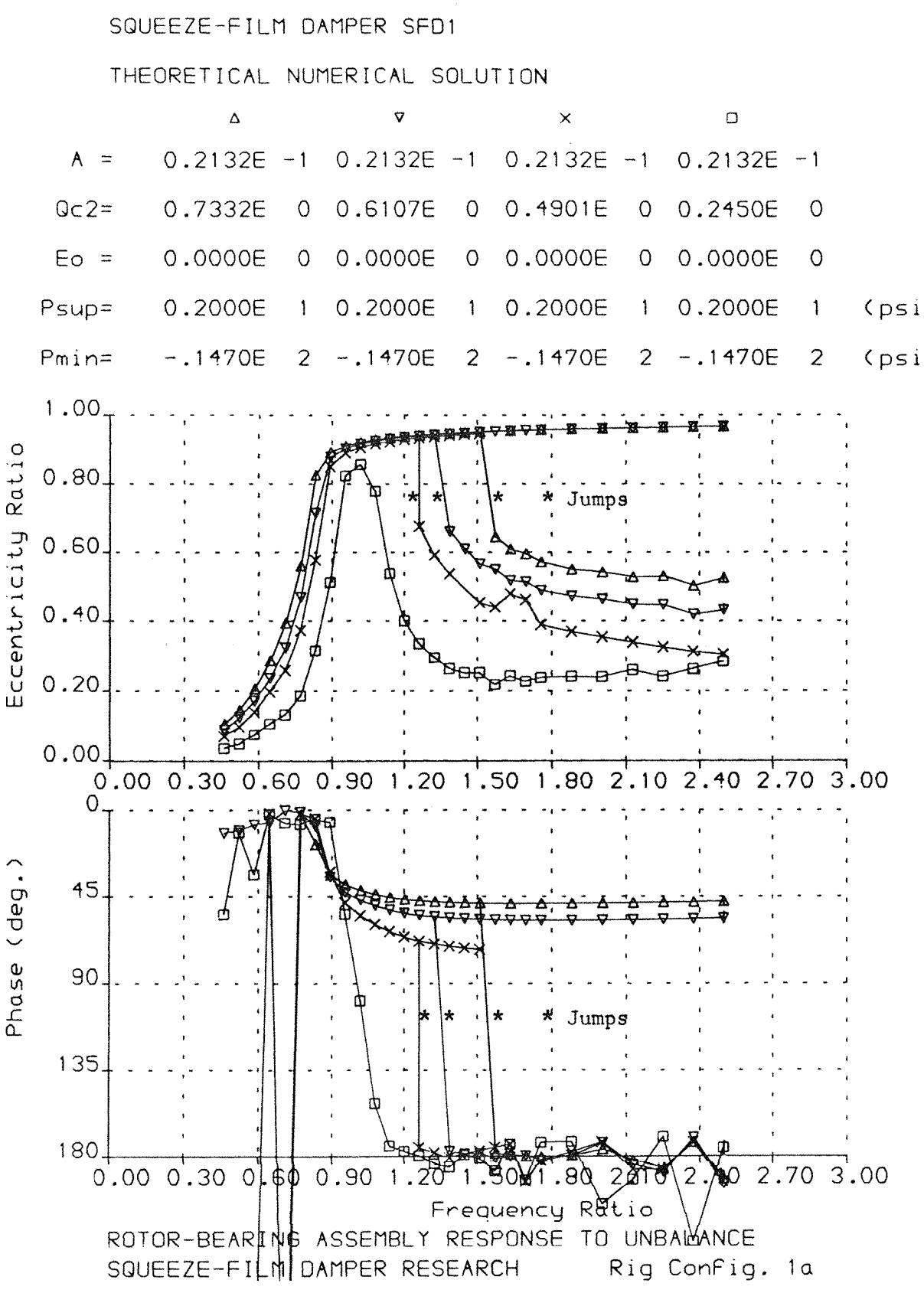
SQUEEZE-FILM DAMPER SFD1
THEORETICAL NUMERICAL SOLUTION
△ ▽ × □
A = 0.2132E -1 0.2132E -1 0.2132E -1 0.2132E -1
Qc2= 0.7332E 0 0.6107E 0 0.4901E 0 0.2450E 0
Eo = 0.0000E 0 0.0000E 0 0.0000E 0 0.0000E 0
Psup= 0.2000E 1 0.2000E 1 0.2000E 1 0.2000E 1 (psi
Pmin= -.1470E 2 -.1470E 2 -.1470E 2 -.1470E 2 (psi
Eccentricity Ratio
1.00
0.80
0.60
0.40
0.20
0.00
* Jumps
Phase (deg.)
0
45
90
135
180
0.00 0.30 0.60 0.90 1.20 1.50 1.80 2.10 2.40 2.70 3.00
Frequency Ratio
ROTOR-BEARING ASSEMBLY RESPONSE TO UNBALANCE
SQUEEZE-FILM DAMPER RESEARCH
Rig Config. 1a

FIGURE 5.9

SQUEEZE-FILM DAMPER SFD1

THEORETICAL NUMERICAL SOLUTION

	△	▽	×	□	
A =	0.2132E -1	0.2132E -1	0.2132E -1	0.2132E -1	
Qc2=	0.7332E 0	0.6107E 0	0.4901E 0	0.2450E 0	
Eo =	0.0000E 0	0.0000E 0	0.0000E 0	0.0000E 0	
Psup=	0.2400E 2	0.6000E 1	0.6000E 1	0.6000E 1	(psi)
Pmin=	-.1470E 2	-.1470E 2	-.1470E 2	-.1470E 2	(psi)

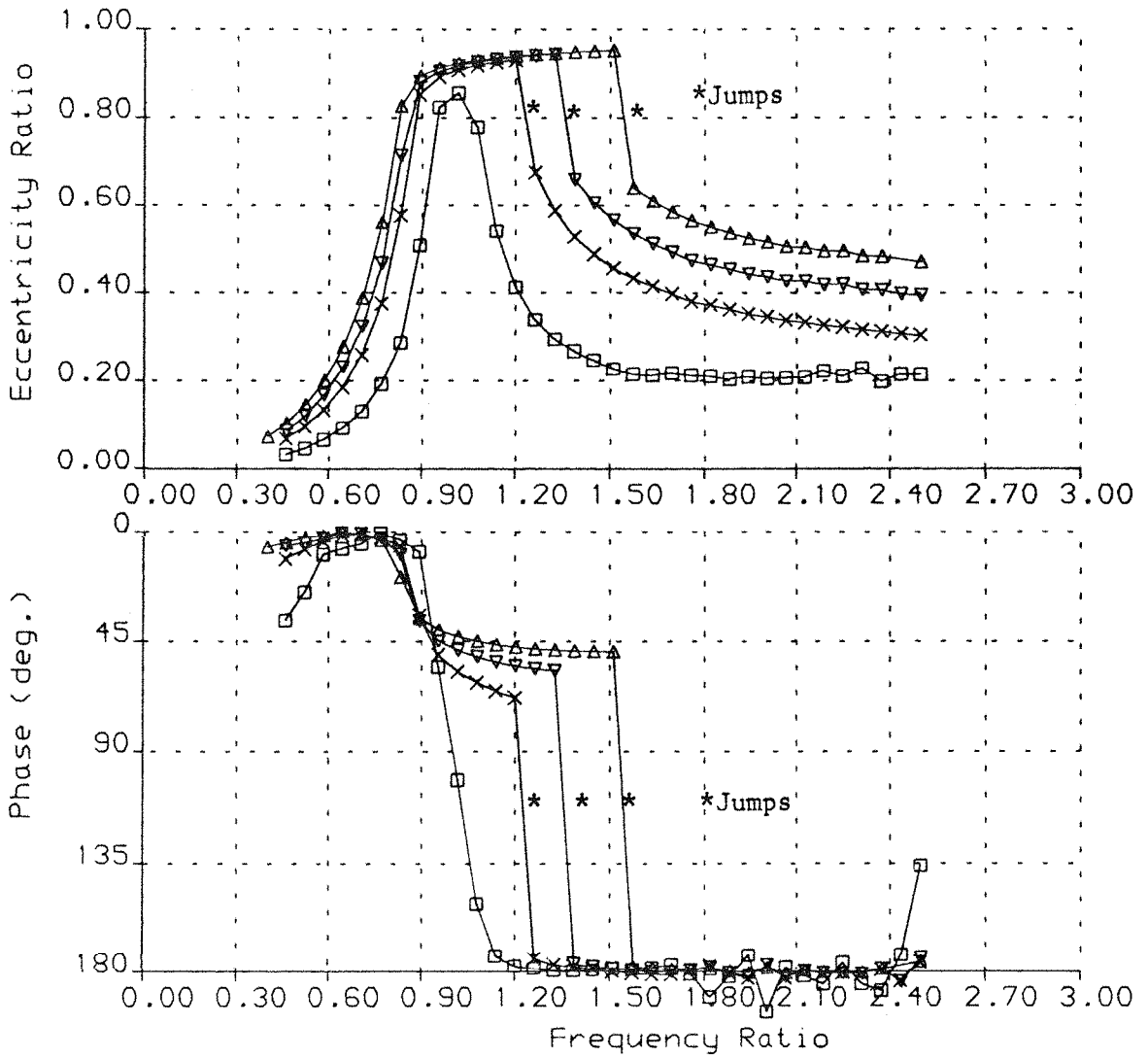

ROTOR-BEARING ASSEMBLY RESPONSE TO UNBALANCE
SQUEEZE-FILM DAMPER RESEARCH Rig Config. 1a

FIGURE 5.10

SQUEEZE-FILM DAMPER SFD1

THEORETICAL NUMERICAL SOLUTION

	△	▽	×	□	
A =	0.8528E -1	0.8528E -1	0.8528E -1	0.8528E -1	
Qc2=	0.7332E 0	0.6107E 0	0.4901E 0	0.2450E 0	
Eo =	0.0000E 0	0.0000E 0	0.0000E 0	0.0000E 0	
Psup=	0.2000E 1	0.2000E 1	0.2000E 1	0.2000E 1	(psi)
Pmin=	-.1470E 2	-.1470E 2	-.1470E 2	-.1470E 2	(psi)

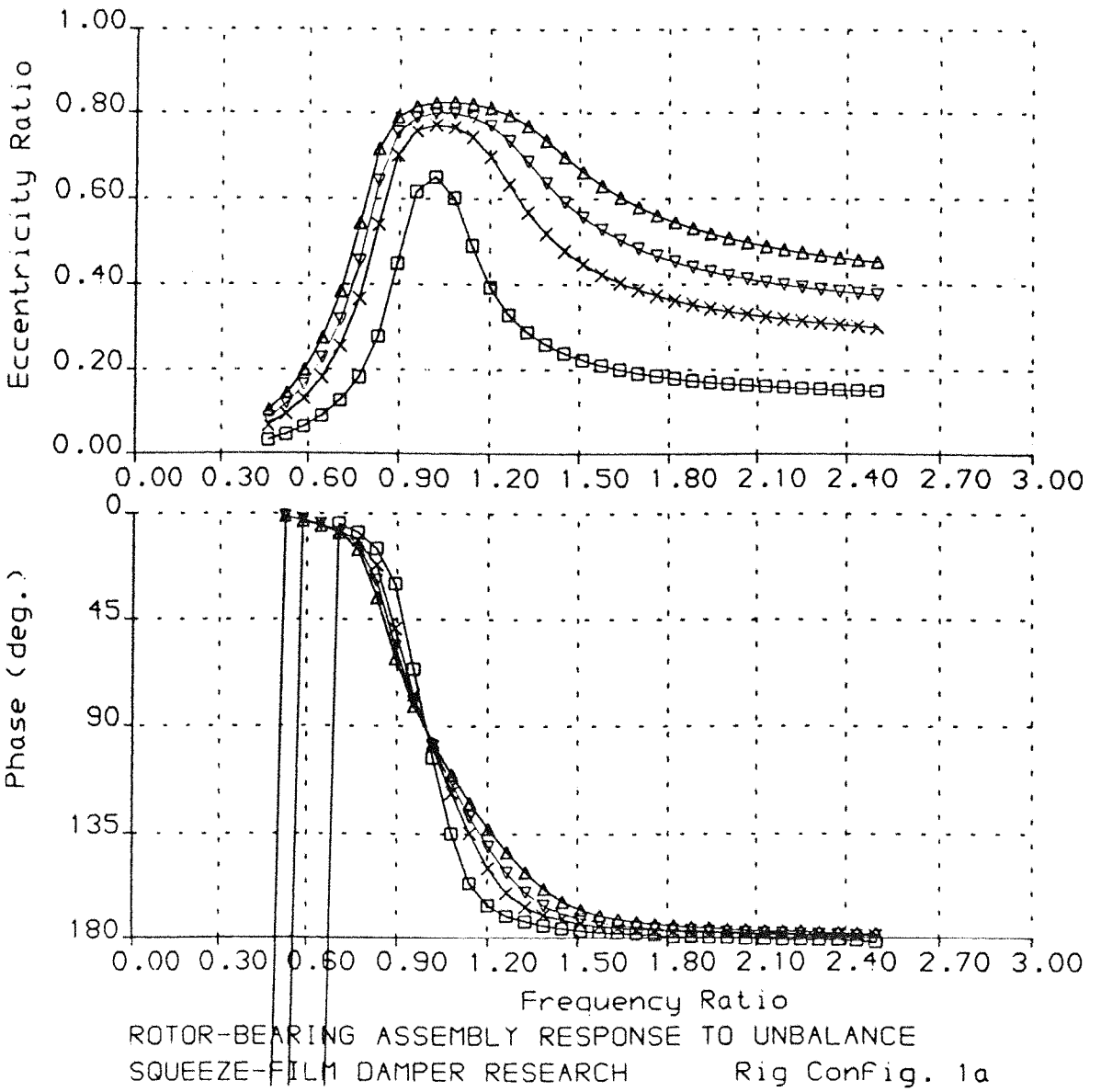

FIGURE 5.11

A = 0.213200E -1

Qc2 = 0.490097E 0

Eo = 0.000000E 0

Psup = 0.200000E 1 (psi)

Pmin = -0.147000E 2 (psi)

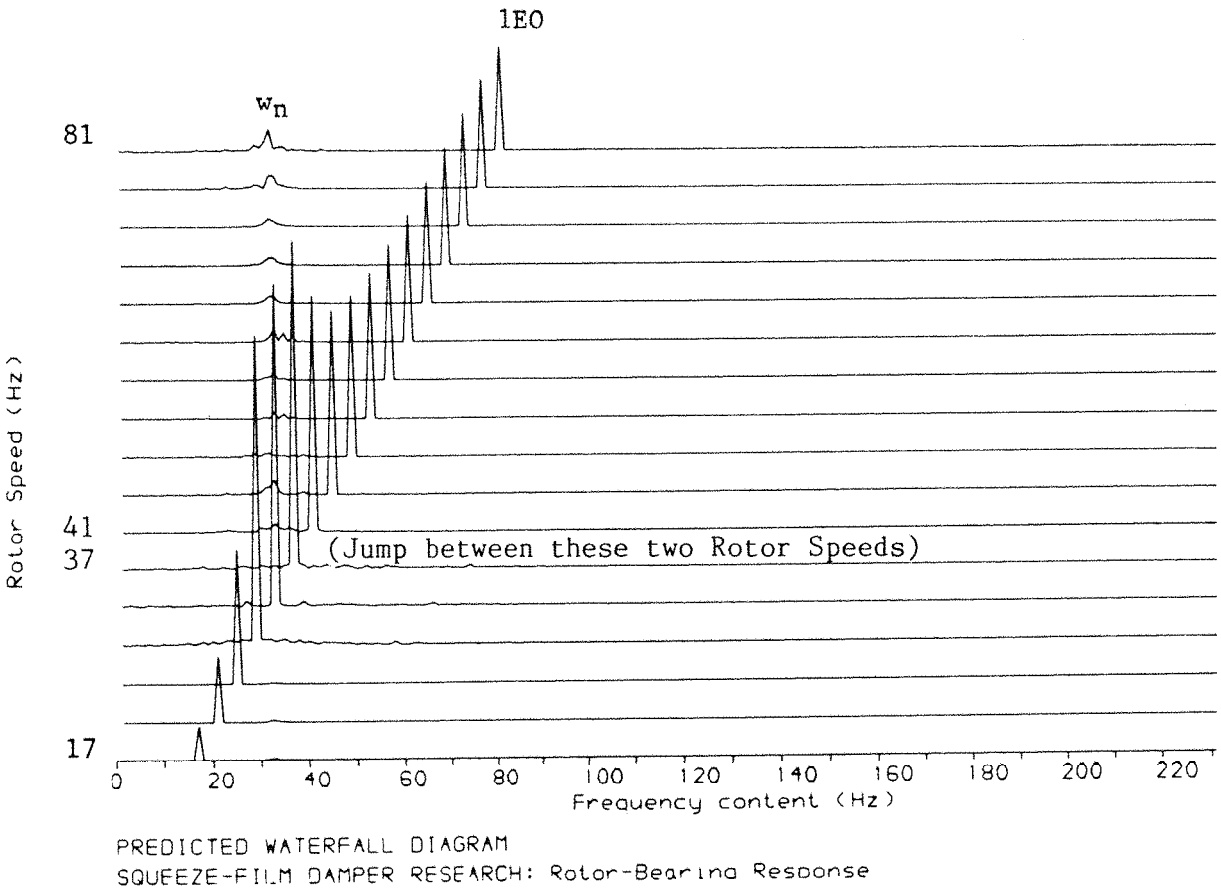

PREDICTED WATERFALL DIAGRAM
SQUEEZE-FILM DAMPER RESEARCH: Rotor-Bearing Response

(Linear Amplitude)

Theoretical Waterfall Diagram

Configuration 1a

FIGURE 5.12

CONFIGURATION 1b

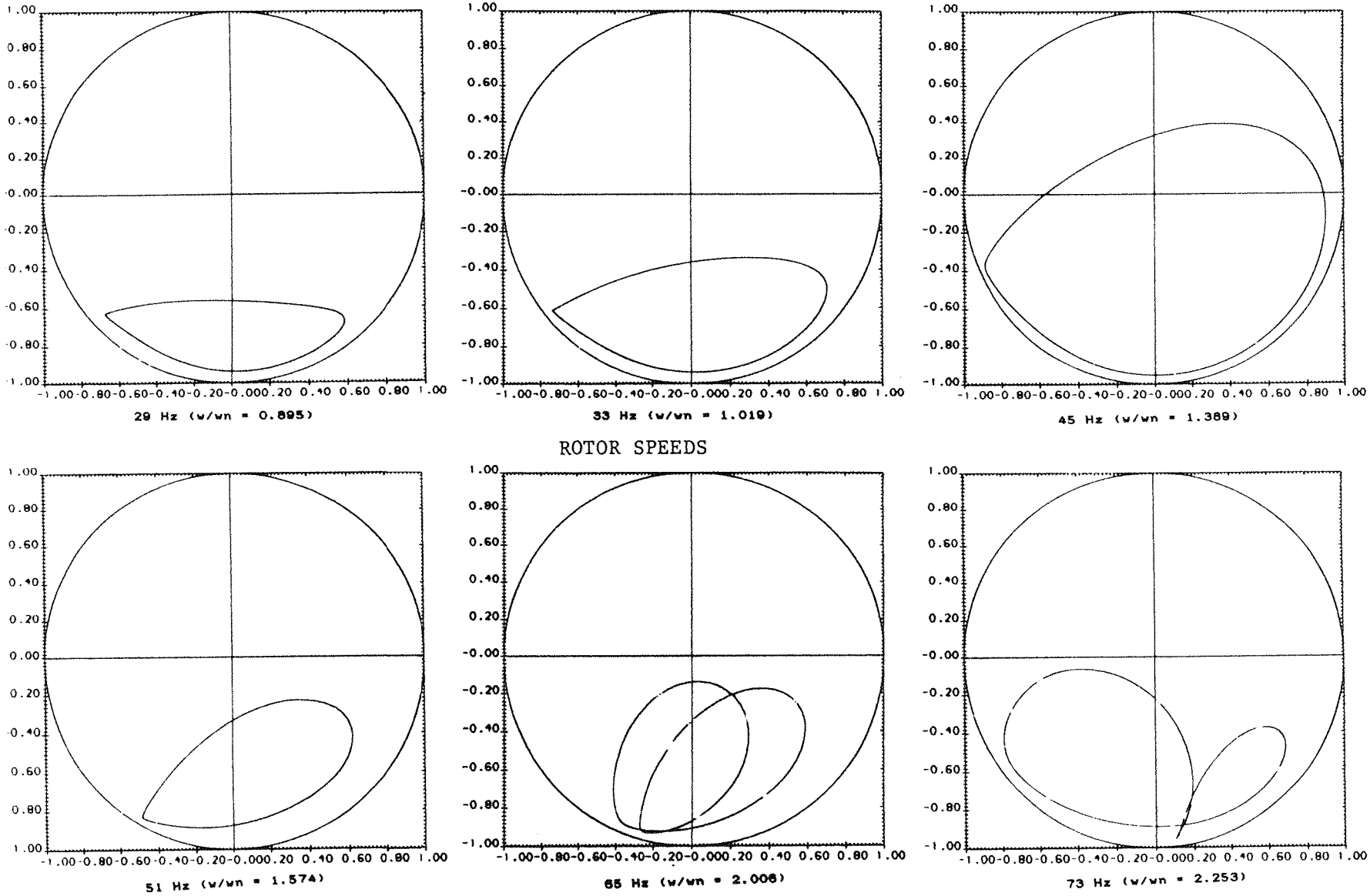

FIGURE 5.13 SFD1 THEORETICAL ORBITS (Q_{c_2} = 0.490, Psup = 2psi, $E_{o_1} \triangleq 0.8$)

SQUEEZE-FILM DAMPER SFD1

THEORETICAL NUMERICAL SOLUTION

	△	▽	×	□	
A =	0.2132E -1	0.2132E -1	0.2132E -1	0.2132E -1	
Qc2=	0.7332E 0	0.6107E 0	0.4901E 0	0.2450E 0	
Eo =	0.8000E 0	0.8000E 0	0.8000E 0	0.8000E 0	
Psup=	0.2000E 1	0.2000E 1	0.2000E 1	0.2000E 1	(psi)
Pmin=	-.1470E 2	-.1470E 2	-.1470E 2	-.1470E 2	(psi)

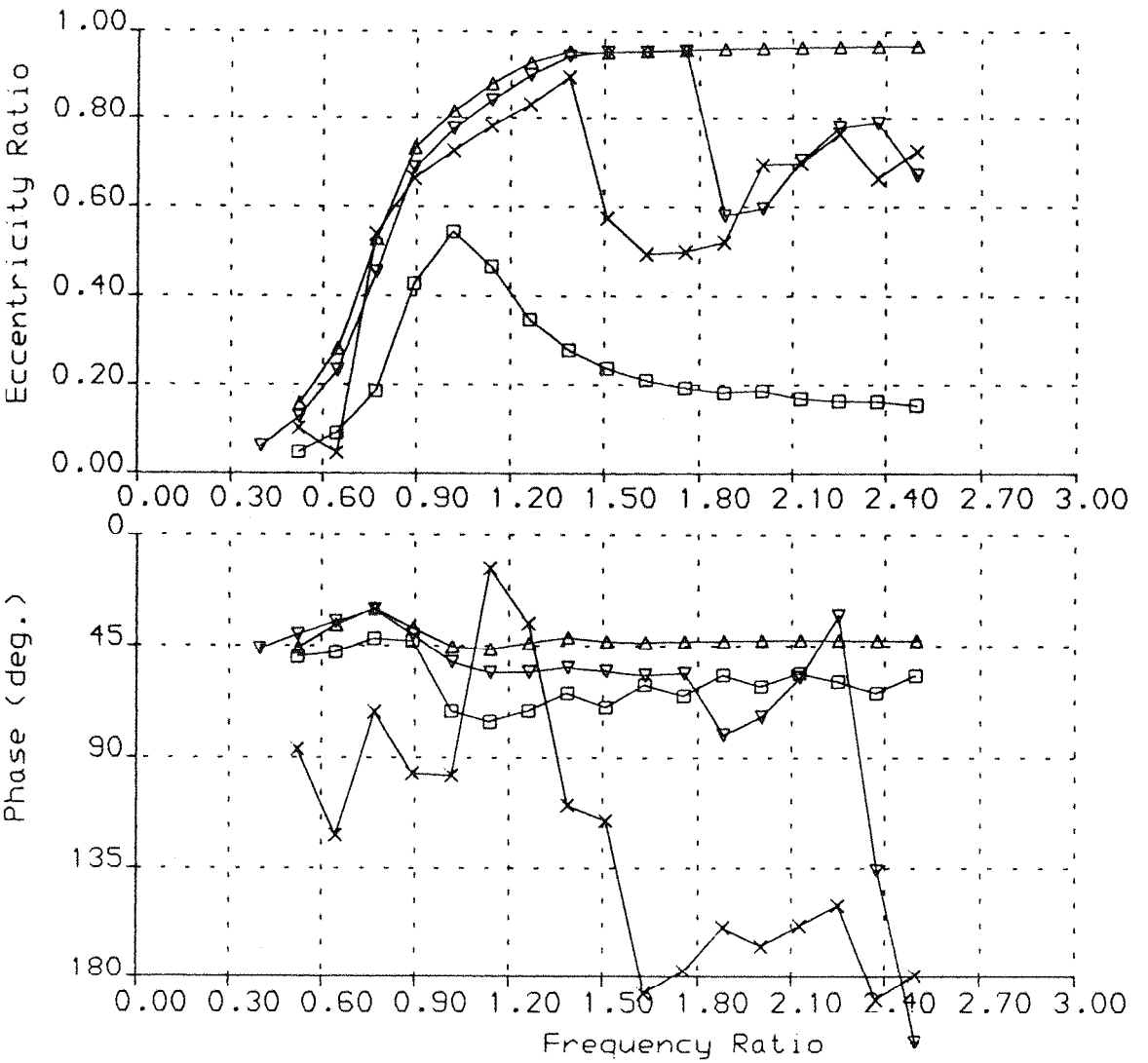

ROTOR-BEARING ASSEMBLY RESPONSE TO UNBALANCE

SQUEEZE-FILM DAMPER RESEARCH Rig Config. 1b

FIGURE 5.14

A = 0.213200E -1

Qc2 = 0.490097E 0

Eo = 0.800000E 0

Psup = 0.200000E 1 (psi)

Pmin = -0.147000E 2 (psi)

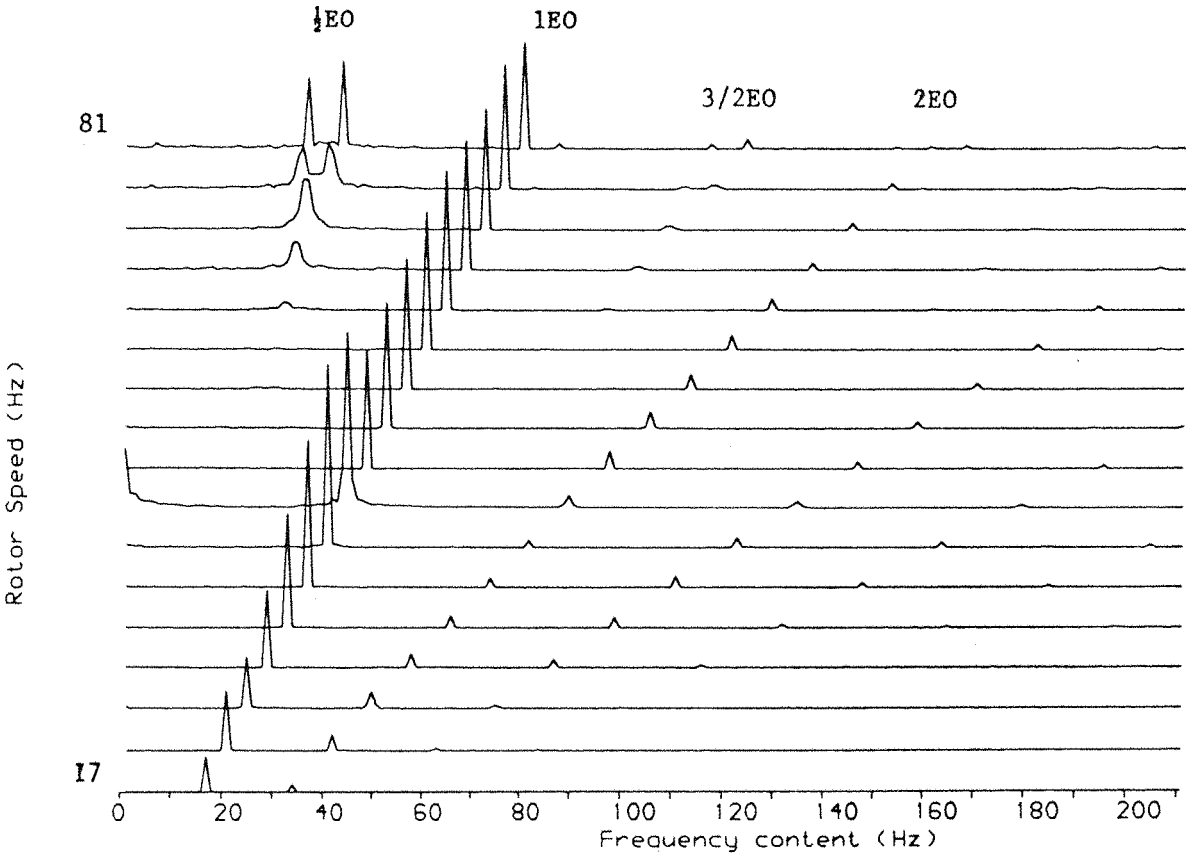

PREDICTED WATERFALL DIAGRAM
SQUEEZE-FILM DAMPER RESEARCH: Rotor-Bearing Response

(Linear Amplitude)

Theoretical Waterfall Diagram

Configuration 1b

FIGURE 5.15

SQUEEZE-FILM DAMPER SFD1

THEORETICAL NUMERICAL SOLUTION

	△	▽	×	□	
A =	0.2132E -1	0.2132E -1	0.2132E -1	0.2132E -1	
Qc2=	0.7332E 0	0.6107E 0	0.4901E 0	0.2450E 0	
Eo =	0.4000E 0	0.4000E 0	0.4000E 0	0.4000E 0	
Psup=	0.2000E 1	0.2000E 1	0.2000E 1	0.2000E 1	(psi)
Pmin=	-.1470E 2	-.1470E 2	-.1470E 2	-.1470E 2	(psi)

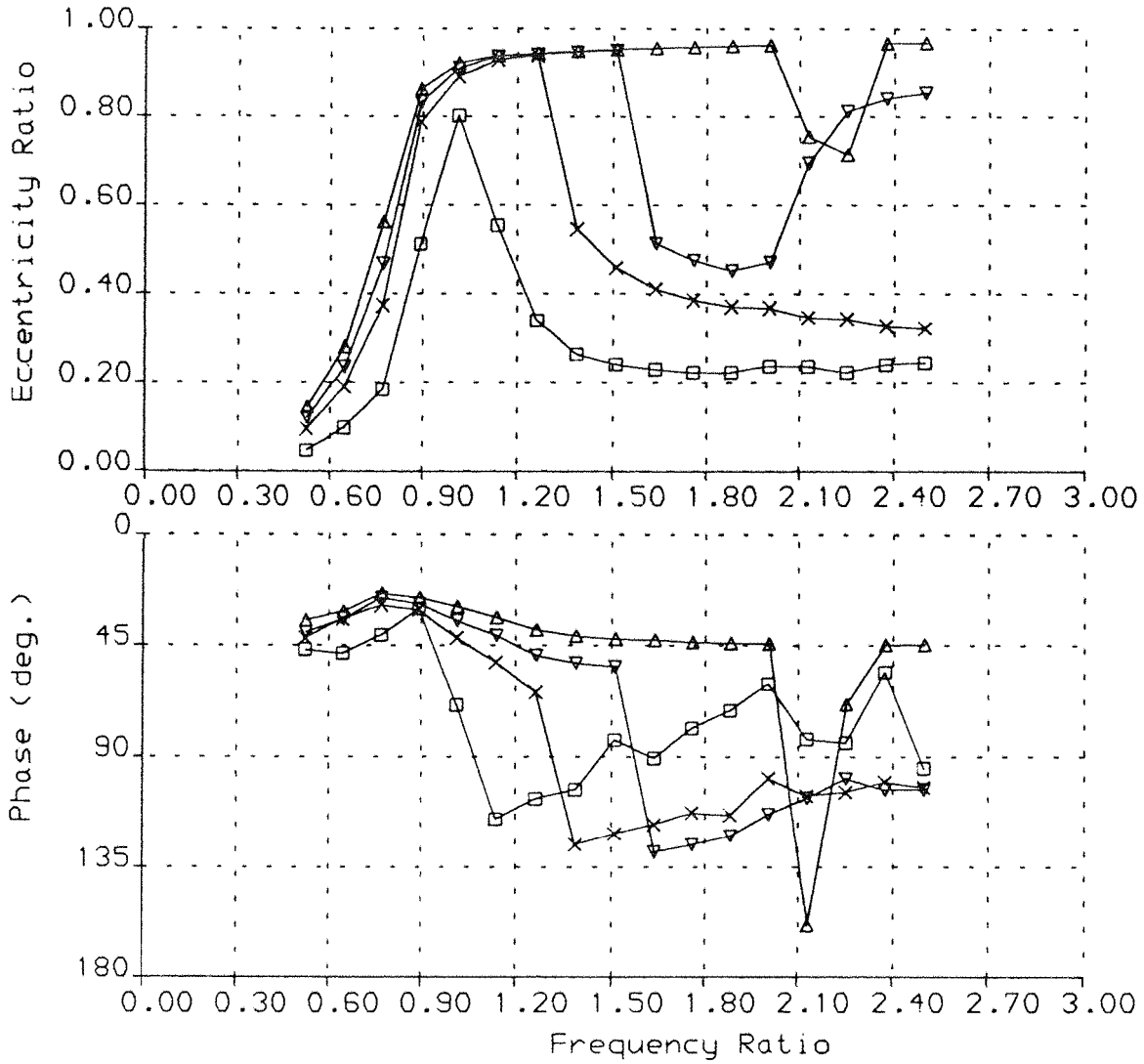

ROTOR-BEARING ASSEMBLY RESPONSE TO UNBALANCE
SQUEEZE-FILM DAMPER RESEARCH Rig Config. 1b

FIGURE 5.16

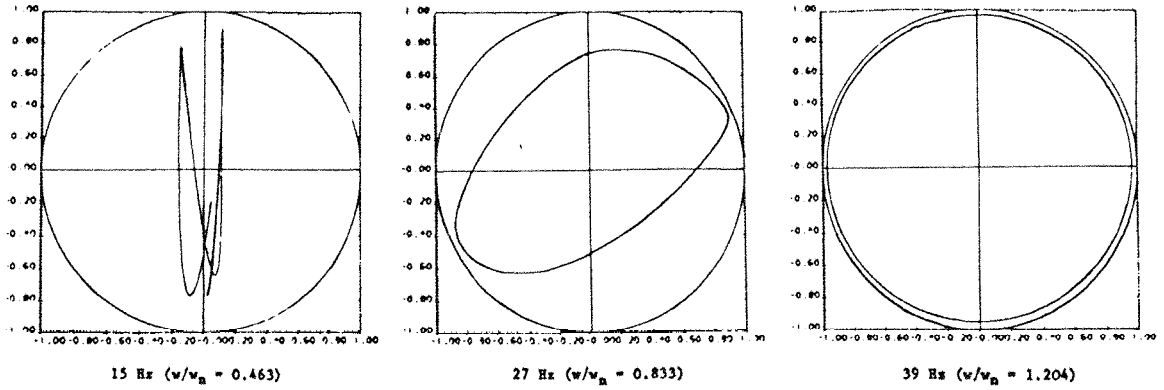

ROTOR SPEEDS

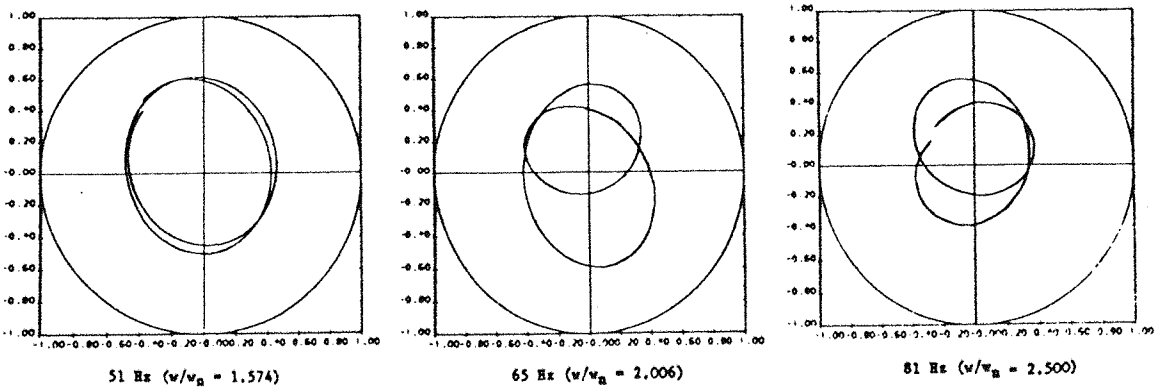

(a) SFD1 THEORETICAL ORBITS

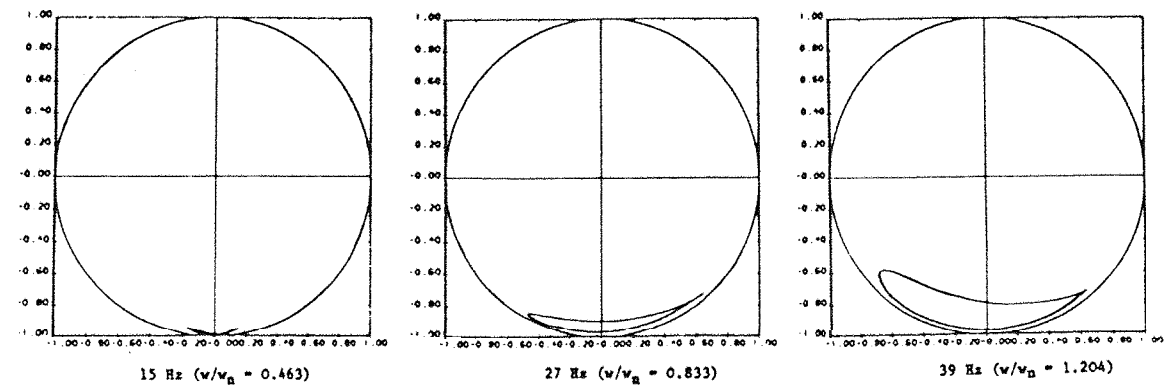

ROTOR SPEEDS

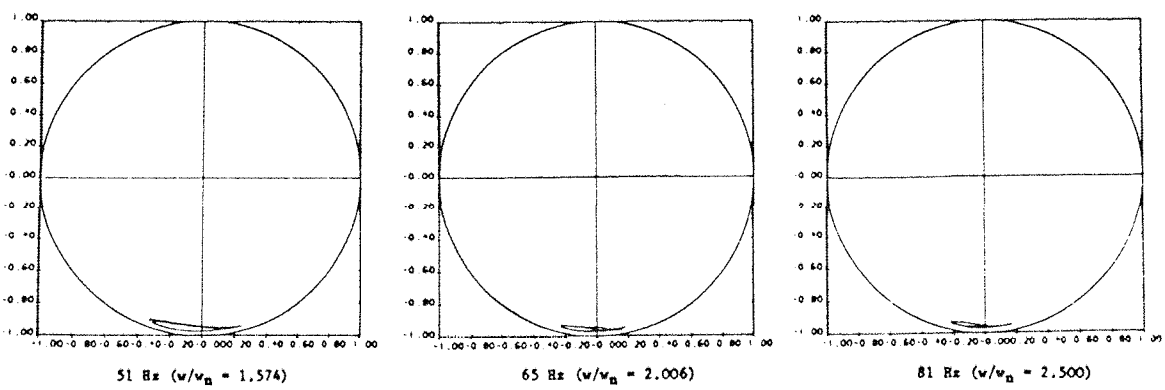

(b) SFD2 THEORETICAL ORBITS

CONFIGURATION 2a (Q_{c_2} = 0.611, Psup = 2 psi, E_{o1} = 0.0)

FIGURE 5.17

(a)

SQUEEZE-FILM DAMPER SFD1

THEORETICAL NUMERICAL SOLUTION

	△	▽	×	□	
A =	0.2132E -1	0.2132E -1	0.2132E -1	0.2132E -1	
Qc2=	0.7332E 0	0.6107E 0	0.4901E 0	0.2450E 0	
Eo =	0.0000E 0	0.0000E 0	0.0000E 0	0.0000E 0	
Psup=	0.2000E 1	0.2000E 1	0.2000E 1	0.2000E 1	(psi)
Pmin=	-.1470E 2	-.1470E 2	-.1470E 2	-.1470E 2	(psi)

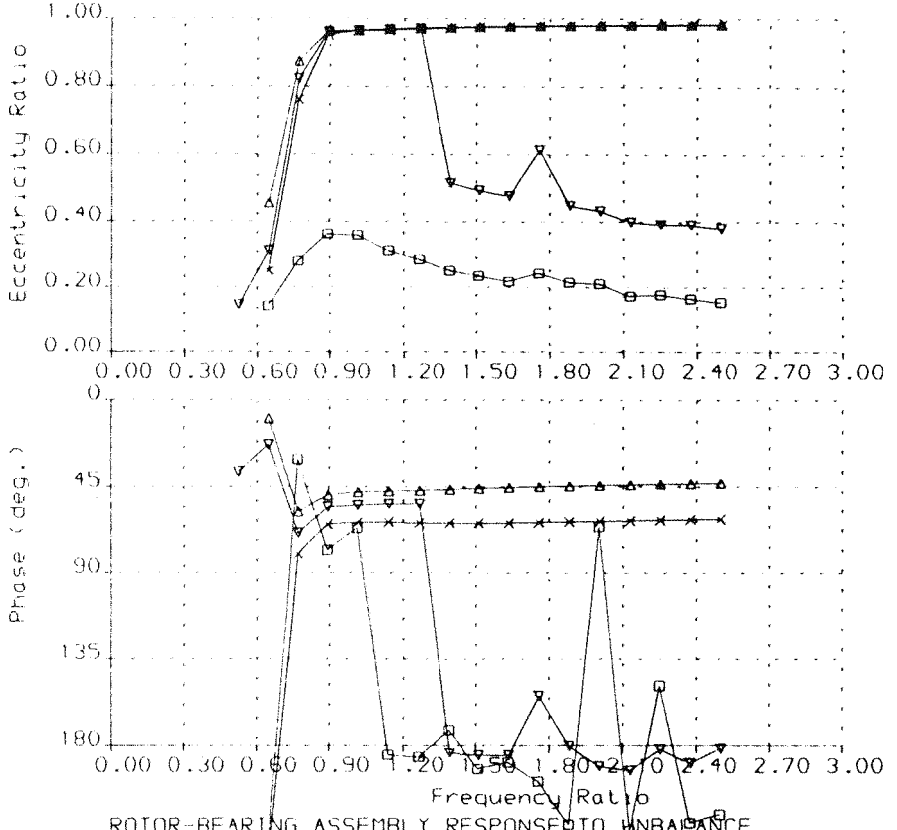

ROTOR-BEARING ASSEMBLY RESPONSE TO UNBALANCE

SQUEEZE-FILM DAMPER RESEARCH Rig Config. 2a

(b)

SQUEEZE-FILM DAMPER SFD2

THEORETICAL NUMERICAL SOLUTION

	△	▽	×	□	
A =	0.4010E -1	0.4010E -1	0.4010E -1	0.4010E -1	
Qc2=	0.7332E 0	0.6107E 0	0.4901E 0	0.2450E 0	
Eo =	0.1000E 1	0.1000E 1	0.1000E 1	0.1000E 1	
Psup=	0.2000E 1	0.2000E 1	0.2000E 1	0.2000E 1	(
Pmin=	-.1470E 2	-.1470E 2	-.1470E 2	-.1470E 2	(

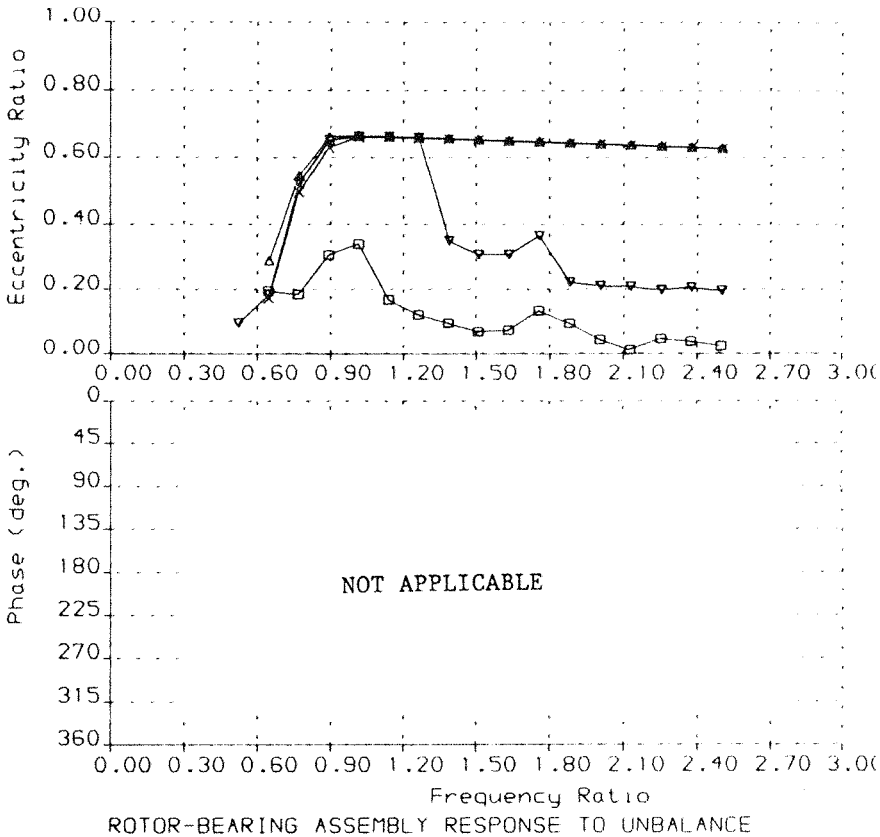

ROTOR-BEARING ASSEMBLY RESPONSE TO UNBALANCE

SQUEEZE-FILM DAMPER RESEARCH Rig Config. 2a

FIGURE 5.18

(a)

SQUEEZE-FILM DAMPER SFD1

THEORETICAL NUMERICAL SOLUTION

	△	▽	×	□	
Λ =	0.2132E -1	0.2132E -1	0.2132E -1	0.2132E -1	
Qc2=	0.7332E 0	0.6107E 0	0.4901E 0	0.2450E 0	
Eo =	0.0000E 0	0.0000E 0	0.0000E 0	0.0000E 0	
Psup=	0.1500E 2	0.1500E 2	0.1500E 2	0.1500E 2	(psi
Pmin=	-.1470E 2	-.1470E 2	-.1470E 2	-.1470E 2	(psi

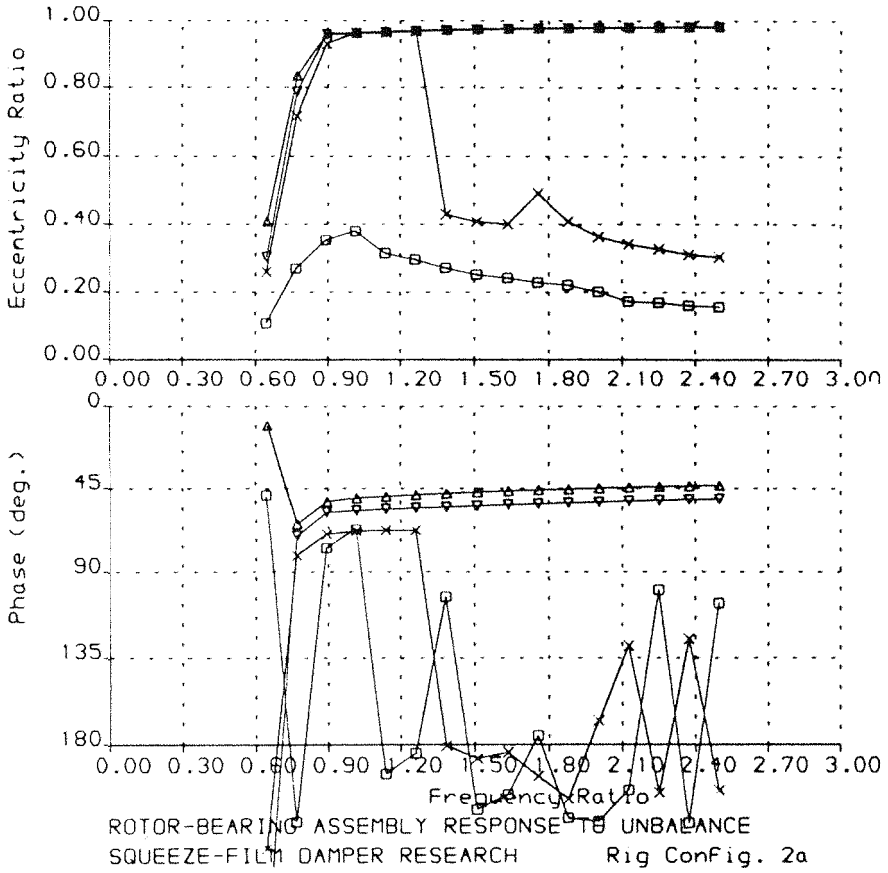

ROTOR-BEARING ASSEMBLY RESPONSE TO UNBALANCE

SQUEEZE-FILM DAMPER RESEARCH Rig Config. 2a

(b)

SQUEEZE-FILM DAMPER SFD2

THEORETICAL NUMERICAL SOLUTION

	△	▽	×	□	
Λ =	0.4010E -1	0.4010E -1	0.4010E -1	0.4010E -1	
Qc2=	0.7332E 0	0.6107E 0	0.4901E 0	0.2450E 0	
Eo =	0.1000E 1	0.1000E 1	0.1000E 1	0.1000E 1	
Psup=	0.1500E 2	0.1500E 2	0.1500E 2	0.1500E 2	(psi)
Pmin=	-.1470E 2	-.1470E 2	-.1470E 2	-.1470E 2	(psi)

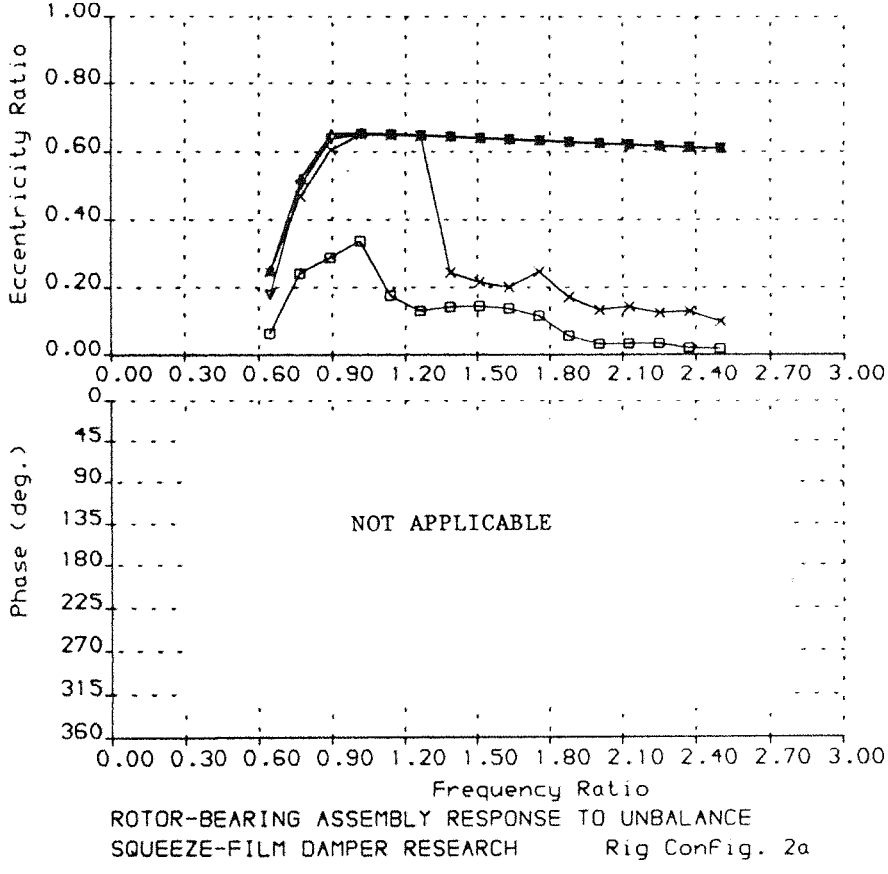

ROTOR-BEARING ASSEMBLY RESPONSE TO UNBALANCE

SQUEEZE-FILM DAMPER RESEARCH Rig Config. 2a

FIGURE 5.19

FIGURE 5.20

SFD1 RESPONSE

A = 0.213200E -1

Qc2 = 0.610707E 0

Eo = 0.000000E 0

Psup = 0.200000E 1 (psi)

Pmin = -0.147000E 2 (psi)

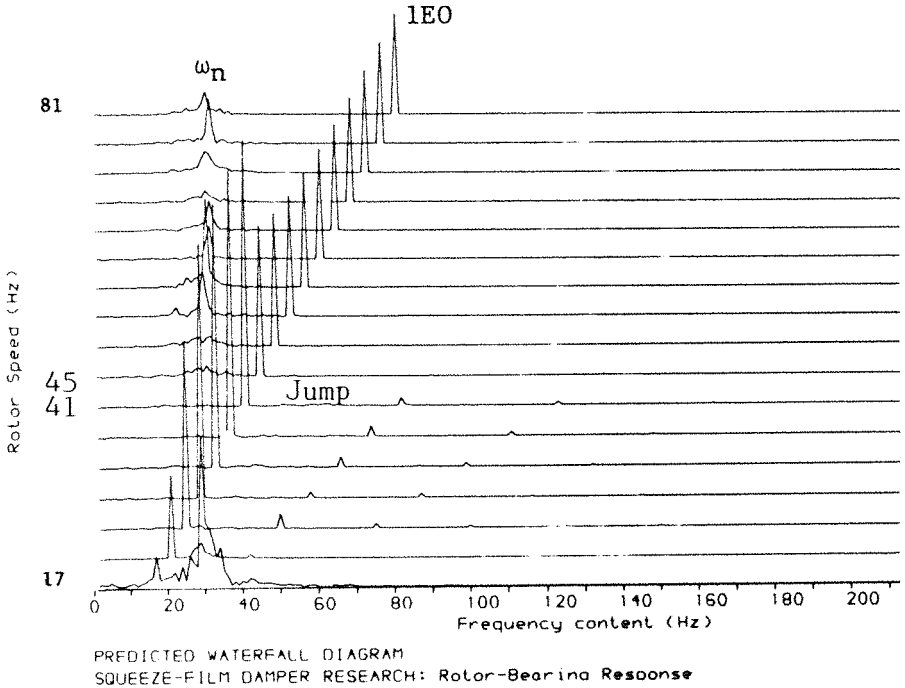

SFD2 RESPONSE

A = 0.401000E -1

Qc2 = 0.610707E 0

Eo = 0.100000E 1

Psup = 0.200000E 1 (psi)

Pmin = -0.147000E 2 (psi)

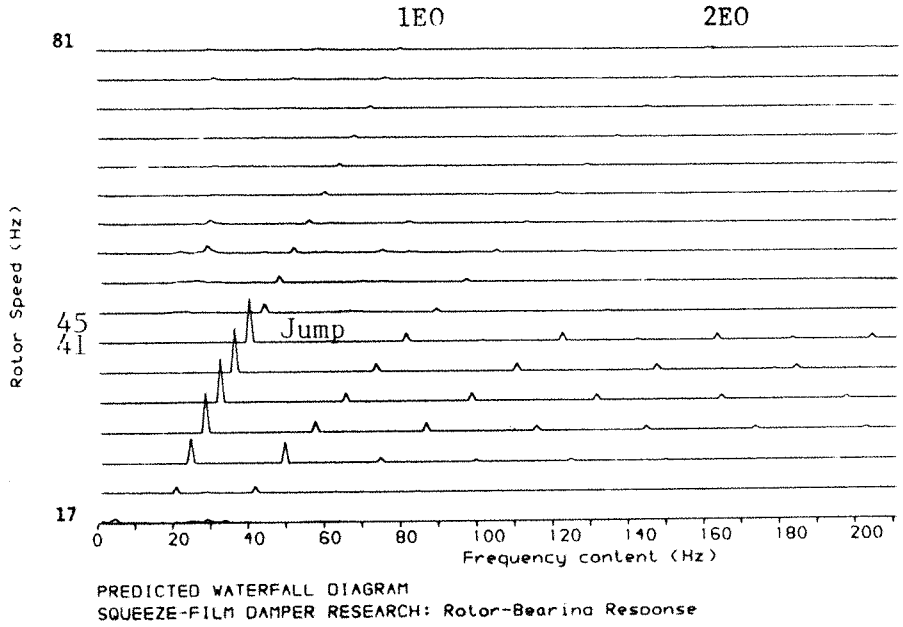

(Linear Amplitude)

Theoretical Waterfall Diagrams

Configuration 2a

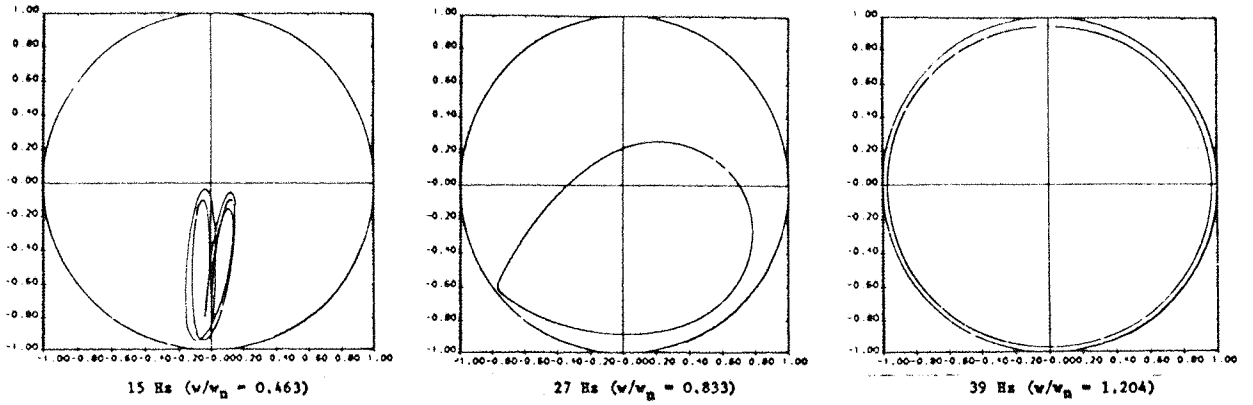

ROTOR SPEEDS

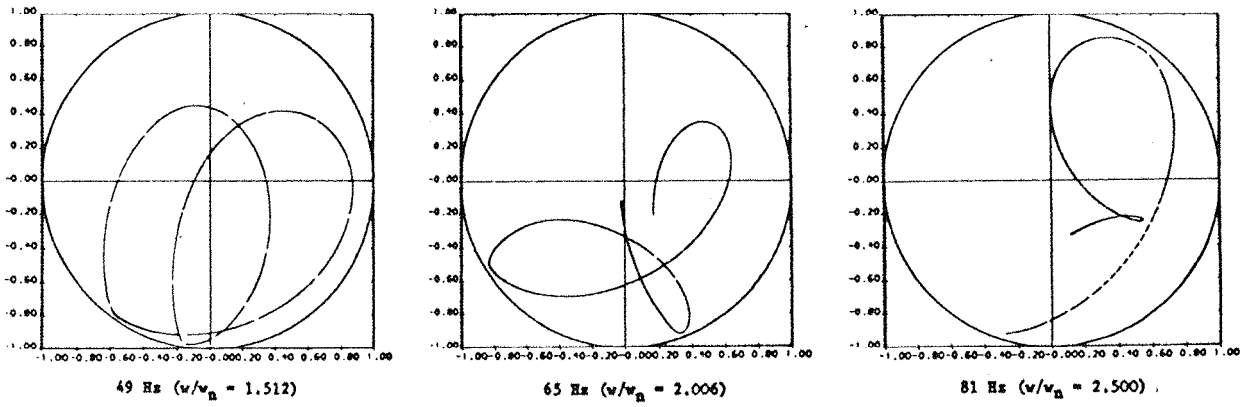

(a) SFD1 THEORETICAL ORBITS

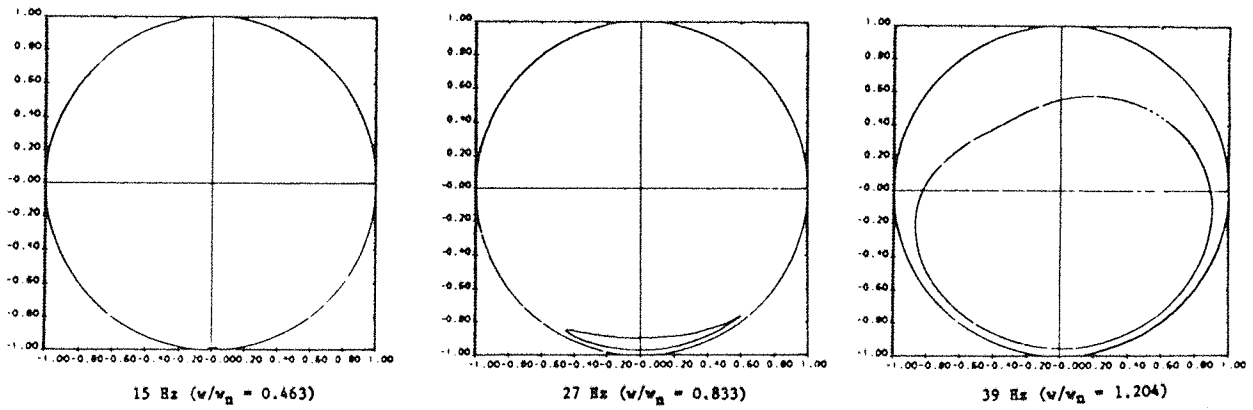

ROTOR SPEEDS

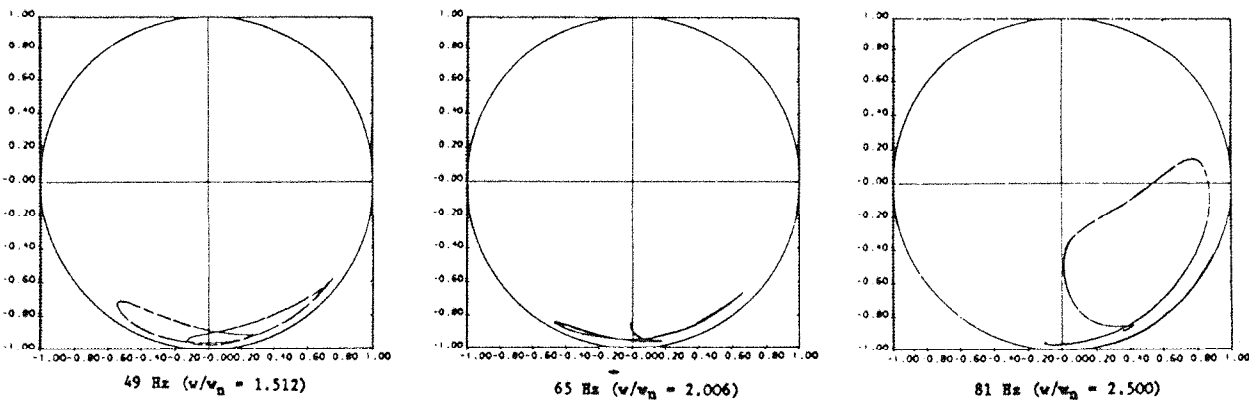

(b) SFD2 THEORETICAL ORBITS

CONFIGURATION 2a (Q_{c_2} = 0.611, Psup = 2 psi, E_{o_1} = 0.5)

FIGURE 5.21

(a)

SQUEEZE-FILM DAMPER SFO1

THEORETICAL NUMERICAL SOLUTION

	△	▽	
A =	0.2132E -1	0.2132E -1	
Qc2=	0.6107E 0	0.6107E 0	
Eo =	0.5000E 0	0.5000E 0	
Psup=	0.1500E 2	0.1500E 2	(psi)
Pmin=	-.1470E 2	-.1470E 2	(psi)

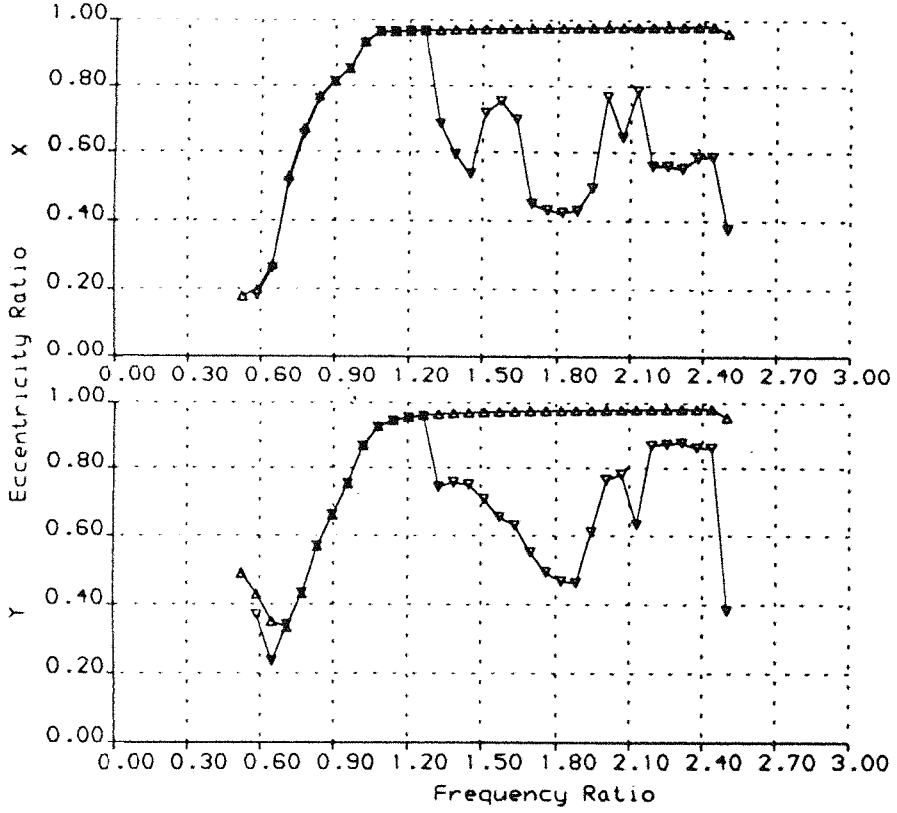

ROTOR-BEARING ASSEMBLY RESPONSE TO UNBALANCE
SQUEEZE-FILM DAMPER RESEARCH Rig Config. 2a

(b)

SQUEEZE-FILM DAMPER SFO2

THEORETICAL NUMERICAL SOLUTION

	△	▽	
A =	0.4010E -1	0.4010E -1	
Qc2=	0.6107E 0	0.6107E 0	
Eo =	0.1000E 1	0.1000E 1	
Psup=	0.1500E 2	0.1500E 2	(psi)
Pmin=	-.1470E 2	-.1470E 2	(psi)

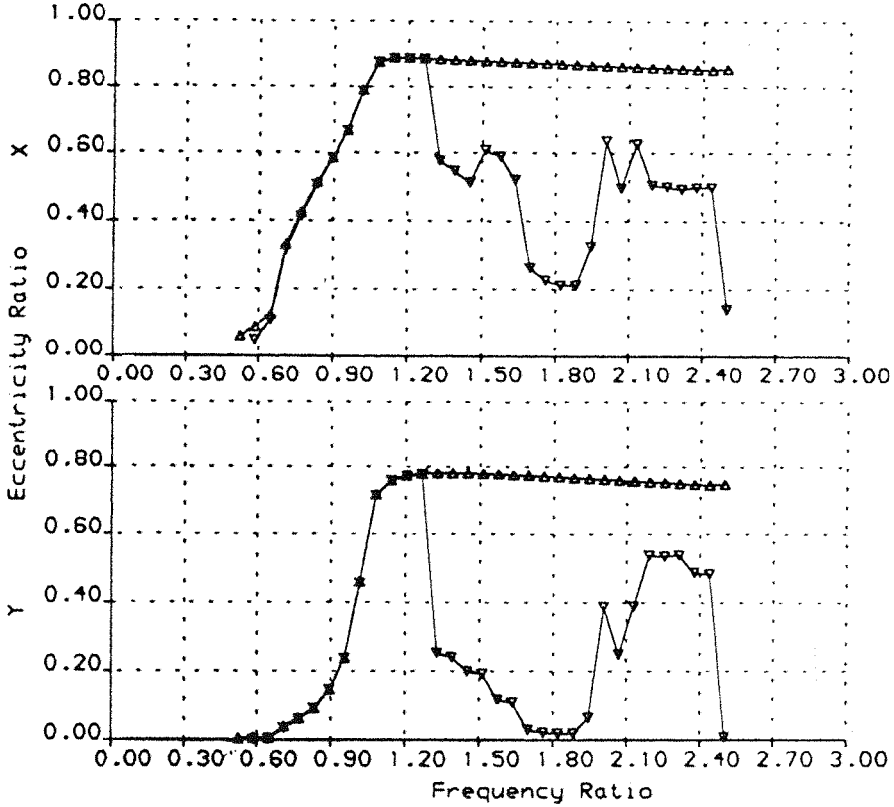

ROTOR-BEARING ASSEMBLY RESPONSE TO UNBALANCE
SQUEEZE-FILM DAMPER RESEARCH Rig Config. 2a

FIGURE 5.22

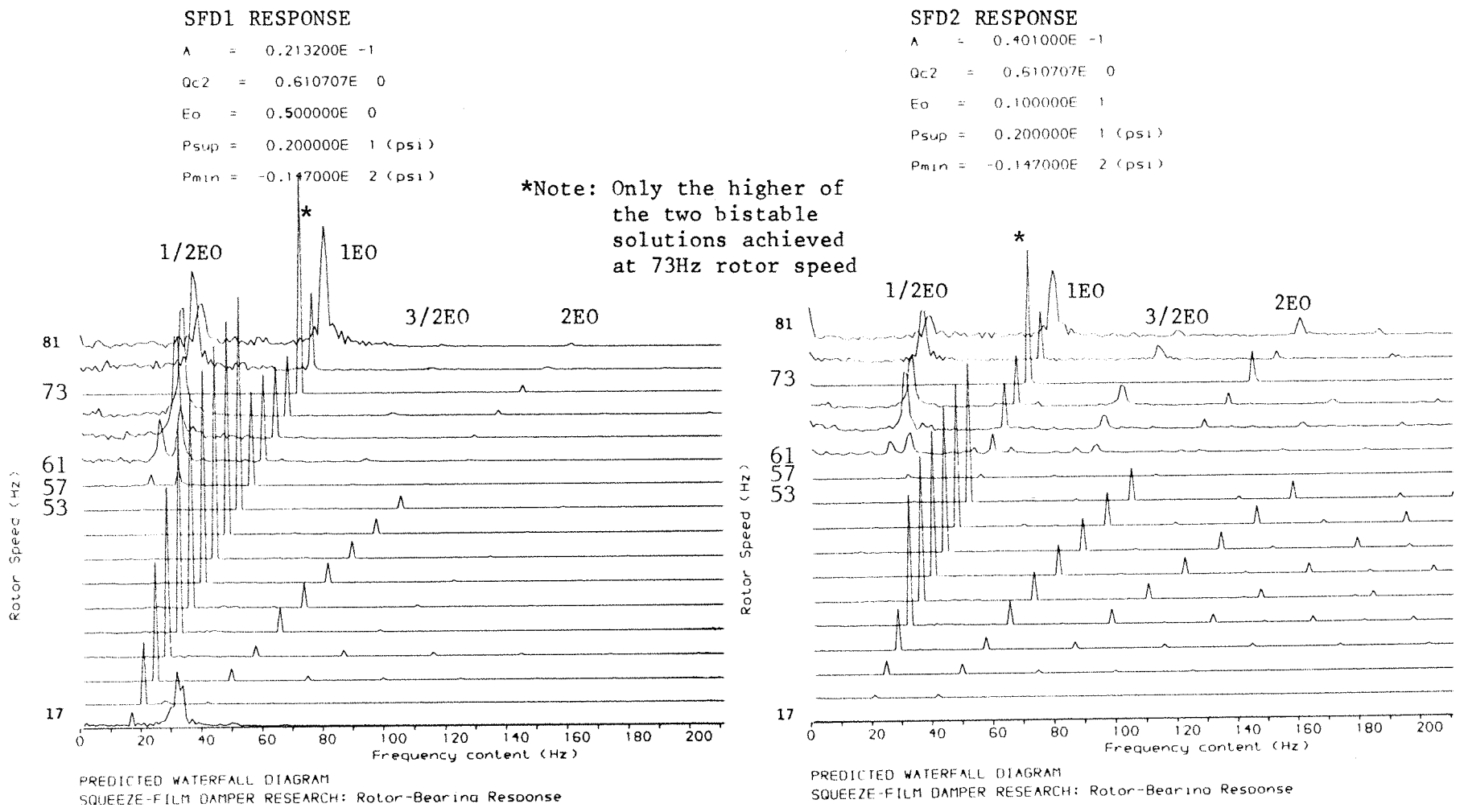

FIGURE 5.23

(Linear Amplitude)

Theoretical Waterfall Diagrams

Configuration 2a

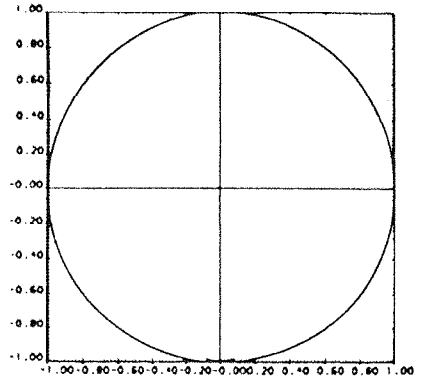

15 Hz (w/w_n = 0.463)

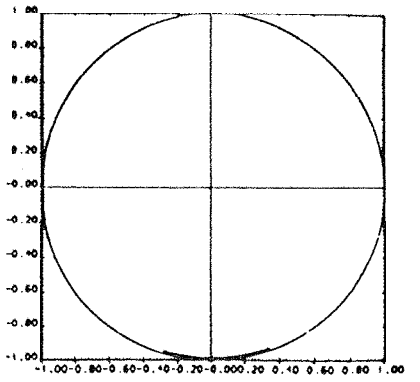

27 Hz (w/w_n = 0.833)

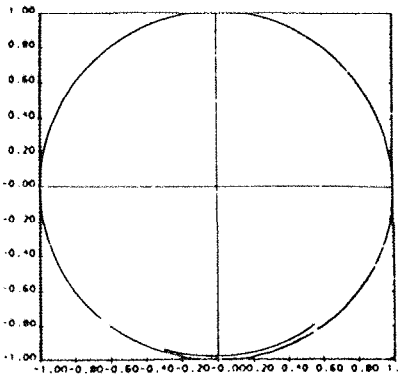

39 Hz (w/w_n = 1.204)

ROTOR SPEEDS

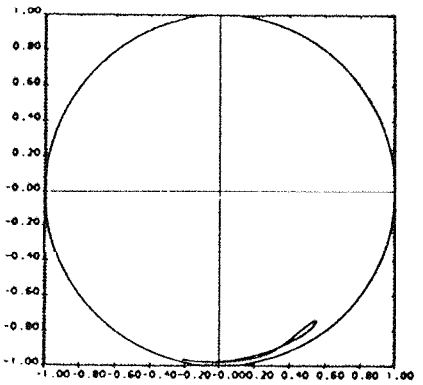

51 Hz (w/w_n = 1.574)

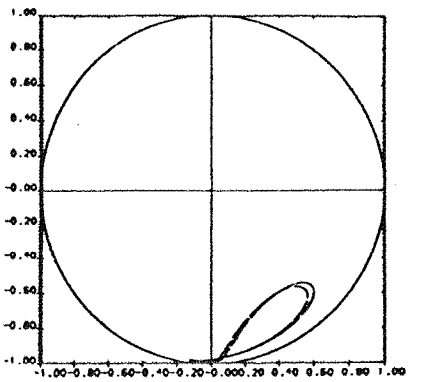

65 Hz (w/w_n = 2.006)

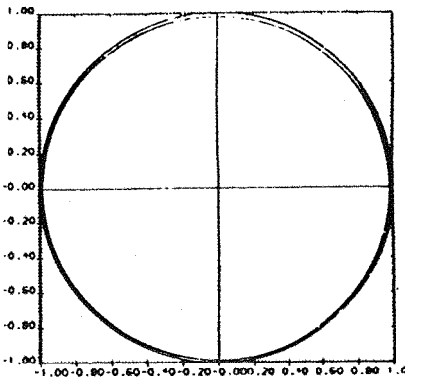

81 Hz (w/w_n = 2.500)

(a) SFD1 THEORETICAL ORBITS

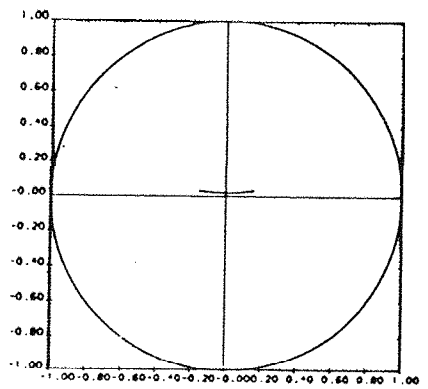

15 Hz (w/w_n = 0.463)

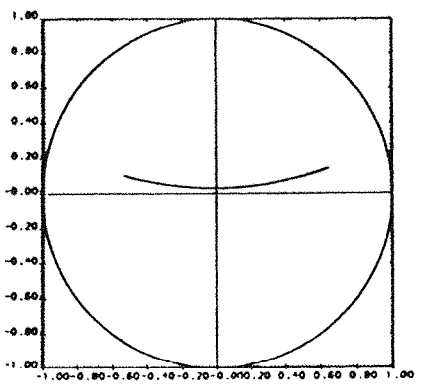

27 Hz (w/w_n = 0.833)

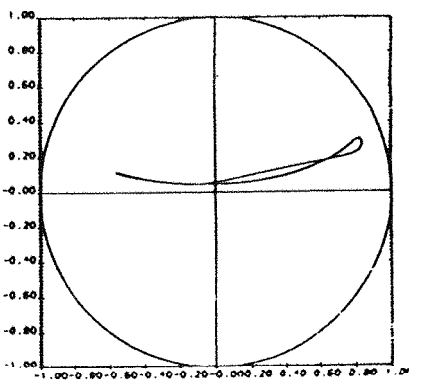

39 Hz (w/w_n = 1.204)

ROTOR SPEEDS

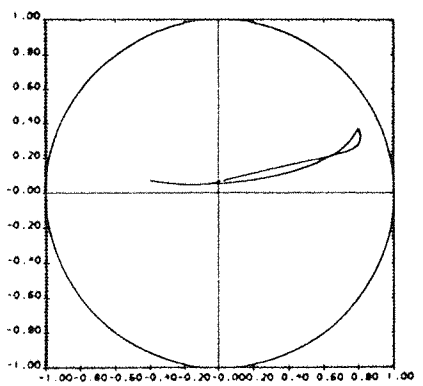

51 Hz (w/w_n = 1.574)

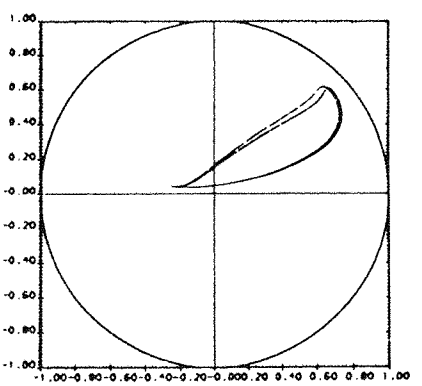

65 Hz (w/w_n = 2.006)

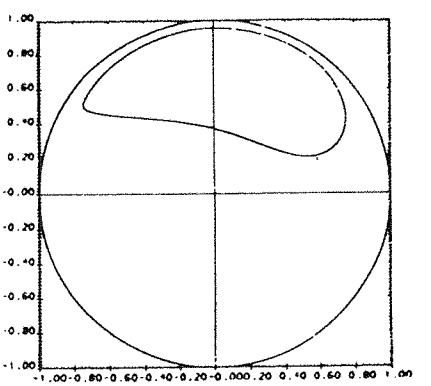

81 Hz (w/w_n = 2.500)

(b) SFD2 THEORETICAL ORBITS

CONFIGURATION 2b (Q_{c_2} = 0.611, Psup = 2 psi)

FIGURE 5.24

(a)

SQUEEZE-FILM DAMPER SFD1

THEORETICAL NUMERICAL SOLUTION

	△	▽	×	□	
A =	0.2132E -1	0.2132E -1	0.2132E -1	0.2132E -1	
Qc2=	0.7332E 0	0.6107E 0	0.4901E 0	0.2450E 0	
Eo =	0.1000E 1	0.1000E 1	0.1000E 1	0.1000E 1	
Psup=	0.2000E 1	0.2000E 1	0.2000E 1	0.2000E 1	(psi)
Pmin=	-.1470E 2	-.1470E 2	-.1470E 2	-.1470E 2	(psi)

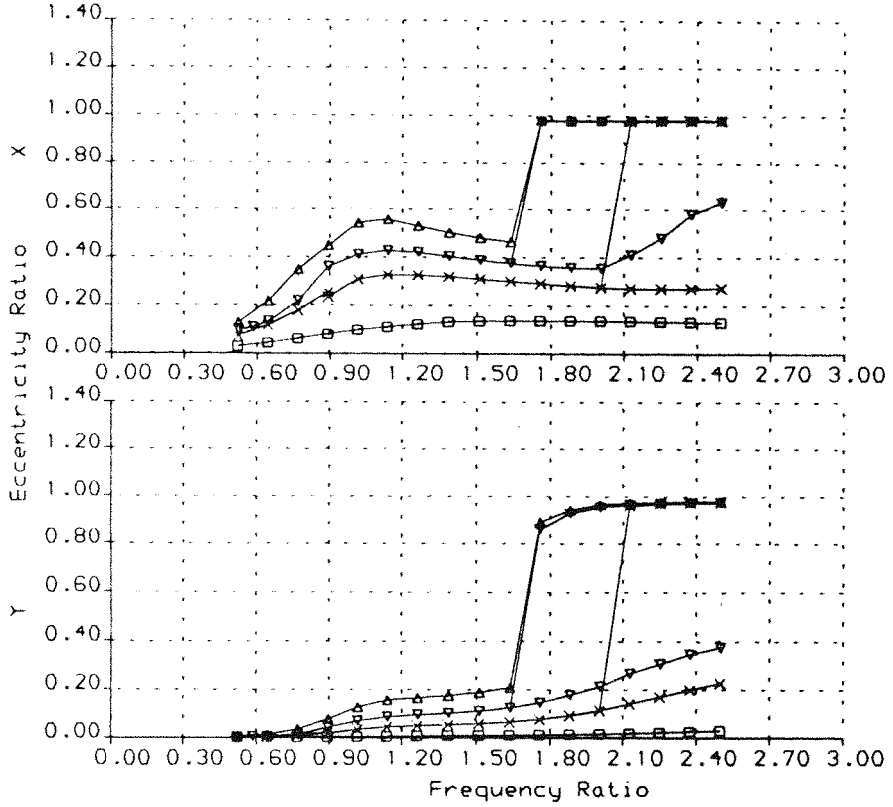

ROTOR-BEARING ASSEMBLY RESPONSE TO UNBALANCE

SQUEEZE-FILM DAMPER RESEARCH Rig Config. 2b

(b)

SQUEEZE-FILM DAMPER SFD2

THEORETICAL NUMERICAL SOLUTION

	△	▽	×	□	
A =	0.4010E -1	0.4010E -1	0.4010E -1	0.4010E -1	
Qc2=	0.7332E 0	0.6107E 0	0.4901E 0	0.2450E 0	
Eo =	0.0000E 0	0.0000E 0	0.0000E 0	0.0000E 0	
Psup=	0.2000E 1	0.2000E 1	0.2000E 1	0.2000E 1	(psi
Pmin=	-.1470E 2	-.1470E 2	-.1470E 2	-.1470E 2	(psi

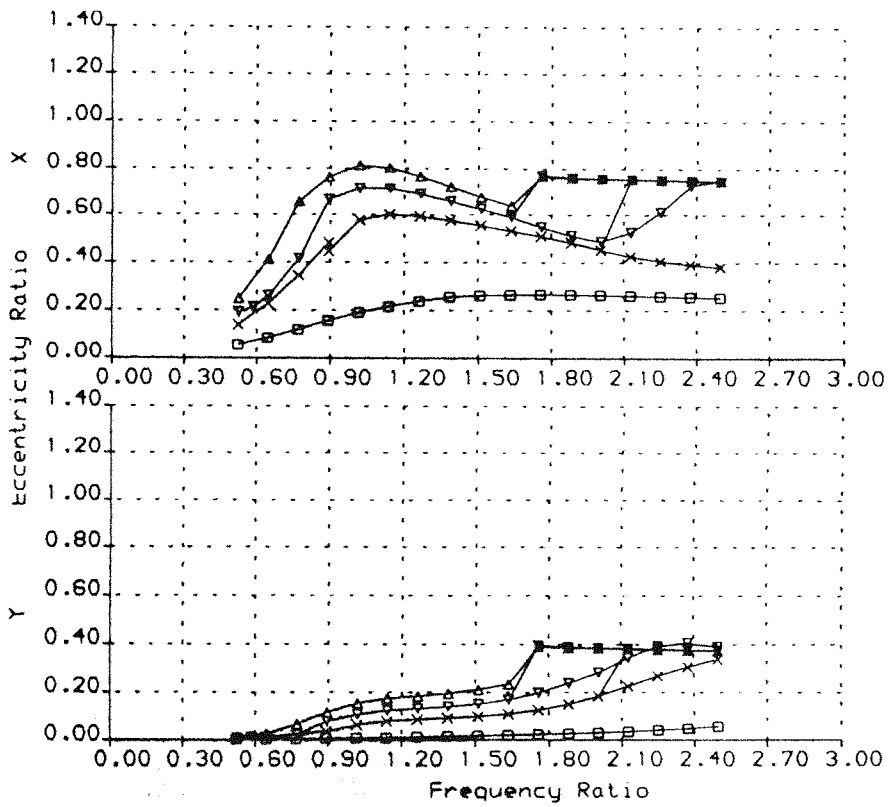

ROTOR-BEARING ASSEMBLY RESPONSE TO UNBALANCE

SQUEEZE-FILM DAMPER RESEARCH Rig Config. 2b

FIGURE 5.25

SQUEEZE-FILM DAMPER SFD1

THEORETICAL NUMERICAL SOLUTION

	△	▽	×	□	
A =	0.2132E -1	0.2132E -1	0.2132E -1	0.2132E -1	
Qc2=	0.7332E 0	0.6107E 0	0.4901E 0	0.2450E 0	
Eo =	0.1000E 1	0.1000E 1	0.1000E 1	0.1000E 1	
Psup=	0.1500E 2	0.1500E 2	0.1500E 2	0.1500E 2	(psi)
Pmin=	-.1470E 2	-.1470E 2	-.1470E 2	-.1470E 2	(psi)

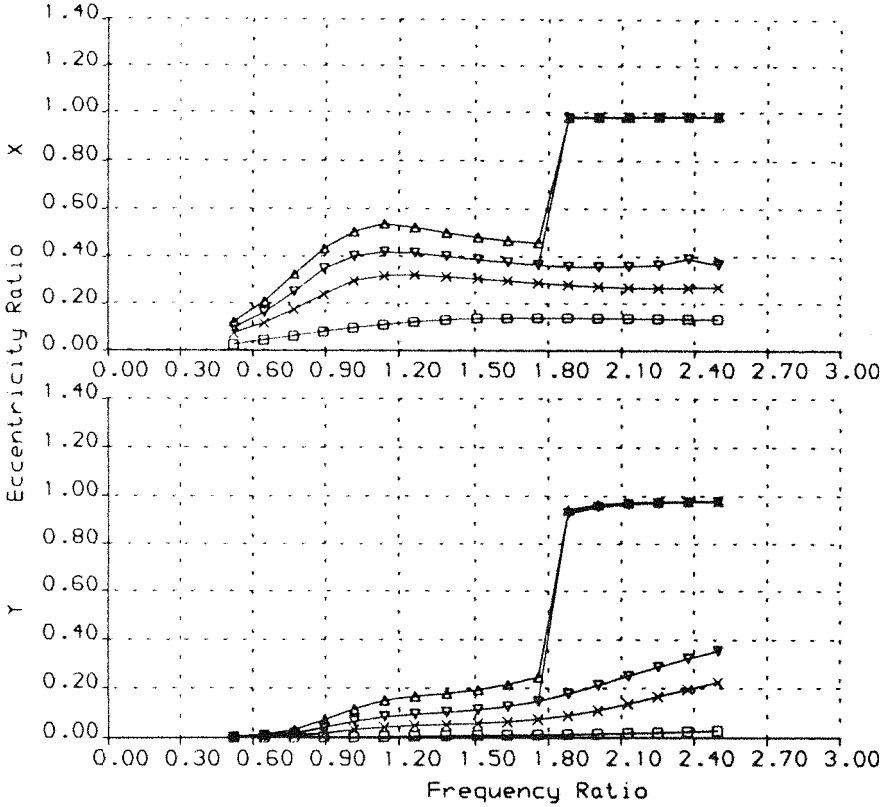

ROTOR-BEARING ASSEMBLY RESPONSE TO UNBALANCE

SQUEEZE-FILM DAMPER RESEARCH Rig Config. 2b

SQUEEZE-FILM DAMPER SFD2

THEORETICAL NUMERICAL SOLUTION

	△	▽	×	□	
A =	0.4010E -1	0.4010E -1	0.4010E -1	0.4010E -1	
Qc2=	0.7332E 0	0.6107E 0	0.4901E 0	0.2450E 0	
Eo =	0.0000E 0	0.0000E 0	0.0000E 0	0.0000E 0	
Psup=	0.1500E 2	0.1500E 2	0.1500E 2	0.1500E 2	(psi
Pmin=	-.1470E 2	-.1470E 2	-.1470E 2	-.1470E 2	(psi

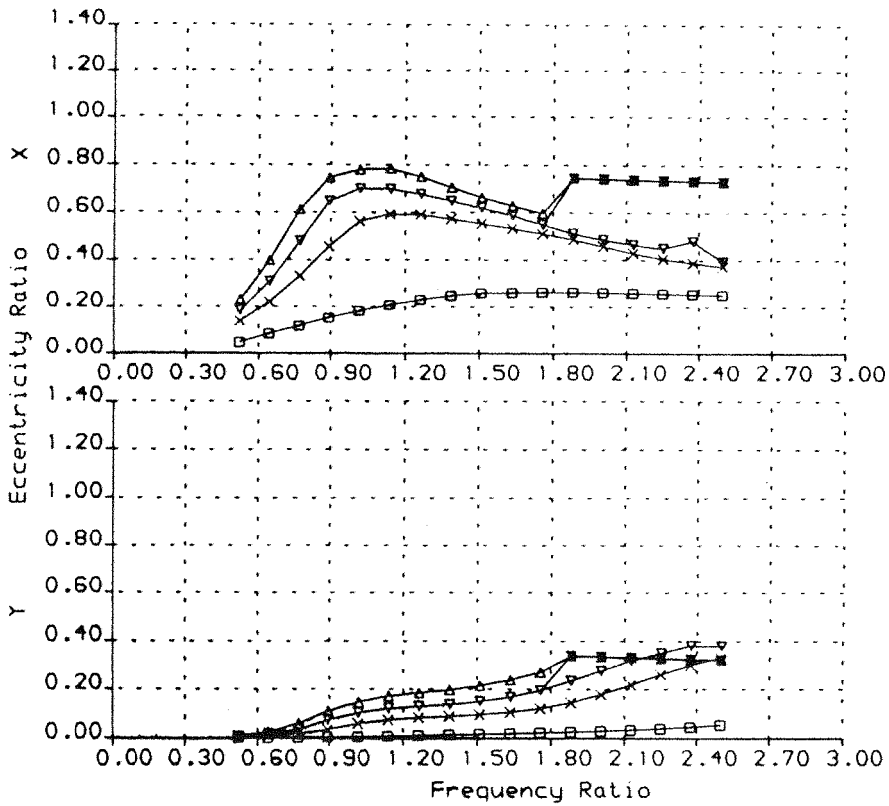

ROTOR-BEARING ASSEMBLY RESPONSE TO UNBALANCE

SQUEEZE-FILM DAMPER RESEARCH Rig Config. 2b

FIGURE 5.26

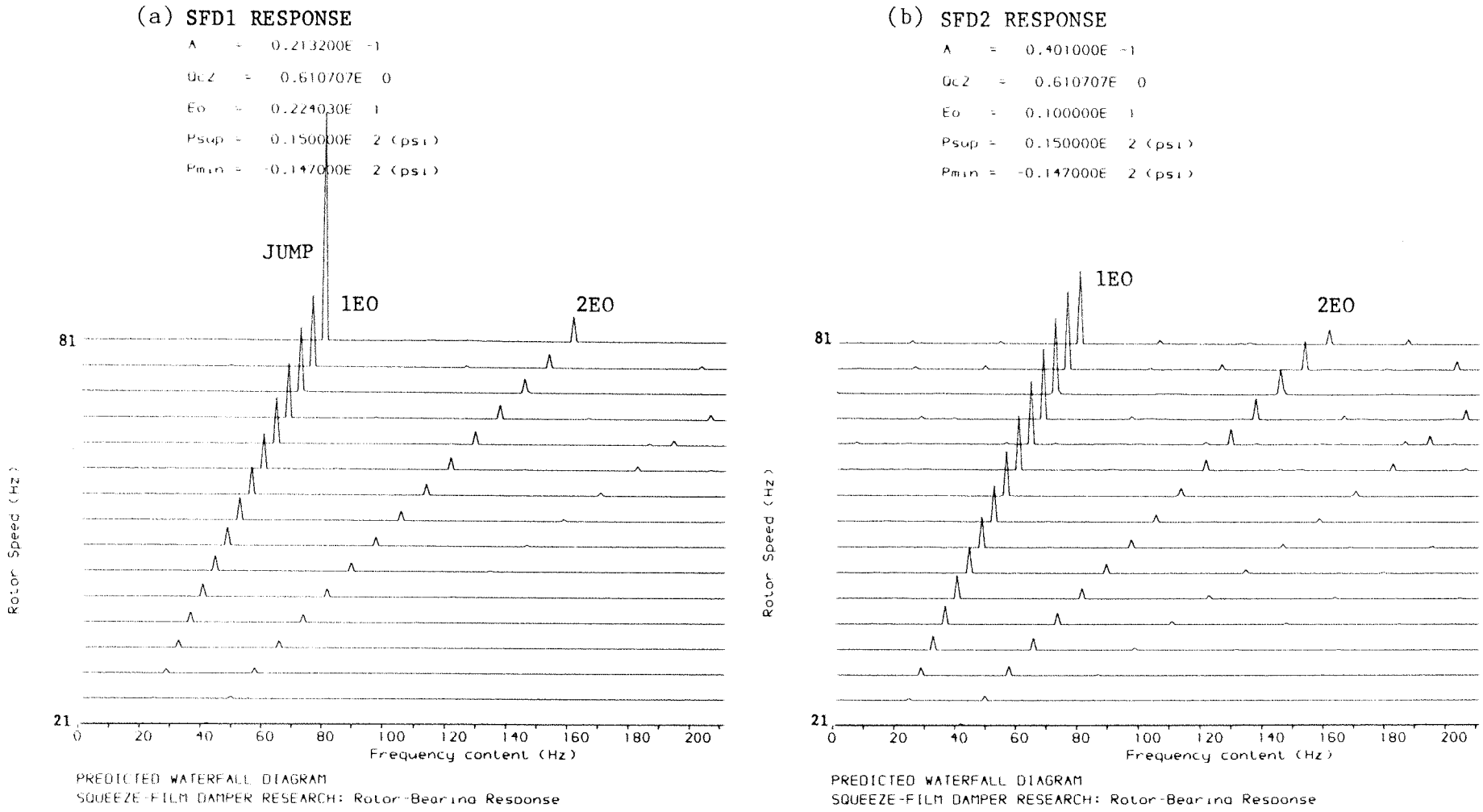

FIGURE 5.27

(Linear Amplitude)

Theoretical Waterfall Diagrams

Configuration 2b

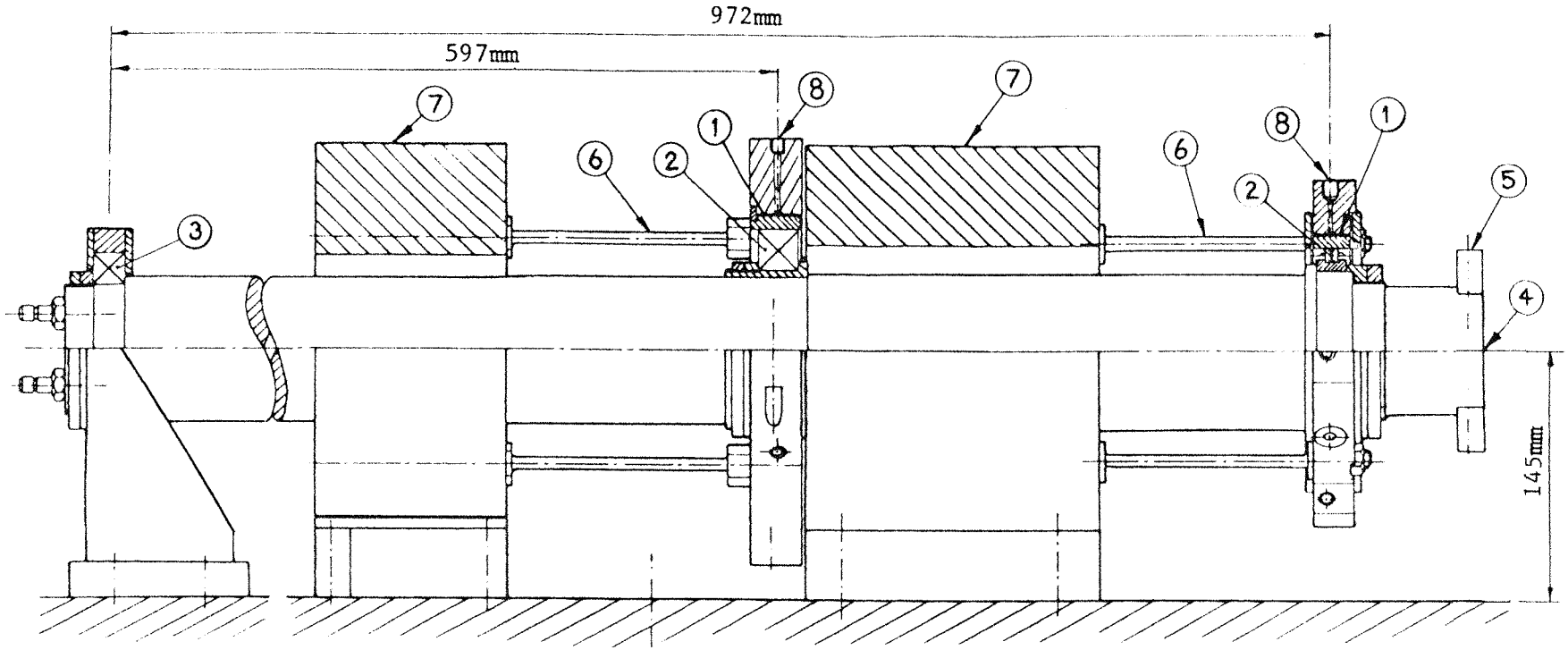

1 Squeeze-Film Damper
2 Rolling Element Bearing
3 Self Aligning Bearing
4 Rotor
5 Unbalance Mass
6 Flexible Bar
7 Foundation Block
8 Oil Supply Port

DETAILS OF EXPERIMENTAL RIG

FIGURE 6.1

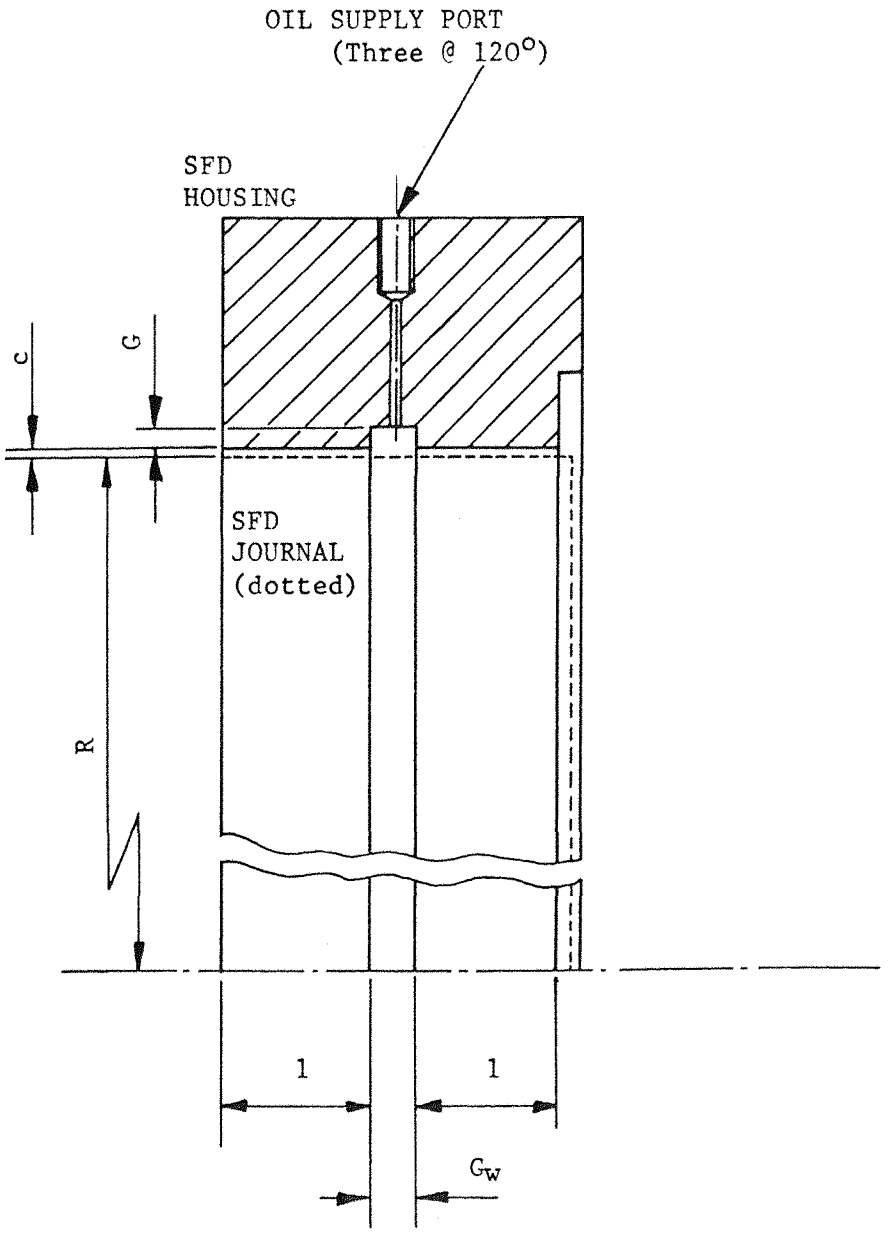

SQUEEZE-FILM DAMPER (SFD) GEOMETRY

FIGURE 6.2

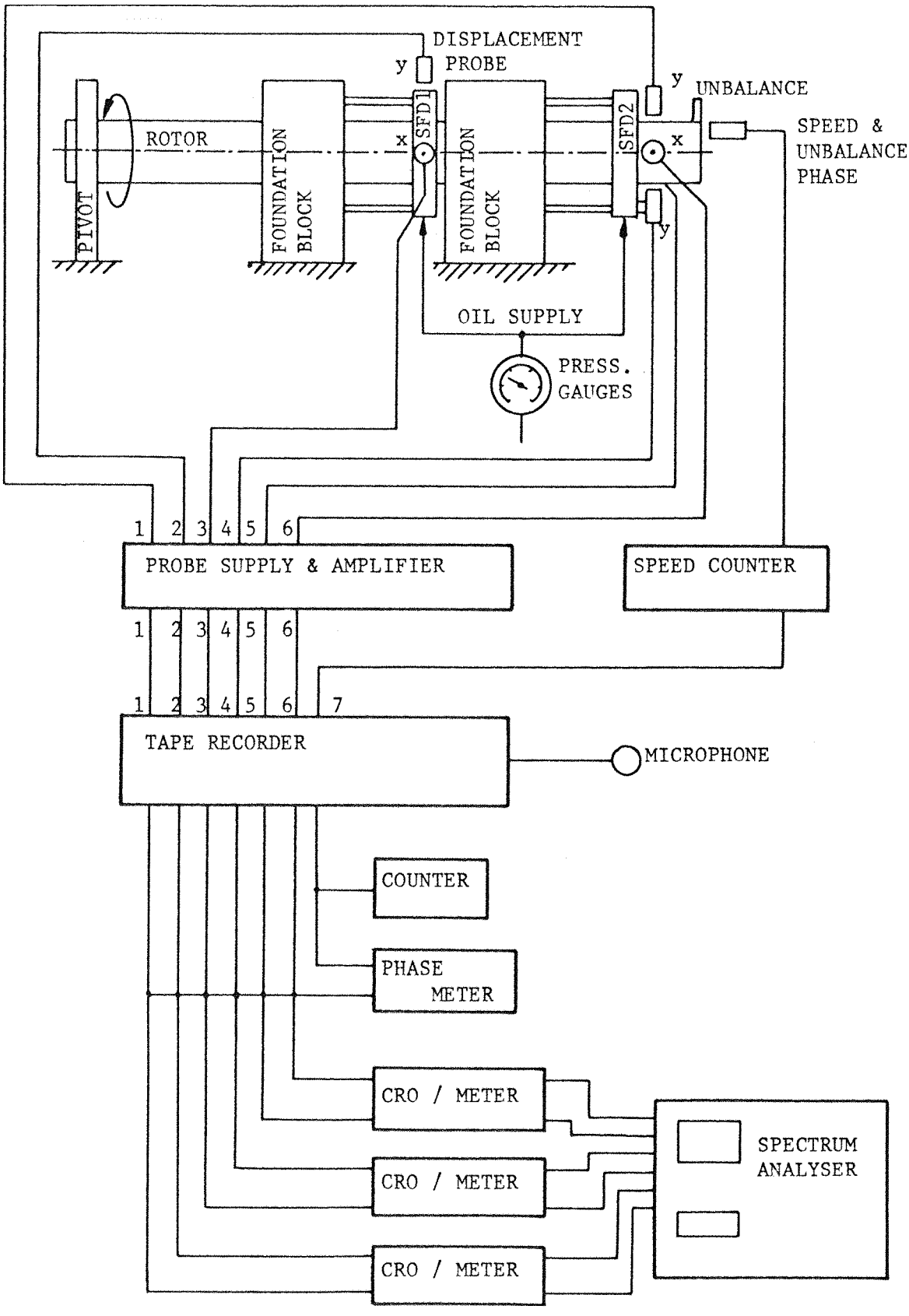

EXPERIMENTAL INSTRUMENTATION DIAGRAM

FIGURE 6.3

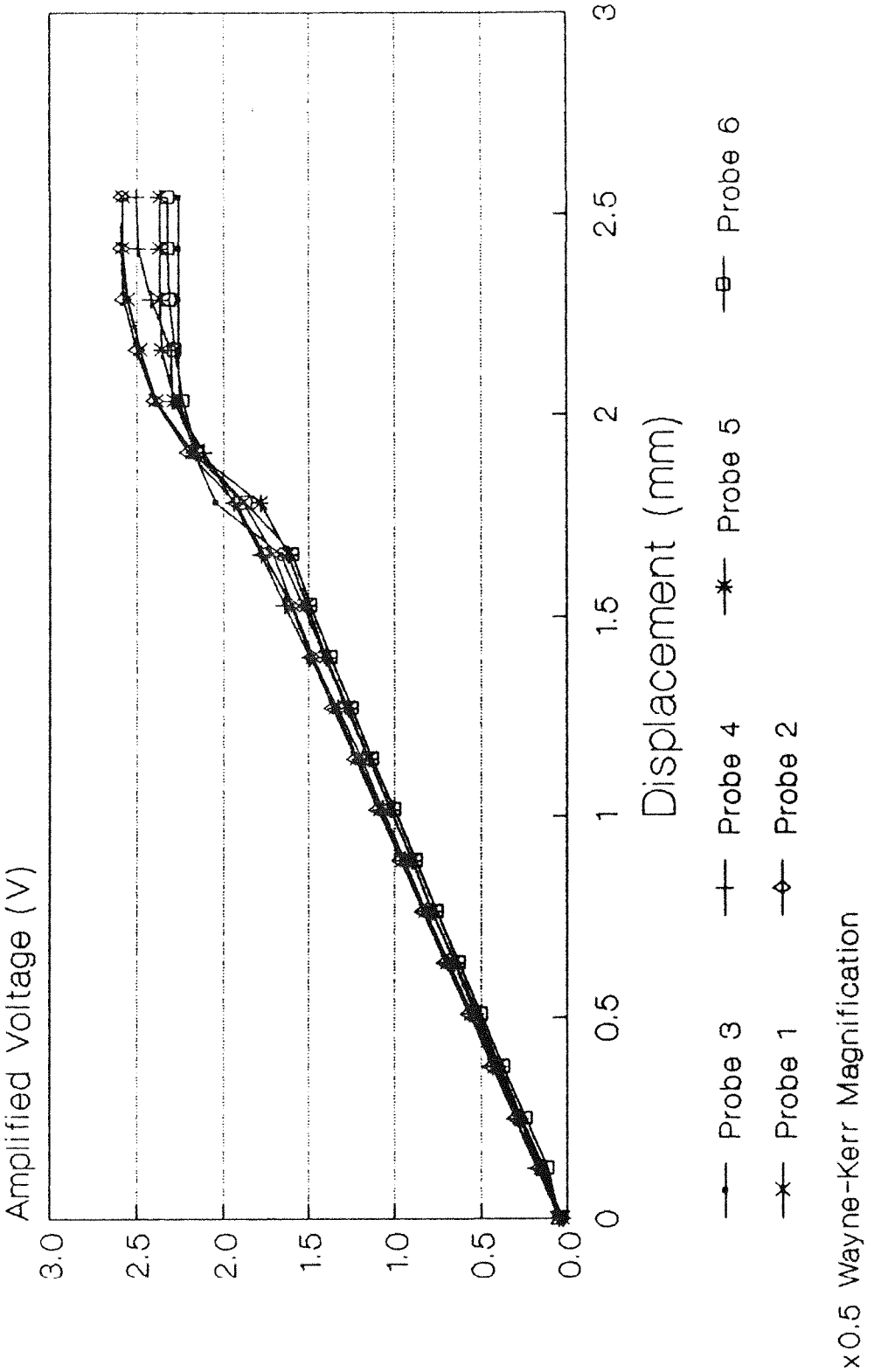

CAPACITANCE DISPLACEMENT PROBE CALIBRATION

FIGURE 6.4

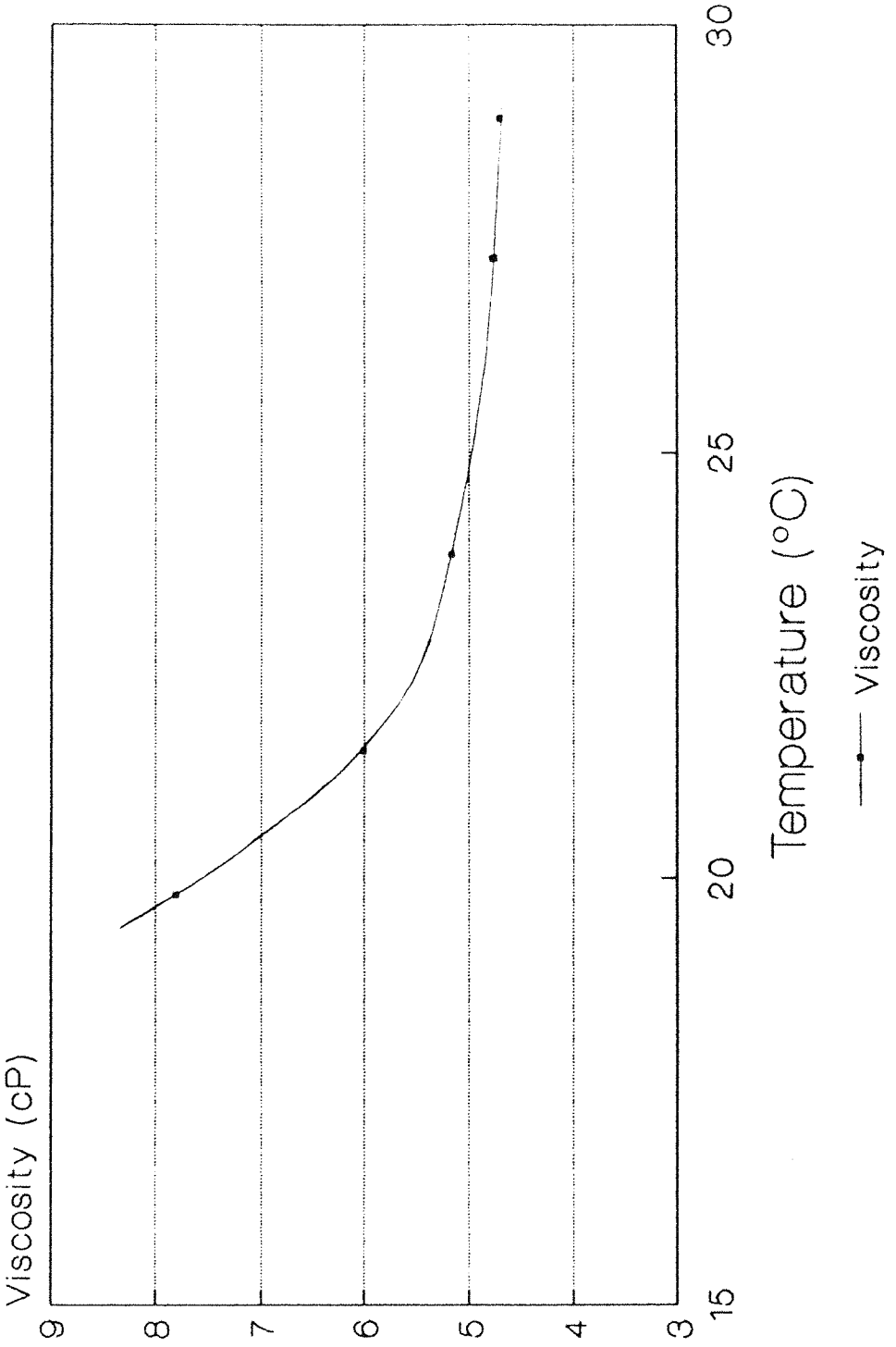

SHELL CALIBRATION FLUID 'C'

FIGURE 6.5

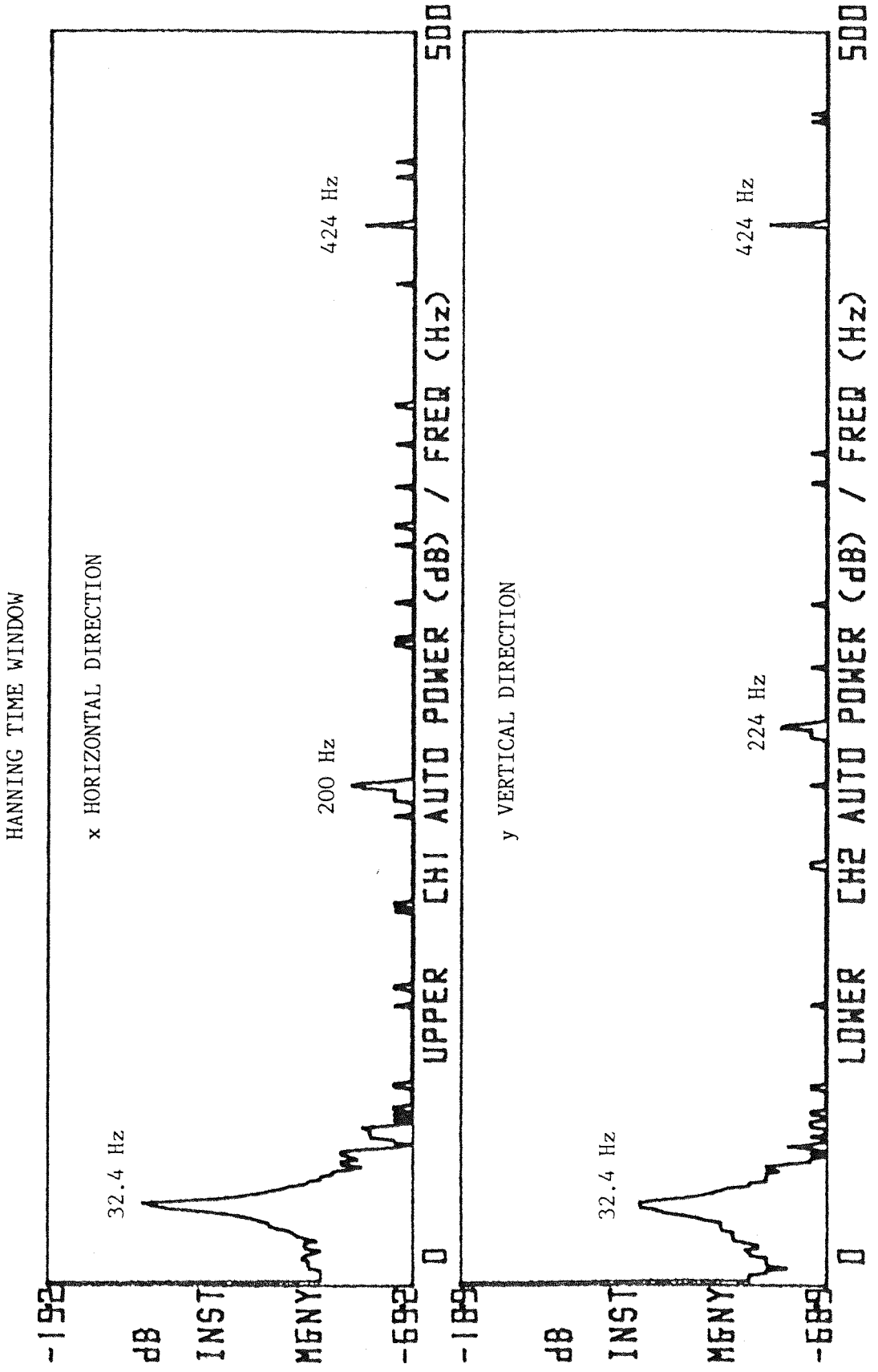

STATIONARY IMPACT TEST
Configuration 1a

FIGURE 6.6a

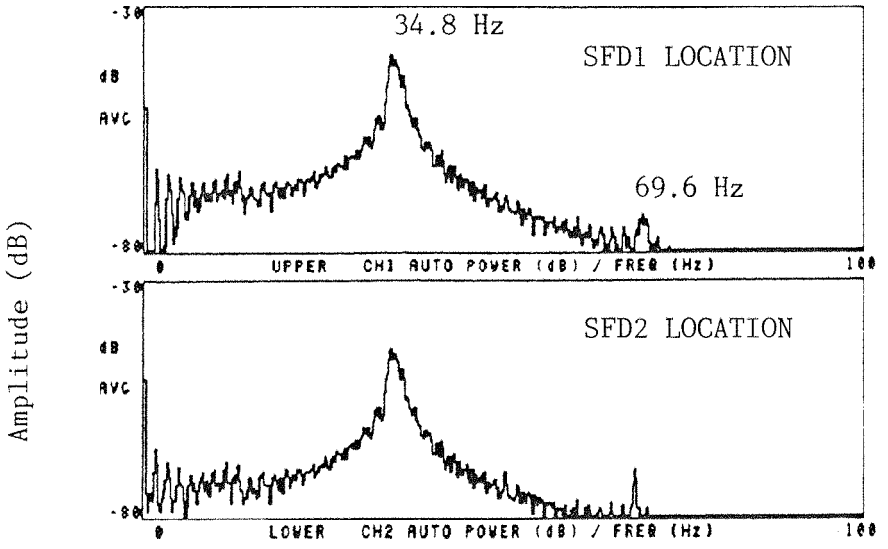

Amplitude (dB)

Frequency (Hz)

x HORIZONTAL DIRECTION

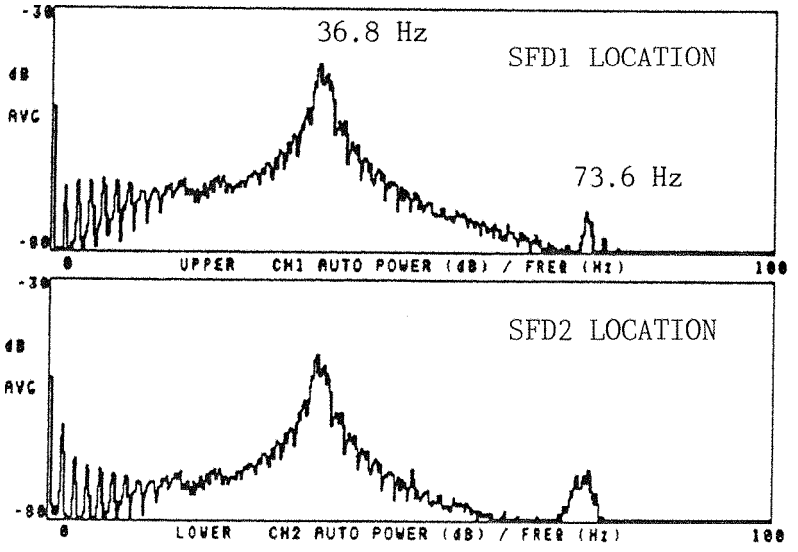

Amplitude (dB)

Frequency (Hz)

y VERTICAL DIRECTION

STATIONARY IMPACT TEST
Configuration 3a

FIGURE 6.6b

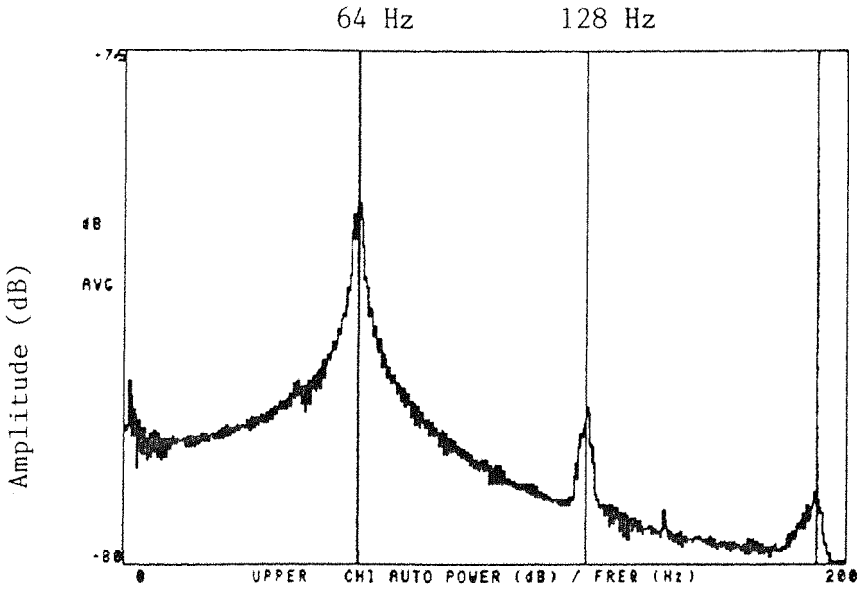

x HORIZONTAL DIRECTION

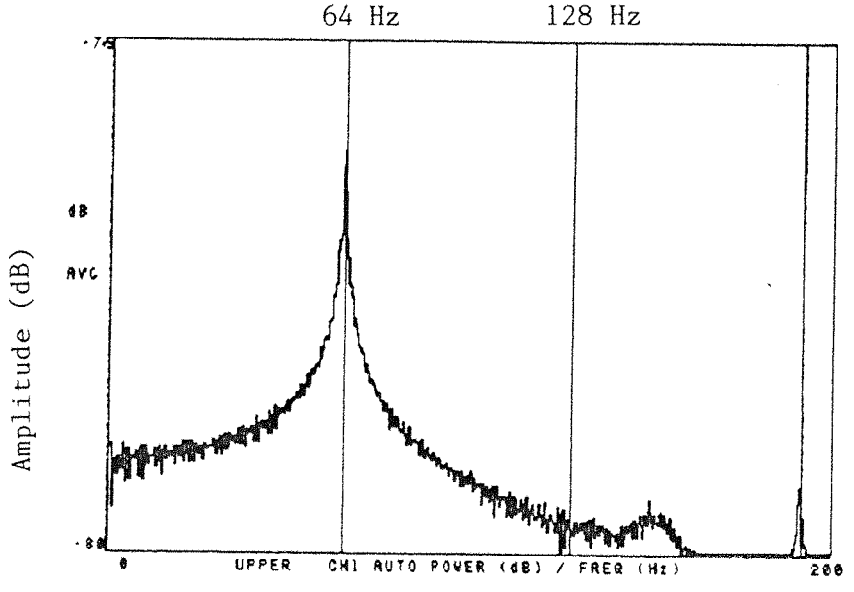

y VERTICAL DIRECTION

STATIONARY IMPACT TEST
SFD1 Flexible Housing Support Assembly

FIGURE 6.7a

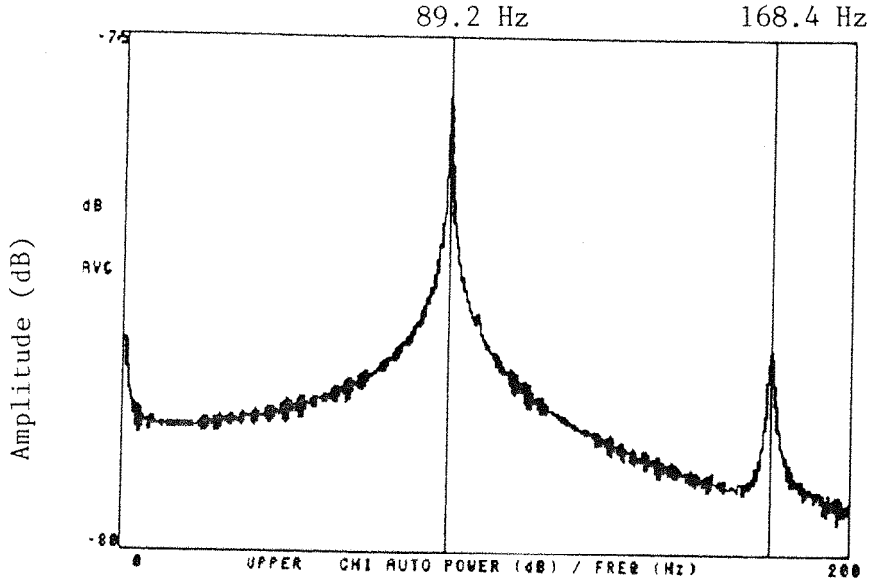

x HORIZONTAL DIRECTION

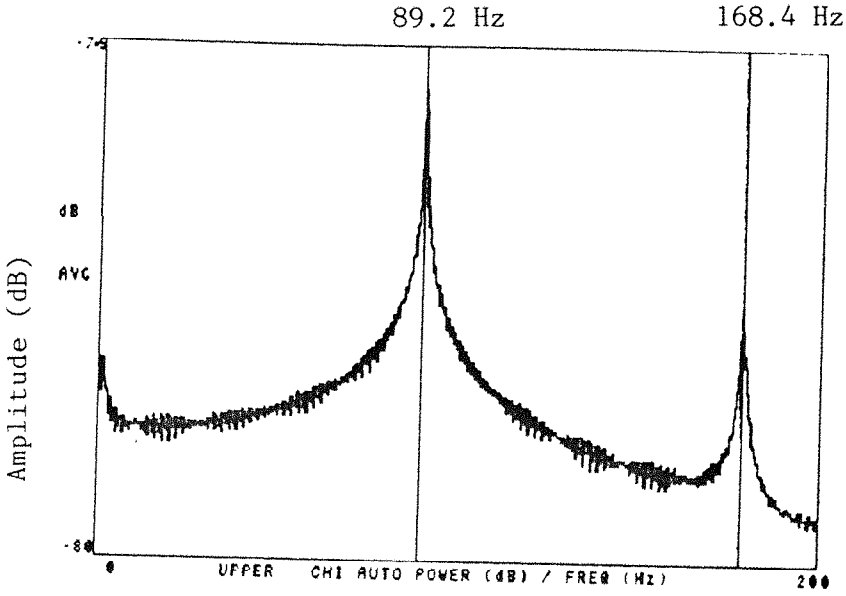

y VERTICAL DIRECTION

STATIONARY IMPACT TEST
SFD2 Flexible Housing Support Assembly

FIGURE 6.7b

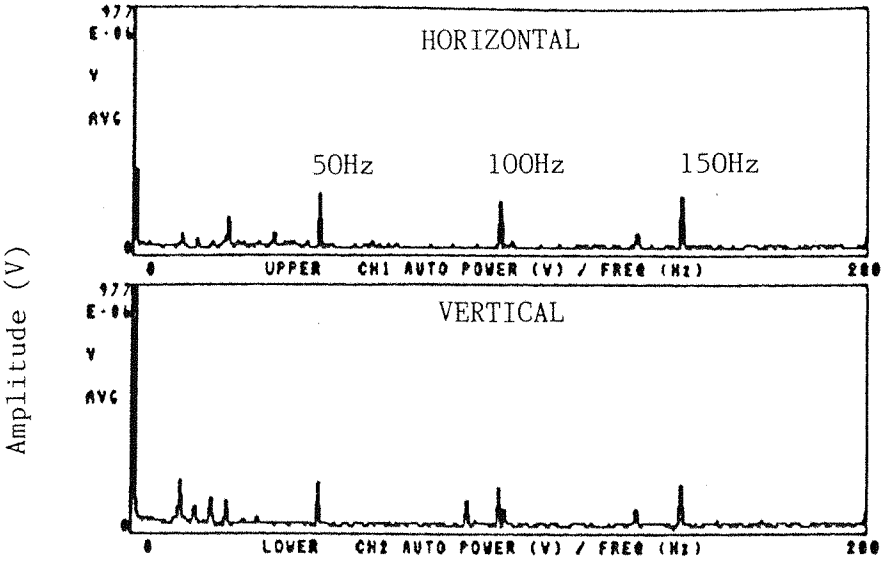

OIL UNITS ALONE

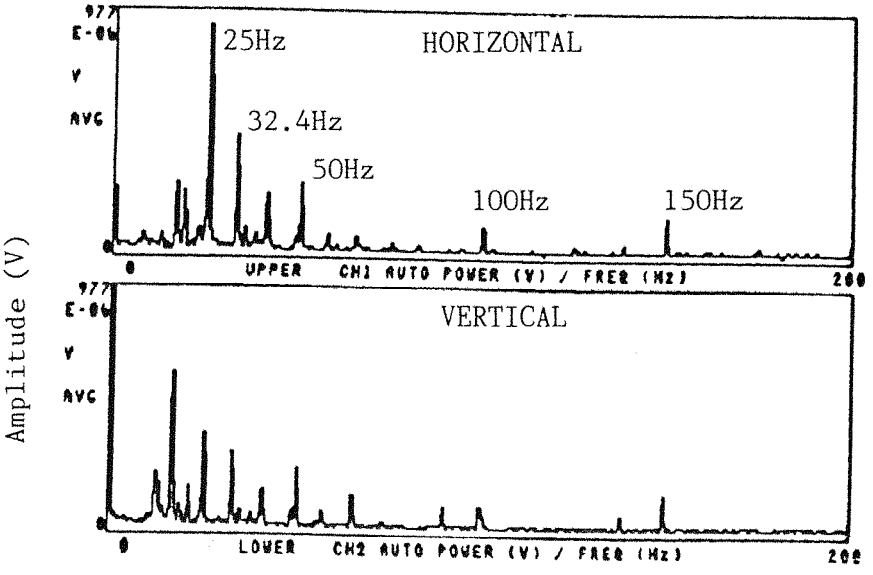

OIL UNITS & DRIVE

AUXILIARY EQUIPMENT SPECTRAL CONTRIBUTIONS

FIGURE 6.8

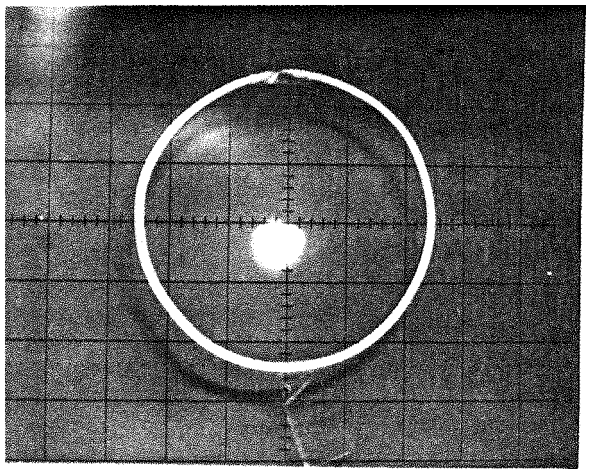

17 Hz (W/Wn = 0.525)

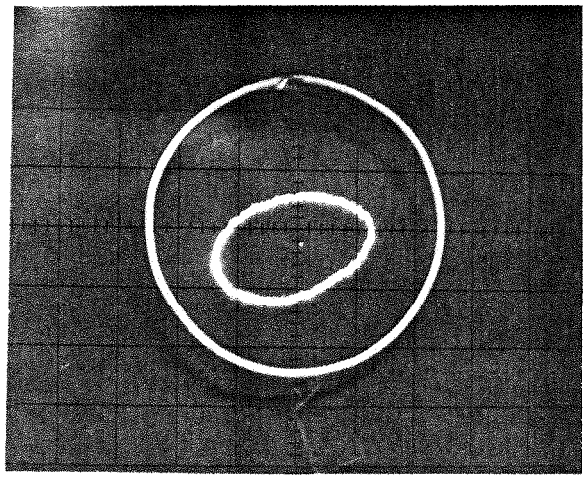

25Hz (W/Wn = 0.772)

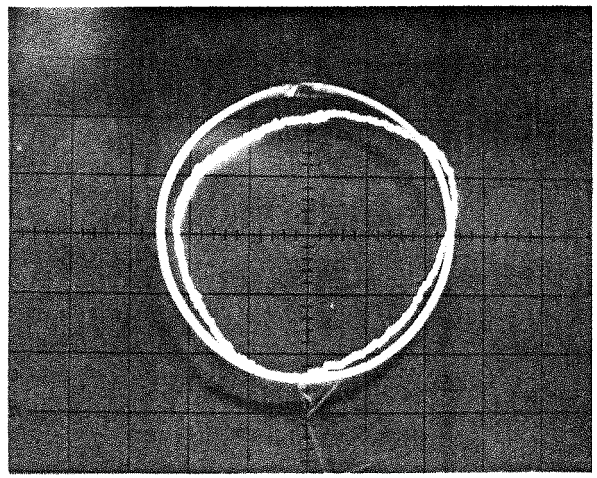

33 Hz (W/Wn = 1.019)

ROTOR SPEED

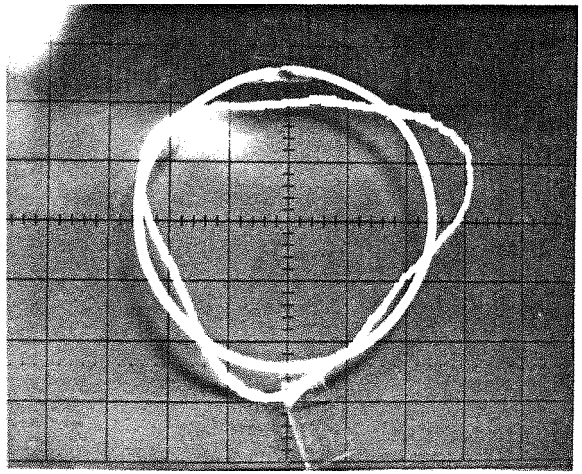

43 Hz (W/Wn = 1.327)

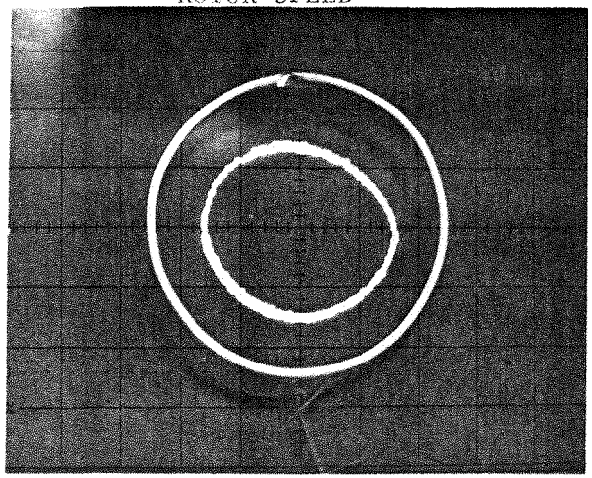

45 Hz (W/Wn = 1.389)

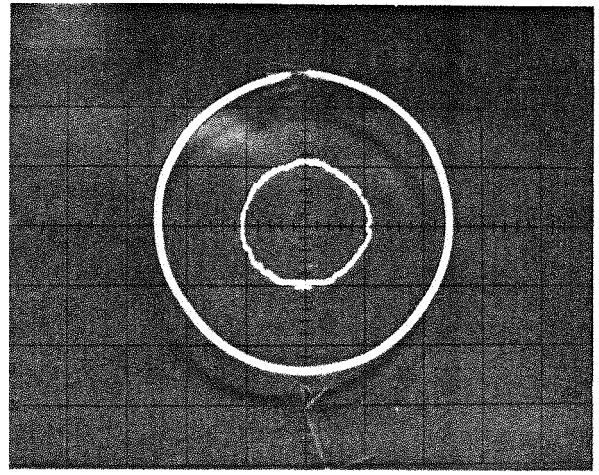

55 Hz (W/Wn = 1.698)

FIGURE 7.1

SFD1 EXPERIMENTAL ORBITS (Configuration 1a, Qc2 = 0.733, Psup = 2psi)

SQUEEZE-FILM DAMPER SFD1 (0.5mm Groove Depth)

EXPERIMENTAL RESULTS

	△	▽	×
A =	0.2132E -1	0.2132E -1	0.2132E -1
Qc2=	0.7332E 0	0.4901E 0	0.2450E 0
Eo =	0.0000E 0	0.0000E 0	0.0000E 0
Psup=	0.2000E 1	0.2000E 1	0.2000E 1 (psi)

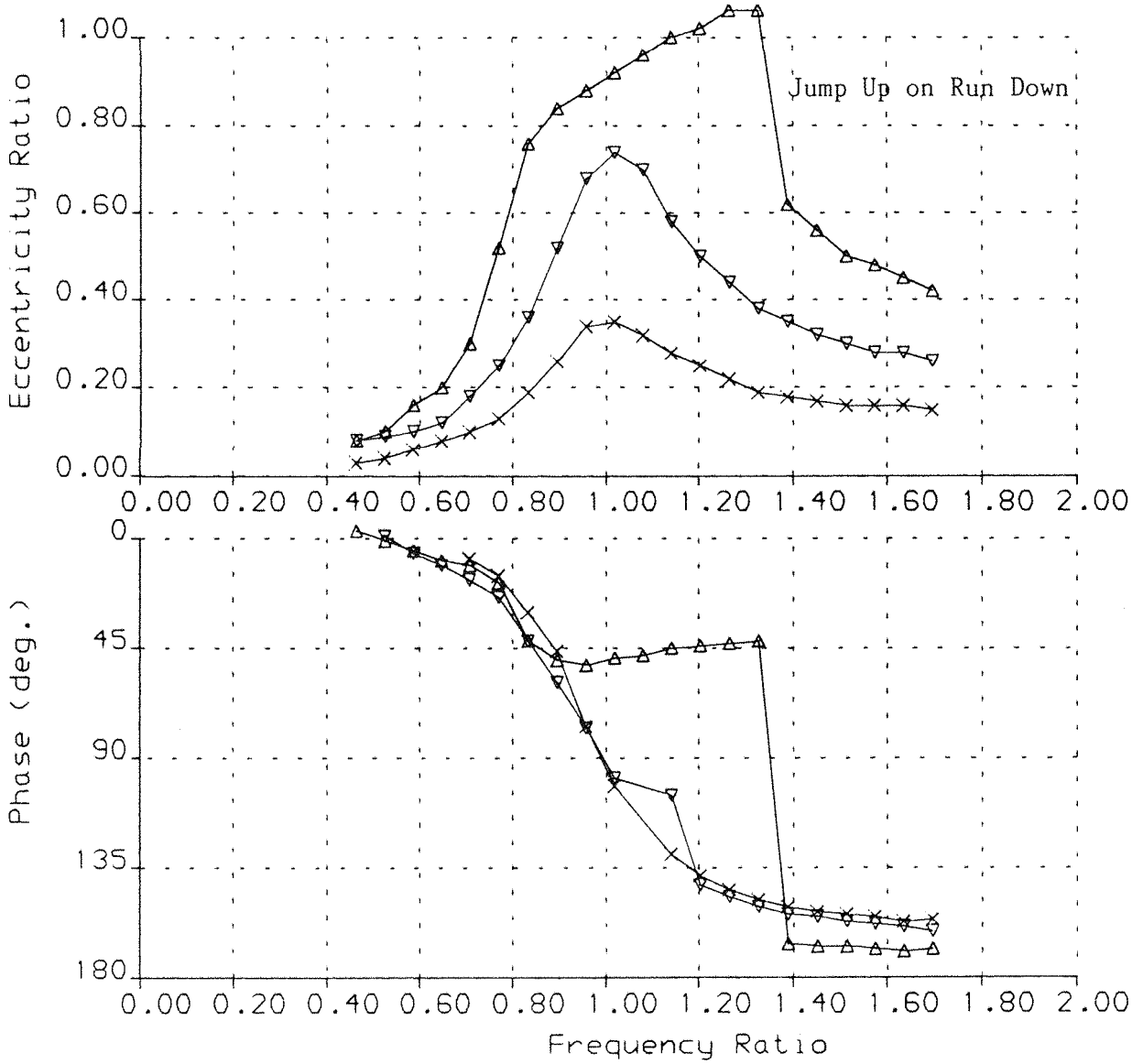

ROTOR-BEARING ASSEMBLY RESPONSE TO UNBALANCE
SQUEEZE-FILM DAMPER RESEARCH Rig Config. 1a

FIGURE 7.2

SQUEEZE-FILM DAMPER SFD1 (0.5mm Groove Depth)

EXPERIMENTAL RESULTS

	△	▽	×
A =	0.2132E -1	0.2132E -1	0.2132E -1
Qc2=	0.7332E 0	0.4901E 0	0.2450E 0
Eo =	0.0000E 0	0.0000E 0	0.0000E 0
Psup=	0.6000E 1	0.6000E 1	0.6000E 1 (psi

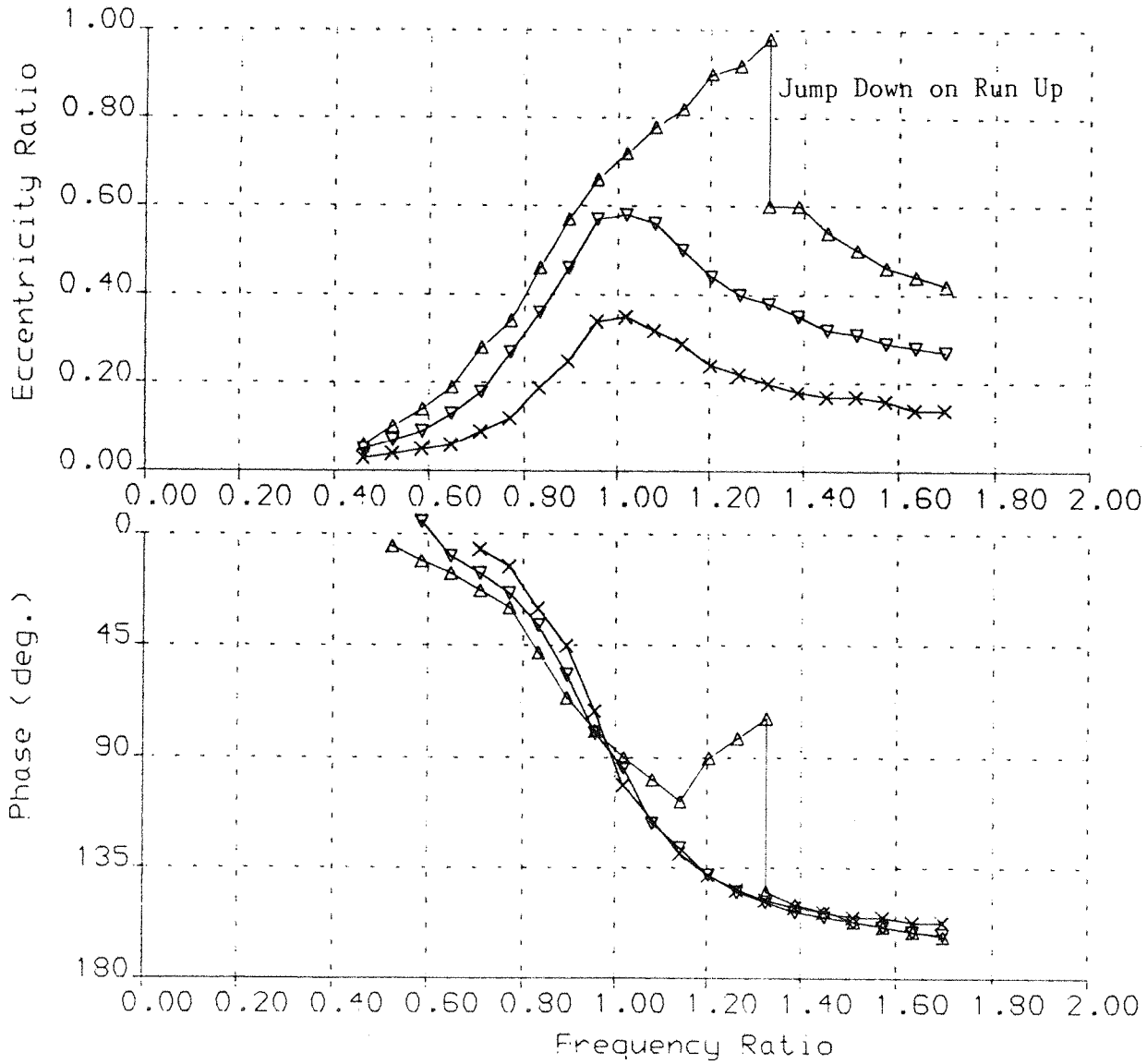

ROTOR-BEARING ASSEMBLY RESPONSE TO UNBALANCE
SQUEEZE-FILM DAMPER RESEARCH Rig Config. 1a

FIGURE 7.3

SQUEEZE-FILM DAMPER SFD1 (2mm Groove Depth)

EXPERIMENTAL RESULTS

	△	▽	×	□
A =	0.2132E -1	0.2132E -1	0.2132E -1	0.2132E -1
Qc2=	0.7332E 0	0.6107E 0	0.6107E 0	0.4901E 0
Eo =	0.0000E 0	0.0000E 0	0.0000E 0	0.0000E 0
Psup=	0.6000E 1	0.6000E 1	0.2000E 2	0.2000E 1 (psi

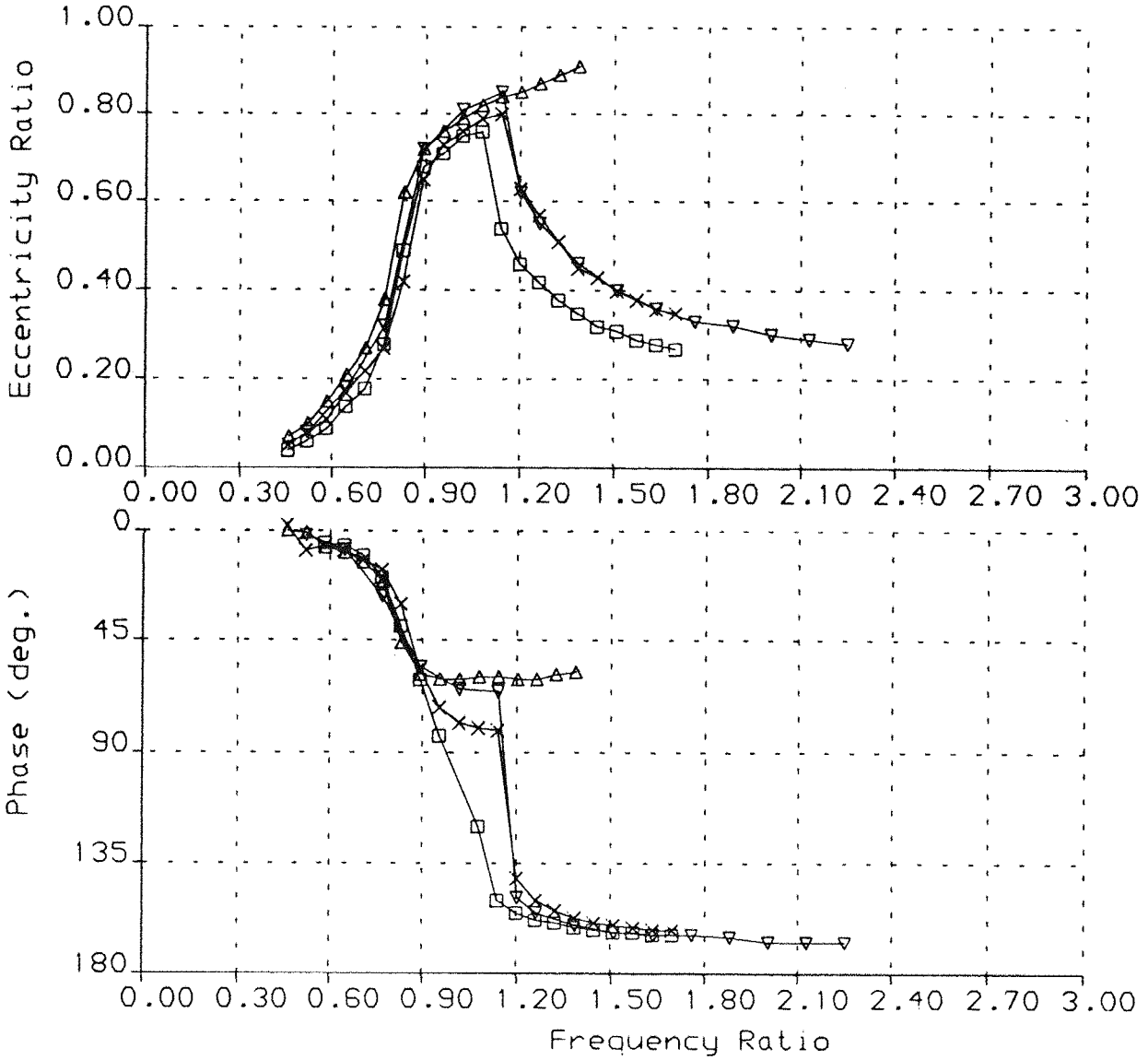

ROTOR-BEARING ASSEMBLY RESPONSE TO UNBALANCE
SQUEEZE-FILM DAMPER RESEARCH Rig Config. 1a

FIGURE 7.4

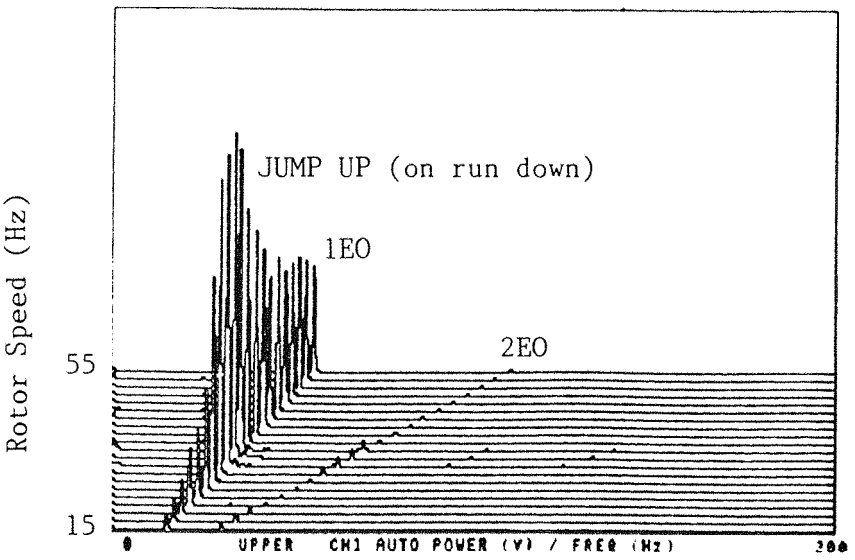

Frequency (Hz)

(Linear Amplitude)

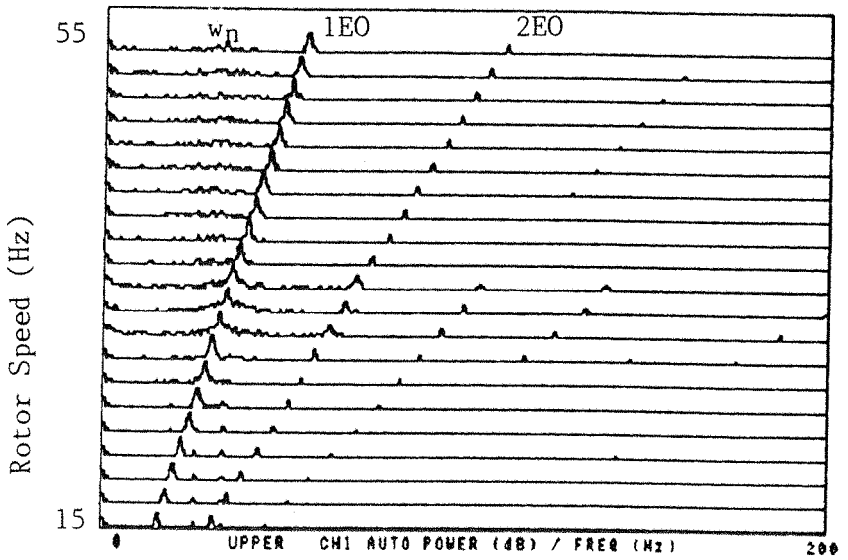

Frequency (Hz)
(dB Amplitude)

EXPERIMENTAL WATERFALL DIAGRAMS

Configuration 1a (Q_{c_2} =0.490, Psup=2psi, Eo_1=0)

FIGURE 7.5

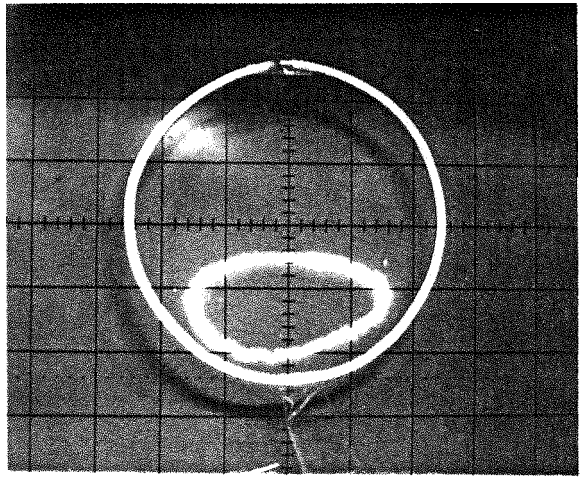

29 Hz (W/Wn = 0.895)

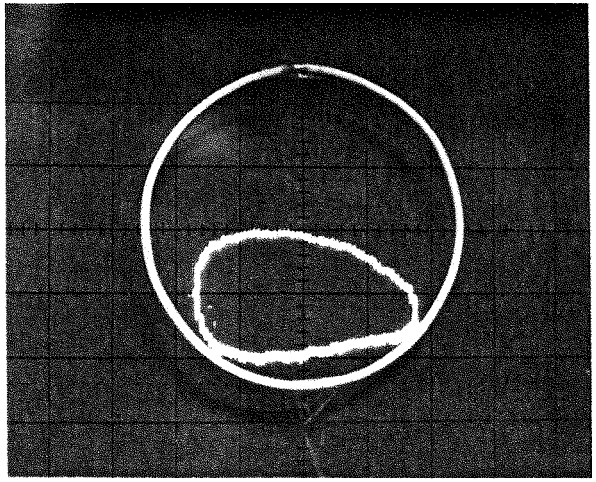

33 Hz (W/Wn = 1.019)

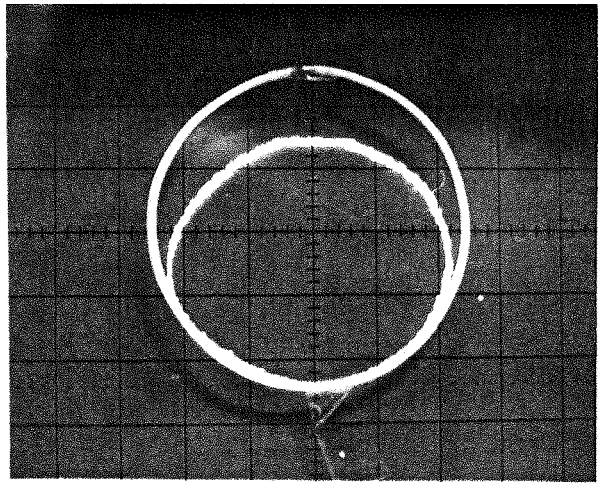

41 Hz (W/Wn = 1.265)

ROTOR SPEED

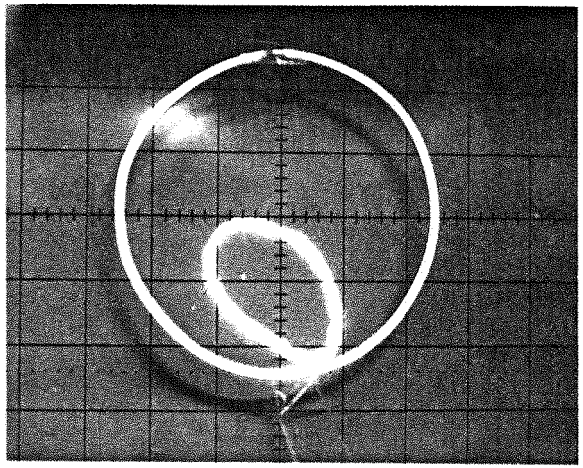

43 Hz (W/Wn = 1.327)

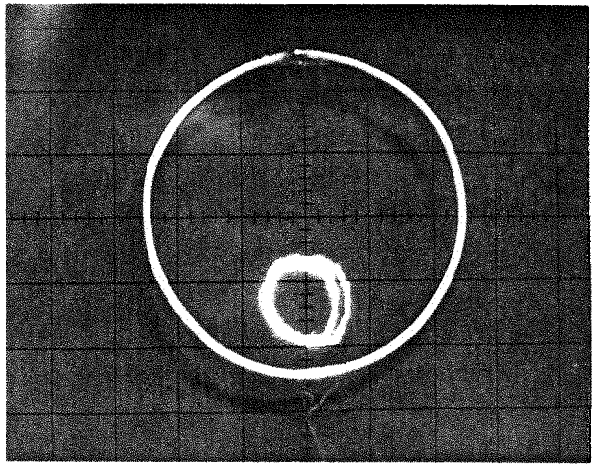

65 Hz (W/Wn = 2.006)

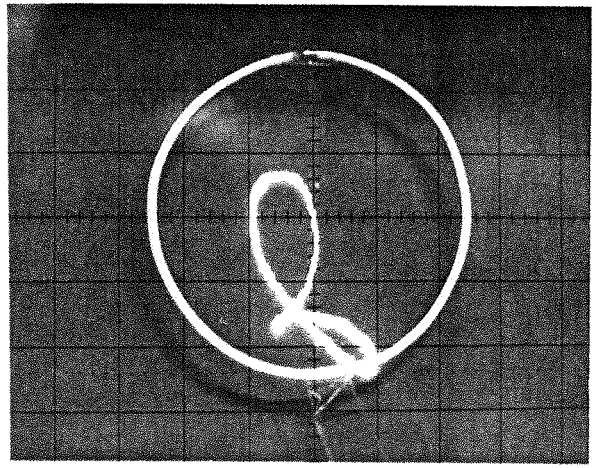

73 Hz (W/Wn = 2.253)

FIGURE 7.6

SFD1 EXPERIMENTAL ORBITS (Configuration 1b, Qc2 = 0.490, Psup = 2psi, Eol = 0.8)

SQUEEZE-FILM DAMPER SFD1 (2mm Groove Depth)

EXPERIMENTAL RESULTS

	△	▽	×	□
A =	0.2132E -1	0.2132E -1	0.2132E -1	0.2132E -1
Qc2=	0.6107E 0	0.4901E 0	0.6107E 0	0.4901E 0
Eo =	0.8000E 0	0.8000E 0	0.4000E 0	0.4000E 0
Psup=	0.2000E 2	0.2000E 1	0.2000E 2	0.2000E 1 (psi

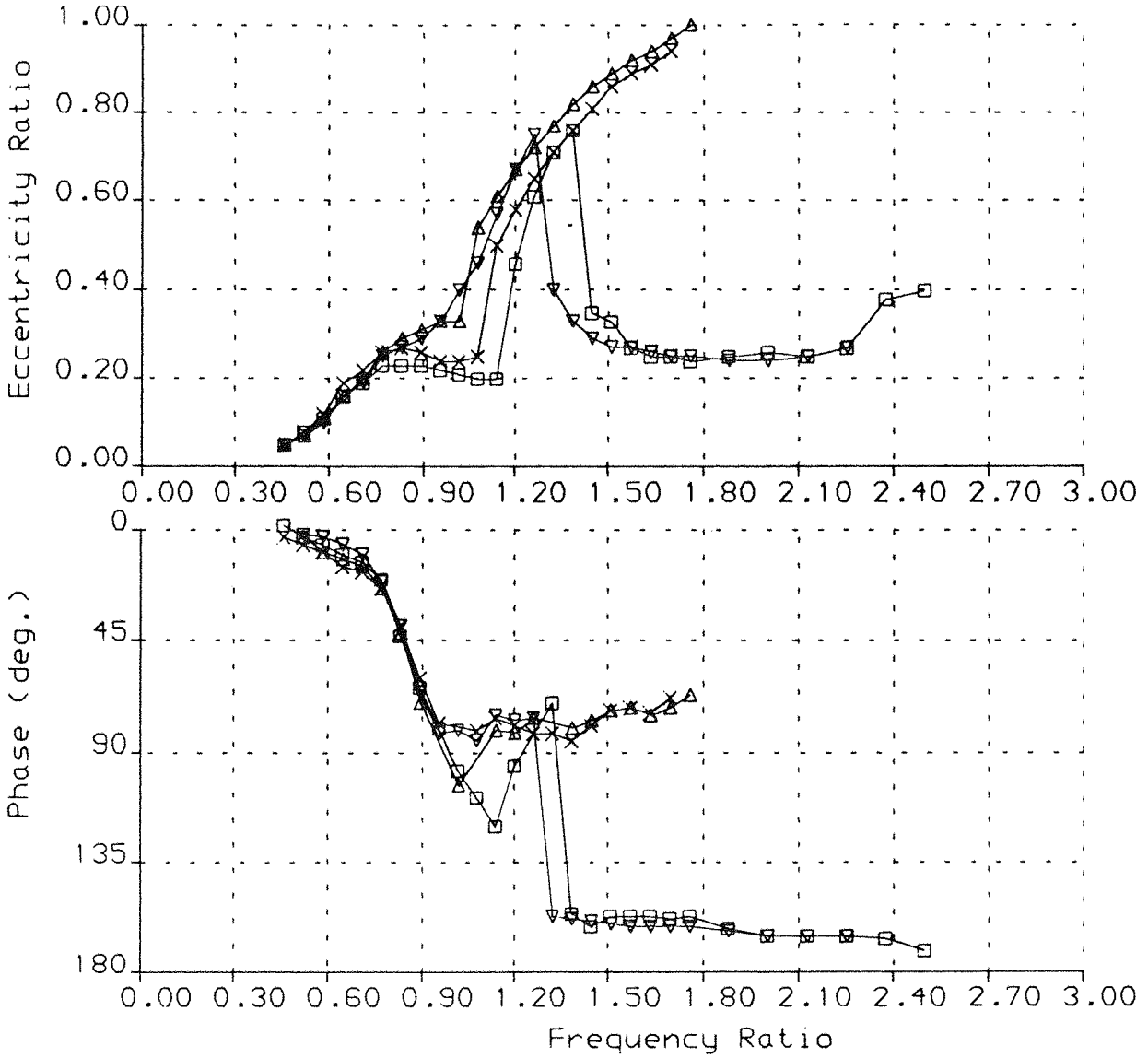

ROTOR-BEARING ASSEMBLY RESPONSE TO UNBALANCE
SQUEEZE-FILM DAMPER RESEARCH Rig Config. 1b

FIGURE 7.7

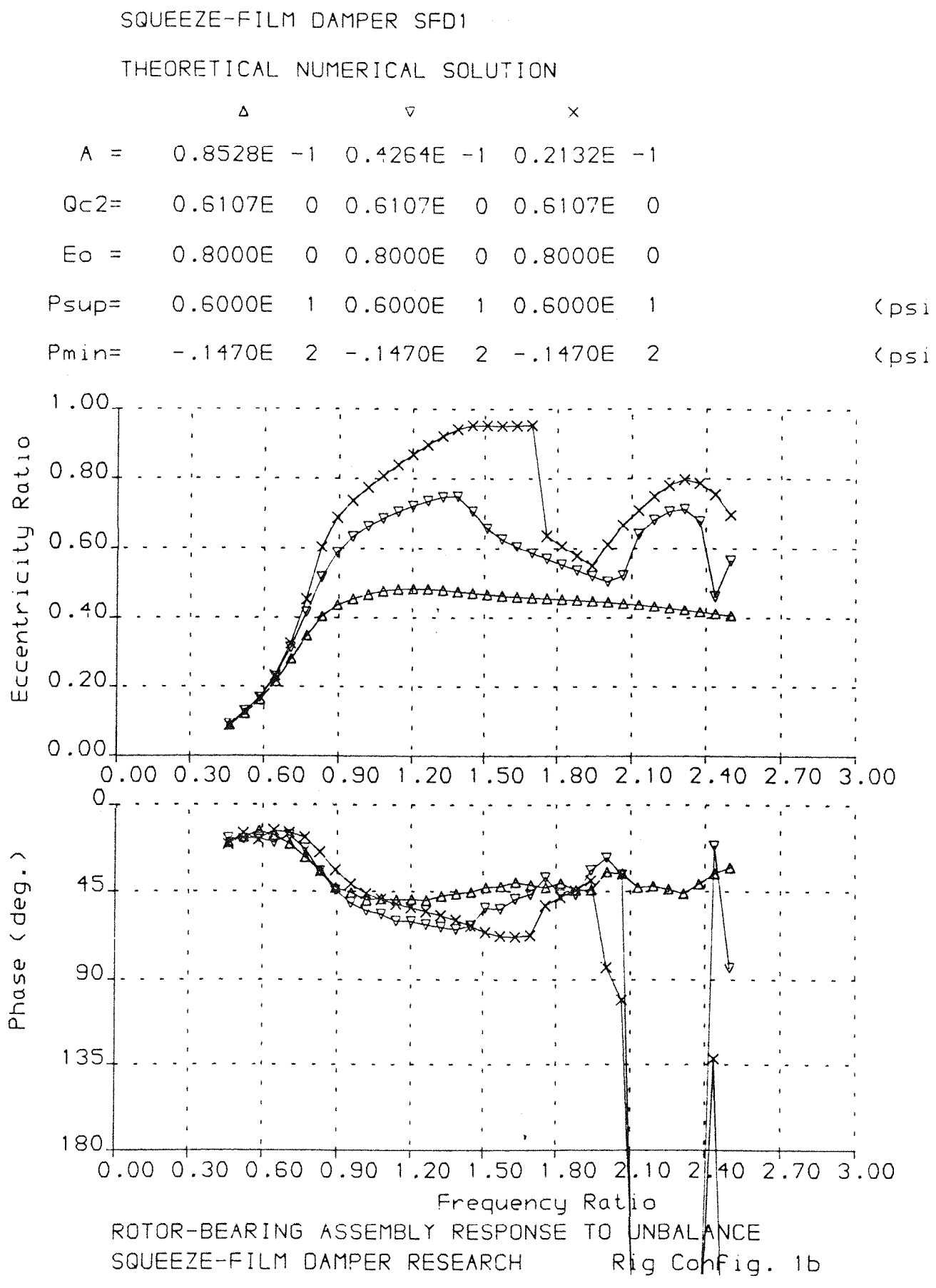
SQUEEZE-FILM DAMPER SFD1
THEORETICAL NUMERICAL SOLUTION
Δ ▽ ×
A = 0.8528E -1 0.4264E -1 0.2132E -1
Qc2= 0.6107E 0 0.6107E 0 0.6107E 0
Eo = 0.8000E 0 0.8000E 0 0.8000E 0
Psup= 0.6000E 1 0.6000E 1 0.6000E 1 (psi
Pmin= -.1470E 2 -.1470E 2 -.1470E 2 (psi
Eccentricity Ratio
1.00
0.80
0.60
0.40
0.20
0.00
0.00 0.30 0.60 0.90 1.20 1.50 1.80 2.10 2.40 2.70 3.00
Phase (deg.)
0
45
90
135
180
0.00 0.30 0.60 0.90 1.20 1.50 1.80 2.10 2.40 2.70 3.00
Frequency Ratio
ROTOR-BEARING ASSEMBLY RESPONSE TO UNBALANCE
SQUEEZE-FILM DAMPER RESEARCH Rig Config. 1b

FIGURE 7.8

SQUEEZE-FILM DAMPER SFD1

THEORETICAL NUMERICAL SOLUTION

	△	▽	×	
A =	0.2132E -1	0.2132E -1	0.2132E -1	
Qc2=	0.6107E 0	0.6107E 0	0.6107E 0	
Eo =	0.8000E 0	0.8000E 0	0.8000E 0	
Psup=	0.6000E 1	0.6000E 1	0.6000E 1	(psi
Pmin=	0.0000E 0	-.1470E 2	-.3000E 2	(psi

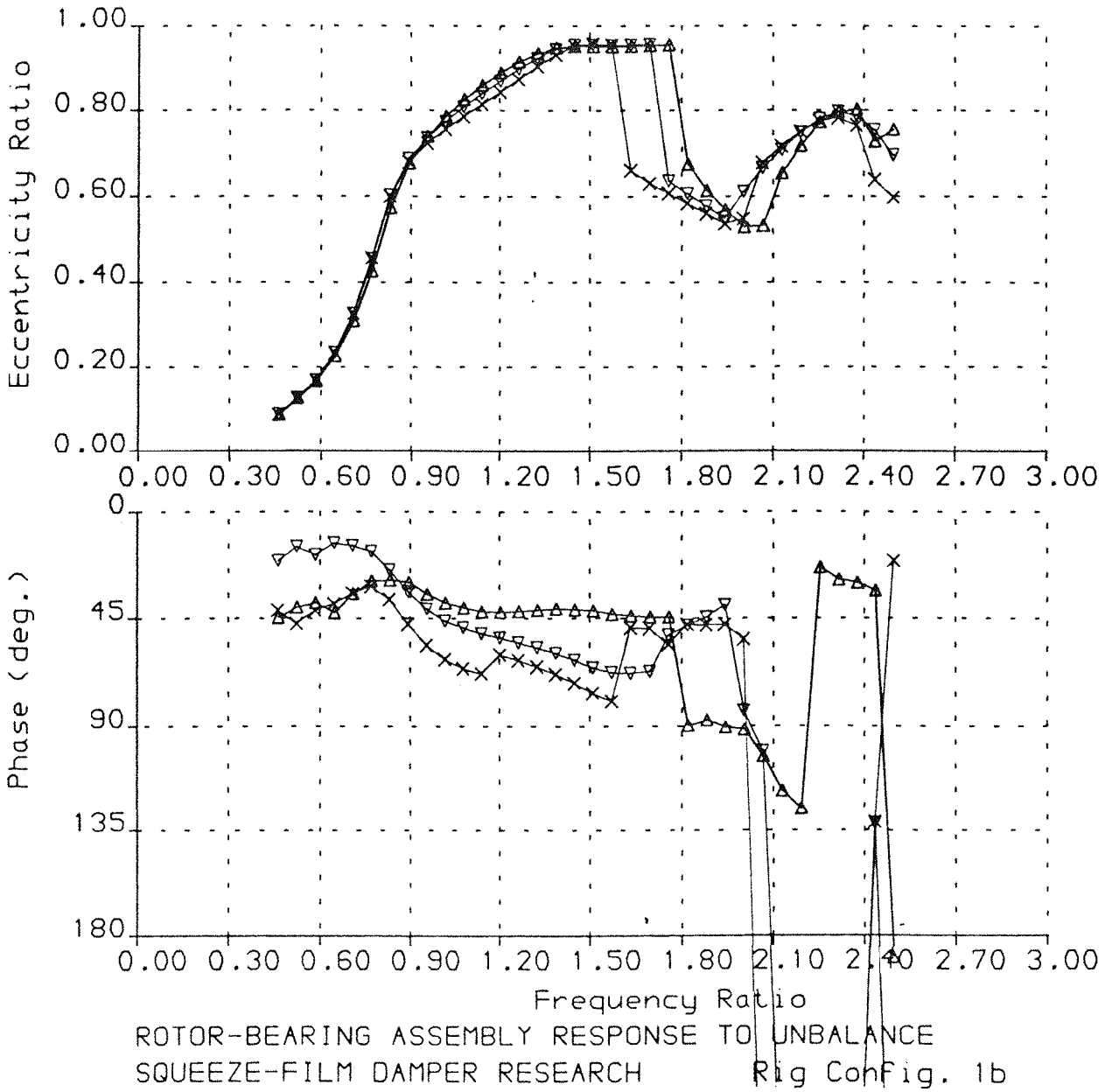

ROTOR-BEARING ASSEMBLY RESPONSE TO UNBALANCE

SQUEEZE-FILM DAMPER RESEARCH Rig Config. 1b

FIGURE 7.9

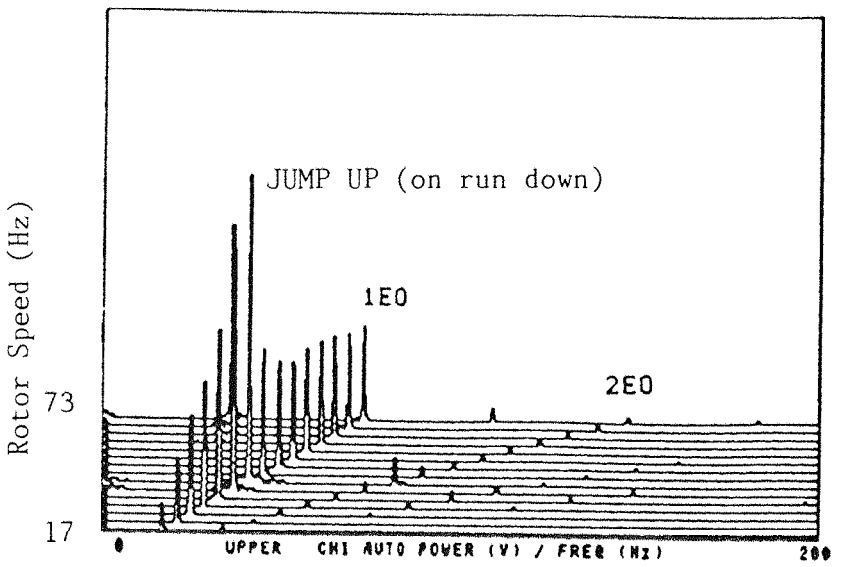

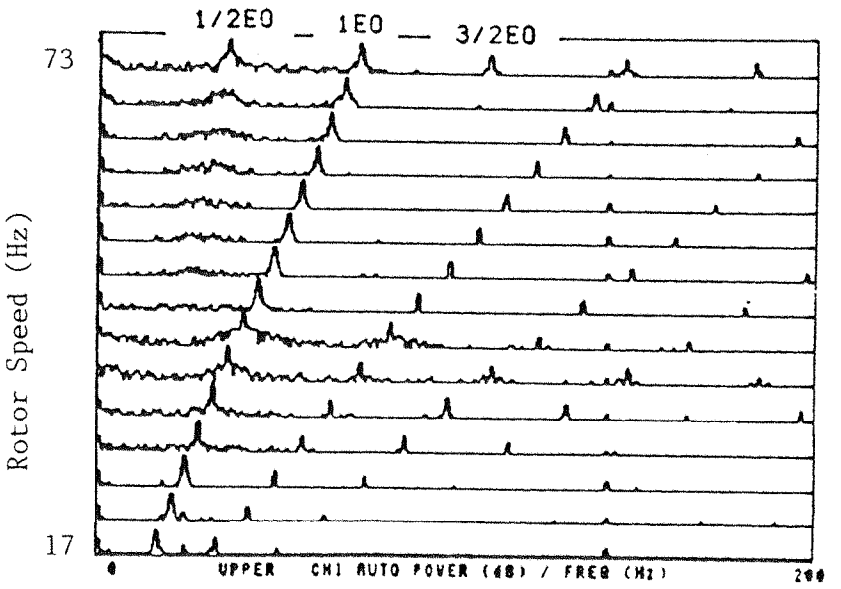

EXPERIMENTAL WATERFALL DIAGRAMS

Configuration 1b (Qc_2=0.490,Psup=2psi, Eo_1=0.8)

FIGURE 7.10

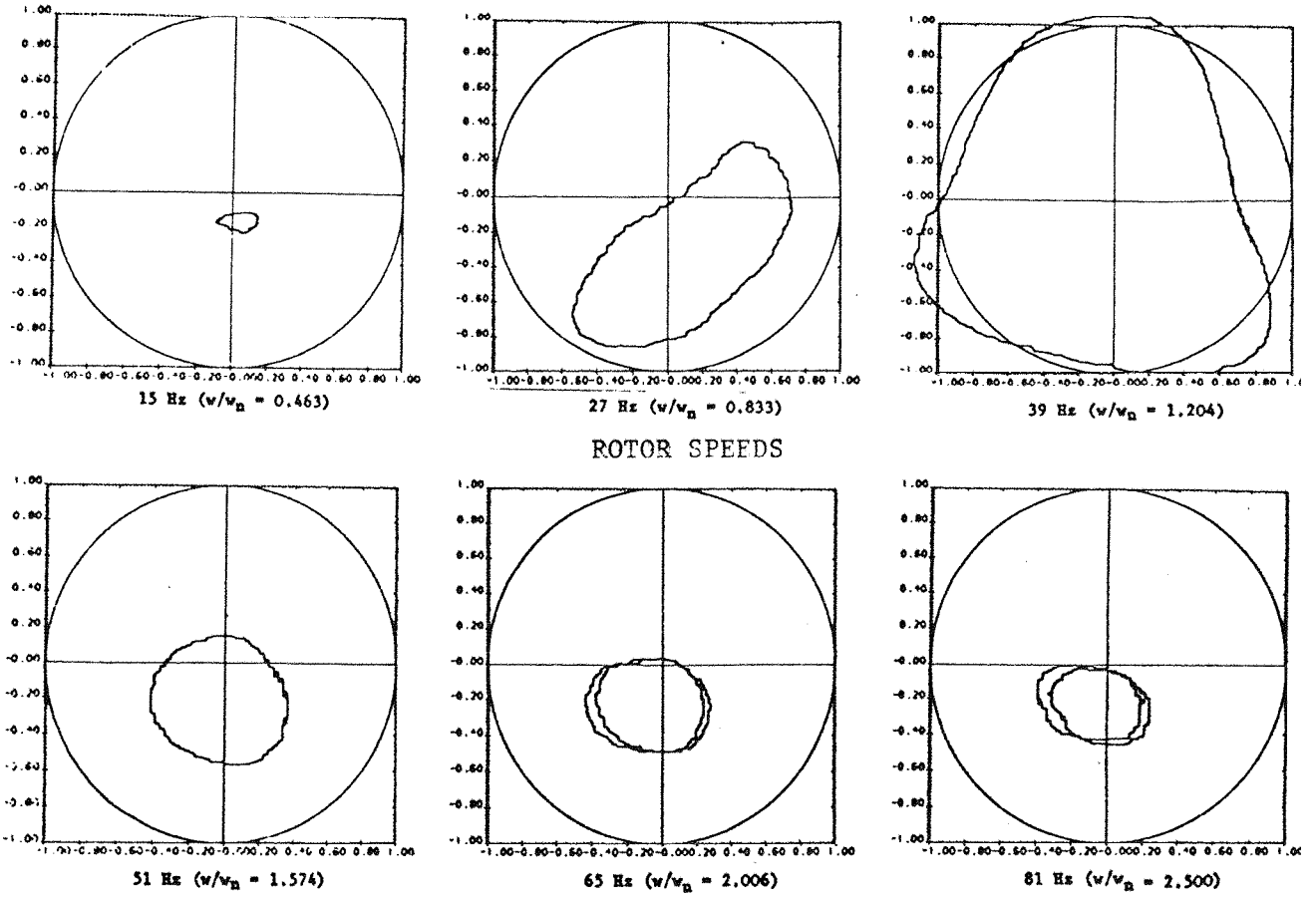

(a) SFD1 EXPERIMENTAL ORBITS

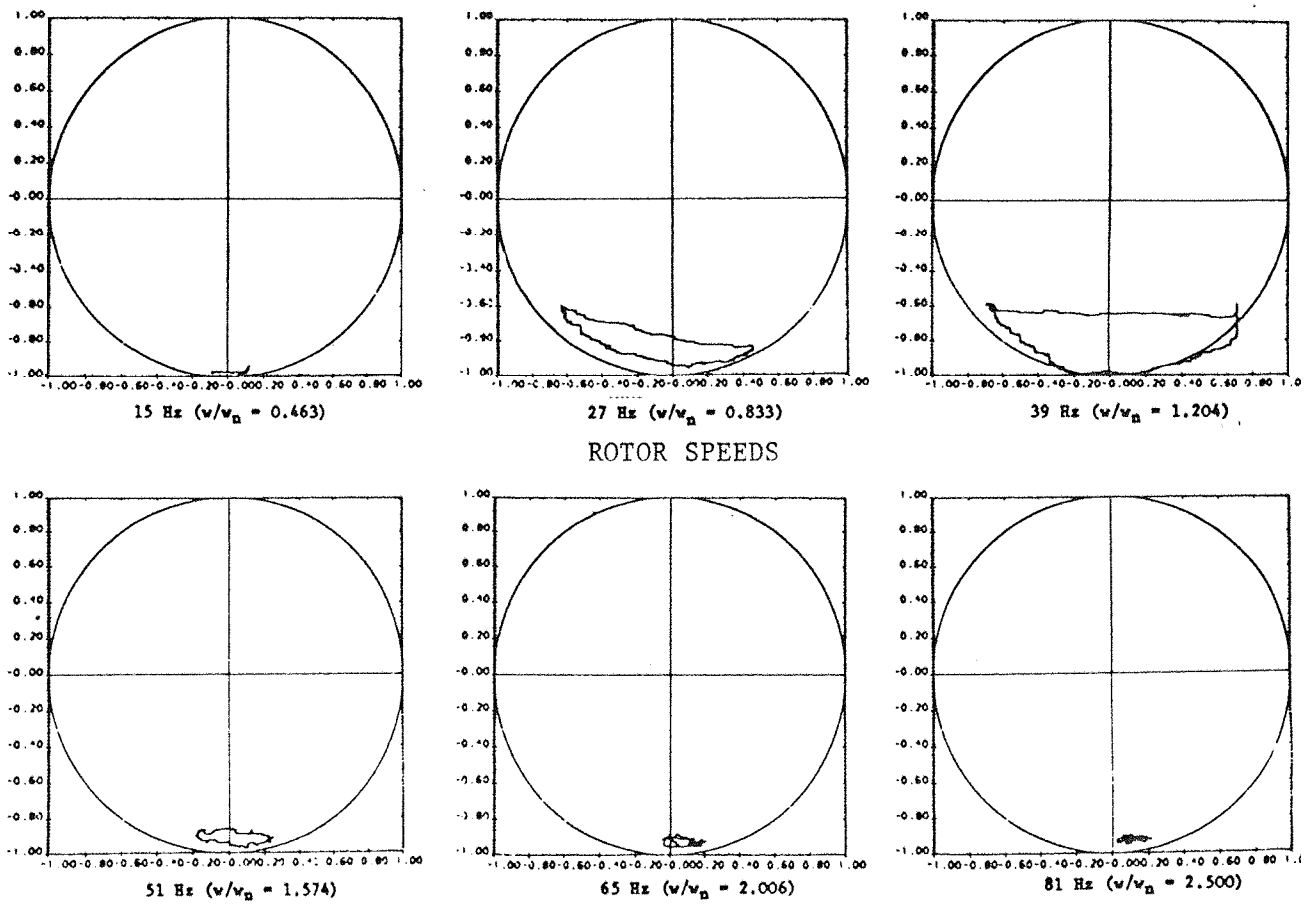

(b) SFD2 EXPERIMENTAL ORBITS

CONFIGURATION 2a (Q_{c_2} = 0.611, Psup = 2 psi, E_{o_1} = 0.0)

FIGURE 7.11

(a)

SQUEEZE-FILM DAMPER SFD1 (2mm Groove Depth)

EXPERIMENTAL RESULTS

	△	▽	×	□	
A =	0.2132E -1	0.2132E -1	0.2132E -1	0.2132E -1	
Qc2=	0.7332E 0	0.6107E 0	0.4901E 0	0.2450E 0	
Eo =	0.0000E 0	0.0000E 0	0.0000E 0	0.0000E 0	
Psup=	0.2000E 1	0.2000E 1	0.2000E 1	0.2000E 1	(psi)

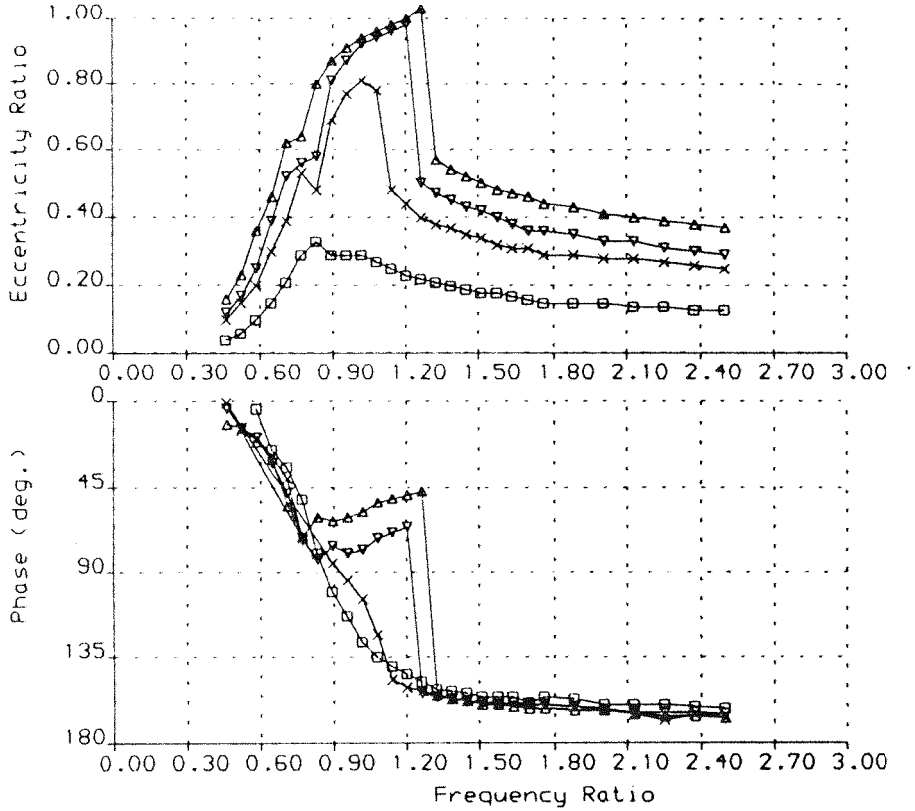

ROTOR-BEARING ASSEMBLY RESPONSE TO UNBALANCE

SQUEEZE-FILM DAMPER RESEARCH Rig Config. 2a

(b)

SQUEEZE-FILM DAMPER SFD2 (2mm Groove Depth)

EXPERIMENTAL RESULTS

	△	▽	×	□	
A =	0.4010E -1	0.4010E -1	0.4010E -1	0.4010E -1	
Qc2=	0.7332E 0	0.6107E 0	0.4901E 0	0.2450E 0	
Eo =	0.1000E 1	0.1000E 1	0.1000E 1	0.1000E 1	
Psup=	0.2000E 1	0.2000E 1	0.2000E 1	0.2000E 1	(psi)

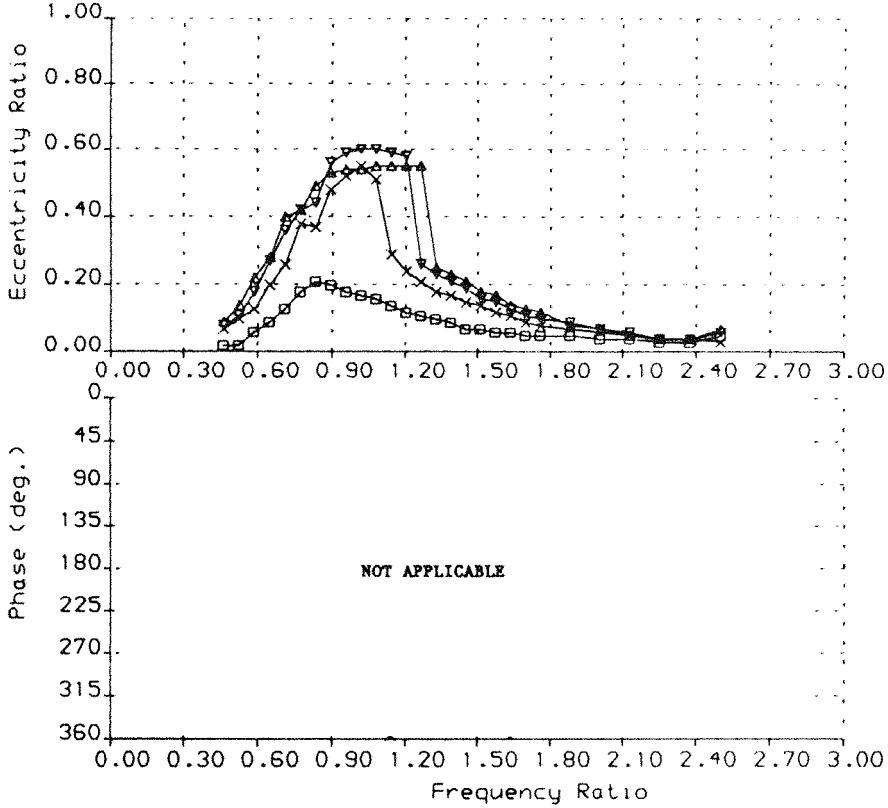

ROTOR-BEARING ASSEMBLY RESPONSE TO UNBALANCE

SQUEEZE-FILM DAMPER RESEARCH Rig Config. 2a

FIGURE 7.12

(a)

SQUEEZE-FILM DAMPER SFD1 (2mm Groove Depth)

EXPERIMENTAL RESULTS

	△	▽	×	□	
A =	0.2132E -1	0.2132E -1	0.2132E -1	0.2132E -1	
Qc2=	0.7332E 0	0.6107E 0	0.4901E 0	0.2450E 0	
Eo =	0.0000E 0	0.0000E 0	0.0000E 0	0.0000E 0	
Psup=	0.1500E 2	0.1500E 2	0.1400E 2	0.1400E 2	(psi)

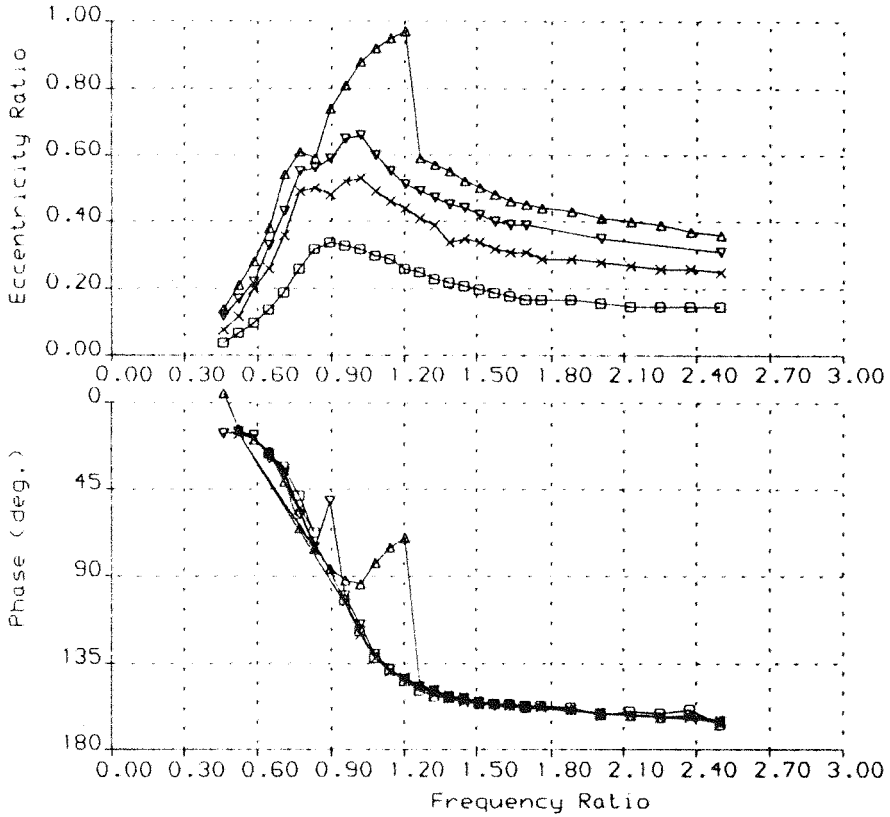

ROTOR-BEARING ASSEMBLY RESPONSE TO UNBALANCE
SQUEEZE-FILM DAMPER RESEARCH Rig Config. 2a

(b)

SQUEEZE-FILM DAMPER SFD2 (2mm Groove Depth)

EXPERIMENTAL RESULTS

	△	▽	×	□	
A =	0.4010E -1	0.4010E -1	0.4010E -1	0.4010E -1	
Qc2=	0.7332E 0	0.6107E 0	0.4901E 0	0.2450E 0	
Eo =	0.1000E 1	0.1000E 1	0.1000E 1	0.1000E 1	
Psup=	0.1500E 2	0.1500E 2	0.1400E 2	0.1400E 2	(psi)

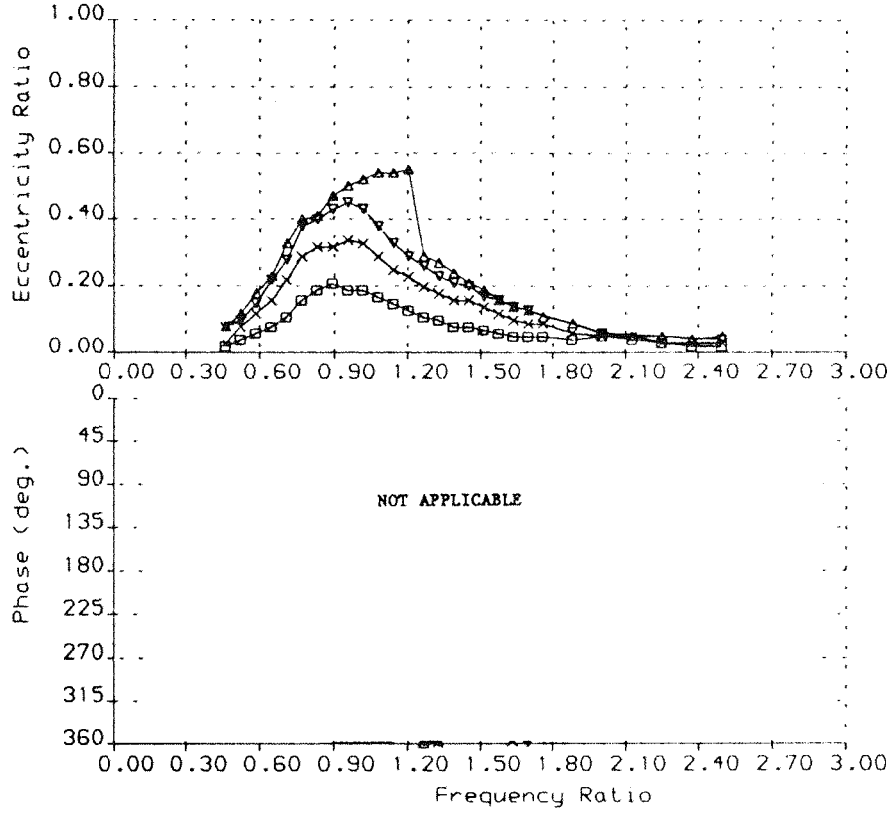

ROTOR-BEARING ASSEMBLY RESPONSE TO UNBALANCE
SQUEEZE-FILM DAMPER RESEARCH Rig Config. 2a

FIGURE 7.13

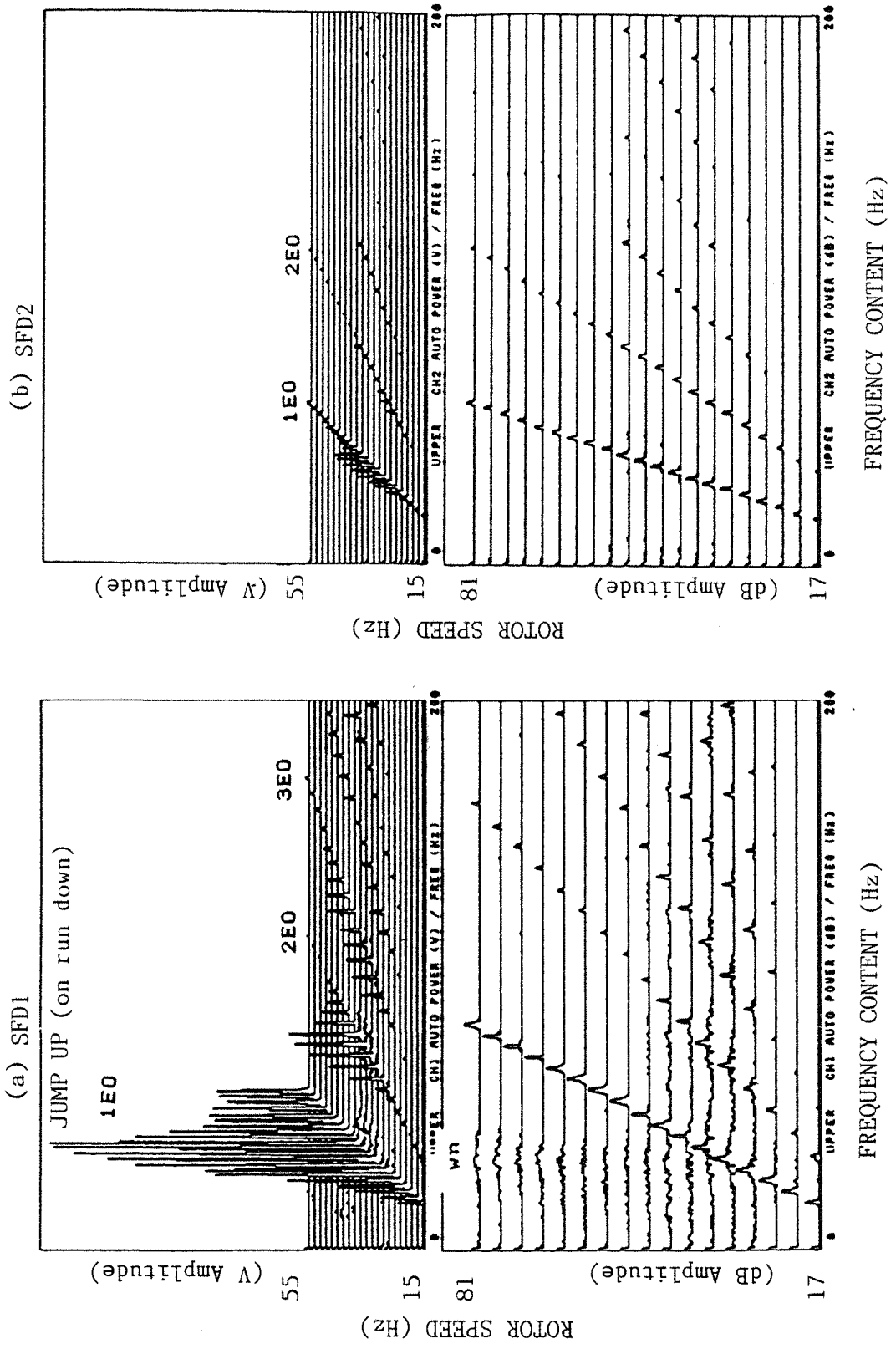

EXPERIMENTAL WATERFALL DIAGRAMS

Configuration 2a (Qc_2=0.611, Psup=2psi, Eo_1=0.0)

FIGURE 7.14

(a)

UNBALANCE FACTOR Qc_2 = 0.733

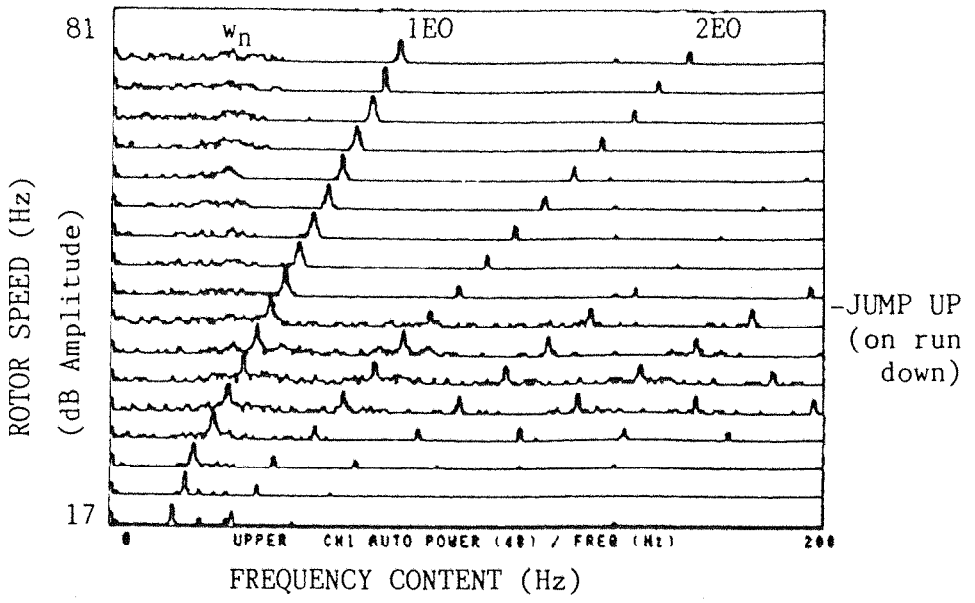

(b)

UNBALANCE FACTOR Qc_2 = 0.245

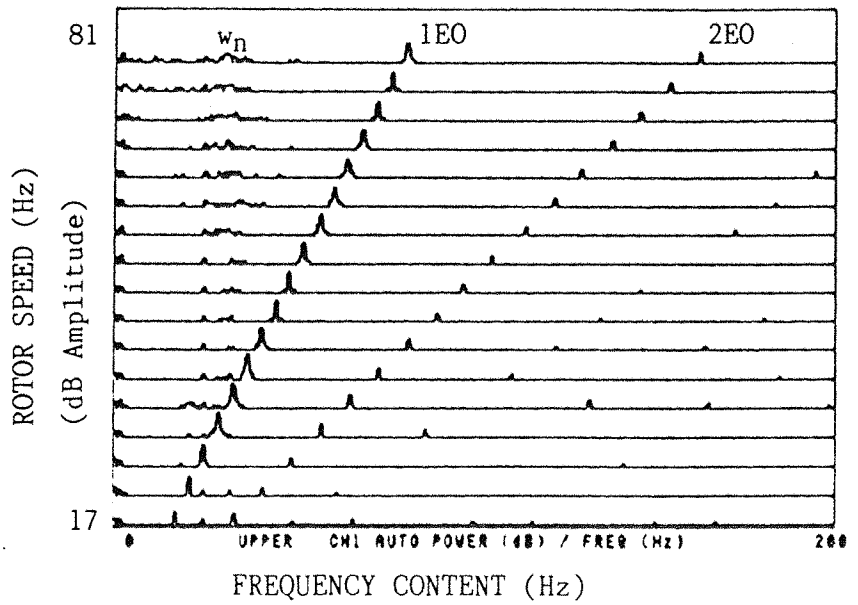

SFD1 EXPERIMENTAL WATERFALL DIAGRAMS

Configuration 2a (Psup=2psi, Eo =0.0)

BROADBAND SPECTRAL RESPONSE CAUSED BY JUMP PHENOMENA

FIGURE 7.15

VIBRATION SPECTRUM

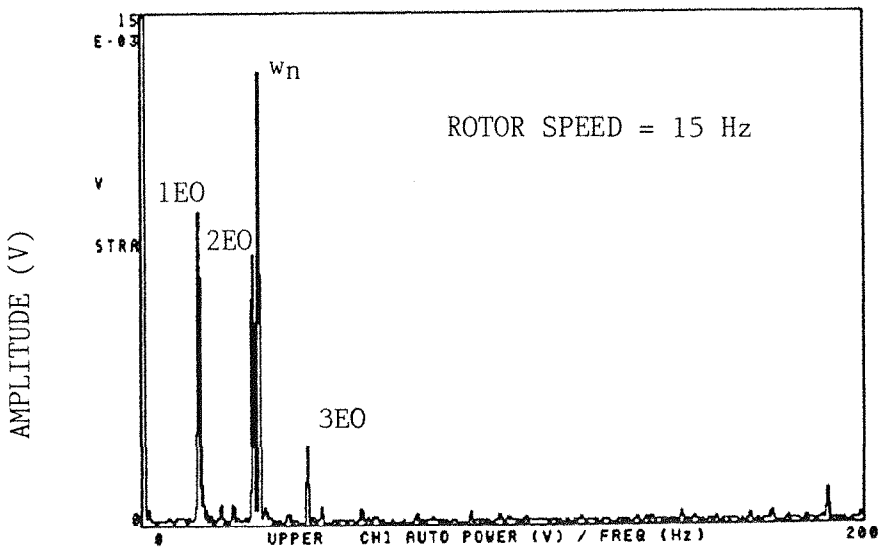

RIG CONFIGURATION

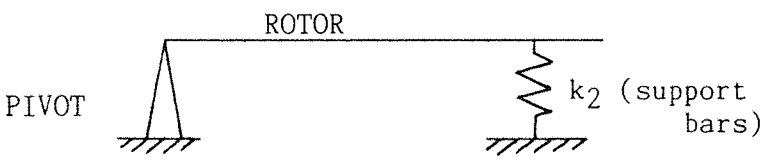

EXPERIMENTAL FREQUENCY ANALYSIS
Configuration 1a (without SFD1)

FIGURE 7.16

(a)

SFD1

Λ = 0.852799E -1 w/wn = 0.462963E 0

Qc2 = 0.610707E 0 Psup = 0.200000E 1 (psi)

Eo = 0.000000E 0 Pmin = -0.147000E 2 (psi)

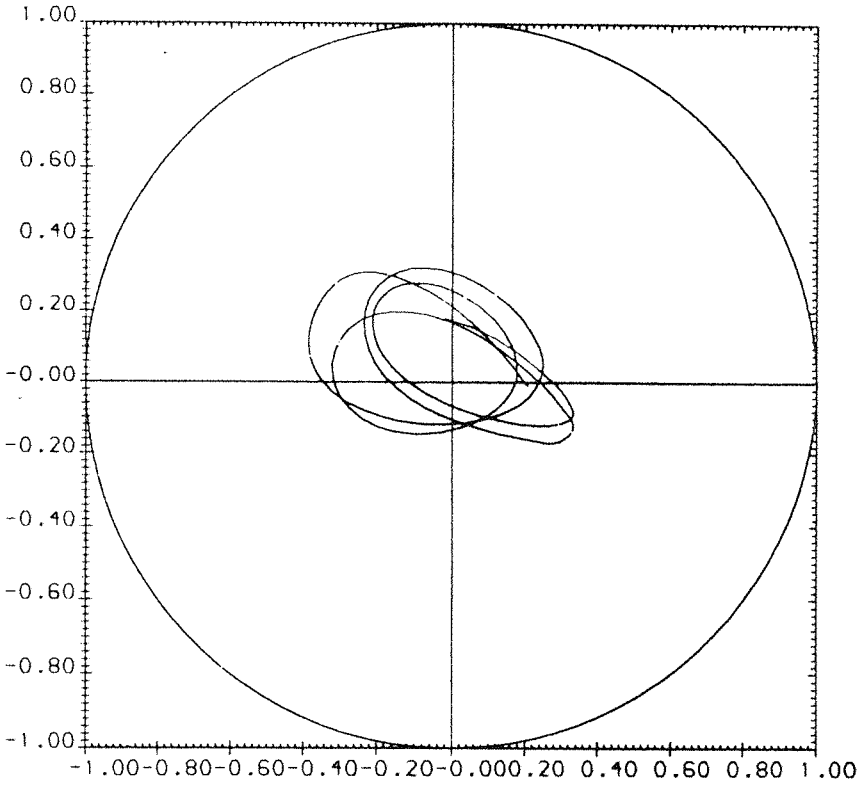

(b)

SFD2

Λ = 0.160400E 0 w/wn = 0.462963E 0

Qc2 = 0.610707E 0 Psup = 0.200000E 1 (psi)

Eo = 0.100000E 1 Pmin = -0.147000E 2 (psi)

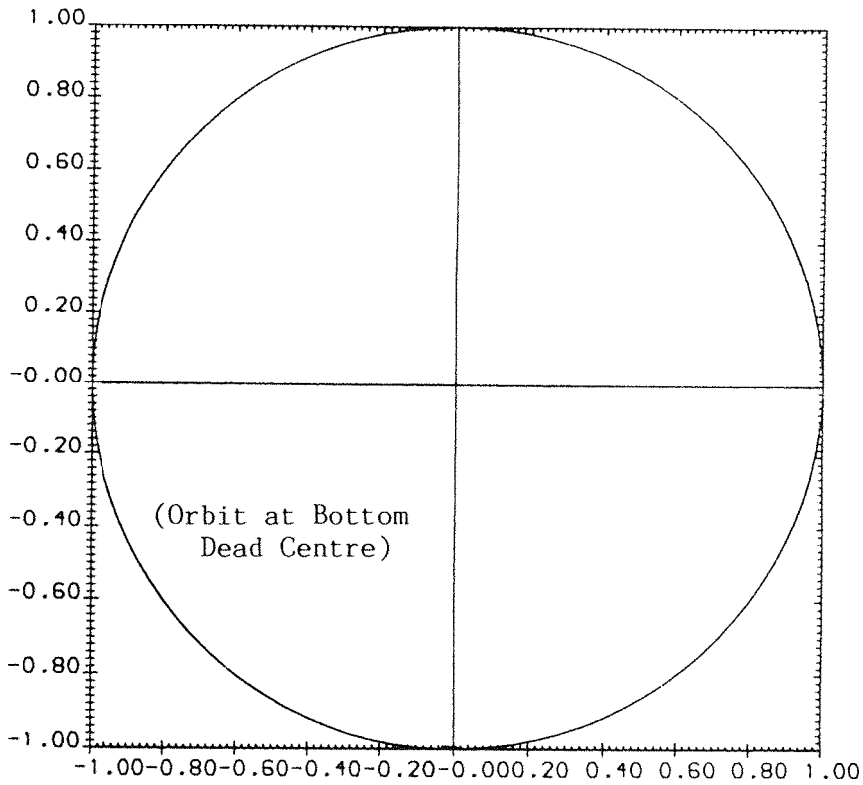

THEORETICAL ORBITS

Configuration 2a

(A_1=0.08528, w/w_n=0.463, Qc =0.611, Psup=2psi, Eo_1=0)

FIGURE 7.17

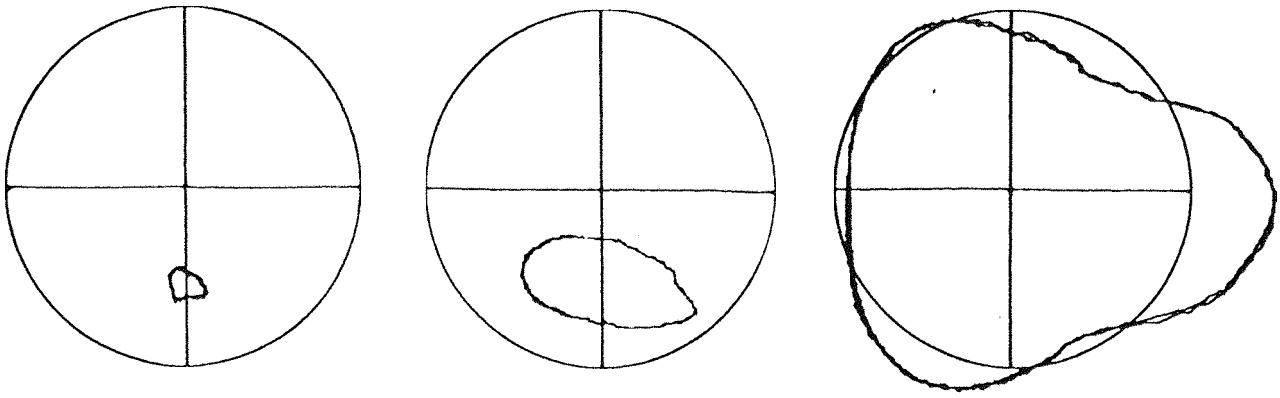

15 Hz (w/w_n=0.463) 27 Hz (w/w_n=0.833) 49 Hz (w/w_n=1.512)

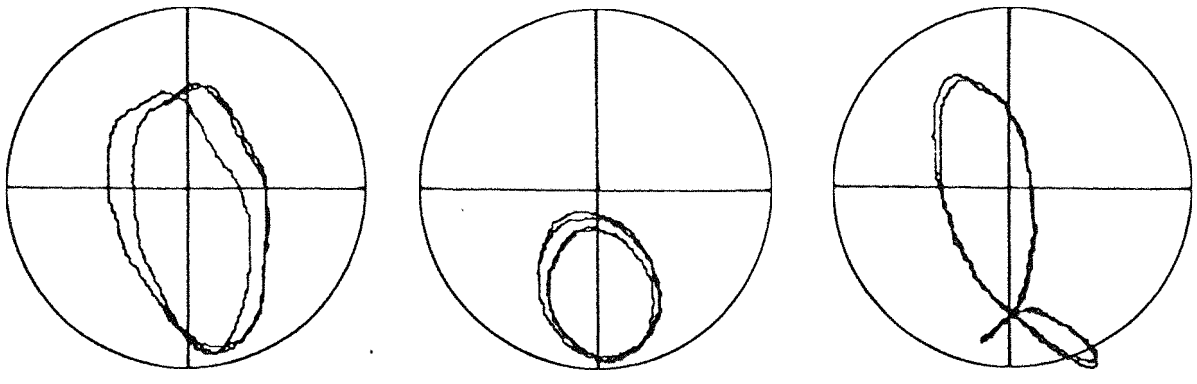

51 Hz (w/w_n=1.574) 65 Hz (w/w_n=2.006) 81 Hz (w/w_n=2.500)

ROTOR SPEEDS

SFD1 EXPERIMENTAL ORBITS

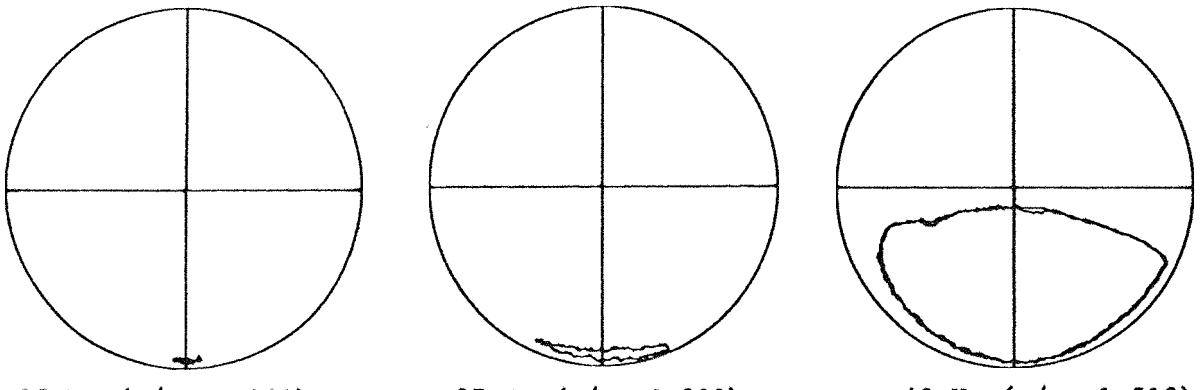

15 Hz (w/w_n=0.463) 27 Hz (w/w_n=0.833) 49 Hz (w/w_n=1.512)

ROTOR SPEEDS

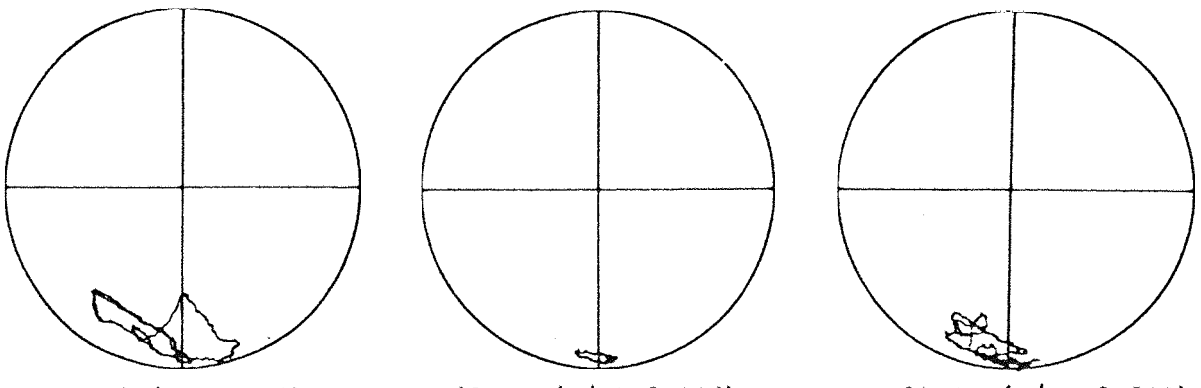

51 Hz (w/w_n=1.574) 65 Hz (w/w_n=2.006) 81 Hz (w/w_n=2.500)

SFD2 EXPERIMENTAL ORBITS

CONFIGURATION 2a (Q_{c_2} = 0.611, Psup = 2 psi, E_{o_1} = 0.5)

FIGURE 7.18

SQUEEZE-FILM DAMPER SFD1 (2mm Groove Depth)

EXPERIMENTAL RESULTS

	Δ	
A =	0.2132E -1	
Qc2=	0.6107E 0	
Eo =	0.5000E 0	
Psup=	0.2000E 1	(psi)

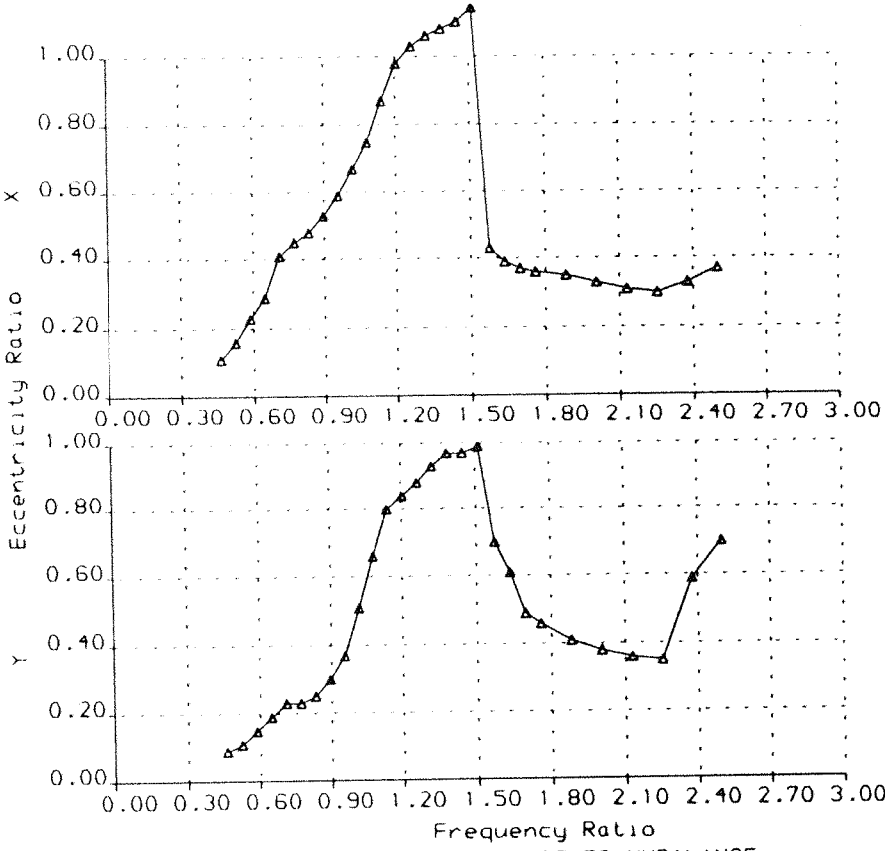

ROTOR-BEARING ASSEMBLY RESPONSE TO UNBALANCE
SQUEEZE-FILM DAMPER RESEARCH Rig Config. 2a

SQUEEZE-FILM DAMPER SFD2 (2mm Groove Depth)

EXPERIMENTAL RESULTS

	Δ	
A =	0.4010E -1	
Qc2=	0.6107E 0	
Eo =	0.1000E 1	
Psup=	0.2000E 1	(psi)

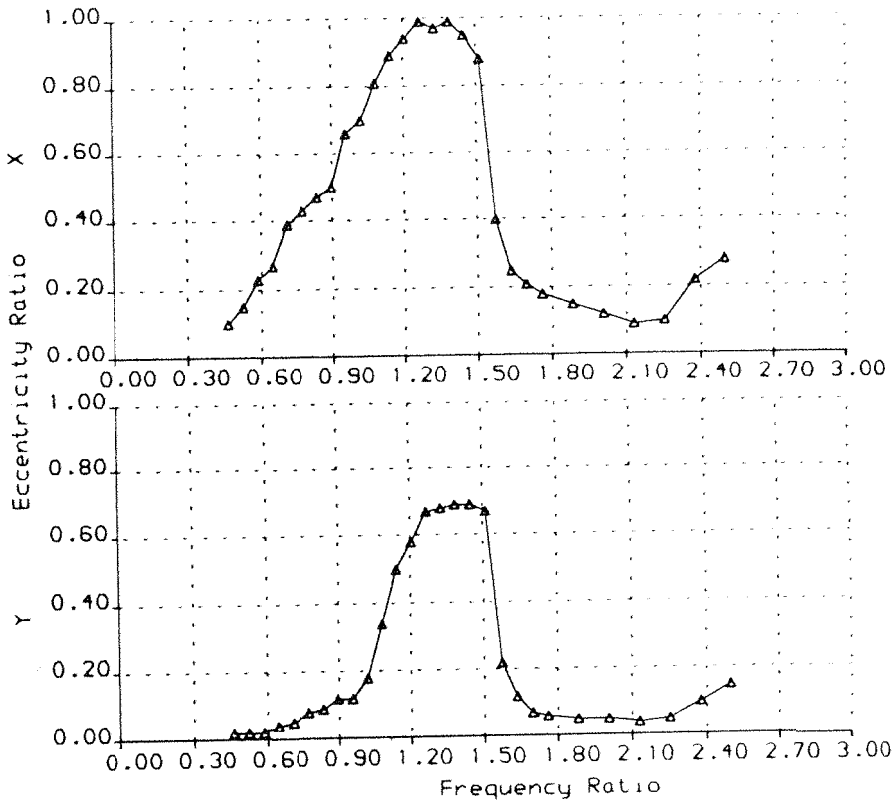

ROTOR-BEARING ASSEMBLY RESPONSE TO UNBALANCE
SQUEEZE-FILM DAMPER RESEARCH Rig Config. 2a

FIGURE 7.19

EXPERIMENTAL WATERFALL DIAGRAMS

Configuration 2a (Qc_2=0.611, Psup=2psi, Eo_1=0.5)

FIGURE 7.20

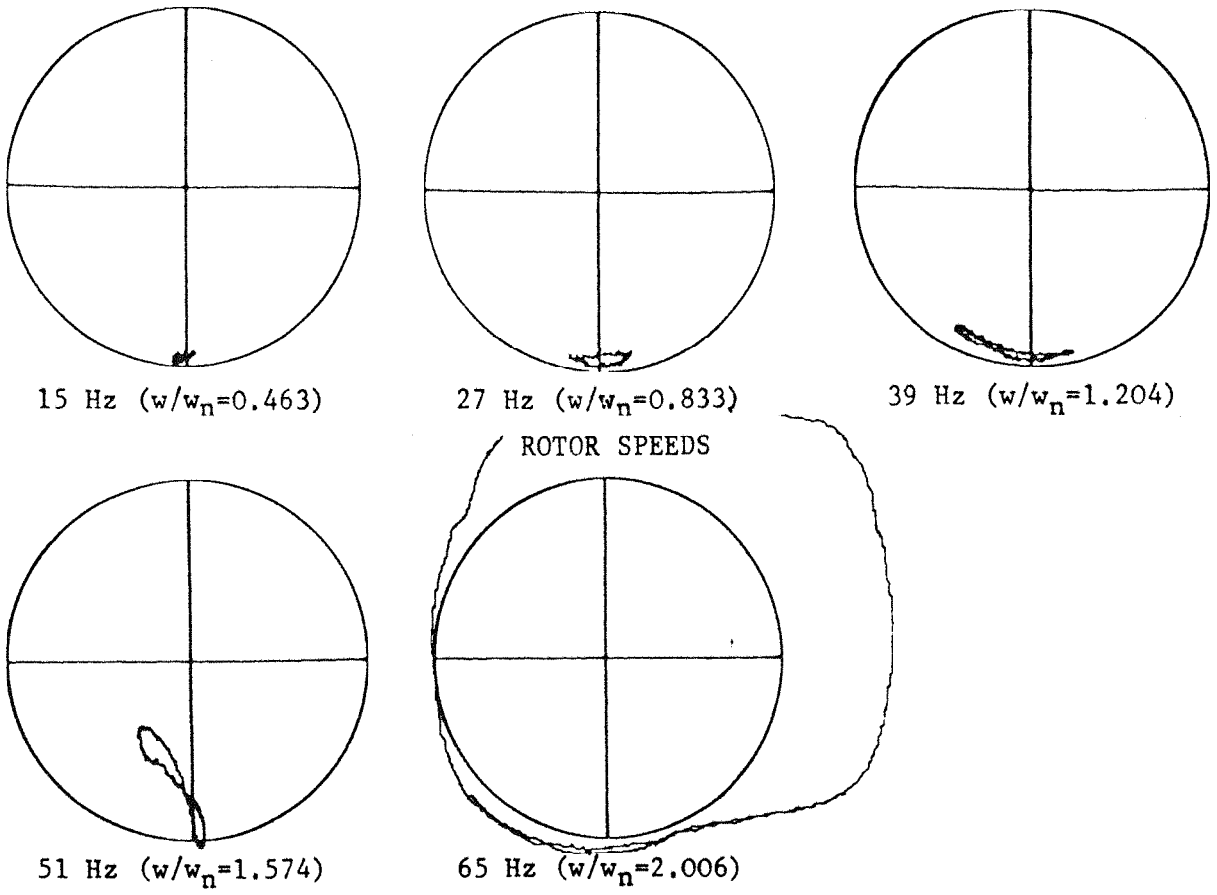

(a) SFD1 EXPERIMENTAL ORBITS

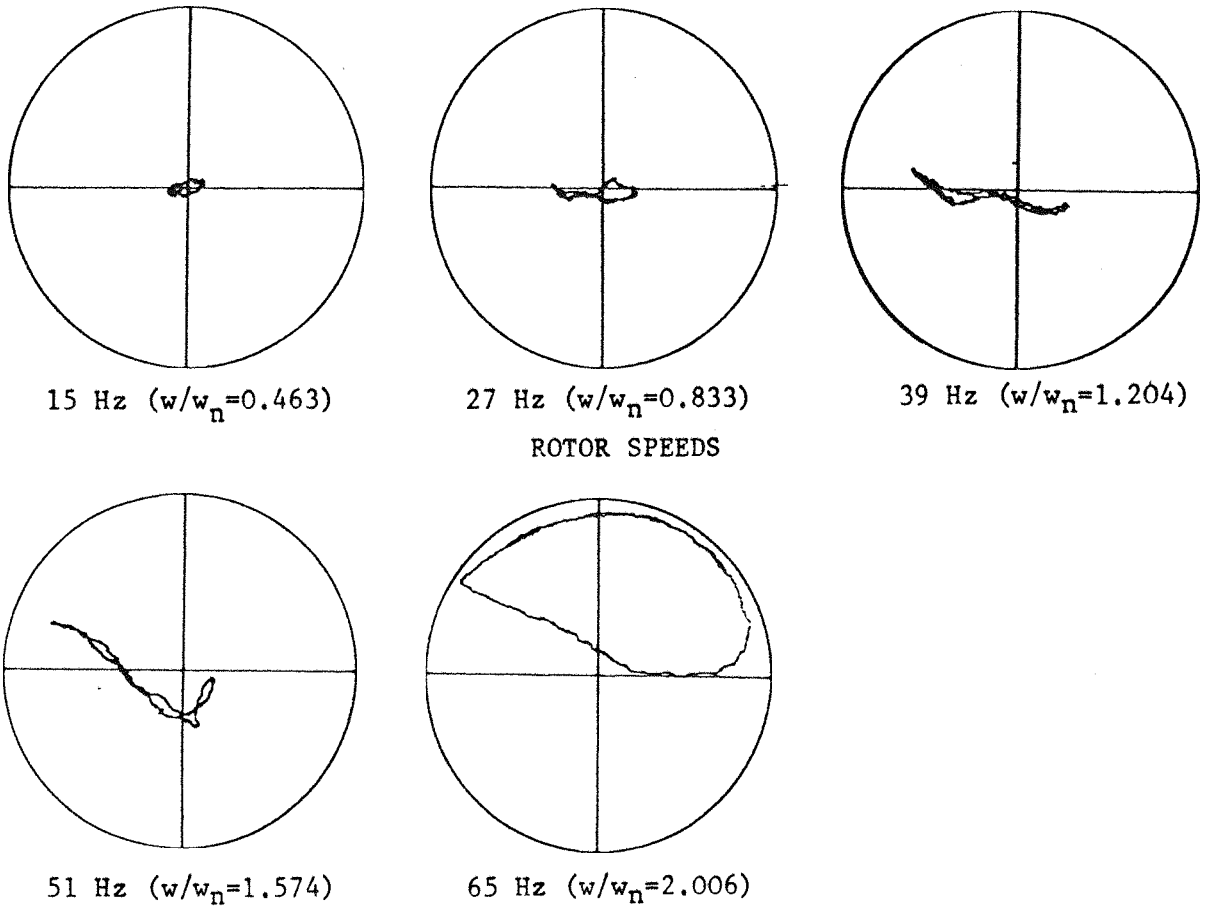

(b) SFD2 EXPERIMENTAL ORBITS

CONFIGURATION 2b (Q_{c_2} = 0.611, Psup = 2 psi)

FIGURE 7.21

(a)

SQUEEZE-FILM DAMPER SFD1 (2mm Groove Depth)

EXPERIMENTAL RESULTS

	△	▽	×	□	
A =	0.2132E -1	0.2132E -1	0.2132E -1	0.2132E -1	
Qc2=	0.7332E 0	0.6107E 0	0.4901E 0	0.2450E 0	
Eo =	0.1000E 1	0.1000E 1	0.1000E 1	0.1000E 1	
Psup=	0.2000E 1	0.2000E 1	0.2000E 1	0.2000E 1	(psi)

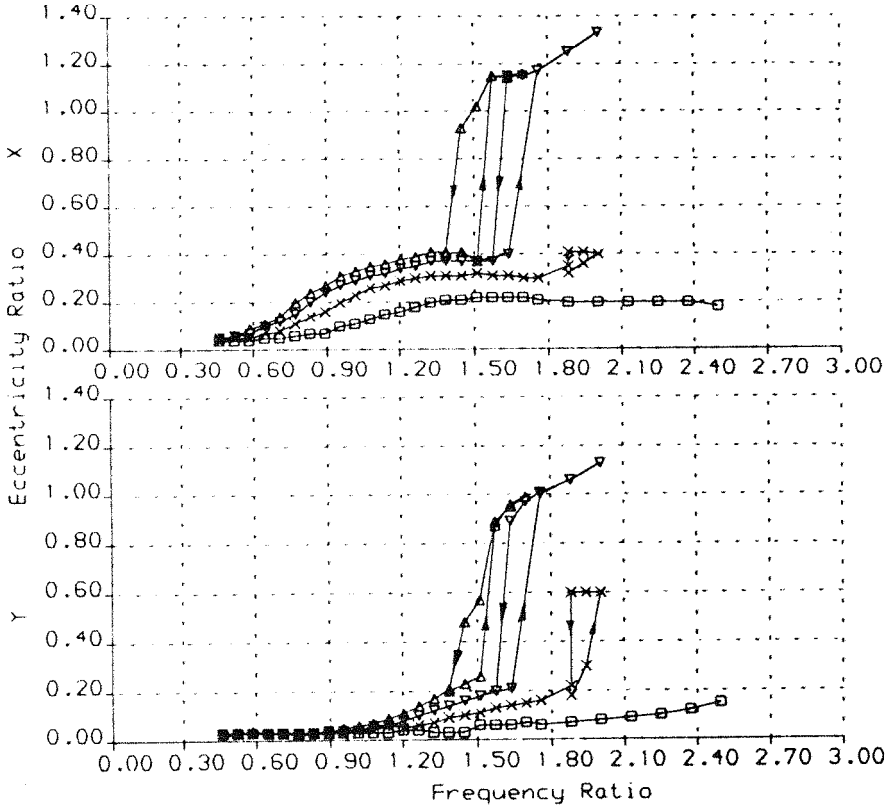

ROTOR-BEARING ASSEMBLY RESPONSE TO UNBALANCE
SQUEEZE-FILM DAMPER RESEARCH Rig Config. 2b

(b)

SQUEEZE-FILM DAMPER SFD2 (2mm Groove Depth)

EXPERIMENTAL RESULTS

	△	▽	×	□	
A =	0.4010E -1	0.4010E -1	0.4010E -1	0.4010E -1	
Qc2=	0.7332E 0	0.6107E 0	0.4901E 0	0.2450E 0	
Eo =	0.0000E 0	0.0000E 0	0.0000E 0	0.0000E 0	
Psup=	0.2000E 1	0.2000E 1	0.2000E 1	0.2000E 1	(psi)

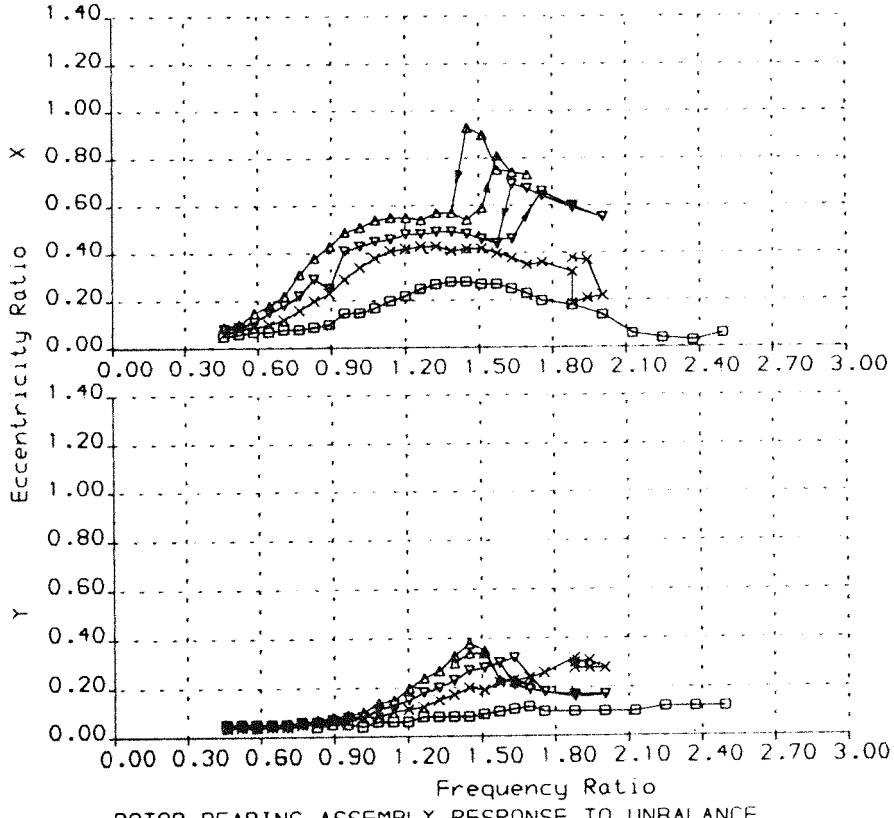

ROTOR-BEARING ASSEMBLY RESPONSE TO UNBALANCE
SQUEEZE-FILM DAMPER RESEARCH Rig Config. 2b

FIGURE 7.22

(a)

SQUEEZE-FILM DAMPER SFD1 (2mm Groove Depth)

EXPERIMENTAL RESULTS

	△	▽	×	□	
A =	0.2132E -1	0.2132E -1	0.2132E -1	0.2132E -1	
Qc2=	0.7332E 0	0.6107E 0	0.4901E 0	0.2450E 0	
Eo =	0.1000E 1	0.1000E 1	0.1000E 1	0.1000E 1	
Psup=	0.1500E 2	0.1500E 2	0.1500E 2	0.1500E 2	(psi)

(b)

SQUEEZE-FILM DAMPER SFD2 (2mm Groove Depth)

EXPERIMENTAL RESULTS

	△	▽	×	□	
A =	0.4010E -1	0.4010E -1	0.4010E -1	0.4010E -1	
Qc2=	0.7332E 0	0.6107E 0	0.4901E 0	0.2450E 0	
Eo =	0.0000E 0	0.0000E 0	0.0000E 0	0.0000E 0	
Psup=	0.1500E 2	0.1500E 2	0.1500E 2	0.1500E 2	(psi

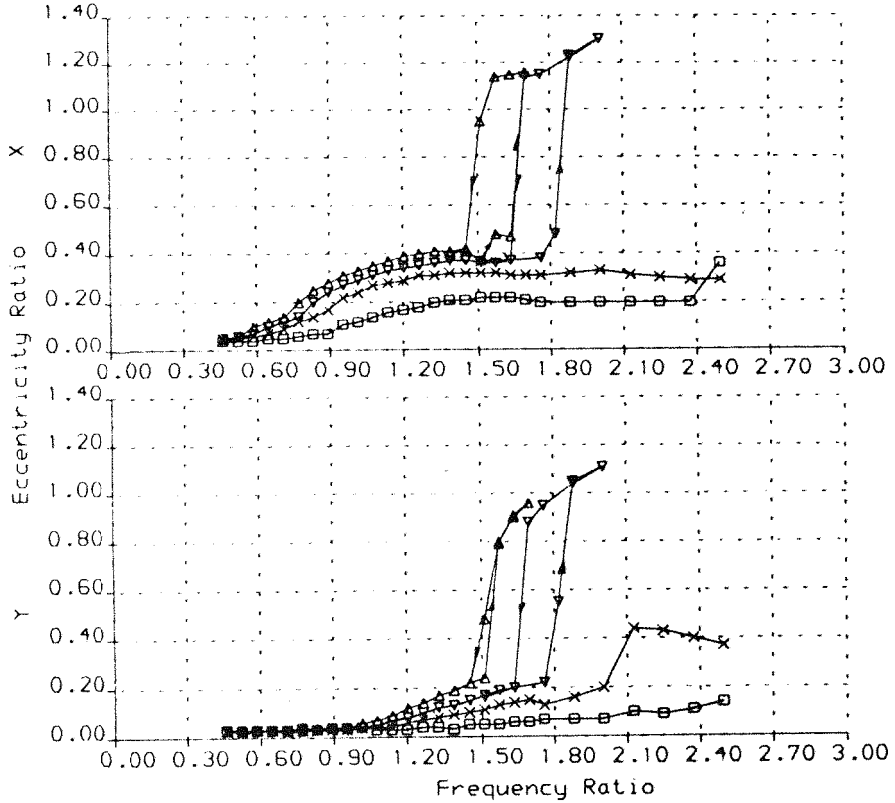

ROTOR-BEARING ASSEMBLY RESPONSE TO UNBALANCE
SQUEEZE-FILM DAMPER RESEARCH Rig Config. 2b

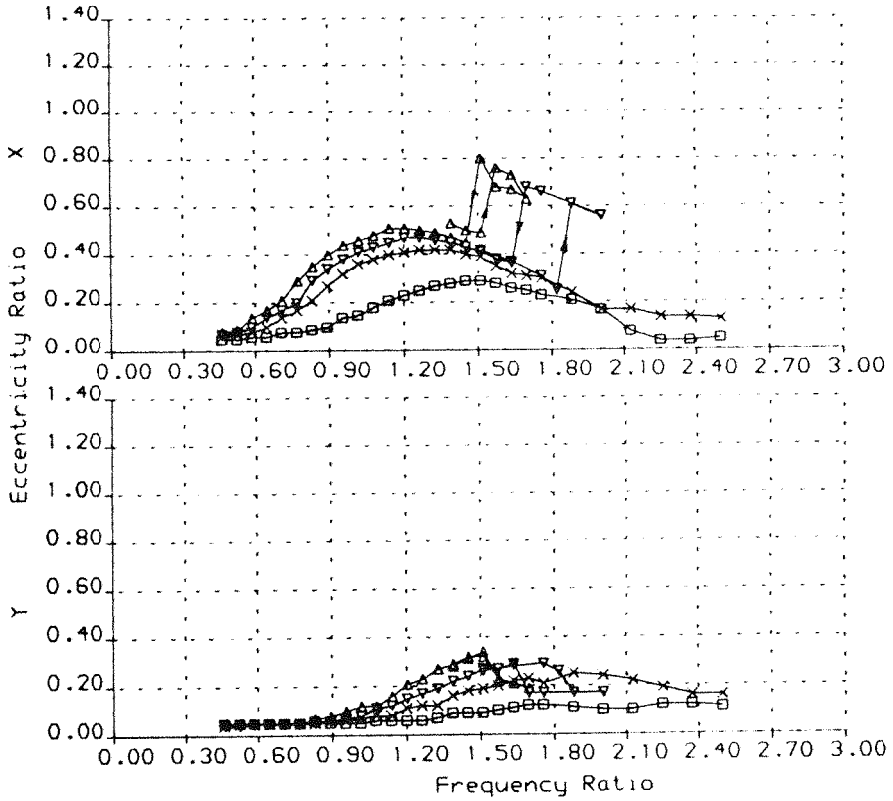

ROTOR-BEARING ASSEMBLY RESPONSE TO UNBALANCE
SQUEEZE-FILM DAMPER RESEARCH Rig Config. 2b

FIGURE 7.23

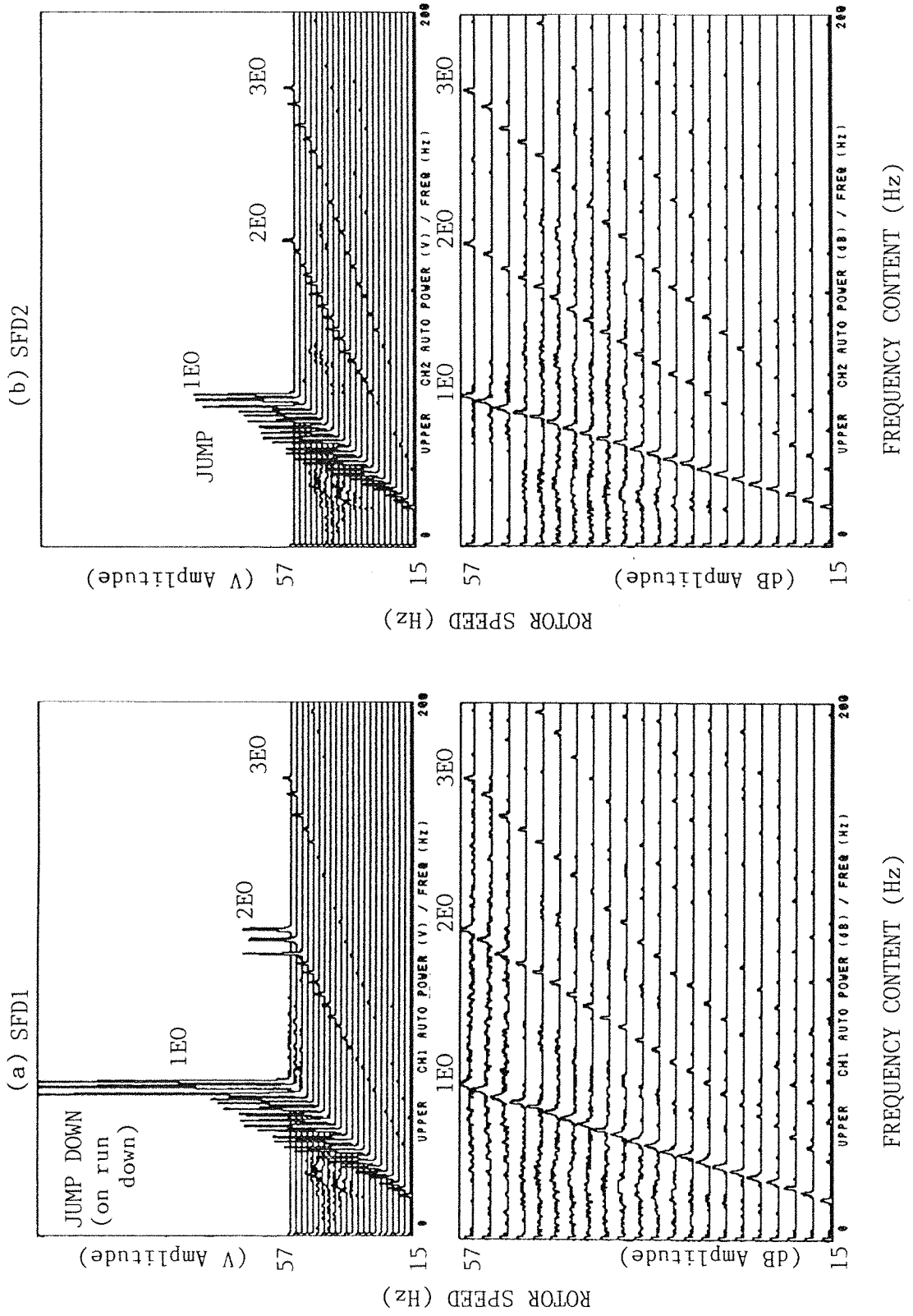

EXPERIMENTAL WATERFALL DIAGRAMS

Configuration 2b (Qc_2=0.611, Psup=2psi)

FIGURE 7.24

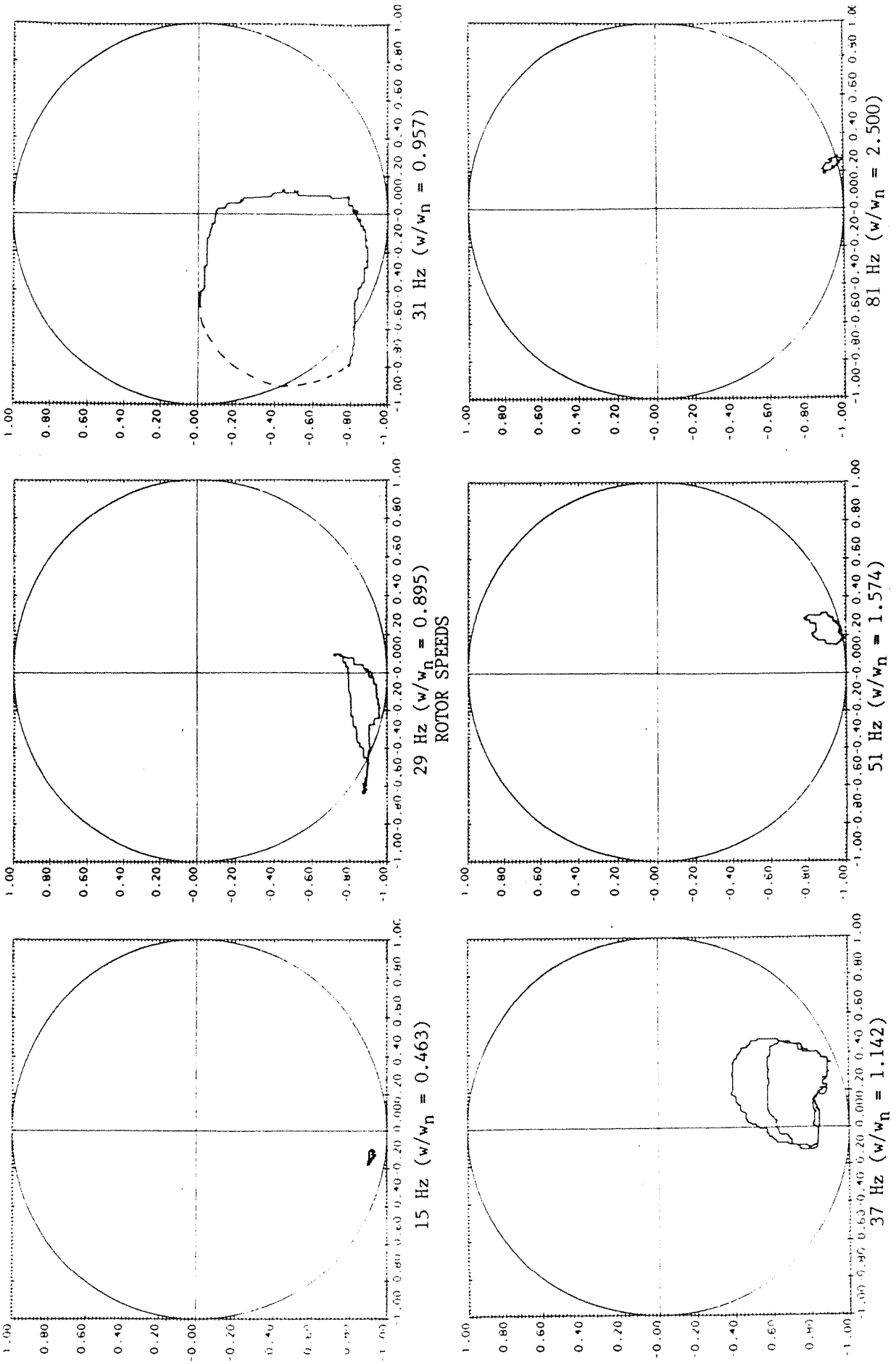

SFD1 EXPERIMENTAL ORBITS

Configuration 3a (Qc_2 =0.611, Psup=2psi)

FIGURE 7.25a

SFD2 EXPERIMENTAL ORBITS

Configuration 3a (Qc_2=0.611, Psup=2psi)

FIGURE 7.25b

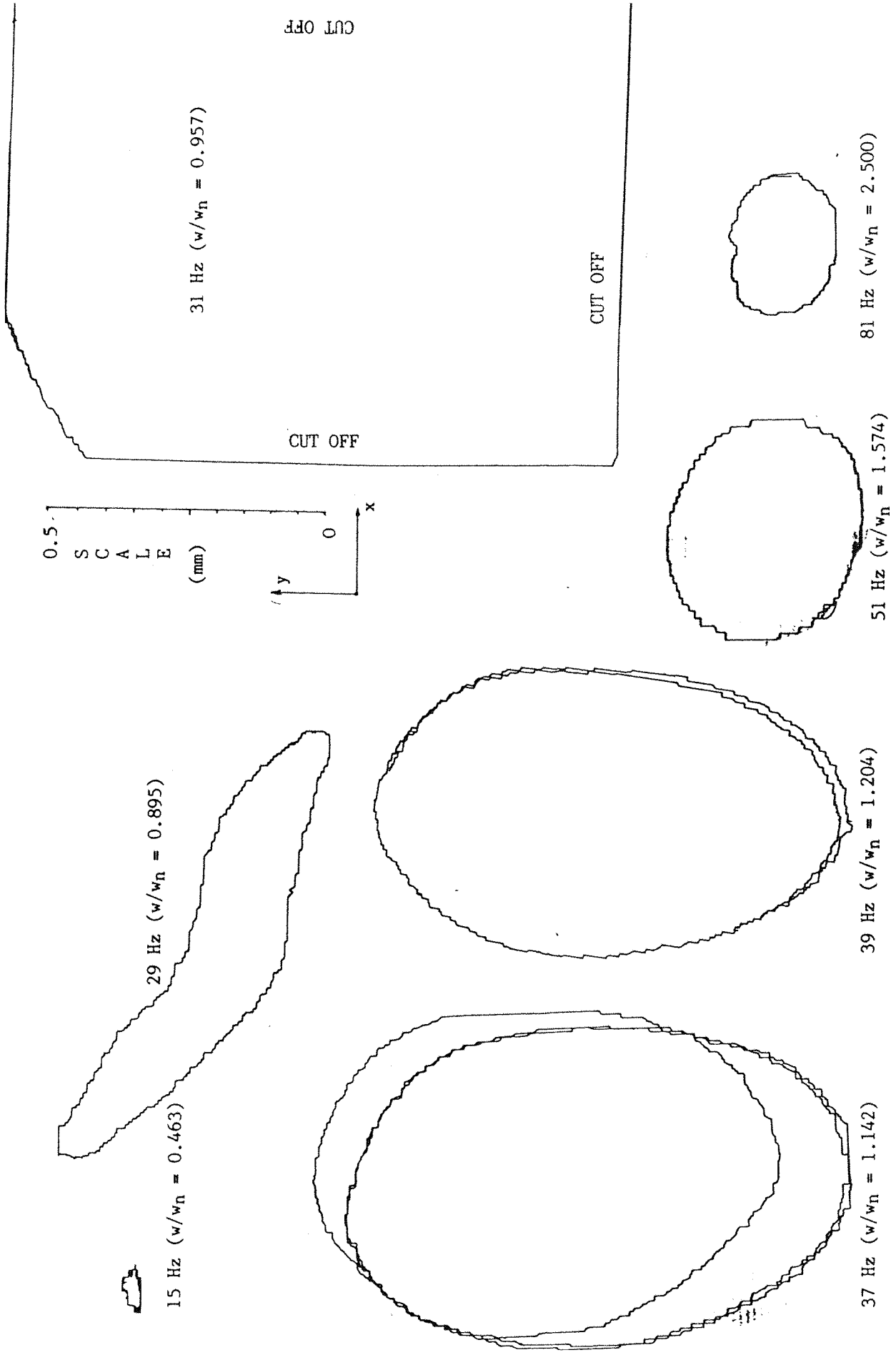

ROTOR ORBITS RELATIVE TO GROUND

Configuration 3a (Qc_2=0.611, Psup=2psi)

FIGURE 7.25c

(a)

SQUEEZE-FILM DAMPER SFD1 (2mm Groove Depth)

EXPERIMENTAL RESULTS

	△	▽	×	□	
A =	0.2132E -1	0.2132E -1	0.2132E -1	0.2132E -1	
Qc2=	0.7332E 0	0.6107E 0	0.4901E 0	0.2450E 0	
Eo =	0.1000E 1	0.1000E 1	0.1000E 1	0.1000E 1	
Psup=	0.2000E 1	0.2000E 1	0.2000E 1	0.2000E 1	(psi)

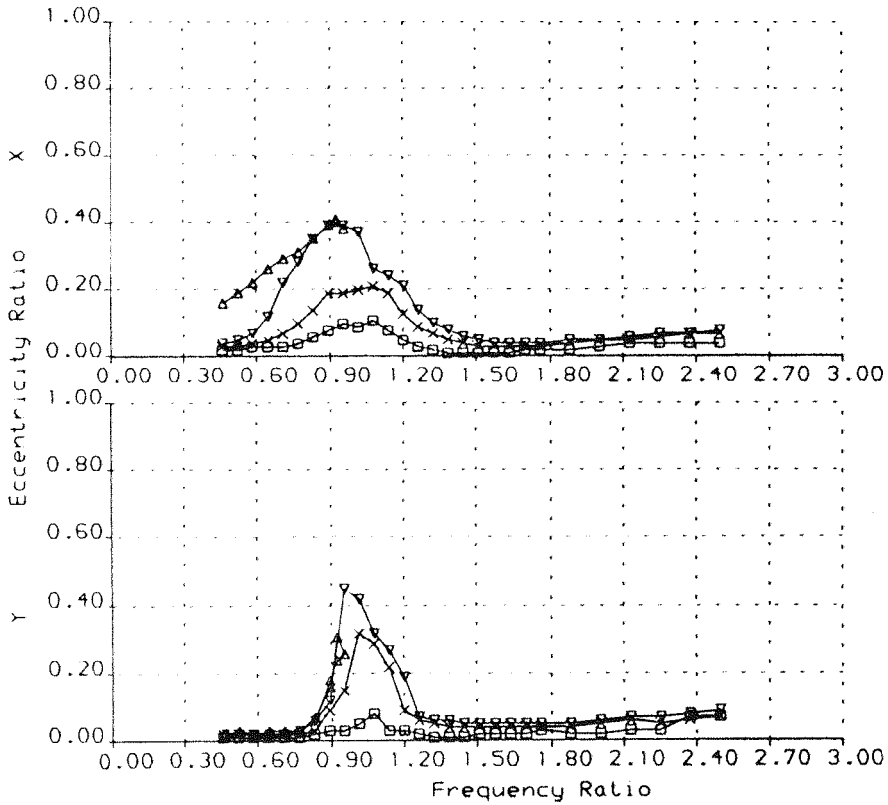

ROTOR-BEARING ASSEMBLY RESPONSE TO UNBALANCE
SQUEEZE-FILM DAMPER RESEARCH Rig Config. 3a

(b)

SQUEEZE-FILM DAMPER SFD2 (2mm Groove Depth)

EXPERIMENTAL RESULTS

	△	▽	×	□	
A =	0.4010E -1	0.4010E -1	0.4010E -1	0.4010E -1	
Qc2=	0.7332E 0	0.6107E 0	0.4901E 0	0.2450E 0	
Eo =	0.1000E 1	0.1000E 1	0.1000E 1	0.1000E 1	
Psup=	0.2000E 1	0.2000E 1	0.2000E 1	0.2000E 1	(psi)

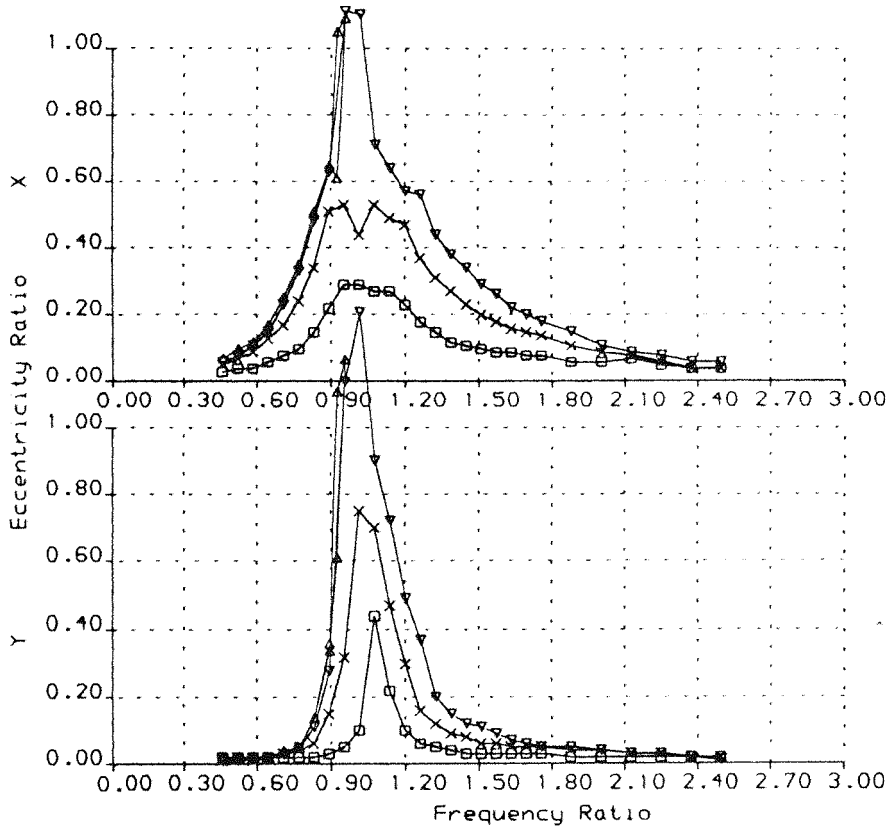

ROTOR-BEARING ASSEMBLY RESPONSE TO UNBALANCE
SQUEEZE-FILM DAMPER RESEARCH Rig Config. 3a

FIGURE 7.26

ROTOR RELATIVE TO GROUND AT SFD2 LOCATION

EXPERIMENTAL RESULTS

	△	▽	×	□
A =	0.4010E -1	0.4010E -1	0.4010E -1	0.4010E -1
Qc2=	0.7332E 0	0.6107E 0	0.4901E 0	0.2450E 0
Eo =	0.1000E 1	0.1000E 1	0.1000E 1	0.1000E 1
Psup=	0.2000E 1	0.2000E 1	0.2000E 1	0.2000E 1 (psi

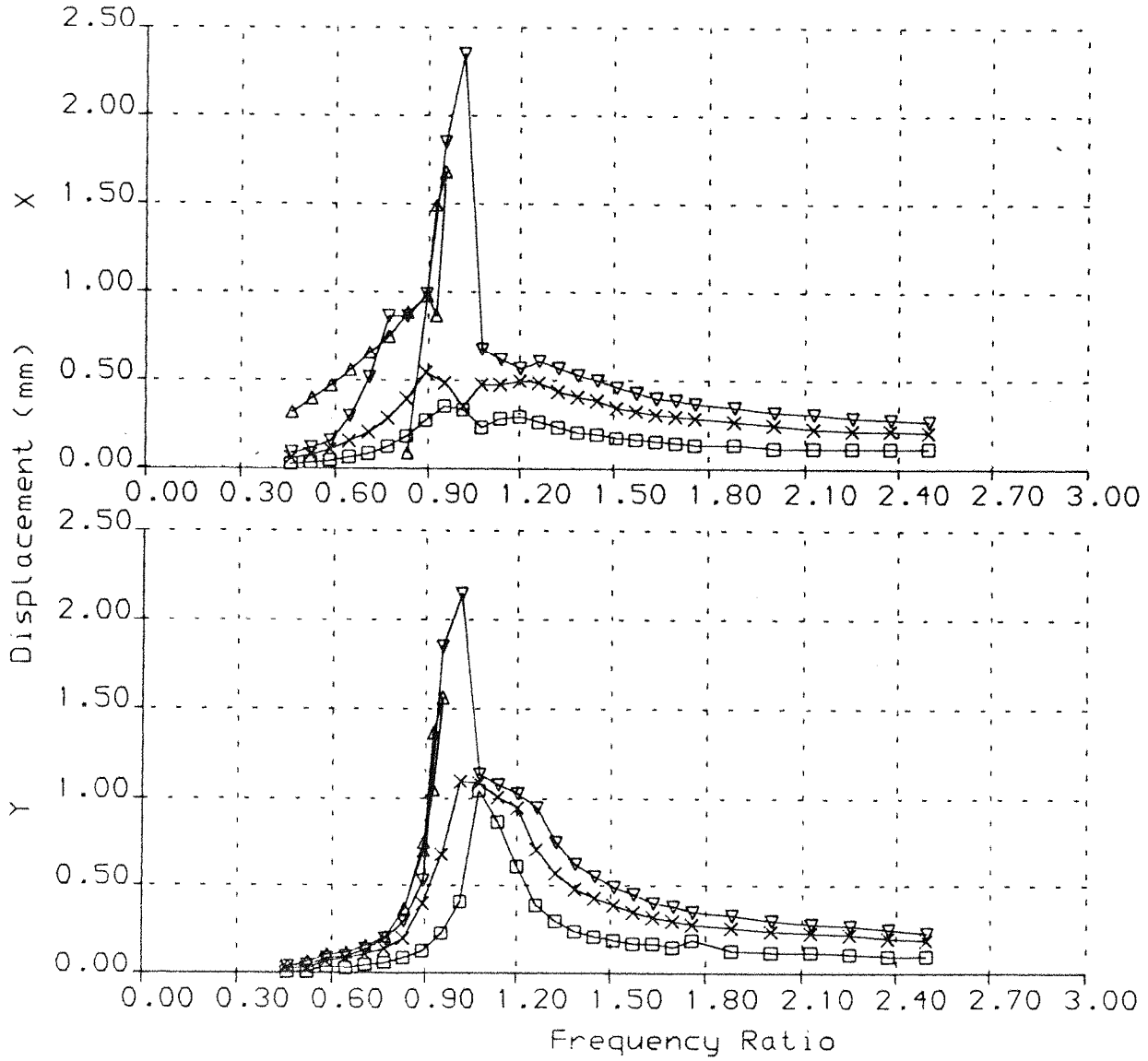

ROTOR-BEARING ASSEMBLY RESPONSE TO UNBALANCE
SQUEEZE-FILM DAMPER RESEARCH Rig Config. 3a

FIGURE 7.26c

(a)

SQUEEZE-FILM DAMPER SFD1 (2mm Groove Depth)

EXPERIMENTAL RESULTS

	△	▽	×	□	
A =	0.2132E -1	0.2132E -1	0.2132E -1	0.2132E -1	
Qc2=	0.7332E 0	0.6107E 0	0.4901E 0	0.2450E 0	
Eo =	0.1000E 1	0.1000E 1	0.1000E 1	0.1000E 1	
Psup=	0.1400E 2	0.1400E 2	0.1400E 2	0.1400E 2	(psi)

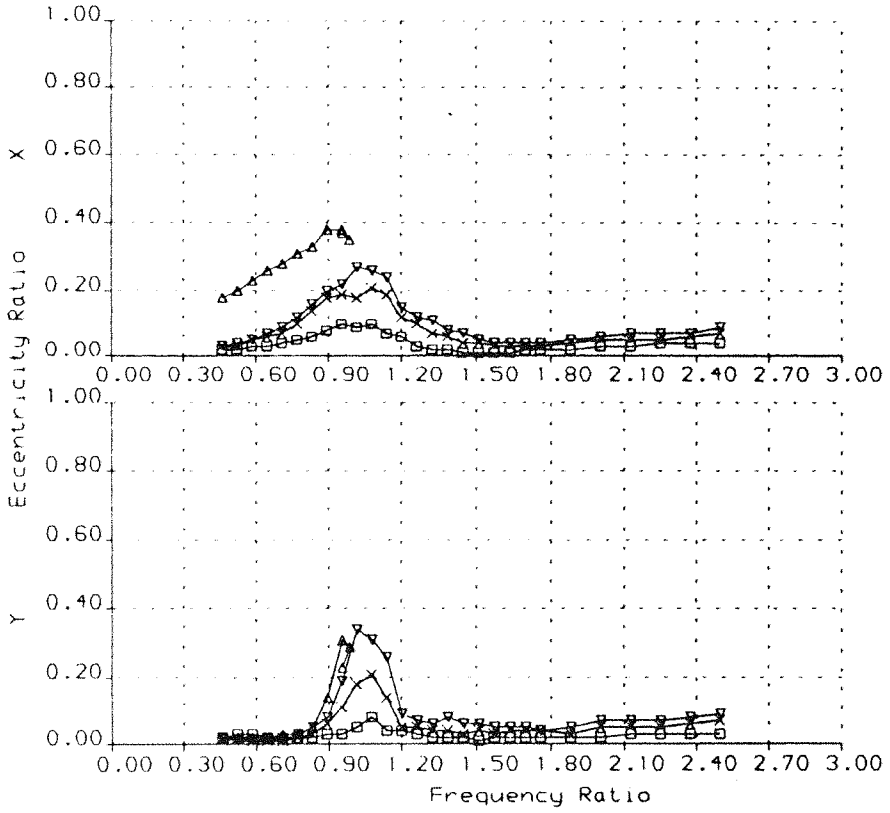

ROTOR-BEARING ASSEMBLY RESPONSE TO UNBALANCE
SQUEEZE-FILM DAMPER RESEARCH Rig Config. 3a

(b)

SQUEEZE-FILM DAMPER SFD2 (2mm Groove Depth)

EXPERIMENTAL RESULTS

	△	▽	×	□	
A =	0.4010E -1	0.4010E -1	0.4010E -1	0.4010E -1	
Qc2=	0.7332E 0	0.6107E 0	0.4901E 0	0.2450E 0	
Eo =	0.1000E 1	0.1000E 1	0.1000E 1	0.1000E 1	
Psup=	0.1400E 2	0.1400E 2	0.1400E 2	0.1400E 2	(psi)

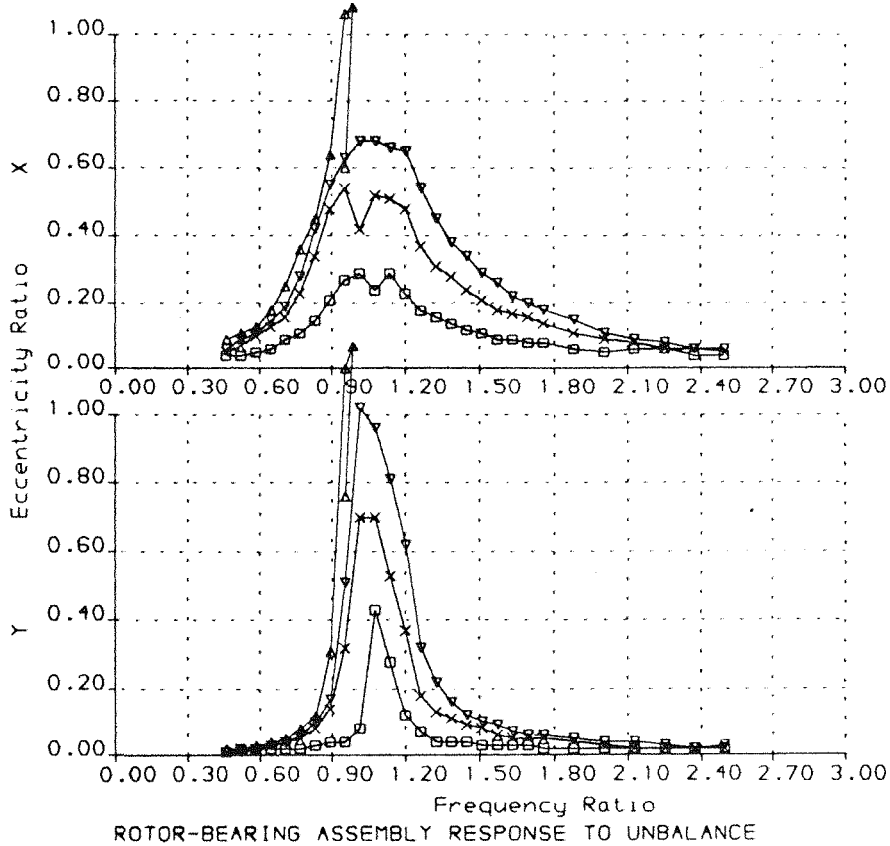

ROTOR-BEARING ASSEMBLY RESPONSE TO UNBALANCE
SQUEEZE-FILM DAMPER RESEARCH Rig Config. 3a

FIGURE 7.27

ROTOR RELATIVE TO GROUND AT SFD2 LOCATION

EXPERIMENTAL RESULTS

	△	▽	×	□
A =	0.4010E -1	0.4010E -1	0.4010E -1	0.4010E -1
Qc2=	0.7332E 0	0.6107E 0	0.4901E 0	0.2450E 0
Eo =	0.1000E 1	0.1000E 1	0.1000E 1	0.1000E 1
Psup=	0.1400E 2	0.1400E 2	0.1400E 2	0.1400E 2 (psi)

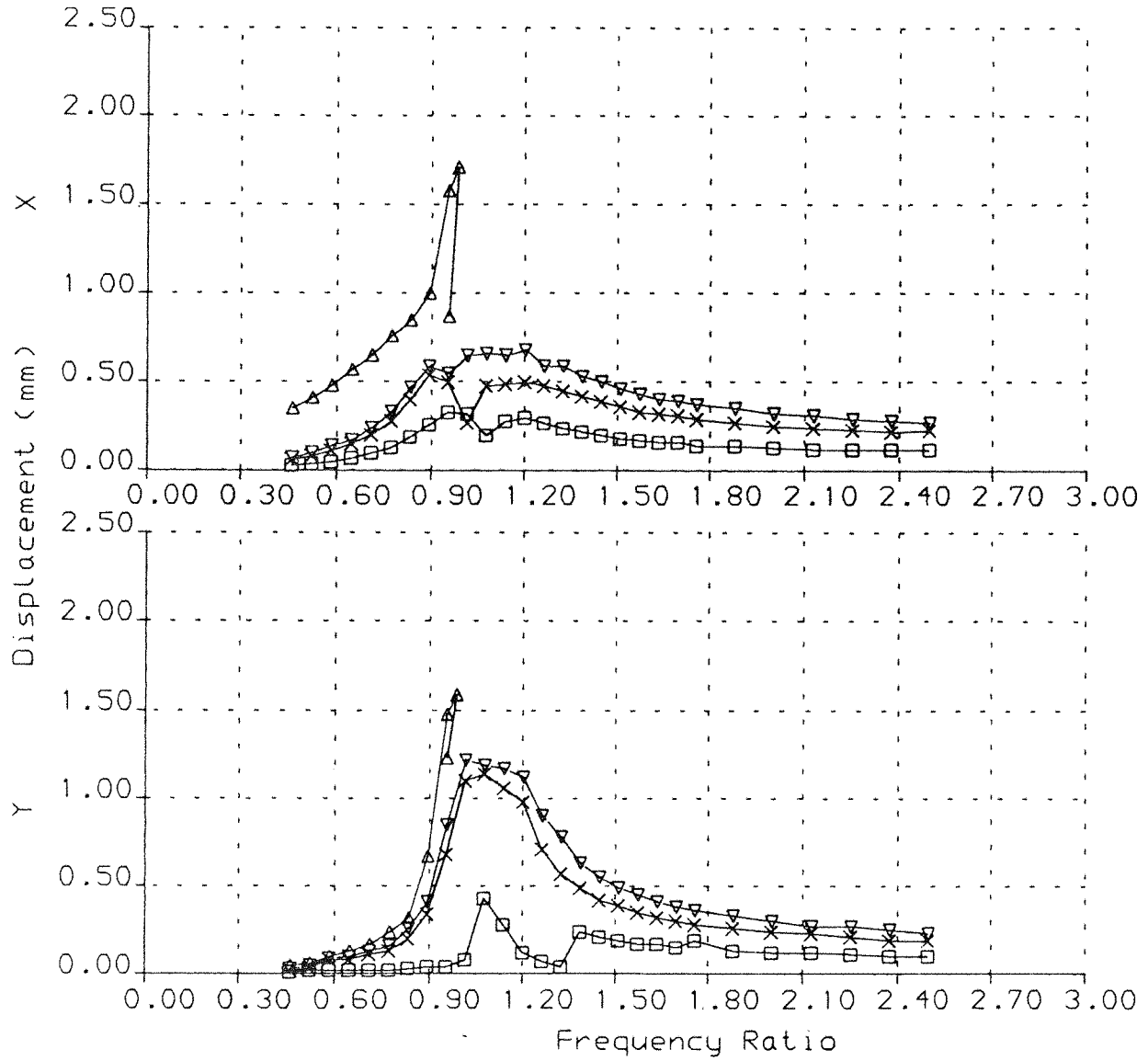

ROTOR-BEARING ASSEMBLY RESPONSE TO UNBALANCE

SQUEEZE-FILM DAMPER RESEARCH Rig Config. 3a

FIGURE 7.27c

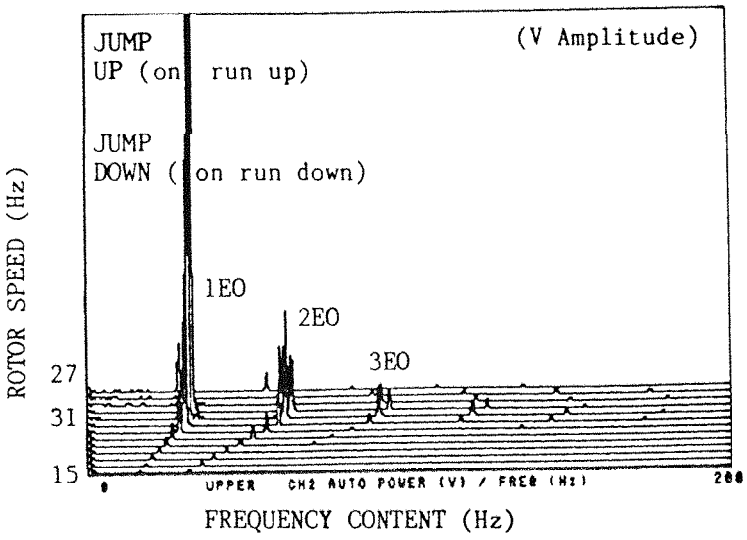

Qc_2 = 0.733
Psup= 2 psi
Eo_1 = 1.0
Eo_2 = 1.0

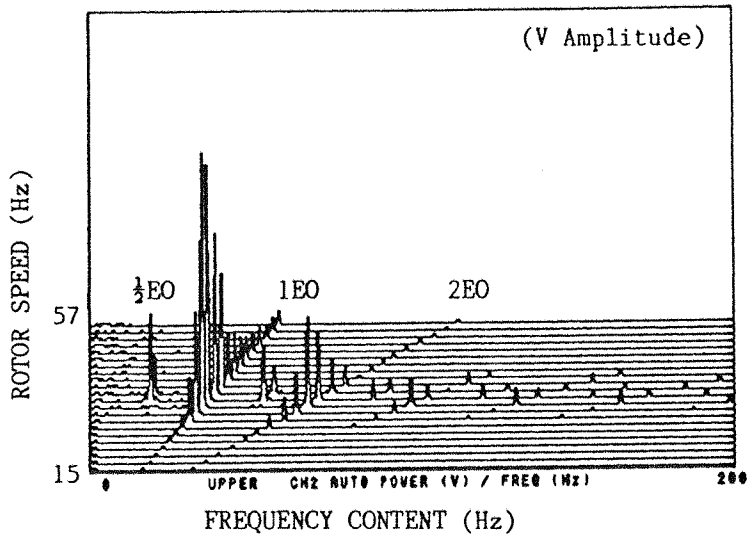

Qc_2 = 0.490
Psup= 2 psi
Eo_1 = 1.0
Eo_2 = 1.0

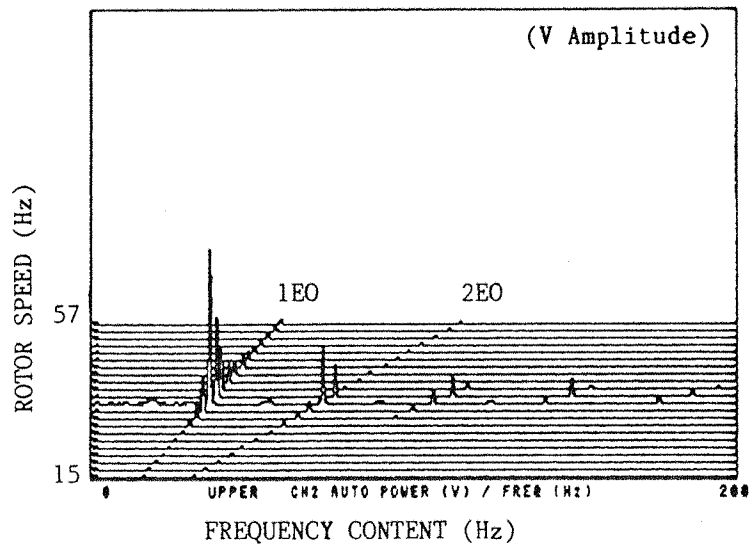

Qc_2 = 0.245
Psup= 2 psi
Eo_1 = 1.0
Eo_2 = 1.0

Configuration 3a

SFD2

EXPERIMENTAL WATERFALL DIAGRAMS

FIGURE 7.28a

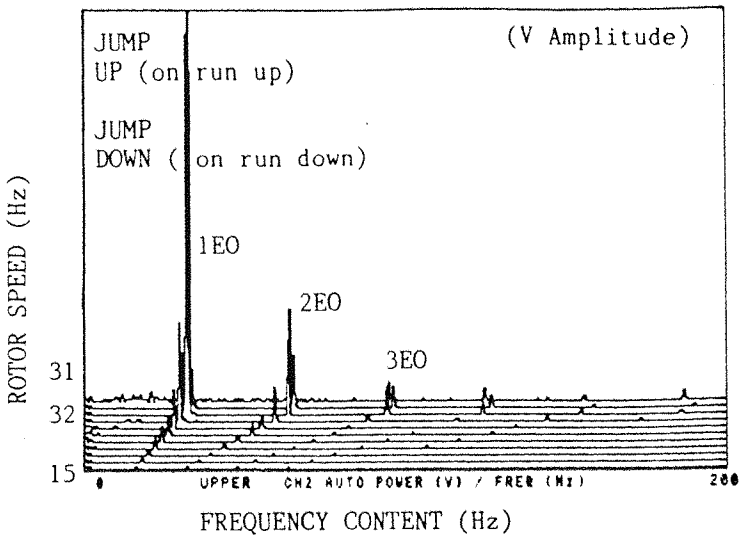

Qc_2 = 0.733
Psup=14 psi
Eo_1 = 1.0
Eo_2 = 1.0

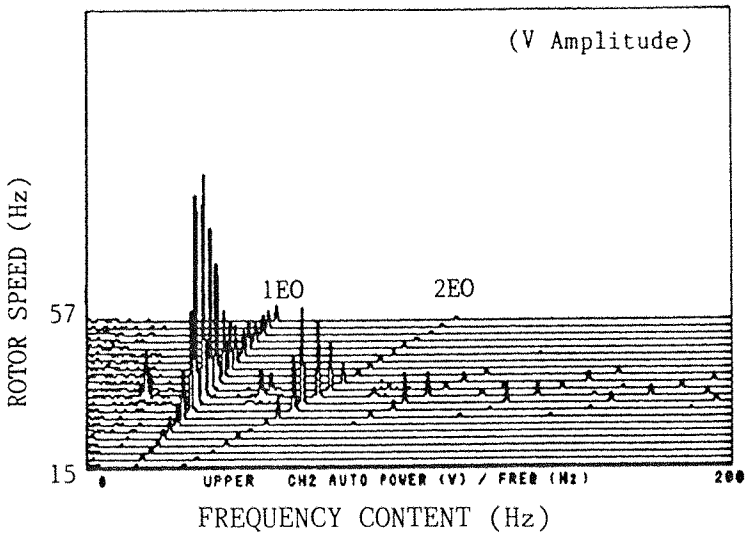

Qc_2 = 0.490
Psup=14 psi
Eo_1 = 1.0
Eo_2 = 1.0

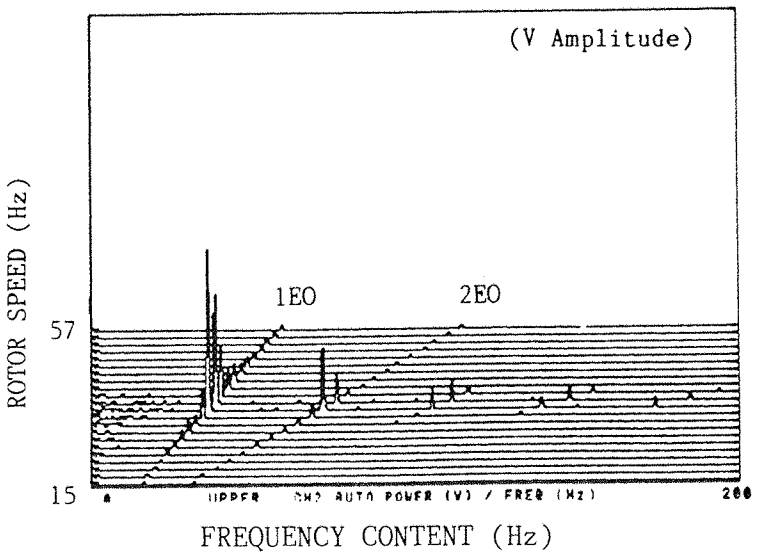

Qc_2 = 0.245
Psup=14 psi
Eo_1 = 1.0
Eo_2 = 1.0

Configuration 3a

ROTOR VIBRATION RELATIVE TO GROUND AT SFD2

EXPERIMENTAL WATERFALL DIAGRAMS

FIGURE 7.28b

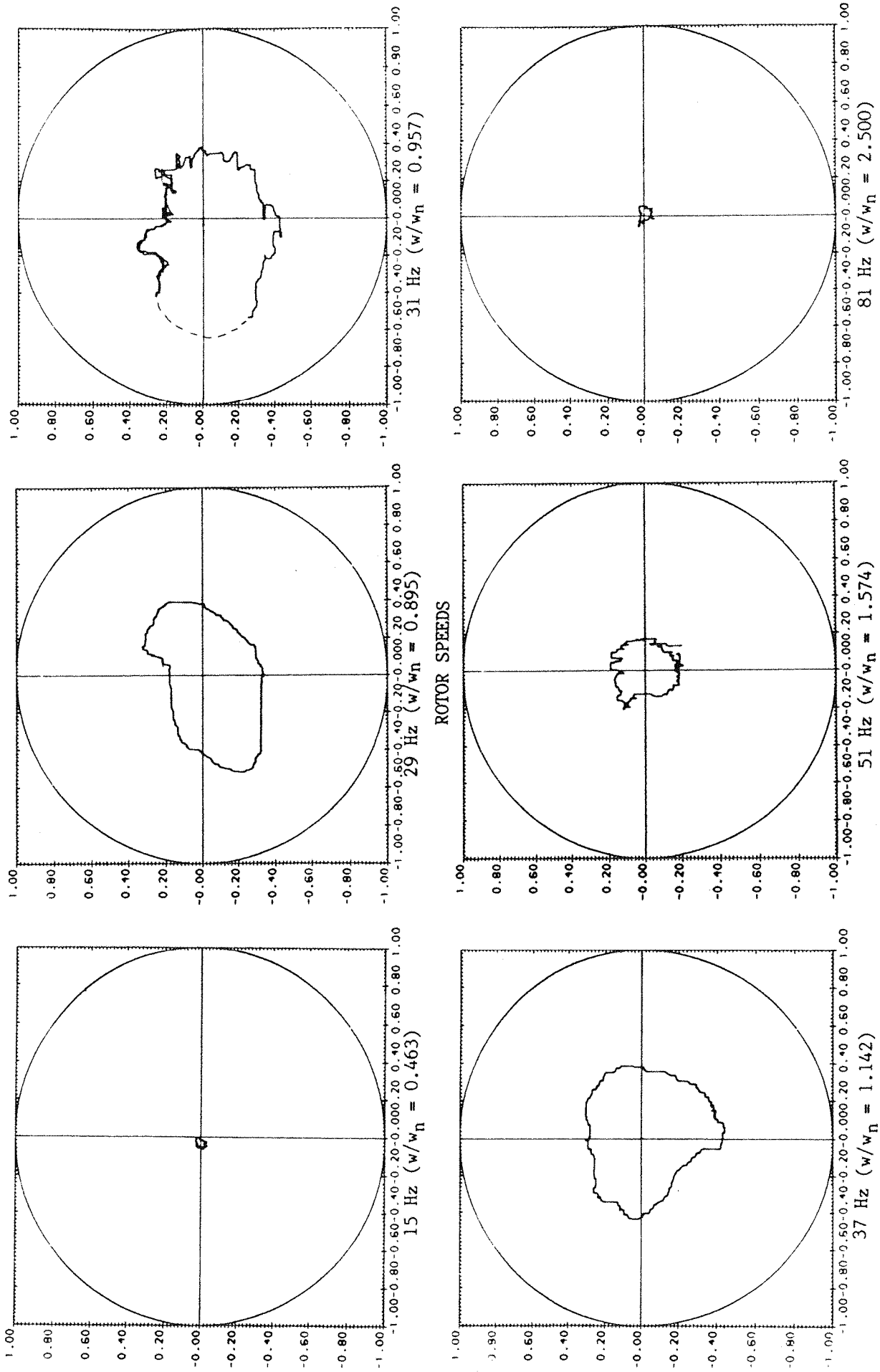

SFD1 EXPERIMENTAL ORBITS

Configuration 3b (Qc_2=0.611, Psup=2psi)

FIGURE 7.29a

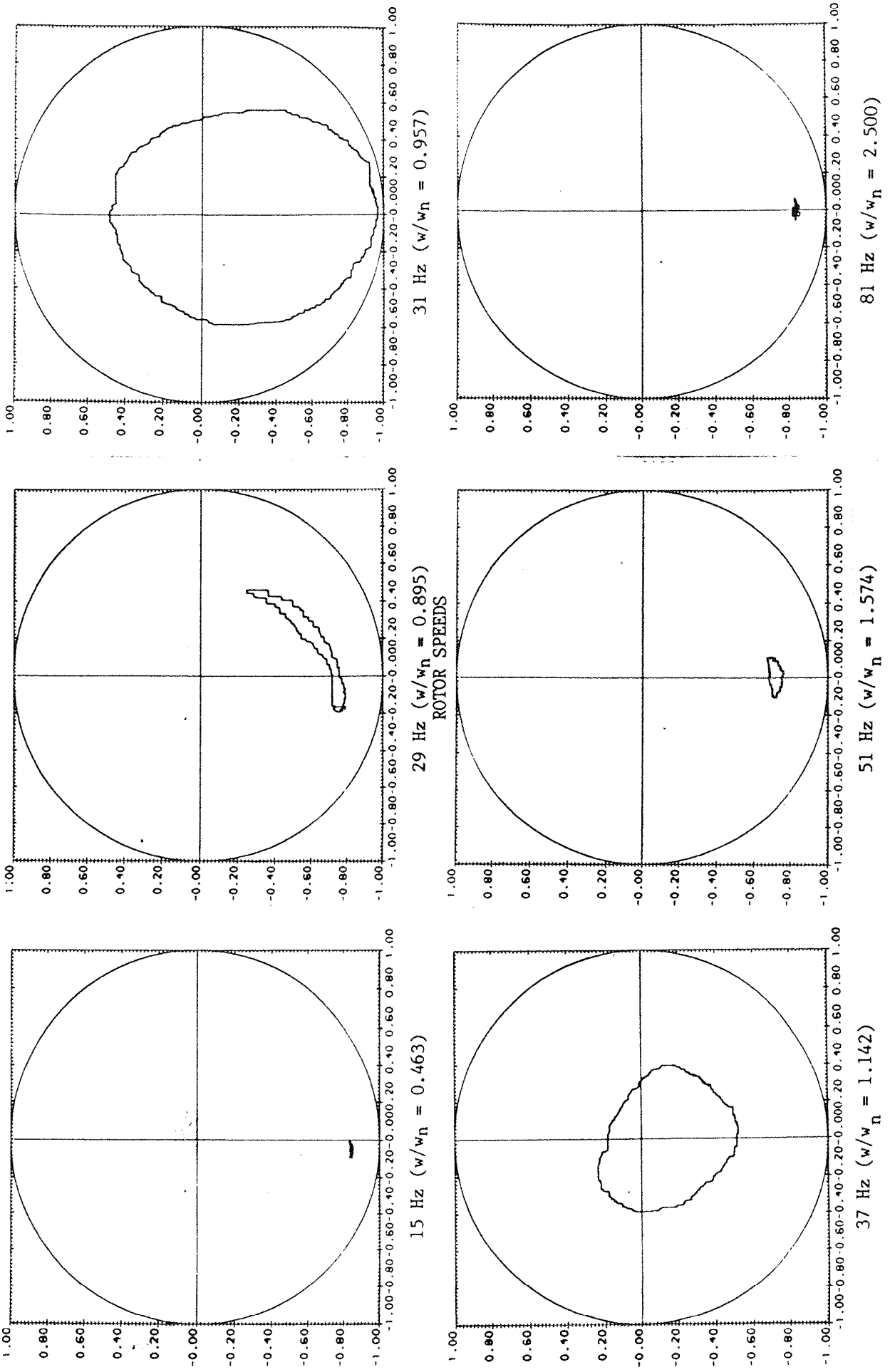

SFD2 EXPERIMENTAL ORBITS

Configuration 3b (Qc_2=0.611, Psup=2psi)

FIGURE 7.29b

ROTOR ORBITS RELATIVE TO GROUND

Configuration 3b (Qc_2=0.611, Psup=2psi)

FIGURE 7.29c

(a)

SQUEEZE-FILM DAMPER SFD1 (2mm Groove Depth)

EXPERIMENTAL RESULTS

	△	▽
A =	0.2132E -1	0.2132E -1
Qc2=	0.6107E 0	0.4901E 0
Eo =	0.0000E 0	0.0000E 0
Psup=	0.2000E 1	0.2000E 1 (psi)

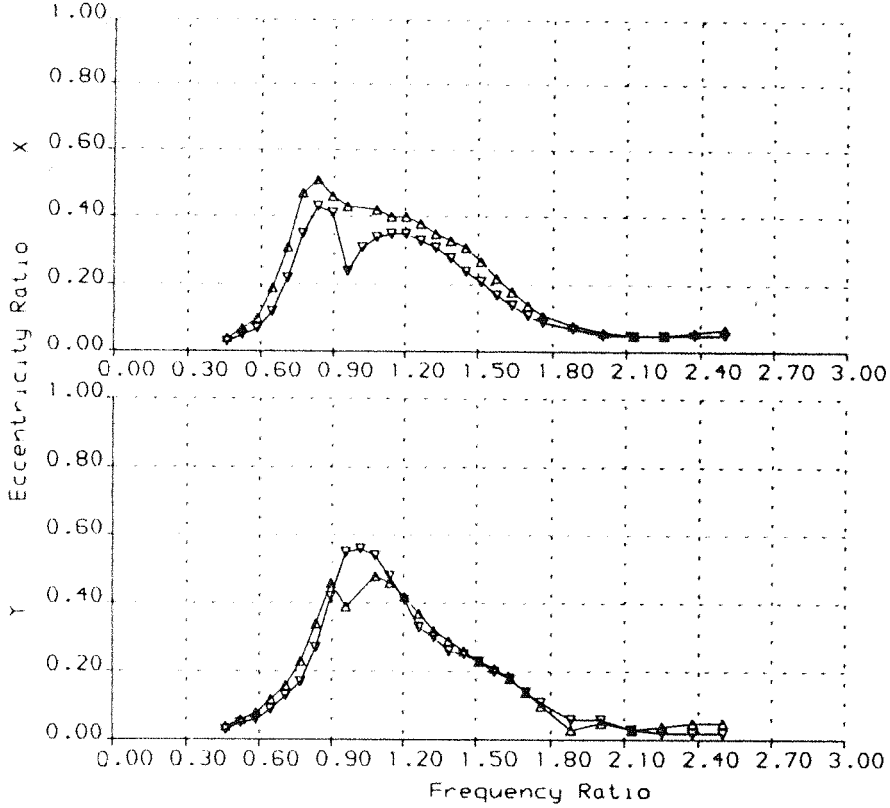

ROTOR-BEARING ASSEMBLY RESPONSE TO UNBALANCE
SQUEEZE-FILM DAMPER RESEARCH Rig Config. 3b

(b)

SQUEEZE-FILM DAMPER SFD2 (2mm Groove Depth)

EXPERIMENTAL RESULTS

	△	▽
A =	0.4010E -1	0.4010E -1
Qc2=	0.6107E 0	0.4901E 0
Eo =	0.1000E 1	0.1000E 1
Psup=	0.2000E 1	0.2000E 1 (psi)

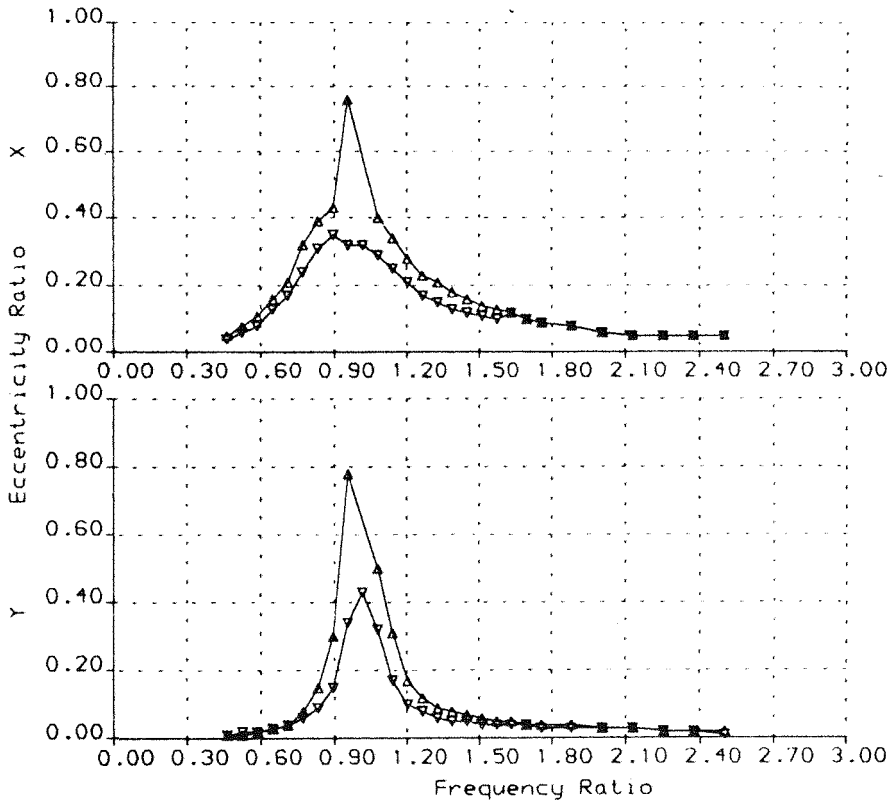

ROTOR-BEARING ASSEMBLY RESPONSE TO UNBALANCE
SQUEEZE-FILM DAMPER RESEARCH Rig Config. 3b

FIGURE 7.30

ROTOR RELATIVE TO GROUND AT SFD2 LOCATION

EXPERIMENTAL RESULTS

	△	▽
A =	0.4010E -1	0.4010E -1
Qc2=	0.6107E 0	0.4901E 0
Eo =	0.1000E 1	0.1000E 1
Psup=	0.2000E 1	0.2000E 1 (psi)

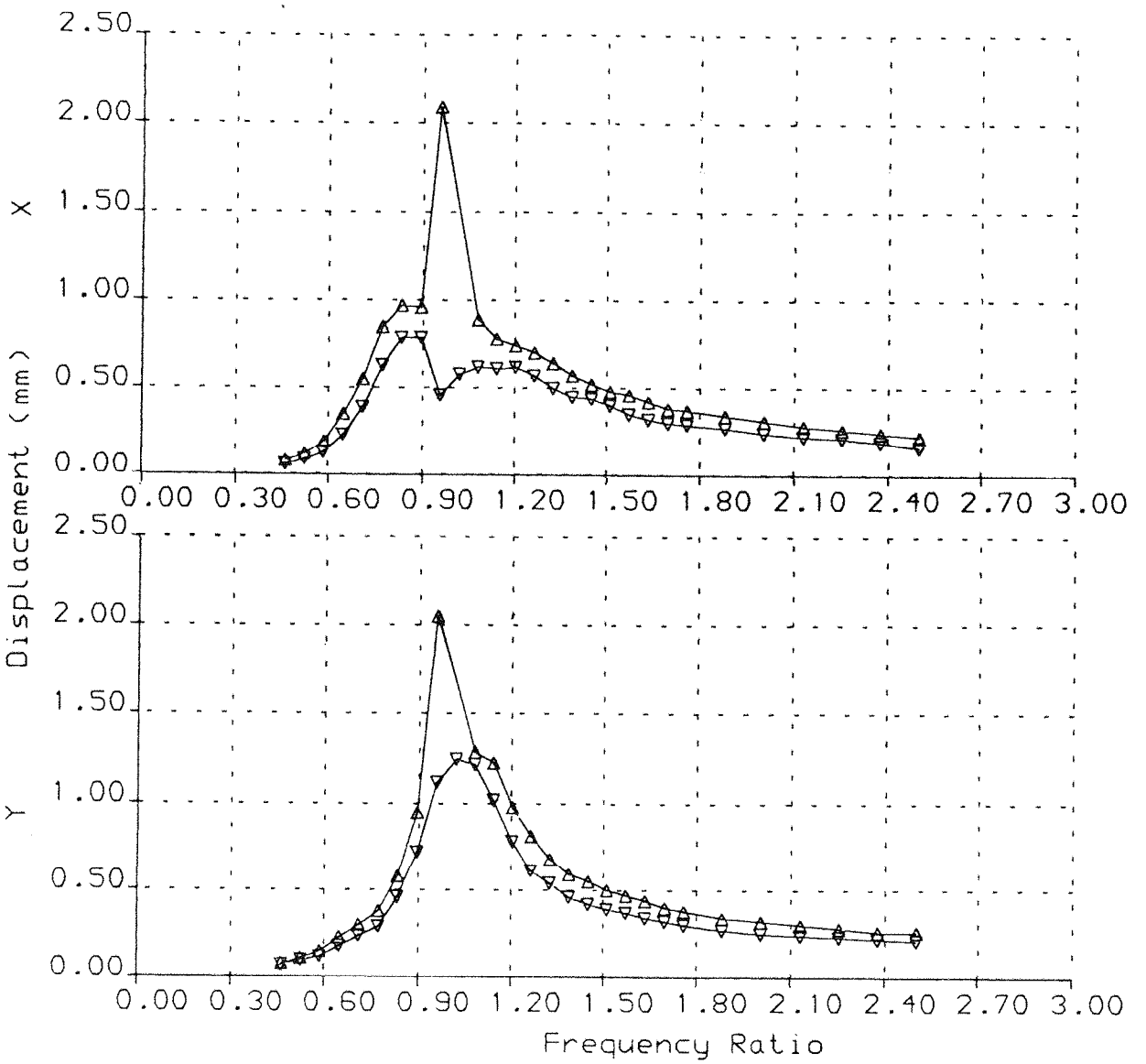

ROTOR-BEARING ASSEMBLY RESPONSE TO UNBALANCE
SQUEEZE-FILM DAMPER RESEARCH Rig Config. 3b

FIGURE 7.30c

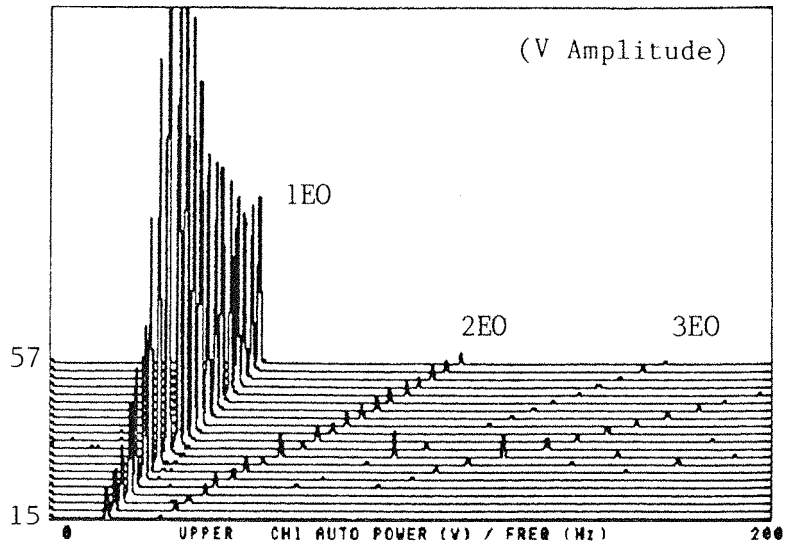

Qc_2 = 0.611
Psup= 2 psi
Eo_1 = 0.0
Eo_2 = 1.0

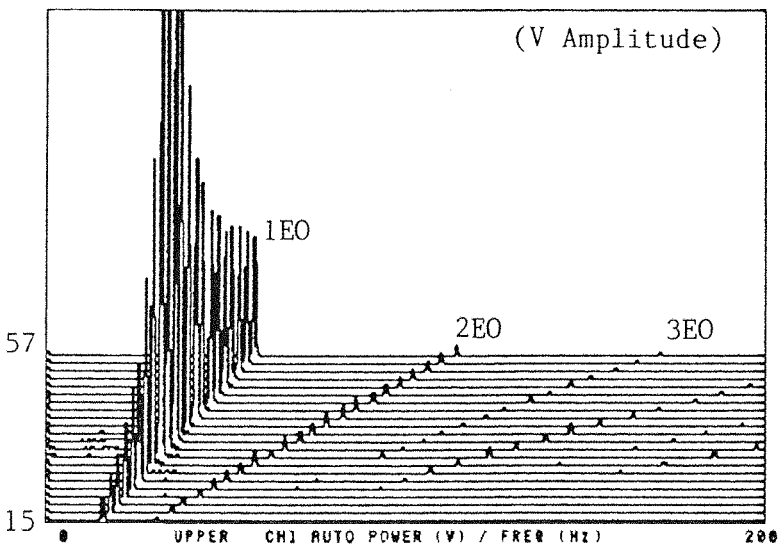

Qc_2 = 0.490
Psup= 2 psi
Eo_1 = 0.0
Eo_2 = 1.0

Configuration 3b

ROTOR VIBRATION RELATIVE TO GROUND AT SFD2

EXPERIMENTAL WATERFALL DIAGRAMS

FIGURE 7.31

PHASE PLANE TRAJECTORIES

(Illustrating the Hardening Spring Response)

FIGURE 9.1

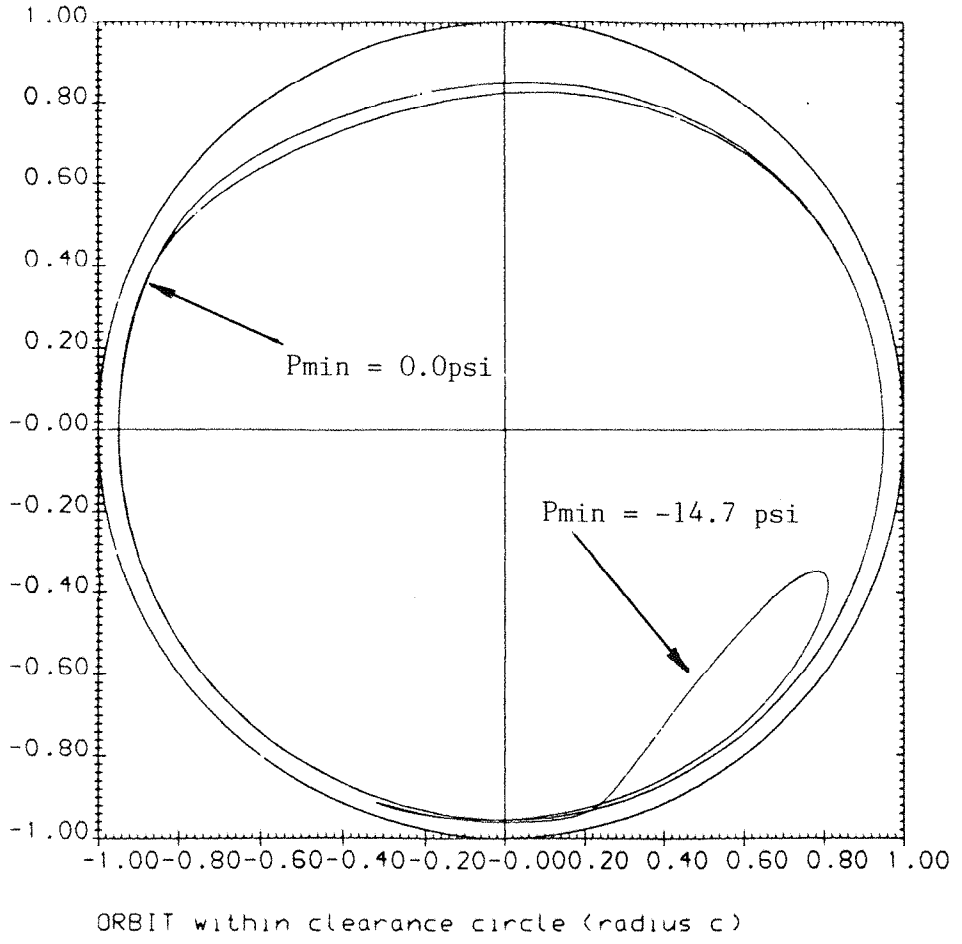

JUMP IN ORBIT SIZE CAUSED BY AN INCREASE IN CAVITATION

FIGURE 9.3

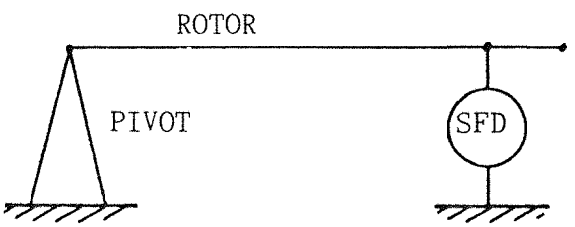

SIMPLE RIG MODEL

FIGURE 9.2

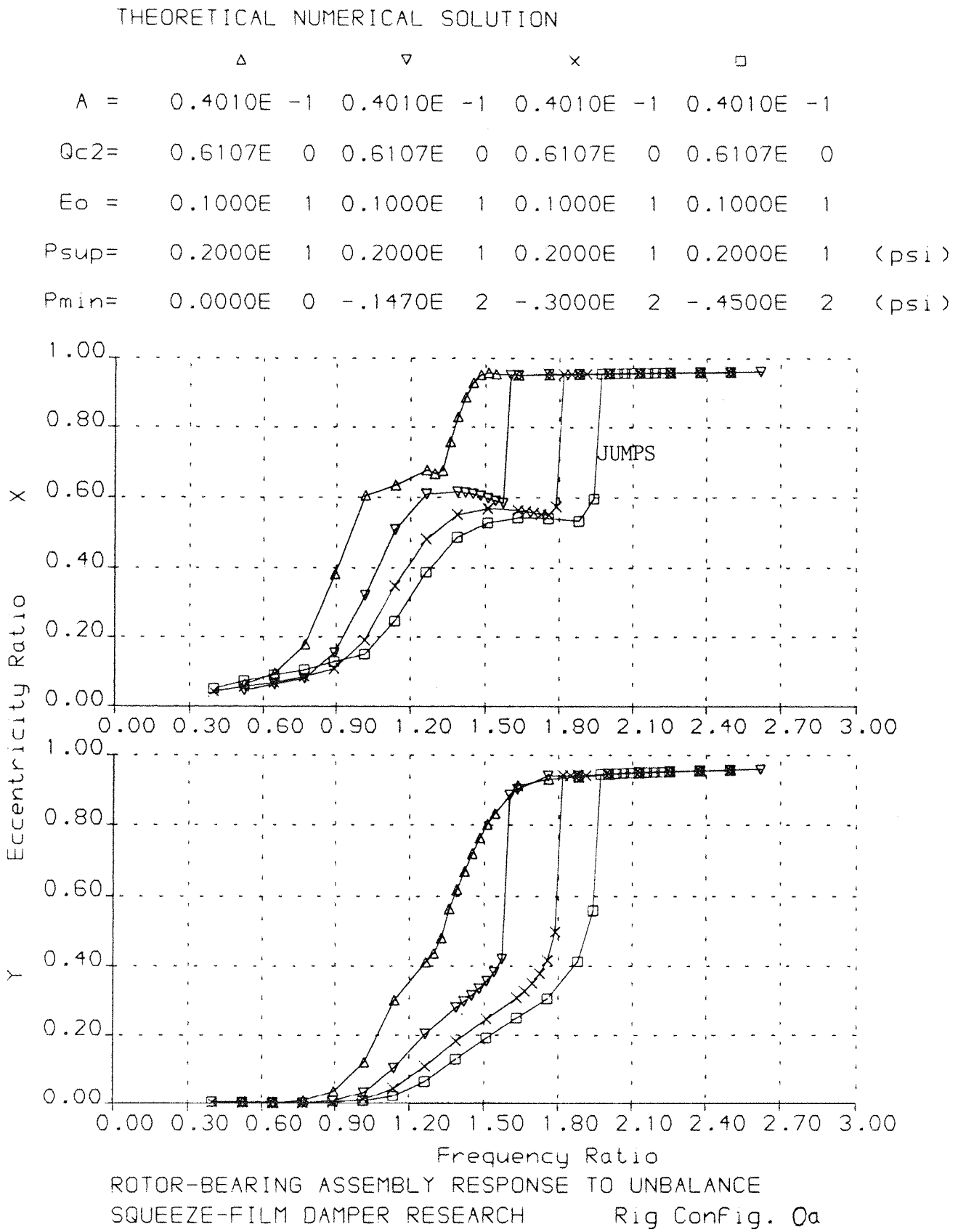

VARIATION IN JUMP SPEED WITH CAVITATION PRESSURE

FIGURE 9.4

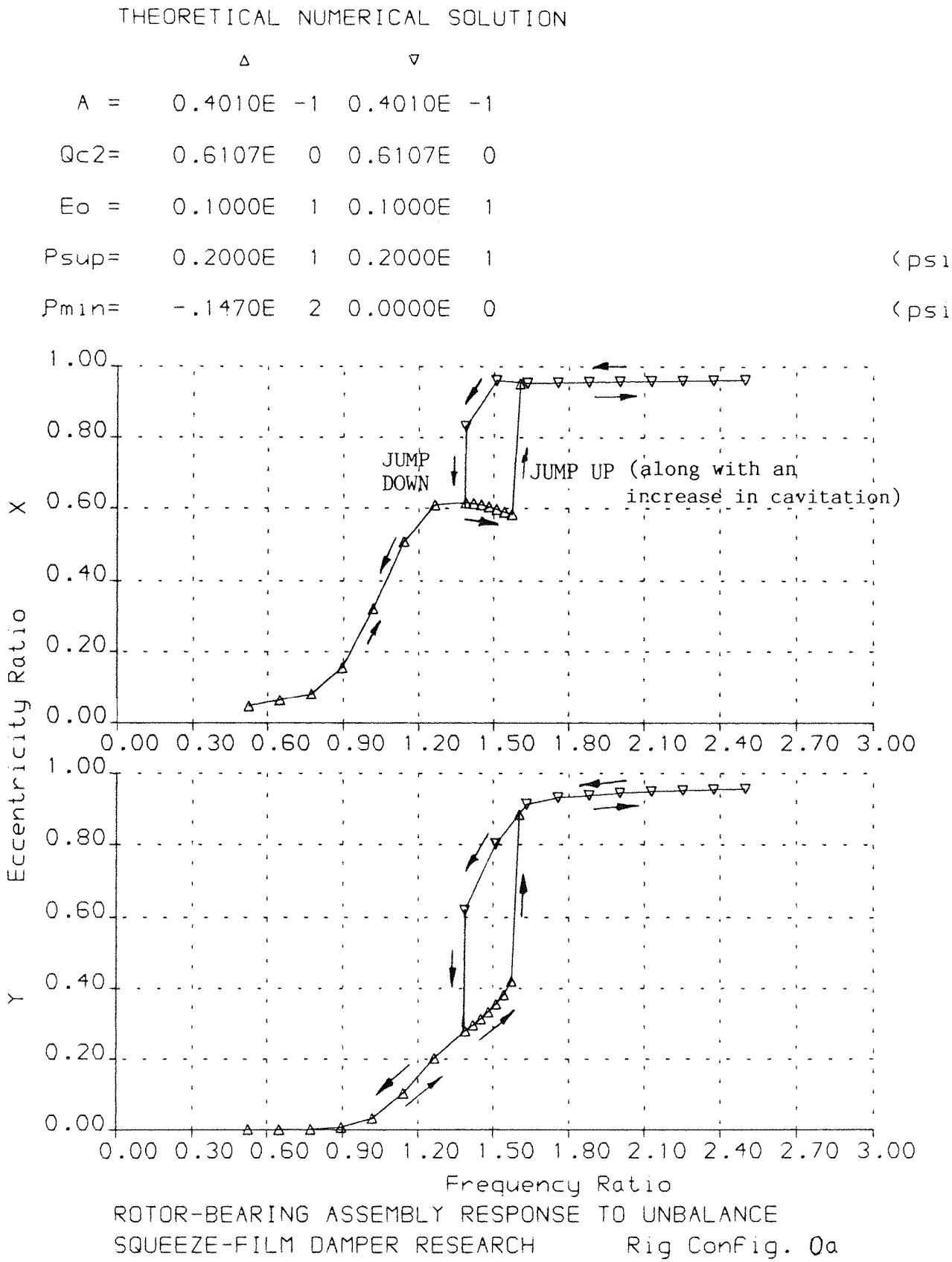

MODELLING JUMP SPEED HYSTERESIS BY
CHANGING CAVITATION PRESSURE

FIGURE 9.5

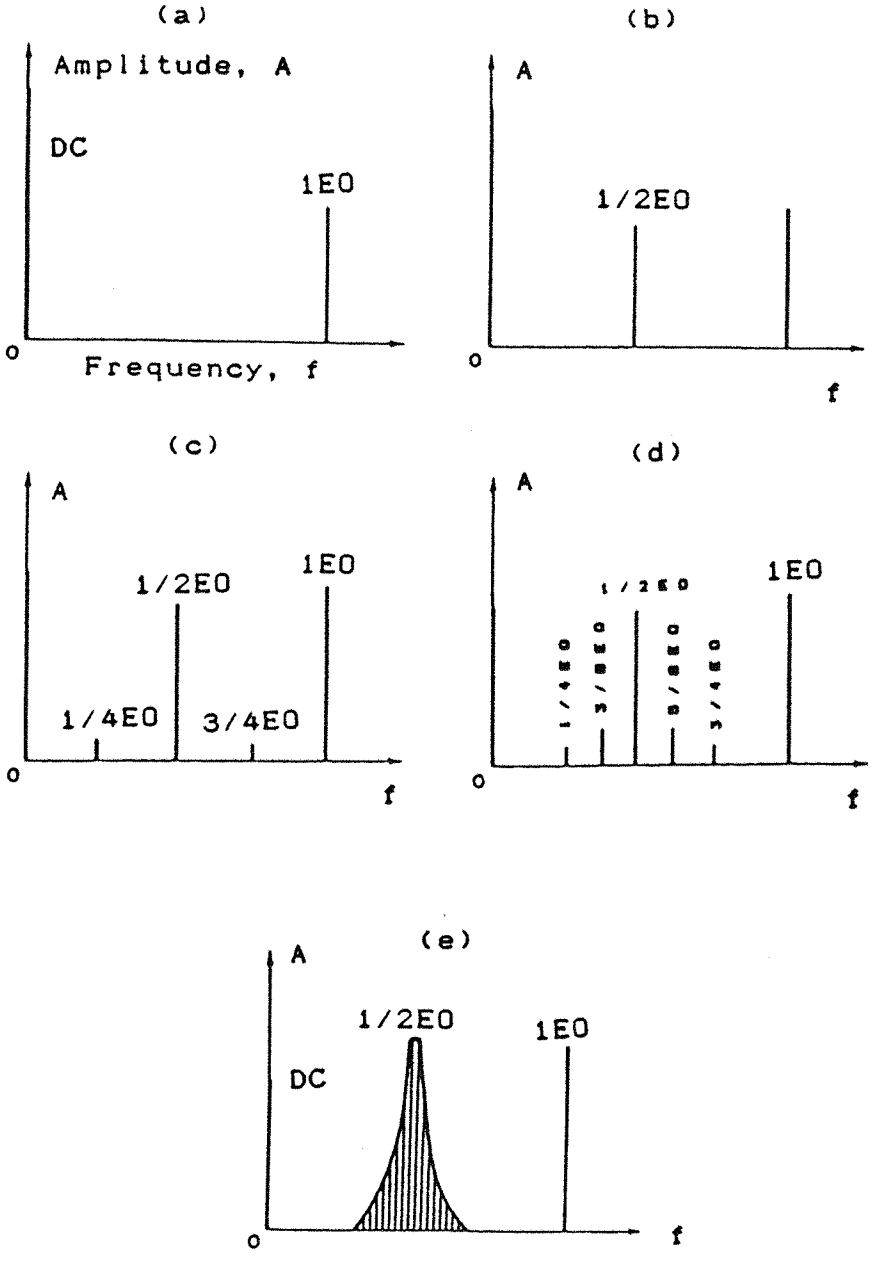

DEVELOPMENT OF HALF ENGINE ORDER
SUBHARMONIC FREQUENCY COMPONENTS

FIGURE 9.6

(a)

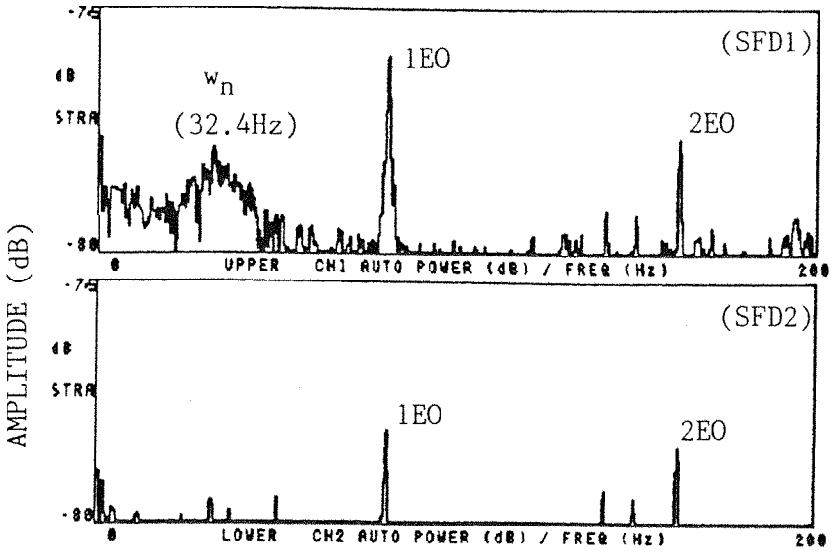

(w/w_n = 2.50, Eo_1 = 0.0)

(b)

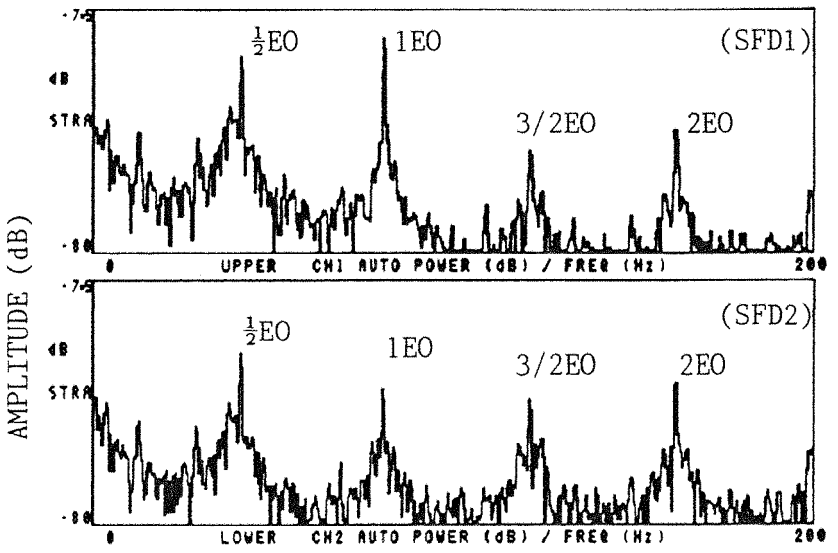

(w/w_n = 2.50, Eo_1 = 0.5)

Configuration 2a (Qc_2=0.611, Psup=2psi)

THE EFFECT OF SFD MISALIGNMENT ON

SUBSYNCHRONOUS RESONANCE

FIGURE 9.7

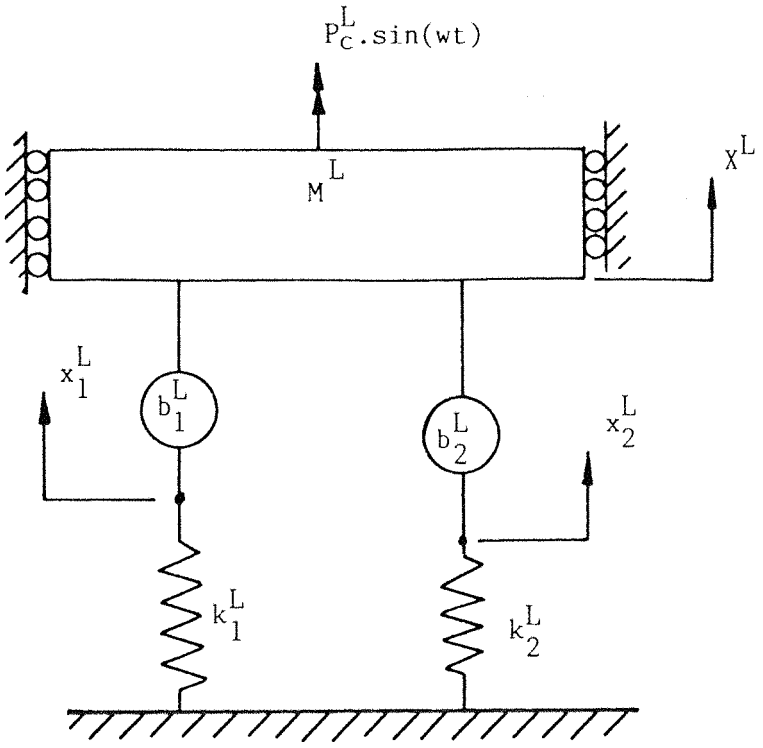

SIMPLE LINEAR MODEL

FIGURE 10.1

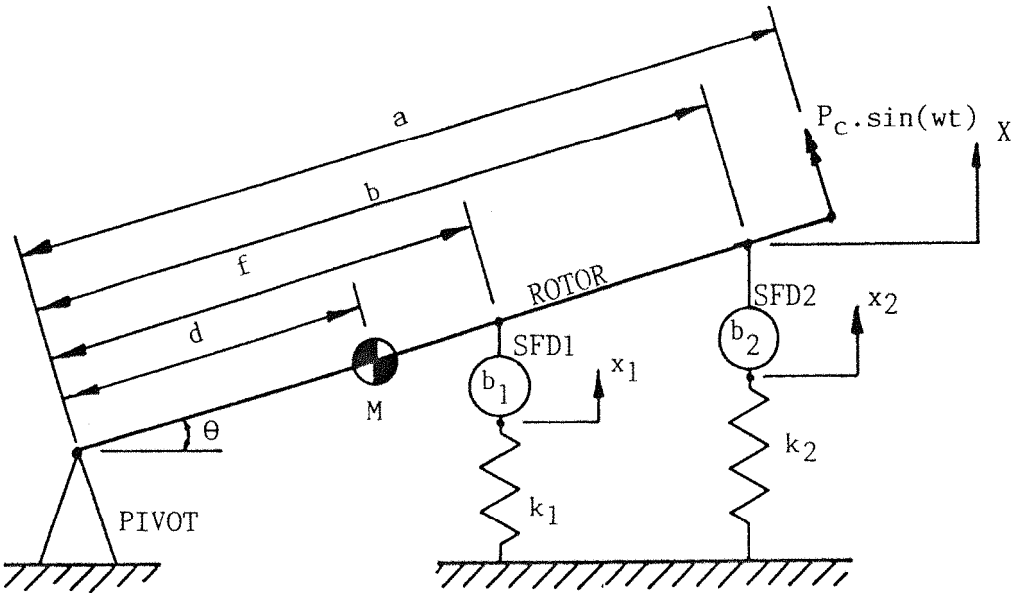

LINEAR RIG MODEL

FIGURE 10.2

Linear Theoretical Solution

	A	B	C	D	
K1 =	0.6081E 6	0.6081E 6	0.6081E 6	0.6081E 6	(N/m)
K2 =	0.1614E 7	0.1614E 7	0.1614E 7	0.1614E 7	(N/m)
b1 =	0.6031E 2	0.2412E 3	0.9650E 3	0.7720E 4	(Ns/m)
b2 =	0.4590E 3	0.9384E 3	0.3588E 4	0.2016E 5	(Ns/m)
Wnat =	0.4747E 2	0.4747E 2	0.4747E 2	0.4747E 2	(Hz)
R =	0.2850E -1	0.1181E 0	0.4725E 0	0.3780E 1	(-)

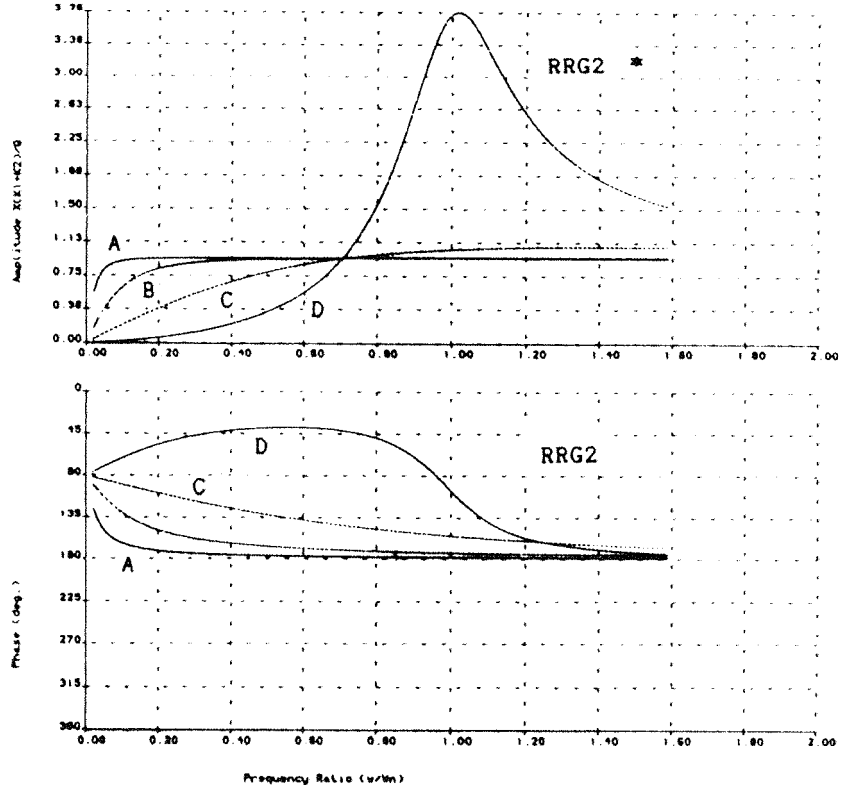

ROTOR-BEARING ASSEMBLY RESPONSE TO UNBALANCE
SQUEEZE-FILM DAMPER RESEARCH

* RRG2 - Rotor Relative to Ground at SFD2

Configuration 3a
FIGURE 10.3

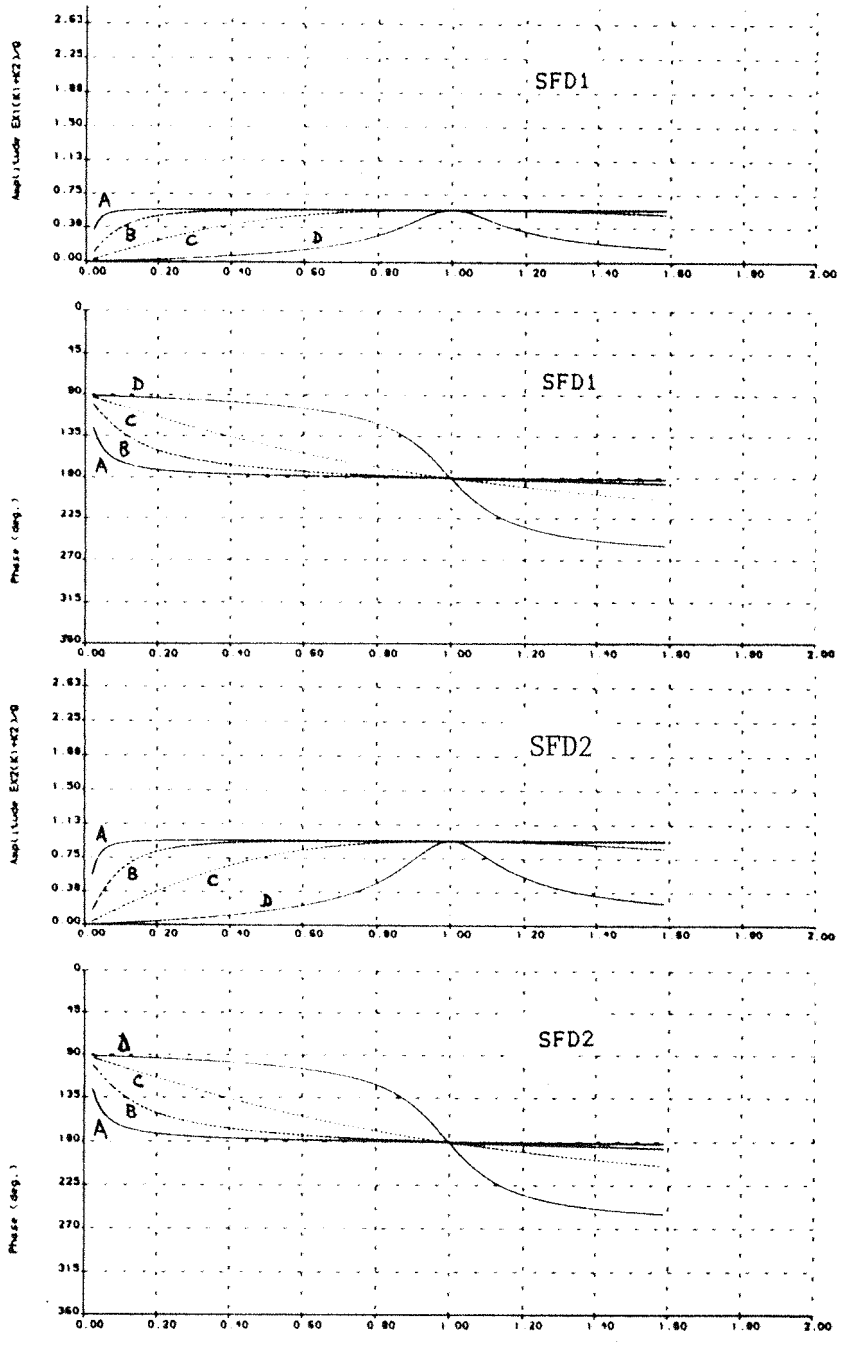

Linear Theoretical Solution

	A	B	C	D	
K1 =	0.6091E 6	0.6081E 6	0.6091E 6	0.6091E 6	(N/m)
K2 =	0.1614E 7	0.1614E 7	0.1614E 7	0.1614E 7	(N/m)
b1 =	0.1208E 2	0.4925E 2	0.1930E 3	0.1544E 4	(Ns/m)
b2 =	0.1588E 3	0.6384E 3	0.2558E 4	0.2048E 5	(Ns/m)
Wnat=	0.4747E 2	0.4747E 2	0.4747E 2	0.4747E 2	(Hz)
B =	0.2310E -1	0.9220E -1	0.3688E 0	0.2851E 1	(-)

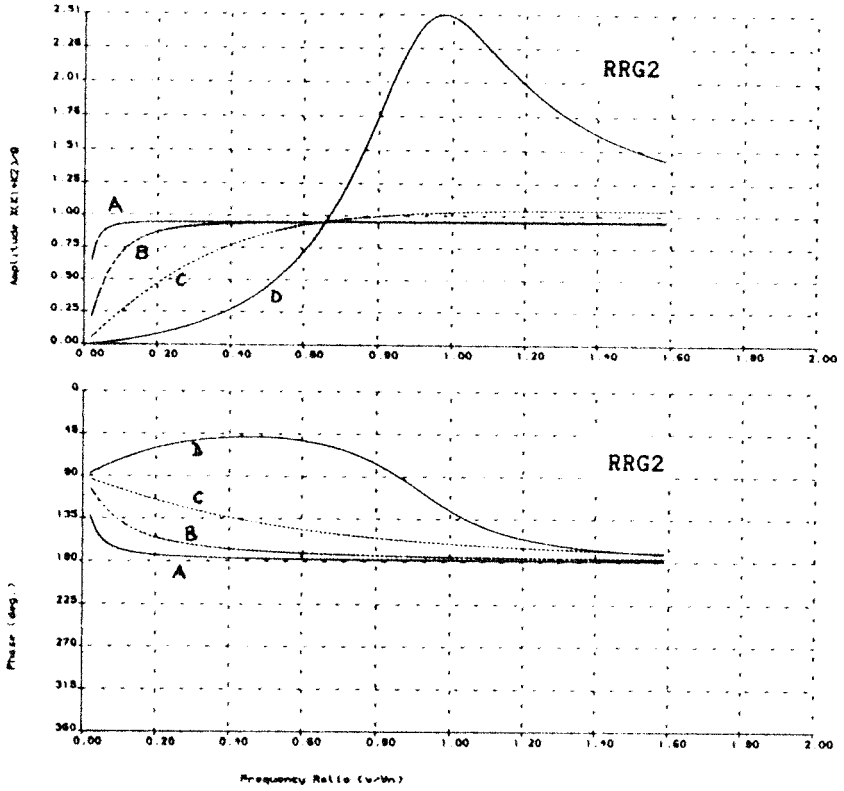

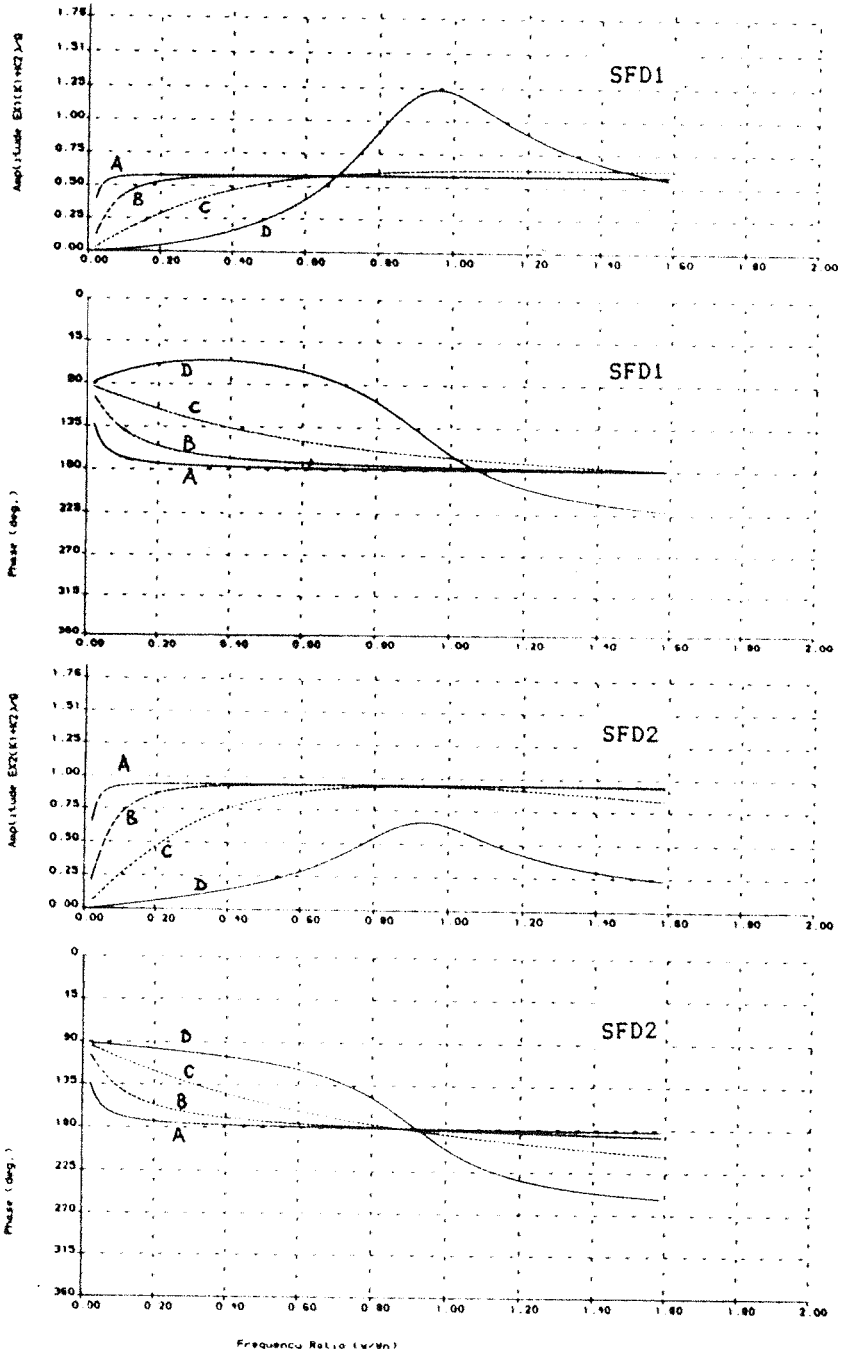

ROTOR-BEARING ASSEMBLY RESPONSE TO UNBALANCE
SQUEEZE-FILM DAMPER RESEARCH

Configuration 3b

FIGURE 10.4

Linear Theoretical Solution

	A	B	C	D	
K1 =	0.6091E 11	0.6091E 11	0.6091E 11	0.6091E 11	(N/m)
K2 =	0.1614E 7	0.1614E 7	0.1614E 7	0.1614E 7	(N/m)
b1 =	0.1206E 4	0.4825E 4	0.1930E 5	0.7719E 5	(Ns/m)
b2 =	0.1598E 5	0.6391E 5	0.2558E 6	0.2046E 6	(Ns/m)
wnat =	0.4044E 2	0.4044E 2	0.4044E 2	0.4044E 2	(Hz)
B =	0.2710E -1	0.1082E 0	0.4330E 0	0.3464E 1	(-)

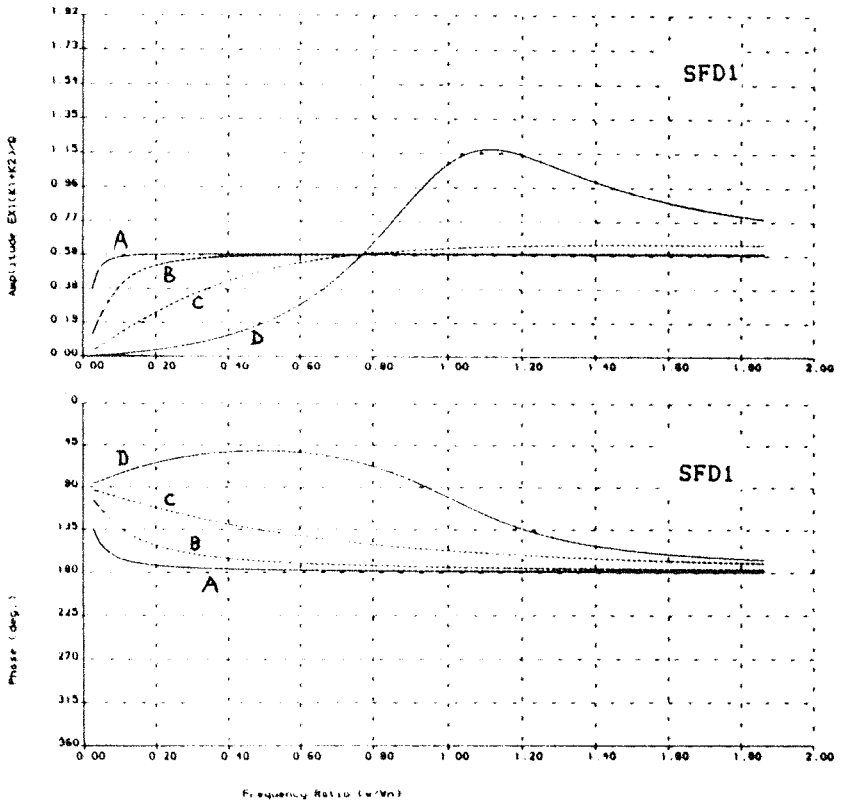

ROTOR-BEARING ASSEMBLY RESPONSE TO UNBALANCE
SQUEEZE-FILM DAMPER RESEARCH

Configuration 2a

FIGURE 10.5

Linear Theoretical Solution

	A	B	C	D	
K1 =	0.6091E 11	0.6091E 11	0.6091E 11	0.6091E 11	(N/m)
K2 =	0.1614E 7	0.1614E 7	0.1614E 7	0.1614E 7	(N/m)
b1 =	0.1206E 4	0.4825E 4	0.1930E 5	0.7719E 5	(Ns/m)
b2 =	0.1598E 5	0.6391E 5	0.2558E 6	0.2046E 6	(Ns/m)
wnat =	0.4044E 2	0.4044E 2	0.4044E 2	0.4044E 2	(Hz)
B =	0.2710E -1	0.1082E 0	0.4330E 0	0.3464E 1	(-)

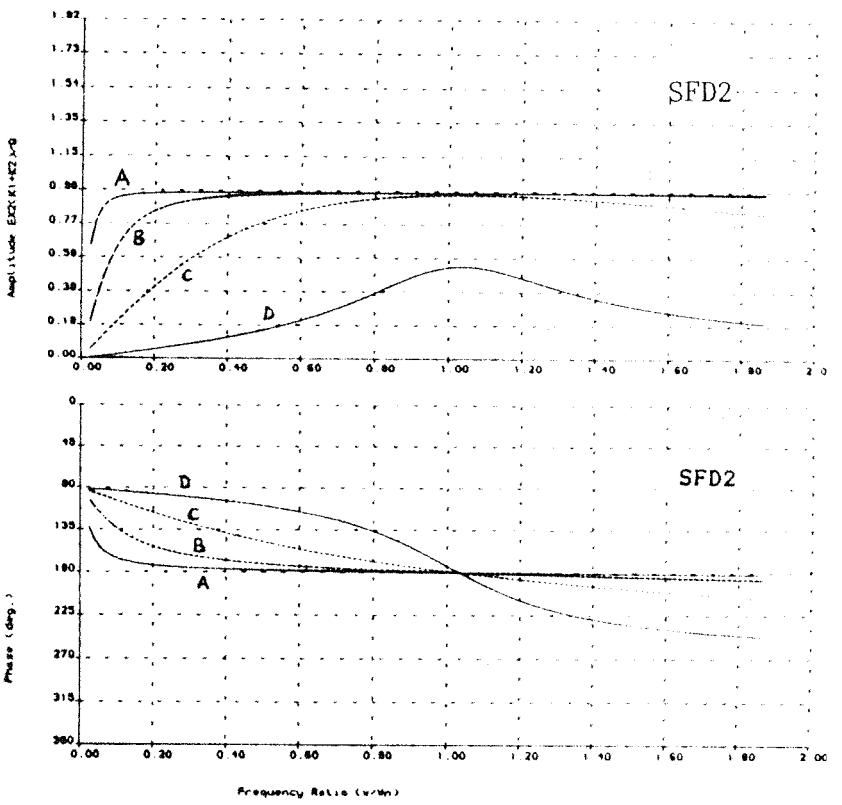

ROTOR-BEARING ASSEMBLY RESPONSE TO UNBALANCE
SQUEEZE-FILM DAMPER RESEARCH

Configuration 2b (Horizontal Direction)

FIGURE 10.6

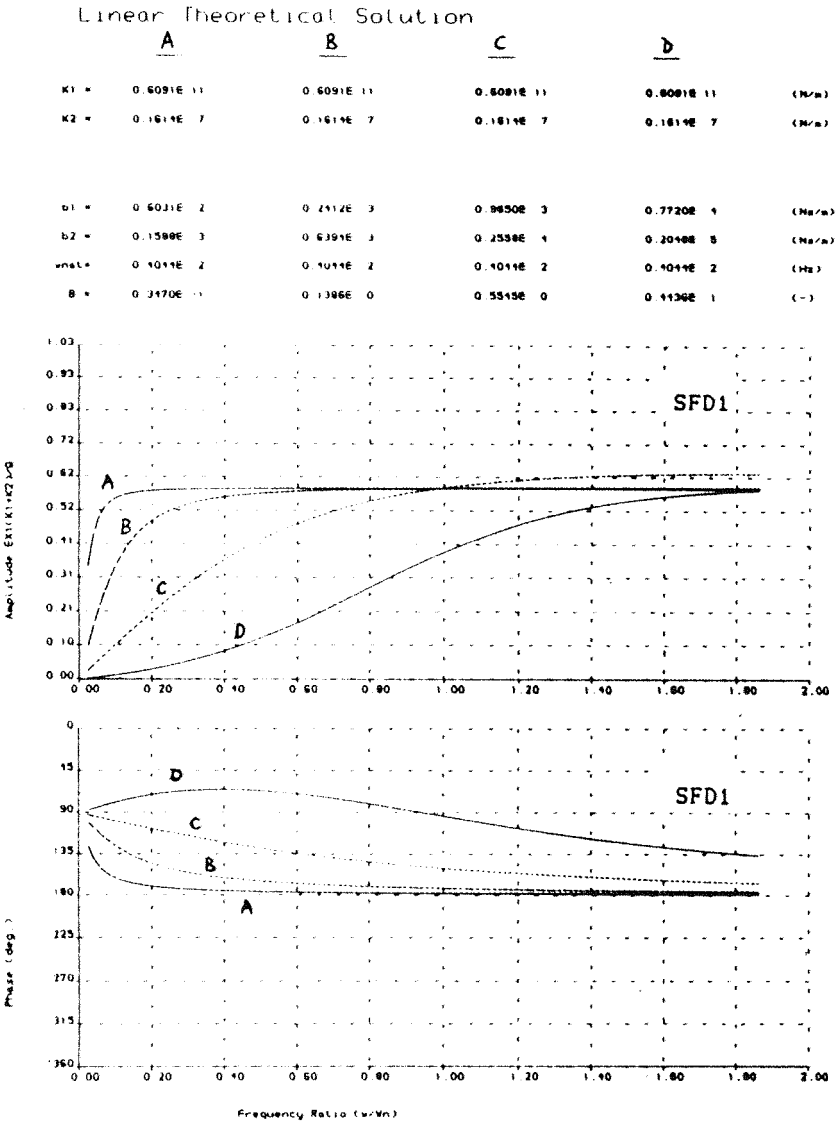

ROTOR-BEARING ASSEMBLY RESPONSE TO UNBALANCE
SQUEEZE-FILM DAMPER RESEARCH

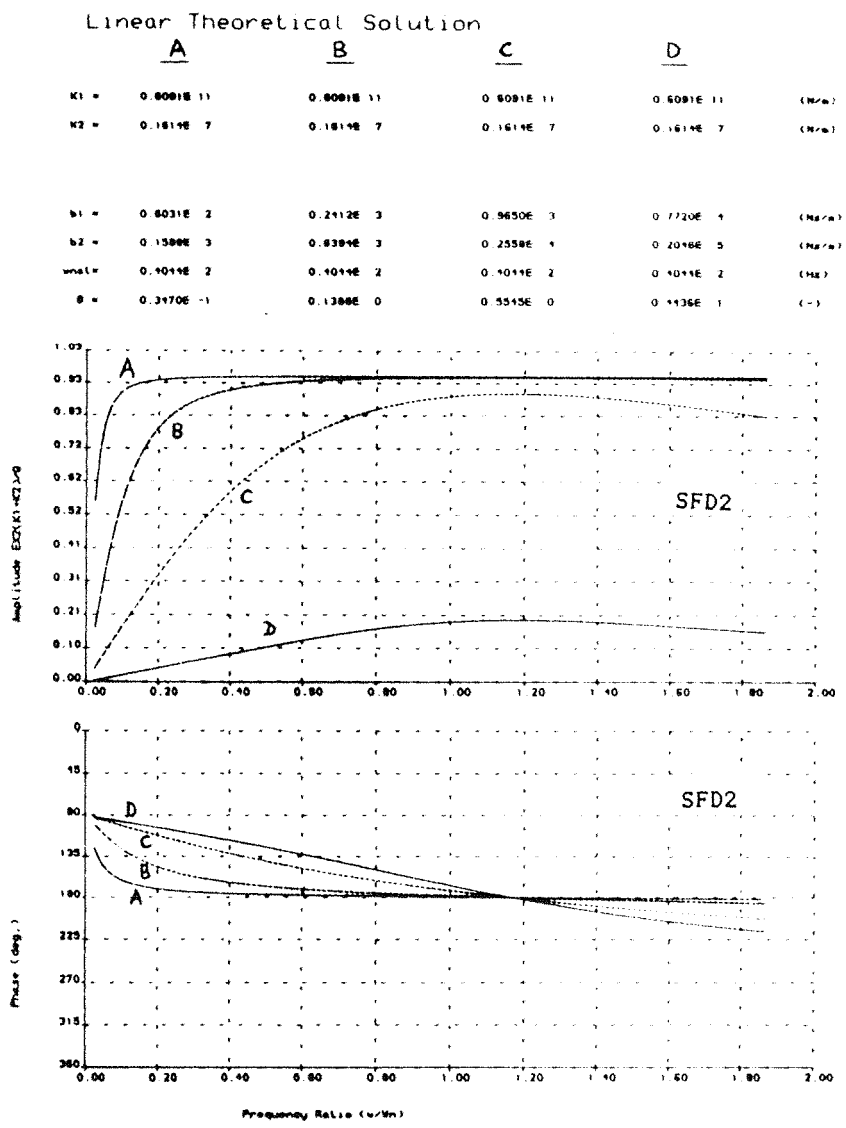

ROTOR-BEARING ASSEMBLY RESPONSE TO UNBALANCE
SQUEEZE-FILM DAMPER RESEARCH

Linear Theoretical Solution

	A	B	C	D	
K1 =	0.6091E 11	0.6091E 11	0.6091E 11	0.6091E 11	(N/m)
K2 =	0.1614E 7	0.1614E 7	0.1614E 7	0.1614E 7	(N/m)
b1 =	0.3015E 3	0.1206E 4	0.4825E 4	0.3860E 5	(Ns/m)
b2 =	0.1598E 3	0.6391E 3	0.2558E 4	0.2046E 5	(Ns/m)
wnat =	0.4044E 2	0.4044E 2	0.4044E 2	0.4044E 2	(Hz)
B =	0.7250E -1	0.2905E 0	0.1162E 1	0.9296E 1	(-)

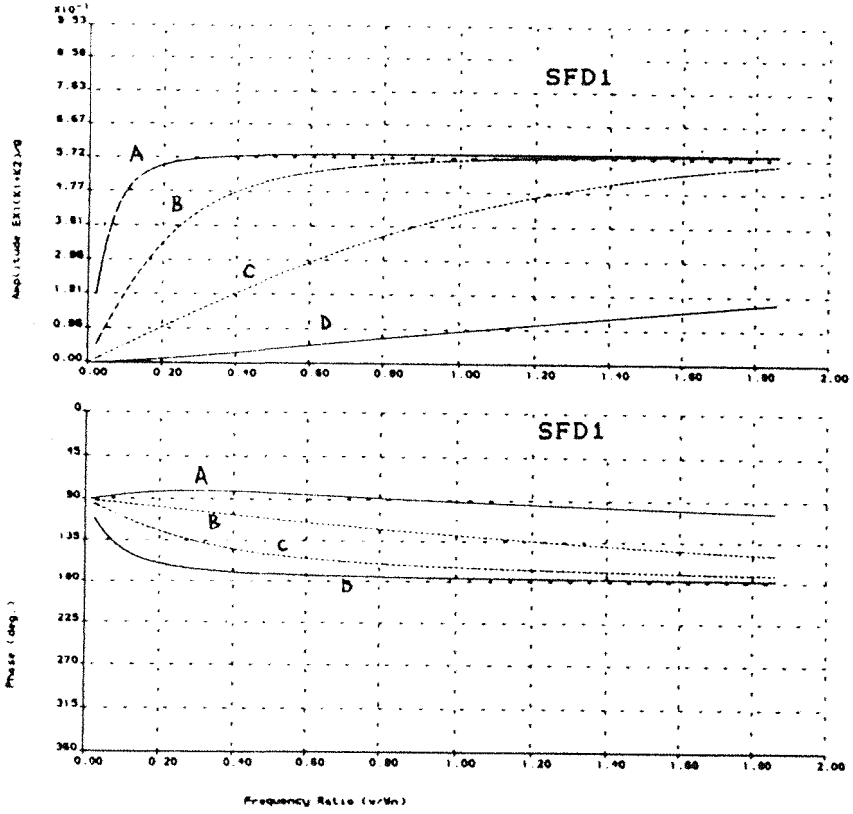

ROTOR-BEARING ASSEMBLY RESPONSE TO UNBALANCE
SQUEEZE-FILM DAMPER RESEARCH

Configuration 2b (Vertical Direction)

FIGURE 10.7

Linear Theoretical Solution

	A	B	C	D	
K1 =	0.6091E 11	0.6091E 11	0.6091E 11	0.6091E 11	(N/m)
K2 =	0.1614E 7	0.1614E 7	0.1614E 7	0.1614E 7	(N/m)
b1 =	0.3015E 3	0.1206E 4	0.4825E 4	0.3860E 5	(Ns/m)
b2 =	0.1598E 3	0.6391E 3	0.2558E 4	0.2046E 5	(Ns/m)
wnat =	0.4044E 2	0.4044E 2	0.4044E 2	0.4044E 2	(Hz)
B =	0.7250E -1	0.2905E 0	0.1162E 1	0.9296E 1	(-)

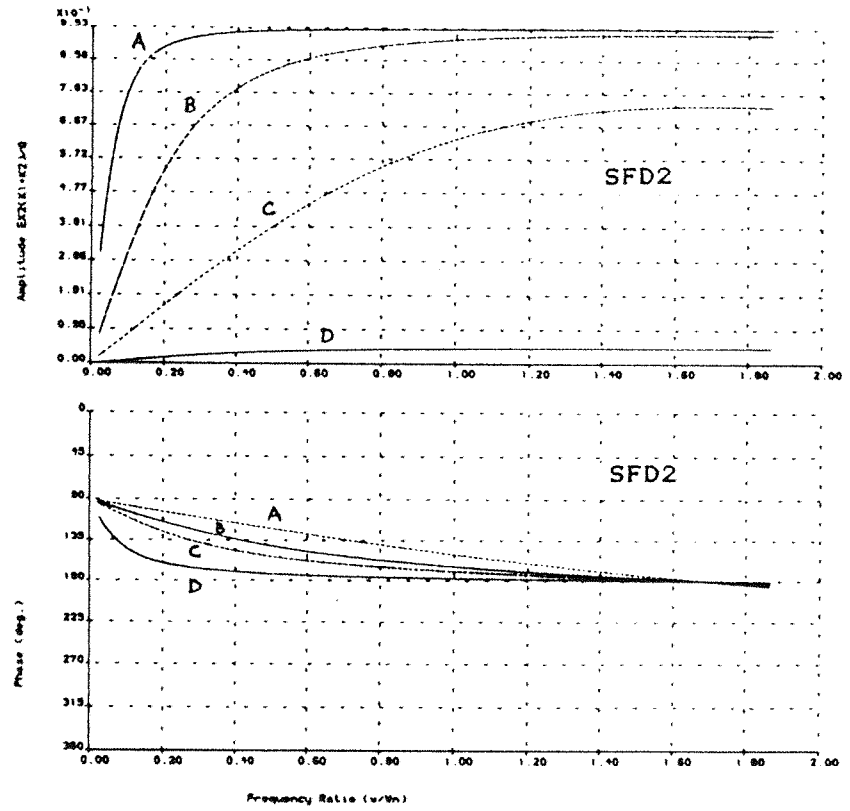

ROTOR-BEARING ASSEMBLY RESPONSE TO UNBALANCE
SQUEEZE-FILM DAMPER RESEARCH

Linear Theoretical Solution

	A	B	C	D	
K1 =	0.6091E 13	0.6091E 13	0.6091E 13	0.6091E 13	(N/m)
K2 =	0.1614E 7	0.1614E 7	0.1614E 7	0.1614E 7	(N/m)
b1 =	0.6031E 2	0.2412E 3	0.9650E 3	0.7720E 4	(Ns/m)
b2 =	0.1598E 11	0.6394E 11	0.2558E 12	0.2046E 13	(Ns/m)
wnat=	0.4044E 2	0.4044E 2	0.4044E 2	0.4044E 2	(Hz)
B =	0.9500E -2	0.3800E -1	0.1519E 0	0.1215E 1	(-)

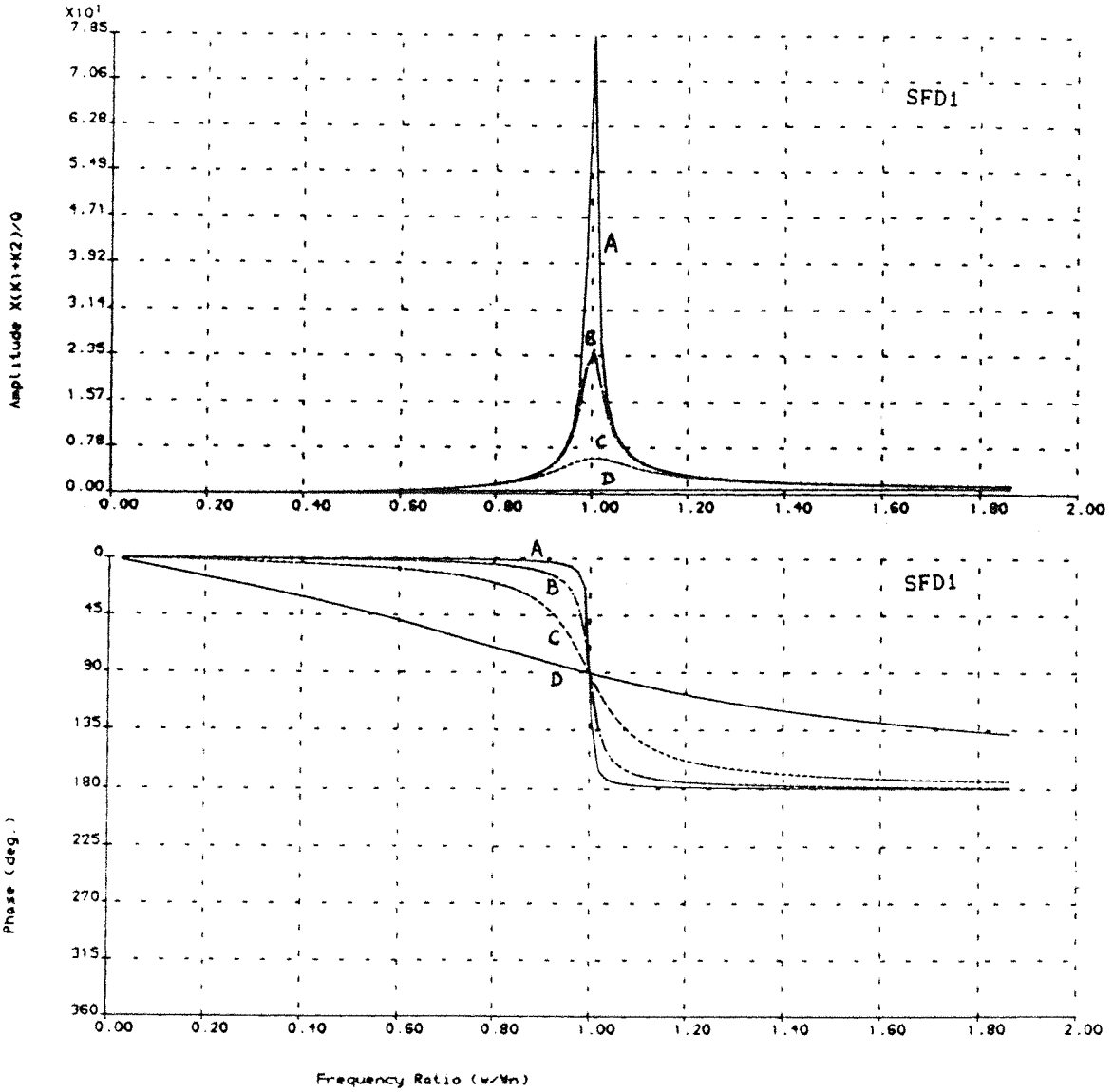

ROTOR-BEARING ASSEMBLY RESPONSE TO UNBALANCE
SQUEEZE-FILM DAMPER RESEARCH

Configurations 1a,b

FIGURE 10.8

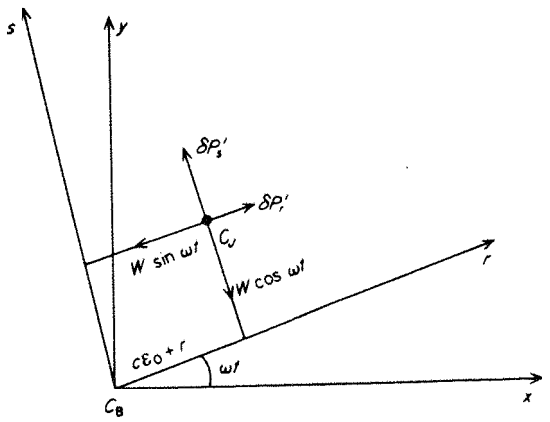

SFD Coordinate Diagram

FIGURE 11.1

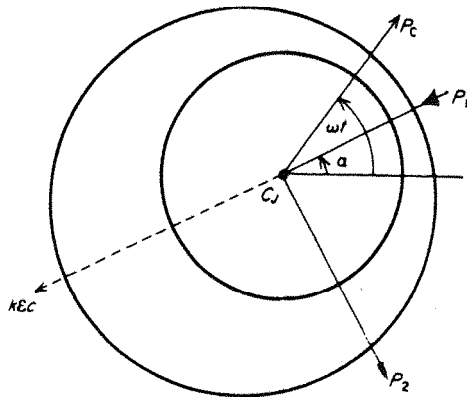

SFD Force Diagram

FIGURE 11.2

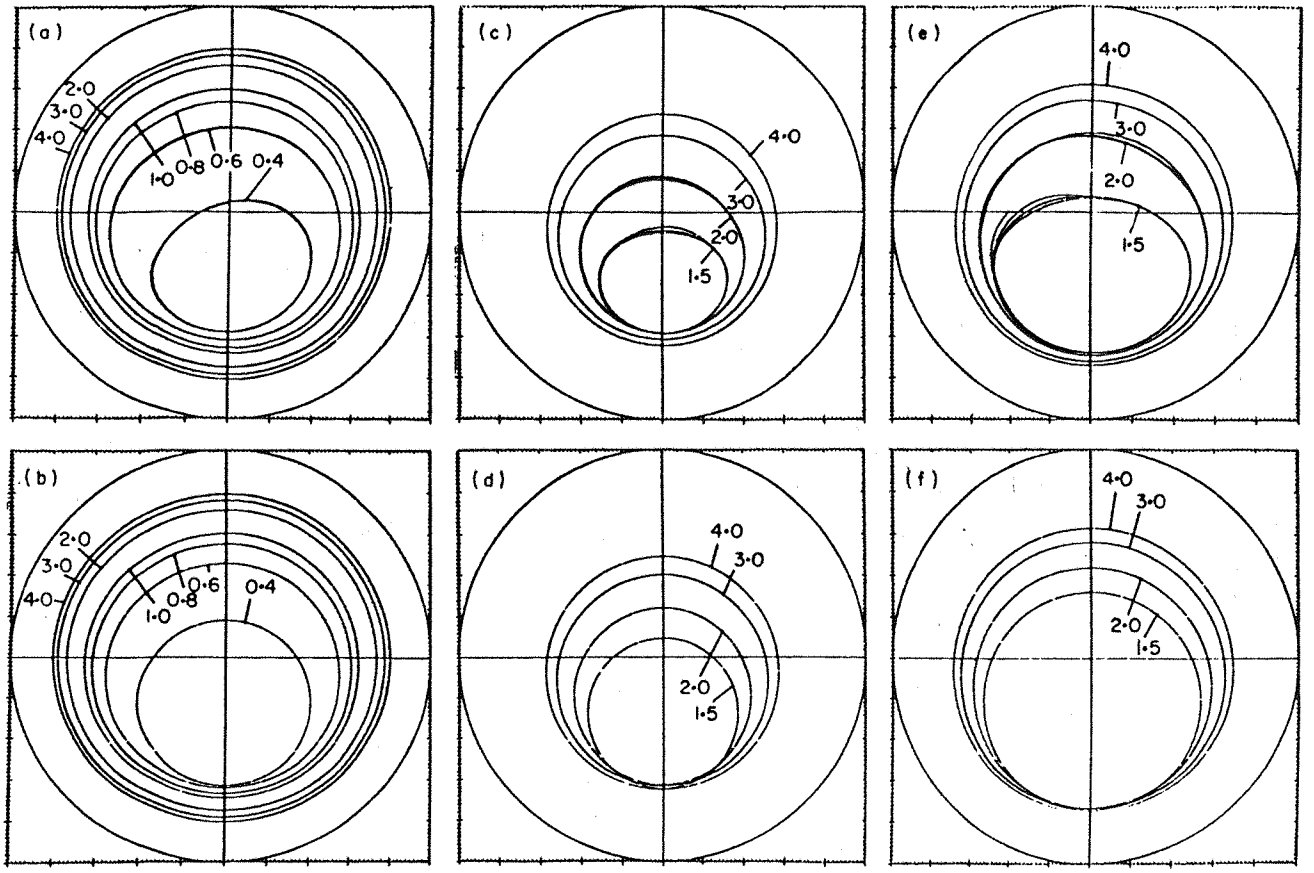

SFD Orbits. (a) Non-Linear, β=0.4, $\overline{W}$=0.2; (b) Linear, β=0.4, $\overline{W}$=0.2;

(c) Non-Linear, β=2.0, $\overline{W}$=1.0; (d) Linear, β=2.0, $\overline{W}$=1.0;

(e) Non-Linear, β=1.0, $\overline{W}$=1.0; (f) Linear, β=1.0, $\overline{W}$=1.0.

FIGURE 11.3

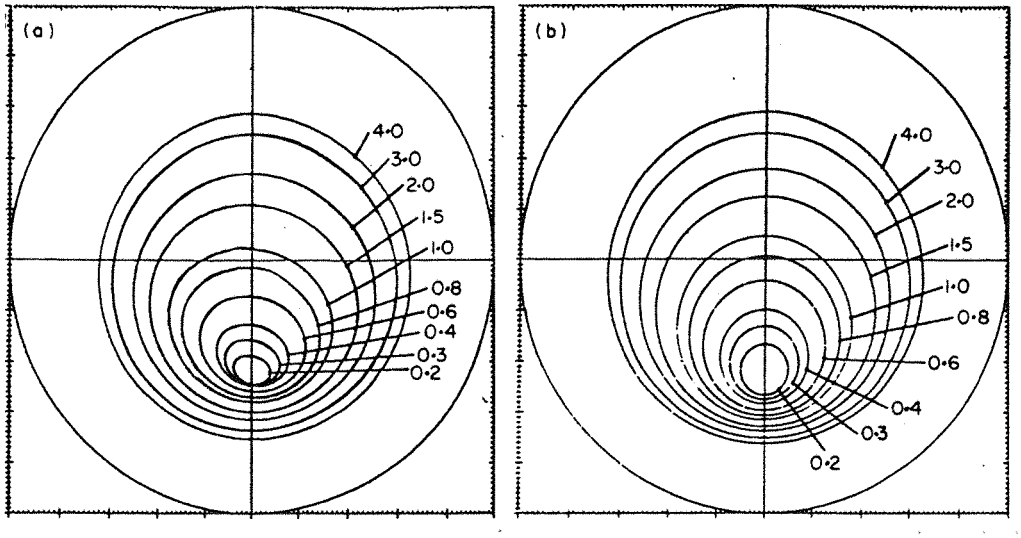

SFD Orbits. (a) Non-Linear, β=1.0, $\overline{W}$=1.0, $\overline{k}$=2.0;

(b) Linear, β=1.0, $\overline{W}$=1.0, $\overline{k}$=2.0.

FIGURE 11.4

HARMONIC BALANCE FLOW DIAGRAM

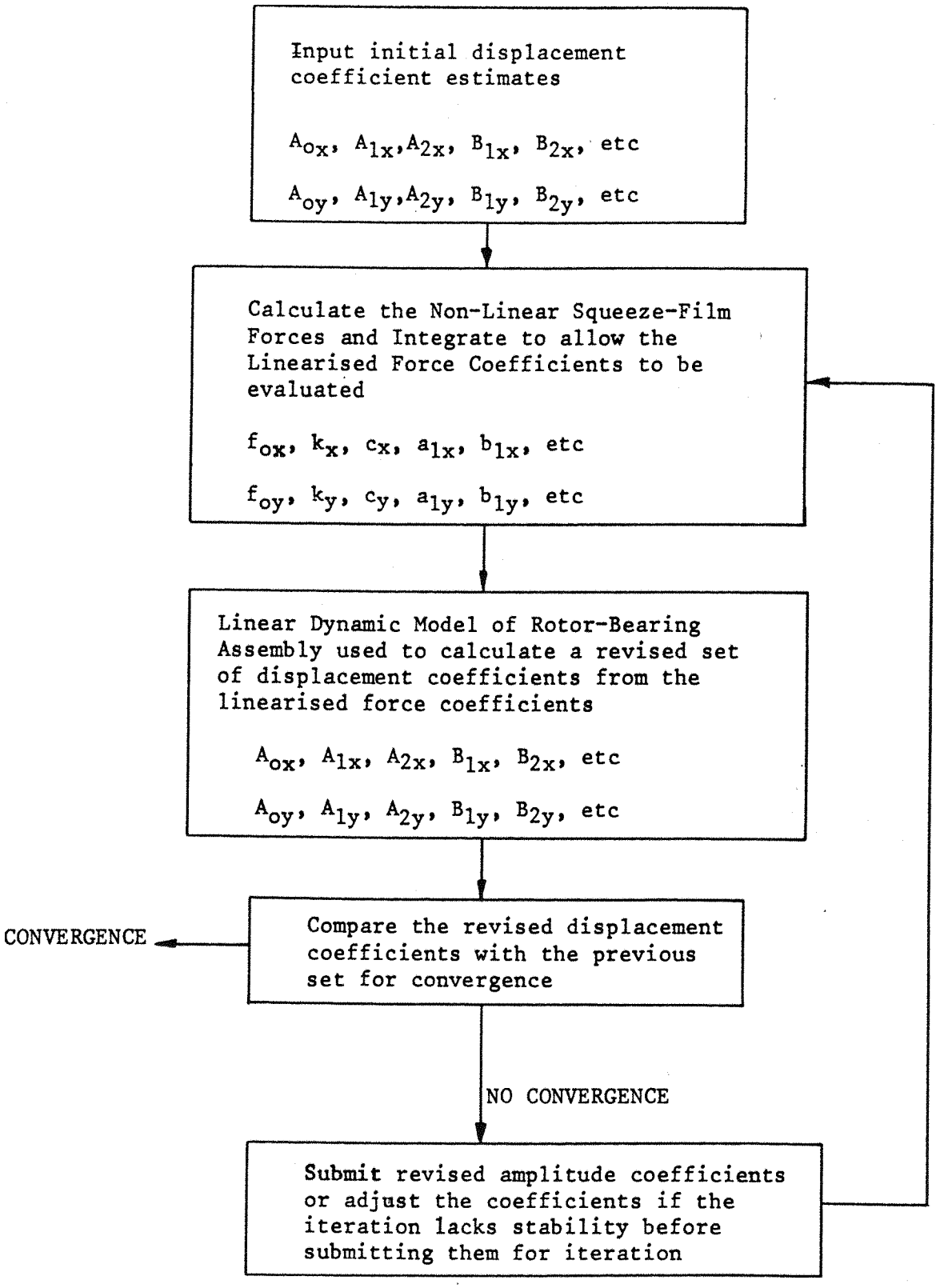

FIGURE 11.5

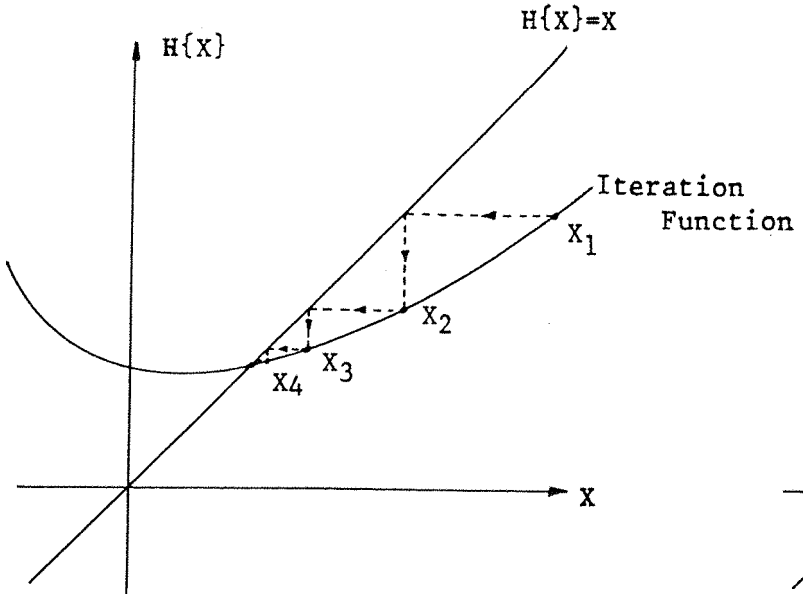

(a) Convergence

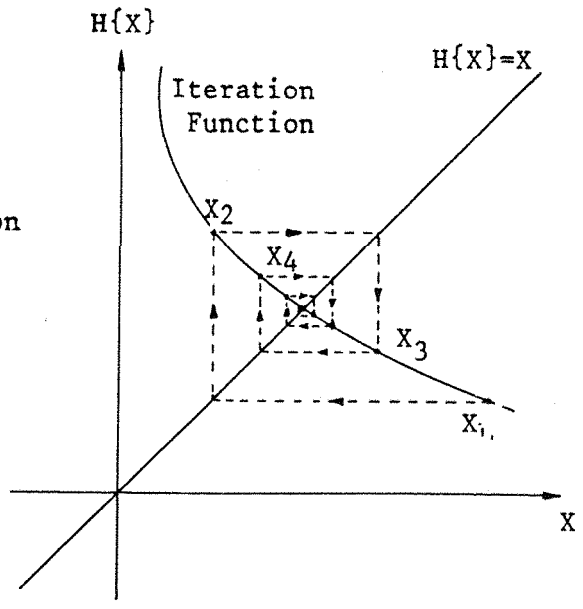

(b) Convergence

FIXED POINT ITERATION METHOD

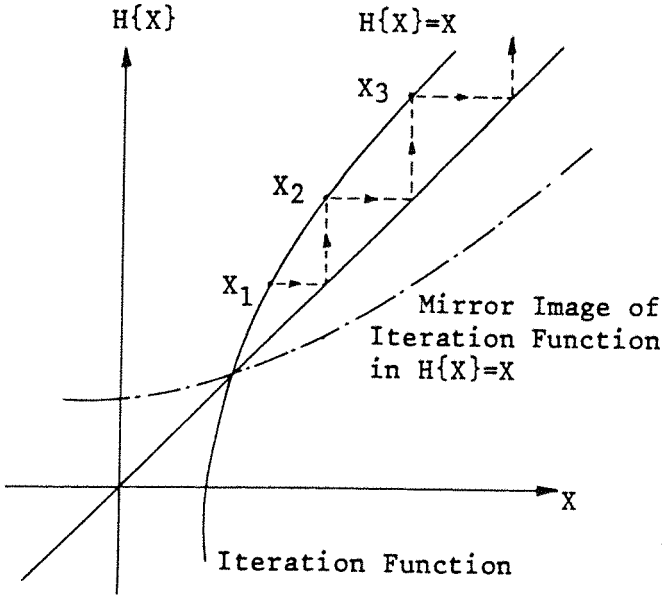

(c) No Convergence

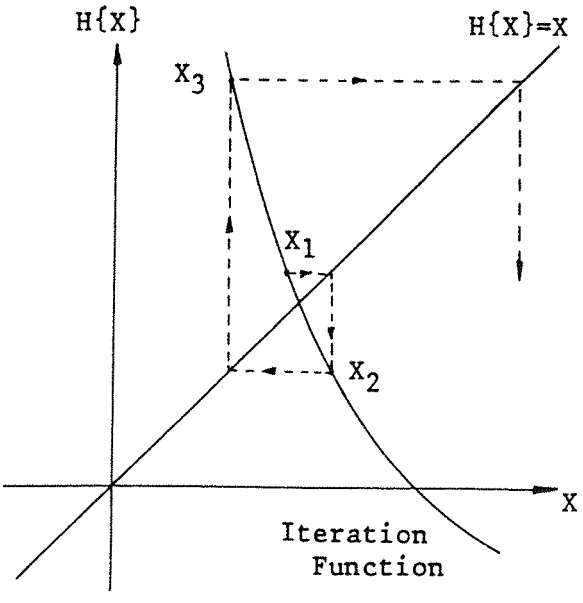

(d) No Convergence

FIGURE A7.1

PLATES

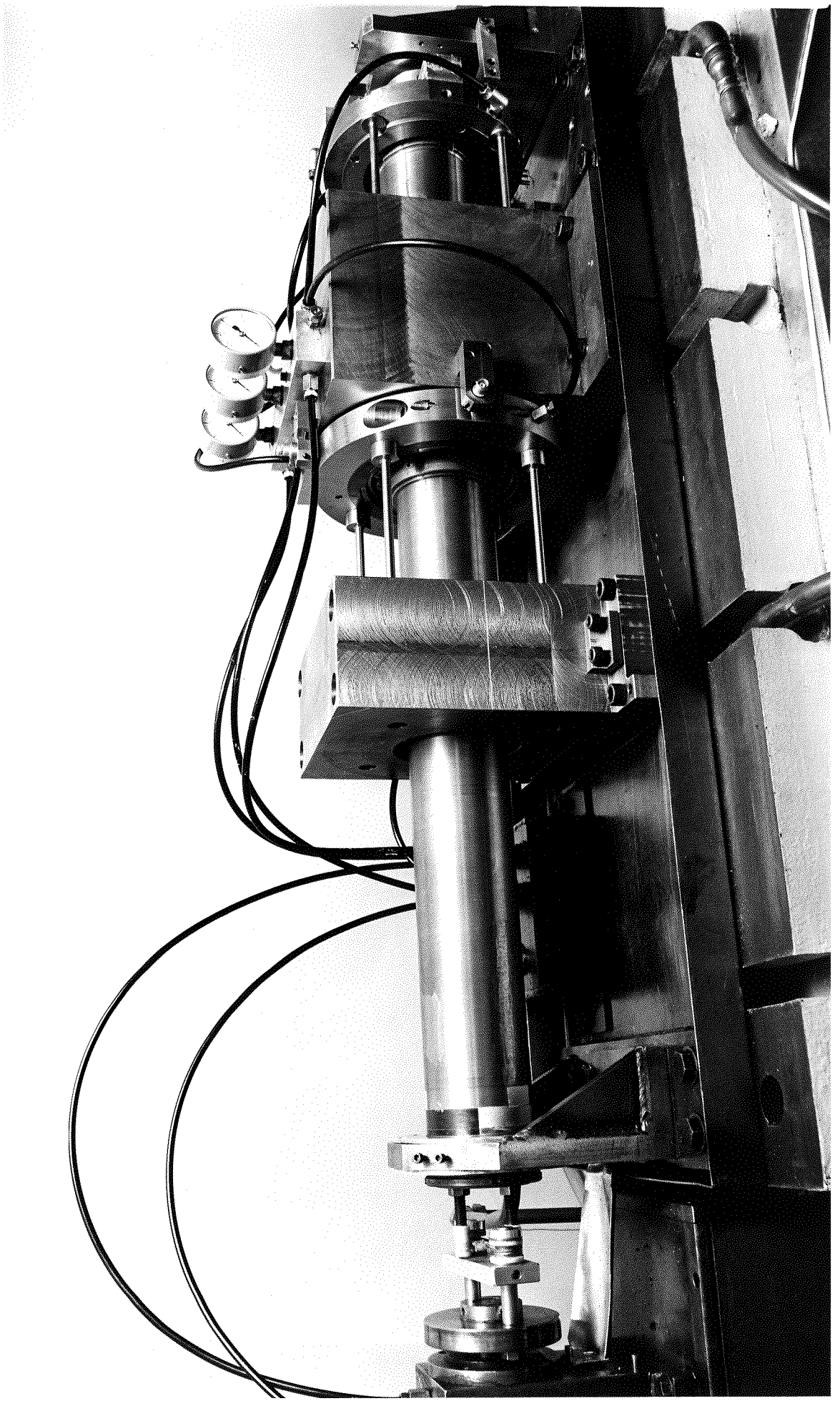

Side Elevation of Test Rig

PLATE 1

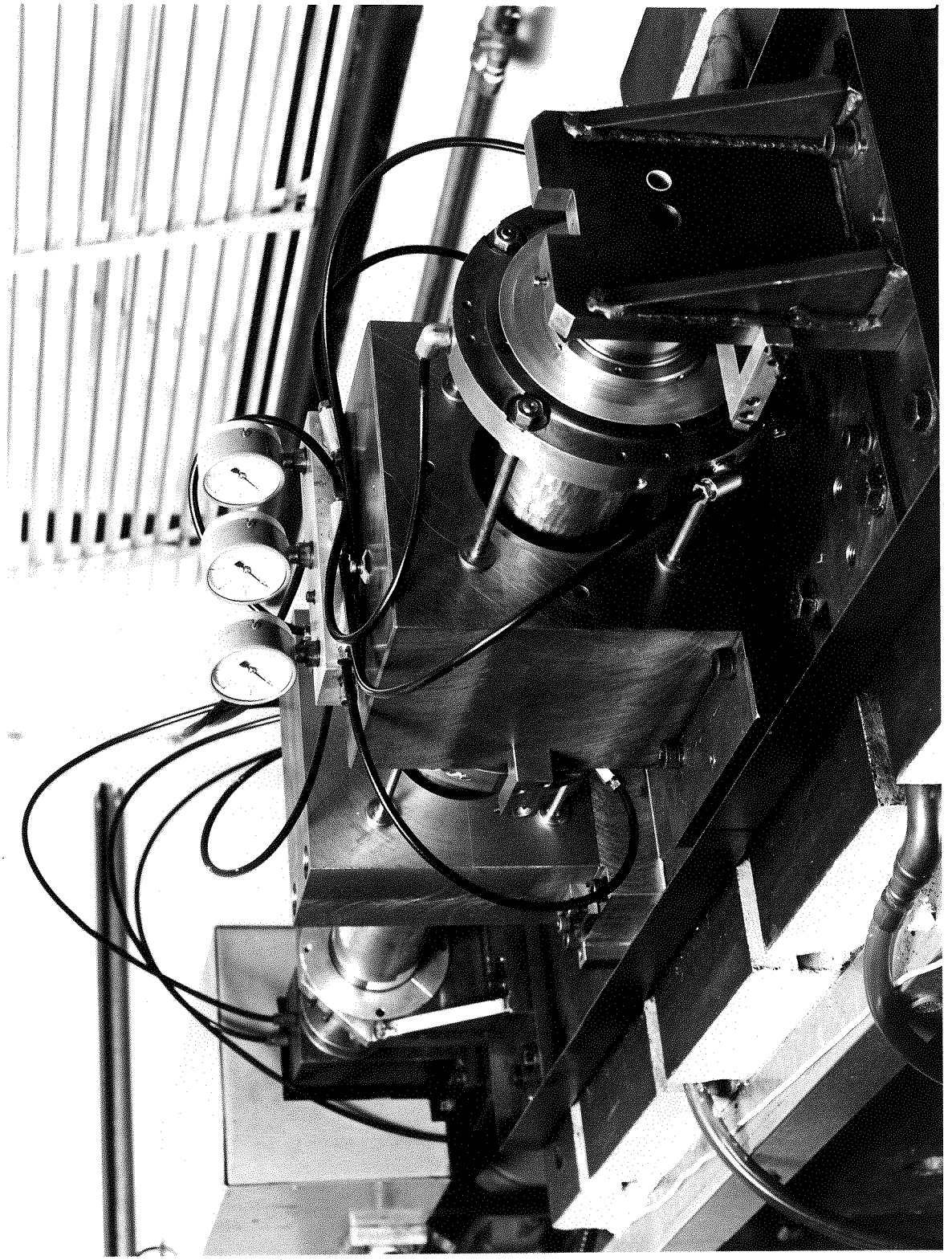

Side Elevation of Test Rig

(from right hand viewpoint)

PLATE 2

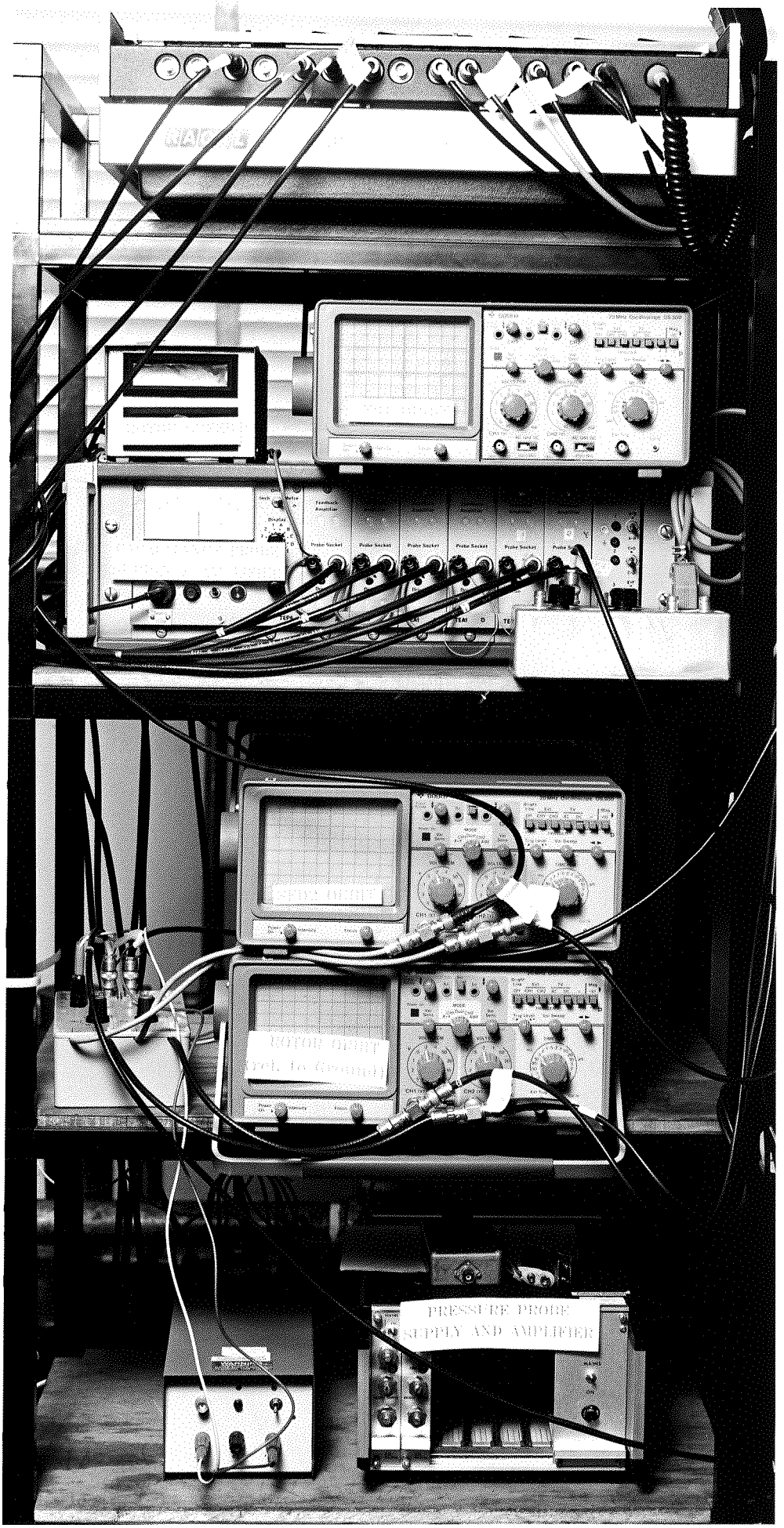

Front Elevation of Instrumentation Stack

PLATE 3

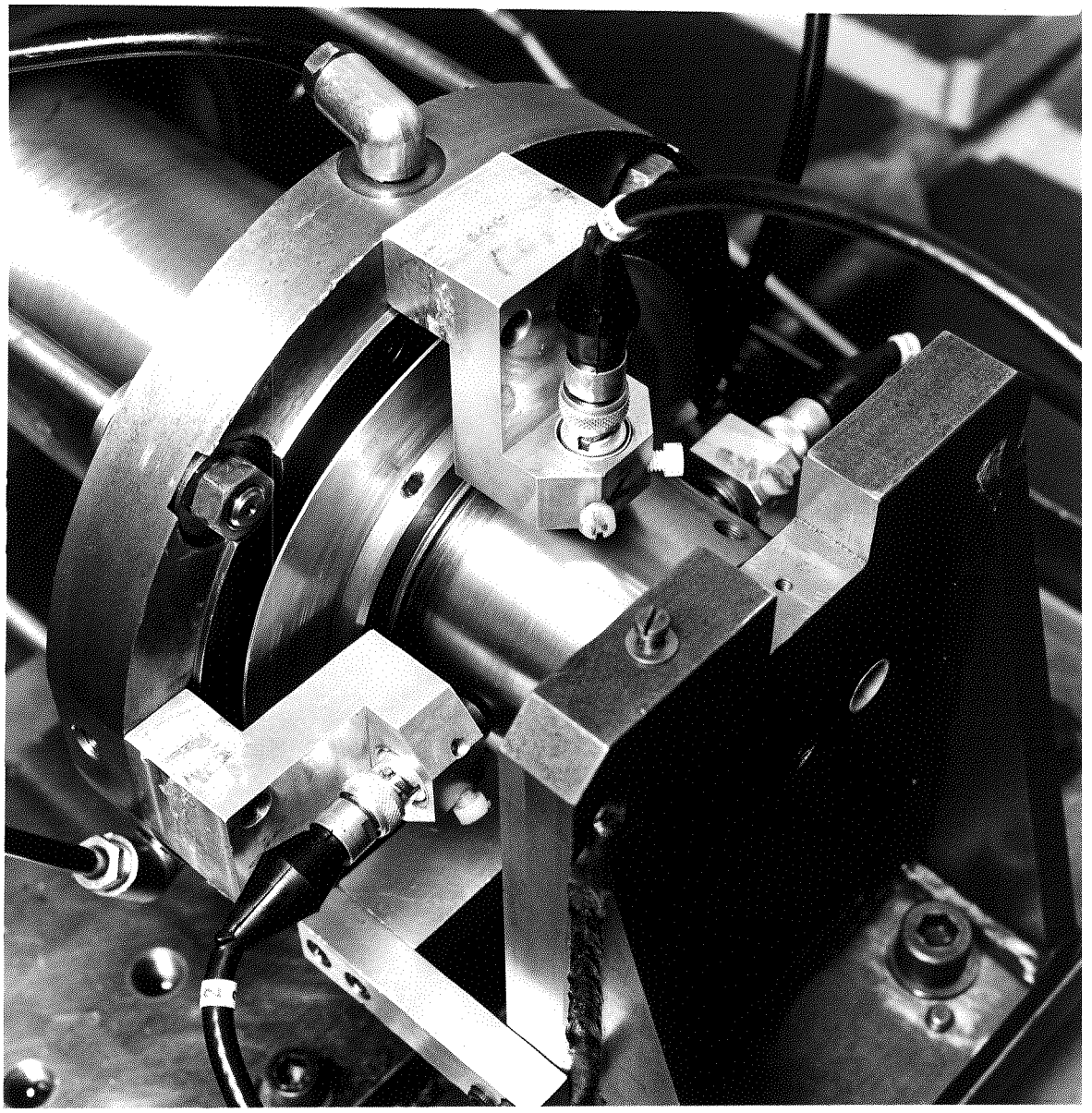

View of Free End of Rotor Showing Mounting of
Displacement Probes

PLATE 4

TABLES

TABLE 1.1 2π Film & π Film Forces

Force	π Film	2π Film
P1	$\frac{2\mu R l^3 w \epsilon^2}{c^2(1-\epsilon^2)^2}$	0
P2	$\frac{\pi\mu R l^3 \epsilon w}{2c^2(1-\epsilon^2)^{1.5}}$	$\frac{\pi\mu R l^3 \epsilon w}{c^2(1-\epsilon^2)^{1.5}}$

TABLE 3.1 Test Rig Configurations

Test Rig Configuration	Static Set Up		Simple Representative Rig Diagram
	E_{o1}	E_{o2}	
1a	0.0	-	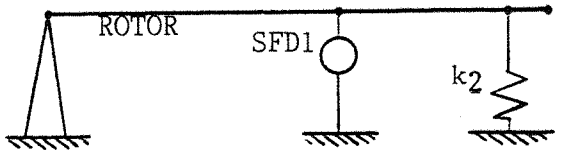
1b	0.4,0.8	-	
2a	0.0,0.5	1.0	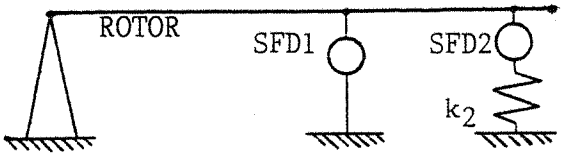
2b	1.0	0.0	
3a	1.0	1.0	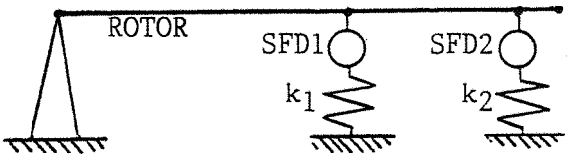
3b	0.0	1.0	

Table 7.1 Configuration 1a Experimental Jump Data

The table below gives information regarding the jumps observed experimentally for an unbalance factor, Qc2, of 0.733.

Psup (psi)	ϵ_1 Max.	ϵ_1 Min.	ϵ_1 Jump	Phase Min. (deg)	Phase Max. (deg)	Phase Jump (deg)	Rotor Speed (Hz)
2	1.06	0.62	0.44	42	166	-104	43-45
4	1.00	0.66	0.34	64	150	-86	42
6	0.98	0.60	0.38	74	145	-71	43

Table 7.2 Configuration 2a SFD1 Experimental Jump Data

The table below gives information regarding the jumps observed experimentally for SFD1, rig configuration 2a (Table 3.1).

Q_{c2}	Psup (psi)	ϵ_1 Max.	ϵ_1 Min.	ϵ_1 Jump	Phase Min. (deg)	Phase Max. (deg)	Rotor Speed (Hz)
0.733	2	1.03	0.57	0.46	47	143	43-41
0.611	2	0.98	0.50	0.48	66	154	41-39
0.490	2	0.78	0.48	0.30	123	147	37-35
0.733	15	0.97	0.59	0.38	70	146	41-39

Table 7.3 Configuration 2a SFD2 Experimental Jump Data

The table below gives information regarding the jumps observed experimentally for SFD2, rig configuration 2a (Table 3.1).

Q_{c2}	Psup (psi)	ϵ_1 Max.	ϵ_1 Min.	ϵ_1 Jump	Phase Min. (deg)	Phase Max. (deg)	Rotor Speed (Hz)
0.733	2	0.55	0.25	0.30	NA*	NA	43-41
0.611	2	0.58	0.26	0.32	NA	NA	41-39
0.490	2	0.51	0.29	0.22	NA	NA	37-35
0.733	15	0.55	0.29	0.26	NA	NA	41-39

* Not Applicable

Table 7.4 Configuration 1a Minimum Jump Frequency Ratios

The table below gives information regarding the jumps up on run down, the minimum jump frequency ratios, observed experimentally and predicted.

Qc2	G (mm)	Psup (psi)	Minimum Jump Frequency Ratio (w/w_n)		% Difference of Theoretical With Respect to Experimental
			Experimental	Theoretical	
0.733	0.5	2	1.36	1.54	+ 13 %
0.733	0.5	6	1.33	1.54	+ 16 %
0.611	2.0	6	1.17	1.36	+ 16 %
0.611	2.0	2	1.17	1.36	+ 16 %
0.490	2.0	2	1.11	1.27	+ 14 %

Table 7.5 Configuration 2a Minimum Jump Frequency Ratios

The table below gives information regarding the jumps up on run down, the minimum jump frequency ratios, observed experimentally and predicted.

Qc2	Psup (psi)	Minimum Jump Frequency Ratio (w/w_n)		% Difference of Theoretical With Respect to Experimental
		Experimental	Theoretical	
0.733	2	1.30	-	+ %
0.611	2	1.23	1.33	+ 8 %
0.490	2	1.11	1.33	+ 20 %
0.733	15	1.23	-	+ %

Table 7.6 Configuration 2b Maximum Jump Frequency Ratios

The table below gives information regarding the jumps up on run up, the maximum jump frequency ratios, observed experimentally and predicted.

Q_{c2}	Psup (psi)	Maximum Jump Frequency Ratio (w/w_n)		% Difference of Theoretical With Respect to Experimental
		Experimental	Theoretical	
0.733	2	1.54	1.70	+ 10 %
0.611	2	1.67	1.70	+ 2 %
0.490	2	1.98	2.07	+ 5 %
0.733	15	1.67	1.82	+ 9 %
0.611	15	1.85	1.82	- 2 %

Table 7.7 Unsimplified Short Bearing Model Film Forces

The table below gives information regarding the non-dimensional SFD1 film forces developed with various supply and cavitation pressures for the following damper parameters;

$A_1 = 0.02132$
$\epsilon_1 = 0.9$
$\epsilon_1' = 0.1$
$\alpha_1 = 4.712$
$\alpha_1' = 1.0$

Psup (psi)	Pmin (psi)	$\bar{P}1$	$\bar{P}2$
0	0	0.20985	0.06050
200	0	0.14208	0.09328
0	-14.7	0.18018	0.07961
2	-14.7	0.17853	0.08028
6	-14.7	0.17559	0.08144
20	-14.7	0.16701	0.08476

Table 7.8 Summary of Non-Linear Phenomena

CONFIGURATION	FREQUENCY RATIO			
	w/Wn 0.5 - 1.0	w/Wn 1.0 - 1.5	w/Wn 1.5 - 2.0	w/Wn 2.0 - 2.5
1a E_{O1}=0.0		JD (HI)	Wn (LOW)	Wn (LOW)
1b E_{O1}=0.4		JU/JD (HI)		½EO (LOW)
1b E_{O1}=0.8		JU/JD (HI)		½EO (HI)
2a E_{O1}=0.0 E_{O2}=1.0		JD (HI)	Wn (Very LOW)	Wn (LOW)
2a E_{O1}=0.5 E_{O2}=1.0		JU / JD	½EO (LOW)	½EO (HI)
2b E_{O1}=1.0 E_{O2}=0.0		½EO (LOW)	½EO (LOW)	½EO (LOW) JU (Very HI)
3a E_{O1}=1.0 E_{O2}=1.0	JU/JD (HI)	½EO (LOW)		
3b E_{O1}=0.0 E_{O2}=1.0	JU/JD (HI)			

NOTATION:

½EO	Half Engine Order (Subharmonic Resonance)
E_{O1}	Static Eccentricity in SFD1
HI	High / Strong
JU	Jump Up (speed increasing)
JD	Jump Down (speed increasing)
LOW	Low / Weak
w	Rotor Speed (Hz)
Wn	Response at Natural Frequency (32.4 Hz)

APPENDICES

APPENDIX 1

SFD Geometry & Other Rig Parameters

SFD1 Damper Geometry

c_1	= 0.000254	m
$(l/c)_1$	= 44.2	-
$(l/R)_1$	= 0.144	-
G_1	= 0.002	m
Gw_1	= 0.004	m
N_1	= 2	-

SFD2 Damper Geometry

c_2	= 0.000216	m
$(l/c)_2$	= 41.6	-
$(l/R)_2$	= 0.132	-
G_2	= 0.002	m
Gw_2	= 0.004	m
N_2	= 2	-

Rig Parameters

a	= 1.019	m
b	= 0.9716	m
d	= 0.5434	m
f	= 0.5968	m
I	= 11.5	$kg.m^2$ per land
k_1	= 505 000	N/m per land
k_2	= 505 000	N/m per land
w_n	= 203.58	rad/s (Configurations 1a to 2b)
μ	= 6.0	cP (average)

APPENDIX 2

The Short Bearing Solution of Reynolds Equation Applied to The Squeeze-Film Damper

The full form of the Reynolds equations [3] dictating the pressure distribution within the SFD fluid film is

$$(1/R^2)(\partial/\partial\phi).\{h^3(\partial P/\partial\phi)\} + (\partial/\partial z).\{ h^3(\partial P/\partial z)\} =$$
$$(6\mu c/R).\{ (\dot{\epsilon}\sin\phi - \epsilon\dot{\alpha}\cos\phi)(dh/d\phi) + h(\dot{\epsilon}\cos\phi + \epsilon\dot{\alpha}\sin\phi) \}$$
$$+ 12\mu c(\dot{\epsilon}\cos\phi + \epsilon\dot{\alpha}\sin\phi)$$

..{A2.1}

Now, observing the SFD geometry,

$c/R << 1$ and,

for a Short Bearing,

$\partial P/\partial\phi << \partial P/\partial z$

because we can assume circumferential fluid flow to be negligible in comparison to the axial flow.

Equation {A2.1} can now be simplified and rewritten in a non-dimensional form:

$$(R/l)^2(\partial/\partial\bar{z})\{ \bar{h}^3\partial\bar{P}/\partial\bar{z} \} = 12(\epsilon'\cos\phi + \epsilon.\alpha'.\sin\phi)$$

..{A2.2}

where $\bar{P} = P(R/c)^2/(\mu w)$,

$\bar{h} = h/c = 1 + \epsilon.\cos\phi$,

$\bar{z} = z/l$ and

$(') = d/d(w.t)$.

Integrating {A2.2} twice with respect to $\bar{z}$ gives

$$\bar{P}(\phi,\bar{z}) = 12.(l/R)^2(\epsilon'.\cos\phi + \epsilon.\alpha'.\sin\phi)\bar{z}^2/(2(1 + \epsilon.\cos\phi)^3)$$
$$+ Z1.\bar{z} + Z2$$

..(A2.3)

The following boundary conditions are used to determine the integration constants, Z1 and Z2.

$$\bar{P} = \bar{P}sup \quad \text{where} \quad \bar{z} = -0.5$$

$$\bar{P} = 0 \quad \text{where} \quad \bar{z} = 0.5$$

and atmospheric pressure (14.7 psi gauge or 1.013 bar absolute) taken as a zero pressure datum.

This yields the result that

$$Z1 = -\bar{P}sup$$

and $$Z2 = \frac{\bar{P}sup}{2} - \frac{1.5(1/R)^2(\epsilon'.\cos\phi + \epsilon.\alpha'.\sin\phi)}{(1 + \epsilon.\cos\phi)^3}$$

Now the form of {A2.3} becomes

$$\bar{P}(\phi,\bar{z}) = \frac{6(1/R)^2(\epsilon'.\cos\phi + \epsilon.\alpha'.\sin\phi)(\bar{z}^2 - 0.25)}{(1 + \epsilon.\cos\phi)^3} + \bar{P}sup(0.5 - \bar{z}) \qquad \ldots(A2.4)$$

This expression, {A2.4}, provides the value of non-dimensional pressure at any point within the fluid film.

Given the damper geometry, position, velocity, fluid supply pressure and the rotor rotational speed then the non-dimensional pressure can be calculated at a number of points which form a mesh, or array, within the SFD. These pressure values form a numerical film pressure map around the bearing which can be used to determine the forces P1, P2 generated by the damper (Fig 1.1).

APPENDIX 3

The 2π Film and π Film Short Bearing Equations

The 2π and π film models assume a statically centred SFD journal supplied with oil at atmospheric pressure, where atmospheric pressure (14.7 psi absolute) is taken as a zero pressure datum. Thus Psup is equal to zero.

A statically centred SFD journal executes circular, centred steady state eccentricity orbits and, thus,

$$\alpha' = 1$$

and $\epsilon' = 0$.

The pressure equation, (A2.4), can now be simplified to become

$$\bar{P}(\phi,\bar{z}) = 6(1/R)^2(\epsilon.\sin\phi(\bar{z}^2 - 0.25))/(1 + \epsilon.\cos\phi)^3 \qquad ..(A3.1)$$

Now, referring to Fig 1.1, the forces are derived by integration of the pressure equation,

$$P1 = - \mu.w(c/R)^2.R.l \int_{\phi_2}^{\phi_1} \int_{-\frac{1}{2}}^{\frac{1}{2}} \bar{P}(\phi,\bar{z}).\cos\phi.d\bar{z}.d\phi$$

$$P2 = - \mu.w(c/R)^2.R.l \int_{\phi_2}^{\phi_1} \int_{-\frac{1}{2}}^{\frac{1}{2}} \bar{P}(\phi,\bar{z}).\sin\phi.d\bar{z}.d\phi \qquad ...(A3.2)$$

Table 1.1 gives the integrated, algebraic form of forces P1 and P2 where :

1. for the 2π film $\phi_1 = 0$ radians ,
   $\phi_2 = 2\pi$ radians and
2. for the π film $\phi_1 = 0$ radians ,
   $\phi_2 = \pi$ radians .

APPENDIX 4

Instrumentation Details

Description	Details
Racal Analogue Tape Recorder	Type STORE 7D Ser.No.T023/.016
Capacitance Probes ('In House')	
Wayne Kerr Power Supply and Amplifier.	Types TEP6 6 x TEA1 ME No.2677628
Mech.Eng.Dept. 'In House' speed voltage pulse counter.	
Bruel & Kjaer Phase Meter	Type 2971 Ser.No.562987
SFD Oil Supply Pressure Gauge (Budenburg)	0 - 60 psi
Solartron Spectrum Analyser	Type FFT 1201 Ser.No.200161
Brookfield Digital Viscometer with UL Adapter	Model LVTD Ser.No.A06259
Gould 20 MHz Oscilloscope	Type OS300 Ser.No.57918007
Gould Storage Digital Oscilloscope	Type OS1420 Ser.No.1941
Kikusui Storage Oscilloscope	Type DSS 6522 Ser.No.2040052
Racal-Dana Universal Counter Timer	Type 9904
Gould Advance Digital Multimeter	Type DMM7 Ser.No.15122
Philips Automatic Multimeter	Type PM2521 Ser.No.DY026062

APPENDIX 5

A Note on Experimental Squeeze-Film Damper Supply Pressure

Laminar axial fluid flow through a circular annulus can be calculated from the following expression:

$$Q = \frac{(p_A - p_B)\,\pi.D.c^3}{12.\mu.L}$$

Where

	Q	=	Fluid Flow Rate (m^3/s)
	p_A	=	Annulus Supply Pressure (N/m^2)
	p_B	=	Annulus Discharge Pressure (N/m^2)
	D	=	Mean Annulus Diameter (m)
	c	=	Annulus Clearance (m)
	μ	=	Fluid Dynamic Viscosity (kg/ms)
	L	=	Annulus Length

Where p_B is atmospheric (as in the case of the damper discharge of the experimental rig) and p_A is equal to the damper supply pressure, P_{SUP} then the expression can be rewritten as

$$Q = \frac{Psup.\pi.D.c^3}{12.\mu.L}$$

This equation for fluid flow can be applied to the static, centred squeeze-film damper (SFD). This expression can be used to observe the theoretical SFD supply pressure drop experienced when the rig was re-configured to involve two SFDs as opposed to one. Initially SFD1 was the only damper supplied with oil and the maximum supply pressure was 24 psi. With SFD1 and SFD2 supplied with oil the maximum supply pressure fell to 15 psi. Thus, for the same flow

$$\frac{\pi.Psup1.D_1.c_1^3}{12.\mu.L_1} = \frac{\pi}{12.\mu}\left[Psup2\left[\frac{D_1.c_1^3}{L_1} + \frac{D_2.c_2^3}{L_2}\right]\right]$$

The above expression can be rearranged to give

$$\left[\frac{P_{sup1}}{P_{sup2}}\right]\left[\frac{D_1.c_1^3/L_1}{D_1.c_1^3/L_1 + D_2.c_2^3/L_2}\right] = 1.0$$

Inserting the values of Psup1 = 24 psi and Psup2 = 15 psi, along with the SFD geometries, which can be derived from Appendix 1, the above left hand expression is found to be equal to 0.98.

Therefore the maximum experimental SFD supply pressures observed with one and two SFDs being supplied do conform to this approximate analysis.

APPENDIX 6

Large Amplitude Vibrations in Rotor Bearing Assemblies

The following is a reproduction of a paper written by Prof R Holmes and co-written by the author of this thesis and was published by the Journal of Sound and Vibration, see Ref [48].

LARGE-AMPLITUDE VIBRATIONS IN ROTOR ASSEMBLIES

R. HOLMES AND J. E. H. SYKES

Department of Mechanical Engineering, University of Southampton, Highfield, Southampton SO9 5NH, England

(*Received* 17 *June* 1988, *and in revised form* 16 *February* 1989)

A procedure is established for rapidly estimating the sizes and dispositions of large-amplitude vibrations resulting from the combined action of rotating and static forces in rotor assemblies incorporating oil-film bearings and dampers. Use is made of displacement and velocity coefficients for perturbation of a journal centre (a) from a static equilibrium position and (b) from a steady state orbit and it is shown that a correspondence exists between the two. Limitations of the method are discussed.

1. INTRODUCTION

Journal bearings are an essential feature of all rotating assemblies and provide the vital load-carrying capacity to support rotors against static and dynamic forces. In particular, oil-film journal bearings are to be found where loads are demanding and speeds are moderate. By virtue of the oil by which they are lubricated they have the capacity additionally to provide damping in response to excitation due to unbalance. However, they can be fickle in that such damping can become negative and uncontrollable instability can result to the equipment being supported.

A squeeze-film on the other hand, is an annulus of oil supplied between the outer race of a rolling-element bearing (or the bush of a sleeve bearing) and its housing. Its main use is as multi-directional damping element for the control of engine vibrations. Such a squeeze-film is often placed in parallel with a soft flexible element to comprise a vibration isolator. By this means the natural frequencies of the rotor assembly are reduced so that they may be traversed well before the normal operating speeds are reached. The purpose of the damper in this application is to reduce to acceptable levels the amplitudes of vibration and transmitted force due to unbalance as these low natural frequencies are traversed.

A squeeze-film damper is also often used on its own between a bearing and its housing, in which case no attempt is made to reduce the natural frequencies of the system, only to reduce vibration while running through the already existing natural frequencies. Rotation of the inner member of the squeeze-film damper is in this case prevented by anti-rotation pins or dogs.

For adequately small-amplitude vibrations arising from small unbalance forces superimposed upon relatively large static loads, journal-bearing oil films are popularly modelled by linear displacement and velocity coefficients referred to a stationary eccentricity vector; see, e.g., reference [1], and, more recently, many others. Attempts have also been made to represent squeeze-film dampers in a similar fashion [2]. However, journal bearing oil films and squeeze-films are highly non-linear in their dynamics and, when amplitudes of unbalance vibration are expected to be moderate, recourse has had to be taken to lengthy time-transient solutions to predict vibration orbits of the rotor-centre; see, e.g., reference [3].

A squeeze-film damper is in effect a journal bearing in which the inner member does not rotate. Because of this there are similarities in the operation of the squeeze-film damper and of the journal bearing which can be exploited in an understanding of their performance characteristics, for cases where fairly large vibrations of the rotor centre are likely to occur.

2. THE JOURNAL BEARING

The starting point for the theoretical consideration of a hydrodynamically generated oil-film in a journal bearing is the well known Reynolds equation, which for incompressible fluids in the laminar regime may be written, when referred to Figure 1, as (a list of notation is given in the Appendix)

$$\frac{1}{R^2}\frac{\partial}{\partial\theta}\left[h^3\frac{\partial p}{\partial\theta}\right]+\frac{\partial}{\partial z}\left[h^3\frac{\partial p}{\partial z}\right]=12\mu c\left[\dot{\varepsilon}\cos\theta-\varepsilon\left(\frac{\omega}{2}-\dot{\alpha}\right)\sin\theta\right]. \tag{1}$$

Subjecting this equation to the boundary conditions $p(\theta, l/2)=p(\theta, -l/2)=0$ and $p=0$ over the area where cavitation occurs, leads to solutions which bear a good resemblance to experimental observations, for steadily loaded and dynamically loaded journal bearings. Solution of equation (1) gives the pressure distribution in the journal-bearing oil-film. By integration of the pressures, the radial and transverse components P_1, P_2 of the force exerted by the oil-film on the journal are obtained.

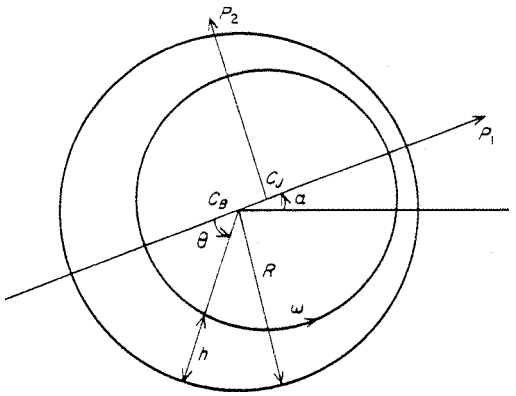

Figure 1. The journal bearing. $C_BC_J = e = \varepsilon c$.

Let us compare the two cases $\dot{\alpha}=0$ (i.e., $\omega/2>\dot{\alpha}$) and $\dot{\alpha}=\omega$ (i.e., $\omega/2<\dot{\alpha}$), with $\dot{\varepsilon}=0$. In Figure 2(a) are shown the forms of the pressure distributions for $\dot{\alpha}=0$ and $\dot{\alpha}=\omega$, with cavitation occurring over about half the film in each case. The oil-film forces P_1 and P_2 involve respectively the integrals $I_1=\int p\cos\theta$ and $I_2=\int p\sin\theta$, where integration is over the appropriate load-carrying (i.e., non-cavitating) portion of the film. As a result, the forms of P_1 and P_2 are shown in Figures 2(b) and (c). From these it may be seen that area P_1 remains unchanged in value as $\dot{\alpha}$ changes, but that P_2 changes sign.

For $\dot{\varepsilon}=0$ and $\dot{\alpha}=\omega$, the pressure distribution rotates with the load vector at angular velocity ω and is a reflection relative to the line of centres C_BC_J of the pressure distribution for the case where $\dot{\alpha}=0$. In Figures 3(a) and (b) are shown the regions of positive hydrodynamic pressure for $\dot{\alpha}=0$ and $\dot{\alpha}=\omega$, respectively. If in each case $\dot{\alpha}$ is now perturbed

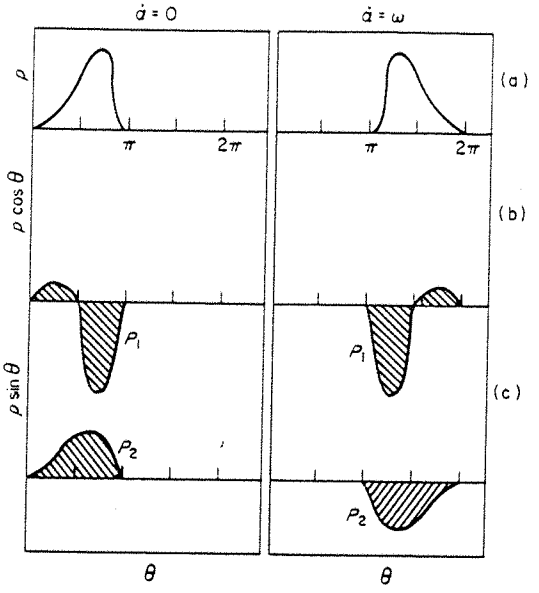

Figure 2. Oil-film pressures and forces.

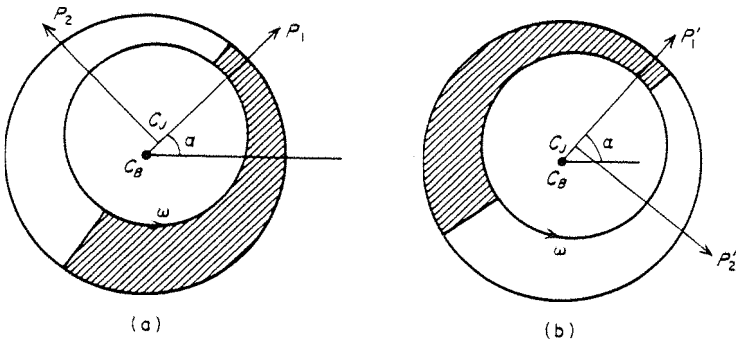

Figure 3. Oil-film force dispositions. (a) $\dot{\alpha} = 0$; (b) $\dot{\alpha} = \omega$.

and a perturbation $\dot{\varepsilon}$ is also introduced, the forces P_1 and P_2 and P_1' and P_2' will contain components due to wedge action and squeeze action as follows:

$$P_{1,2} = \dot{\varepsilon} F_{1,2}(\varepsilon) + (\omega/2 - \dot{\alpha}) h_{1,2}(\varepsilon).$$

If $\dot{\alpha}$ is represented by a small perturbation $\dot{\alpha}_s$,

$$P_{1,2} = \dot{\varepsilon} F_{1,2}(\varepsilon) + (\omega/2 - \dot{\alpha}_s) h_{1,2}(\varepsilon). \tag{3}$$

For $\dot{\alpha} = \omega + \dot{\alpha}_s$,

$$P'_{1,2} = \dot{\varepsilon} F_{1,2}(\varepsilon) + (\omega/2 + \dot{\alpha}_s) h_{1,2}(\varepsilon). \tag{4}$$

In Figure 4 the perturbed position of C_j is shown, in relation to stationary co-ordinates r, s, together with the forces P_1 and P_2 given in equation (3). C is the journal position resulting from the application of a static load alone, and C_B is the bearing centre. Thus

$$P_r = P_1 \cos \alpha_s - P_1 \sin \alpha_s, \qquad P_s = P_1 \sin \alpha_s + P_2 \cos \alpha_s.$$

For small α_s,

$$\delta P_r = \delta P_1 - P_2 \delta \alpha_s, \qquad \delta P_s = P_1 \delta \alpha_s + \delta P_2.$$

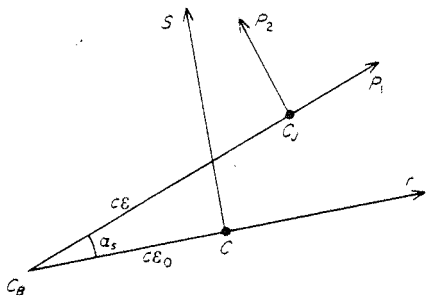

Figure 4. Force system.

Using equation (3) and making $\dot{\varepsilon} \ll \omega$, $\dot{\alpha}_s \ll \omega$, one obtains

$$\delta P_r = F_1 \delta\dot{\varepsilon} + \frac{\omega}{2}\frac{\partial h_1}{\partial \varepsilon}\delta\varepsilon - h_1\delta\dot{\alpha} - \frac{\omega}{2}h_2\delta\alpha_s, \qquad \delta P_s = F_2\delta\dot{\varepsilon} + \frac{\omega}{2}\frac{\partial h_2}{\partial \varepsilon}\delta\varepsilon - h_2\delta\dot{\alpha} + \frac{\omega}{2}h_1\delta\alpha_s, \tag{5}$$

in which $\delta\varepsilon = r/c$ and $\delta\alpha_s = s/c\varepsilon$.

Returning to Figure 4, we now assume that ε_0 is an eccentricity vector rotating at shaft angular velocity, ω. Under these conditions we make C the journal centre under the action of a dynamic load, also rotating at shaft angular velocity, ω. P_1, P_2 are replaced by P_1', P_2' as in Figure 3(b).

Again for small α_s, $\dot{\varepsilon} \ll \omega$ and $\dot{\alpha}_s \ll \omega$, we obtain, using equations (4),

$$\delta P_r' = \delta P_1' + P_2'\delta\alpha_s = F_1\delta\dot{\varepsilon} + \frac{\omega}{2}\frac{\partial h_1}{\partial\varepsilon}\delta\varepsilon + h_1\delta\dot{\alpha}_s + \frac{\omega h_2}{2}\delta\alpha_s,$$

$$\delta P_s' = -\delta P_2' + P_1'\delta\alpha_s = -F_2\delta\dot{\varepsilon} - \frac{\omega}{2}\frac{\partial h_2}{\partial\varepsilon}\delta\varepsilon - h_2\delta\dot{\alpha}_s + \frac{\omega h_1}{2}\delta\alpha_s, \tag{6}$$

where again $\delta\varepsilon = r/c$ and $\delta\alpha_s = s/c\varepsilon$. Comparing equations (5) with equations (6) reveals that all direct coefficients are equal and of the same sign, but that all cross-coefficients are equal and of opposite sign.

A popular assumption for many journal bearings is that they are short in relation to their diameter. If a bearing land is sufficiently short ($l/D \leqslant 0{\cdot}5$) then the first term on the left side of equation (1) may be dropped with little loss of accuracy. Capriz [3] has shown that if we then assume that cavitation occurs over half the film, P_1 and P_2 may be written as

$$P_1 = \lambda\pi(l/R)^2\left[-\dot{\varepsilon}g_2 + \left(\frac{\omega}{2} - \dot{\alpha}\right)\varepsilon g_1\right], \qquad P_2 = \lambda\pi(l/R)^2\left[-\dot{\varepsilon}g_1 + \left(\frac{\omega}{2} - \dot{\alpha}\right)\varepsilon g_3\right], \tag{7}$$

in which

$$g_1 = \frac{-2\varepsilon\cos^3\theta_1}{(1-\varepsilon^2\cos^2\theta_1)^2},$$

$$g_2 = \frac{\varepsilon\sin\theta_1[3+(2-5\varepsilon^2)\cos^2\theta_1]}{(1-\varepsilon^2)^2(1-e^2\cos^2\theta_1)} + \frac{(1+2\varepsilon^2)}{(1-\varepsilon^2)^{5/2}}\left\{\frac{\pi}{2} + \tan^{-1}\left(\frac{\varepsilon\sin\theta_1}{(1-\varepsilon^2)^{1/2}}\right)\right\},$$

$$g_3 = \frac{\varepsilon\sin\theta_1(1-2\cos^2\theta_1+\varepsilon^2\cos^2\theta_1)}{(1-\varepsilon^2)(1-\varepsilon^2\cos^2\theta_1)^2} + (1-\varepsilon^2)^{-3/2}\left\{\frac{\pi}{2} + \tan^{-1}\left(\frac{\varepsilon\sin\theta_1}{(1-\varepsilon^2)^{1/2}}\right)\right\}, \tag{8}$$

and θ_1, $\theta_1 + \pi$ is the region effectively occupied by the oil film.

As equation (1) indicates, θ_1 is given by

$$\tan \theta_1 = (2\dot{\varepsilon}/\omega)/\varepsilon(1-2\dot{\alpha}/\omega). \tag{9}$$

If we consider the case of Figure 3(a) such that $\dot{\alpha}/\omega \ll 1$, then it may be observed that $\tan \theta_1 \to 2\dot{\varepsilon}/\omega\varepsilon$, which approaches zero as $\dot{\varepsilon}/\omega \to 0$. Thus $\theta_1 = 0$ and $\theta_2 = \pi$. Any first order movement of the oil film around the bearing circumference will produce a first order change in pressure and, since force is the integral of pressure times circumferential coverage, the resultant change in force will be only of second order. Thus, for these small motions, equations (8) become

$$g_1 = \frac{-2\varepsilon}{(1-\varepsilon^2)^2}, \qquad g_2 = \frac{1+2\varepsilon^2}{(1-\varepsilon^2)^{5/2}}\frac{\pi}{2}, \qquad g_3 = \frac{\pi}{2}\frac{1}{(1-\varepsilon^2)^{3/2}}. \tag{10}$$

For $\dot{\alpha} \doteq \omega$ and $\dot{\varepsilon}/\omega \ll 1$ (Figure 3(b)), equation (9) gives $\theta_1 = \pi$. Hence, in equations (8), g_1 shows a sign reversal from that given in equation (10), while g_2 and g_3 remain unchanged. This in turn produces sign reversals in all the cross-coefficients, as expected from the more general reasoning given earlier.

The foregoing is based on the premise that one can assume that any cavitation zone in an oil film under rotating load is similar to that in a statically loaded oil film. Some early work of Cole and Hughes [4] does suggest, albeit for fairly low loading, that the cavitation zones are similar.

The values of the displacement and velocity coefficients are important in determining the reposition of the circular orbit resulting from the application of an external rotating load, when a static load is added.

2.1. EFFECT OF STATIC LOAD

Shown in Figure 5 is the journal centre, C_j, in a rotating-co-ordinate system r, s with the application of a static load W and incremental oil-film forces $\delta P'_r$ and $\delta P'_s$ defined as

$$\delta P'_r = -a_{rr}r - b_{rr}\dot{r} - a_{rs}s - b_{rs}\dot{s}, \qquad \delta P'_s = -a_{ss}s - b_{ss}\dot{s} - a_{sr}r - b_{sr}\dot{r}. \tag{11}$$

Thus,

$$m[\ddot{s} - s\omega^2 + 2\dot{r}\omega] = \delta P'_s - W\cos\omega t, \qquad m[\ddot{r} - r\omega^2 - 2\dot{s}\omega] = \delta P'_r - W\sin\omega t. \tag{12}$$

Solving for the complementary functions gives an indication of the stability of the system for a given orbit radius $c\varepsilon_0$, and predicts the tendency or otherwise to move out to a different orbit radius.

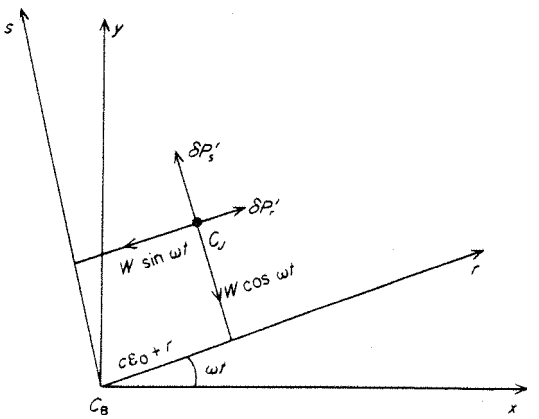

Figure 5. Static and dynamic forces.

Solving equations (12) for their particular integrals and putting $r = y \sin \omega t + x \cos \omega t$ gives

$$y = W(a_1 c_1 + b_1 \omega d_1)/(a_1^2 + \omega^2 b_1^2), \qquad x = W(a_1 d_1 - b_1 \omega c_1)/(a_1^2 + \omega^2 b_1^2), \tag{13}$$

where

$$\begin{aligned} a_1 &= b_{rr} b_{ss} \omega^2 - (a_{ss} - 2m\omega^2)(a_{rr} - 2m\omega^2) - (b_{sr} + 2m\omega)(b_{rs} - 2m\omega)\omega^2 + a_{sr} a_{rs}, \\ b_1 &= -b_{ss}(a_{rr} - 2m\omega^2) - b_{rr}(a_{ss} - 2m\omega^2) + a_{rs}(b_{sr} + 2m\omega) + a_{sr}(b_{rs} - 2m\omega), \\ c_1 &= \omega b_{rs} + a_{ss} - 4m\omega^2, \qquad d_1 = \omega b_{ss} - a_{rs}. \end{aligned} \tag{14}$$

The linearized coefficients a_{rr}, b_{rr}, etc., are functions of ε_0, and hence of the radius of the circular orbit. ε_0 is dependent upon the rotating force (provided by unbalance, say), together with the operating parameters of the journal bearing.

2.2. RESPONSE DUE TO UNBALANCE

A journal within its bearing is shown in diagrammatic form in Figure 6. Orbital motion results from a dynamic force P_c due to some cause, such as unbalance. The amplitude of this orbital motion depends upon P_c, P_1' and P_2', the last two forces arising hydrodynamically from the oil film as in Figure 3(b).

The equations governing the concentric motion of the shaft centre are then

$$P_c \cos(\omega t - \alpha) + P_1' = -mc\varepsilon_0 \omega^2, \qquad P_c \sin(\omega t - \alpha) - P_2' = 0. \tag{15}$$

In equations (15) the oil-film forces, P_1' and P_2', can be shown from equations (8) to be given, for concentric motion, by

$$\begin{aligned} P_1' &= (-\mu R l^3 \omega / c^2)[\varepsilon_0^2/(1-\varepsilon_0^2)^2], \\ P_2' &= (\pi \mu R l^3 \omega / 4c^2)[\varepsilon_0/(1-\varepsilon_0^2)^{3/2}], \end{aligned} \tag{16}$$

and relate to a half-cavitated oil film.

Equations (15) may be made non-dimensional by dividing by $mc\omega^2$ to give

$$\begin{aligned} Q_c \cos(\omega t - \alpha) &= -\varepsilon_0 + [\varepsilon_0^2/(1-\varepsilon_0^2)^2](\mu R/m\omega)(l/c)^3, \\ Q_c \sin(\omega t - \alpha) &= [\varepsilon_0/4(1-\varepsilon_0^2)^{3/2}](\pi \mu R/m\omega)(l/c)^3, \end{aligned} \tag{17}$$

where $Q_c = P_c/mc\omega^2$.

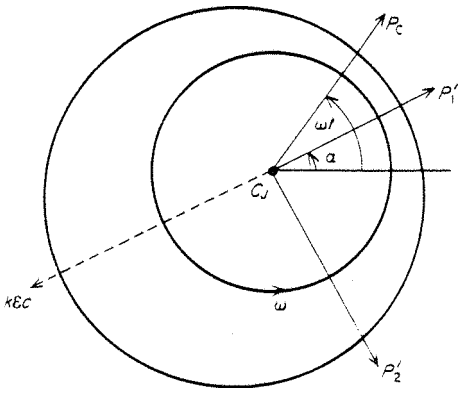

Figure 6. Journal bearing or squeeze-film damper.

If P_c arises due to mass unbalance mu, then $P_c = mu\omega^2$ and $Q_c = u/c$. By putting $\beta = (\mu R/m\omega)(l/c)^3$, equations (17) may be rewritten to give

$$(u/c)\cos(\omega t - \alpha) = -\varepsilon_0 + \beta\varepsilon_0^2/(1-\varepsilon_0^2)^2,$$
$$(u/c)\sin(\omega t - \alpha) = (\pi\beta/4)\varepsilon_0/(1-\varepsilon_0^2)^{3/2}. \tag{18}$$

Hence

$$(u/c)^2 = \frac{\beta^2\varepsilon_0^2}{(1-\varepsilon_0^2)^3}\left[\frac{\pi^2}{16} + \frac{\varepsilon_0^2}{(1-\varepsilon_0^2)}\right] + \varepsilon_0^2 - \frac{2\beta\varepsilon_0^3}{(1-\varepsilon_0^2)^2}. \tag{19}$$

One can now find y and x (equations (13)) by using the coefficients for a half-cavitated oil film [1], suitably modified as in equation (6), and compare the orbits and their positions with the corresponding orbits and positions obtained by solving the full non-linear equations (7). In the notation of equations (11), the modified coefficients are as follows:

$$a_{rr} = 2\omega\gamma\frac{\varepsilon_0(1+\varepsilon_0^2)}{(1-\varepsilon_0^2)^3}, \qquad a_{rs} = -\omega\gamma\frac{\pi}{4}\frac{1}{(1-\varepsilon_0^2)^{3/2}}, \qquad a_{ss} = \omega\gamma\frac{\varepsilon_0}{(1-\varepsilon_0^2)^2},$$
$$a_{sr} = \omega\gamma\frac{\pi}{4}\frac{(1+2\varepsilon_0^2)}{(1-\varepsilon_0^2)^{5/2}}, \qquad b_{rr} = \frac{\pi\gamma}{2}\frac{(1+2\varepsilon_0^2)}{(1-\varepsilon_0^2)^{5/2}}, \qquad b_{rs} = 2\gamma\frac{\varepsilon_0}{(1-\varepsilon_0^2)^2},$$
$$b_{sr} = 2\gamma\frac{\varepsilon_0}{(1-\varepsilon_0^2)^2}, \qquad b_{ss} = \frac{\pi\gamma}{2}\frac{1}{(1-\varepsilon_0^2)^{3/2}}. \tag{20}$$

Although this case is subject to the reservations relating to cavitation zones expressed earlier, it will be a demanding test of the efficacy of the linear treatment. Other oil films are unlikely to be significantly more non-linear than the half film.

For this case we find that equations (14) reduce to

$$a_1 = -3a_{sr}a_{rs} - 4a_{ss}^2 - a_{rr}a_{ss} + 2m\omega^2(a_{rr} + a_{ss}),$$
$$b_1 = (2a_{rs}/\omega)(a_{rr} + a_{ss}) + 2m\omega(a_{sr} - a_{rs}), \qquad c_1 = 3a_{ss} - 4m\omega^2, \qquad d_1 = -3a_{rs}; \tag{21}$$

ε_0 is determined by the value of β and of u/c in equation (19).

y and x in equations (13) are further determined by the value of W. Equations (13) may be made non-dimensional by writing

$$y/c = \bar{W}(\bar{a}\bar{c} + \bar{b}\bar{d})/[(\bar{a})^2 + (\bar{b})^2], \qquad x/c = \bar{W}(\bar{a}\bar{d} - \bar{b}\bar{c})/[(\bar{a})^2 + (\bar{b})^2], \tag{22}$$

where

$$\bar{W} = W/mc\omega^2, \qquad \bar{a} = a_1/m^2\omega^4, \qquad \bar{b} = \omega b_1/m^2\omega^4, \qquad \bar{c} = c_1/m\omega^2, \qquad \bar{d} = d_1/m\omega^2.$$

a_1, b_1, c_1 and d_1 are given by equations (21), in which a_{rr}, a_{ss}, etc., are functions of $\mu R(l/c)^3$, as in equations (20). A set of non-dimensional parameters governing equations (22) is, by inspection of equations (19), $\bar{W}$, u/c and $\bar{W}/\beta = Wc^2/\mu l^3 R\omega$, the latter being recognized as a commonly used load parameter.

In Figures 7(a)-(f) are shown comparisons between journal-centre orbits relevant to a variety of bearing and load conditions with those obtained by solving the full non-linear equations (7). u/c values used are indicated in the figures.

It may be observed that the linear treatment provides a convenient means of estimating the sizes and positions of journal-centre orbits when the linear orbits encircle the bearing centre, for moderate values of the load parameter $\bar{W}/\beta$. Even for a high load-parameter (Figures 7(e) and (f)), good estimates are achieved for the sizes of the major axes of those journal-centre orbits which again encircle the bearing centre.

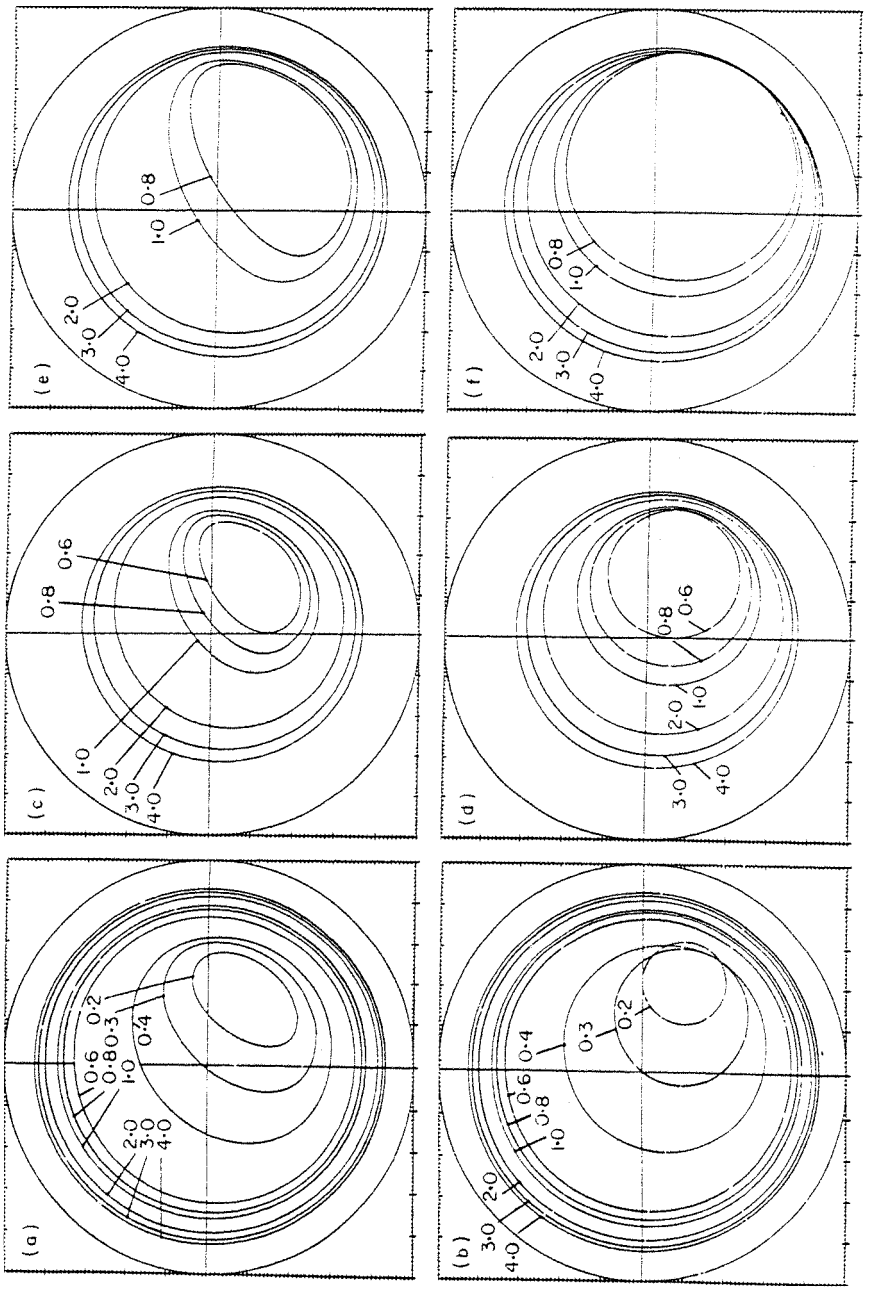

Figure 7. Journal-centre orbits. (a) Non-linear, $\beta = 0{\cdot}4$, $\bar{W} = 0{\cdot}2$; (b) linear, $\beta = 0{\cdot}4$, $\bar{W} = 0{\cdot}2$; (c) non-linear, $\beta = 2{\cdot}0$, $\bar{W} = 1{\cdot}0$; (d) linear, $\beta = 2{\cdot}0$, $\bar{W} = 1{\cdot}0$; (e) non-linear $\beta = 1{\cdot}0$, $\bar{W} = 1{\cdot}0$; (f) linear, $\beta = 1{\cdot}0$, $\bar{W} = 1{\cdot}0$.

3. THE SQUEEZE-FILM DAMPER

The particular feature of a squeeze-film damper is that the journal (inner member) is prevented from rotating either by a centralizing spring or by anti-rotation pins called dogs. Both these devices allow orbital motion of the journal centre, which in turn allows energy dissipation by the oil in the damper clearance space. For the case of centralizing springs, as the name implies, the unloaded journal is brought to the centre of the clearance space. Any static load then deflects the journal to a static equilibrium position and any subsequent dynamic load causes the journal centre to move in orbital motion around this static equilibrium position. If this motion is of small magnitude, it might be argued that one can determine its size by using the coefficients found for the journal bearing [1], suitably adapted by putting $\omega = 0$. However, this conceals the difficulty that, if one puts $\omega = 0$ in equation (9), then

$$\tan \theta_1 = \dot{\varepsilon}/-\varepsilon\dot{\alpha}. \tag{23}$$

Thus θ_1 will no longer equal zero. It might then be argued that one can consider forces due to any orbital motion as consisting of superimposed forces arising from purely radial ($\dot{\varepsilon}$) and purely transverse ($\varepsilon\dot{\alpha}$) motions, for which cases one could make $\tan \theta_1 = \infty$ and zero respectively: i.e., $\theta_1 = \pi/2$ and zero. However, this is obviously inadmissible, since $\dot{\varepsilon}$ and $\varepsilon\dot{\alpha}$ are strongly coupled through equation (23) which in turn governs equations (8).

A way out of this essentially non-linear problem is to think not in terms of a small orbital motion about a static equilibrium position but again of a small static deflection from an equilibrium orbit, the latter resulting from a rotating load of constant magnitude. This is reasonable since, whereas the journal bearings of most rotating machines are designed to withstand large static loads with superimposed relatively small rotating loads, squeeze-film dampers often have the assistance of a centralizing spring to counteract any static load and the squeeze-film itself is used to help withstand any rotating load.

One can then again work in a rotating-co-ordinate system. The consequences of this mean that one can again determine, relative to rotating co-ordinates, a set of displacement and velocity coefficients for the squeeze-film damper for perturbations of the inner member or "journal" from an equilibrium *orbit*, which will be similar to the corresponding coefficients in stationary co-ordinates for a journal bearing for dynamic perturbation of the journal from an equilibrium *point*.

Following a procedure similar to that used for large excursions of a journal in a journal bearing we can now set up equations similar to equations (4), except that $\omega/2$ is replaced by ω, owing to the fact that the angular velocity of the inner member (the journal) is now zero instead of ω. As a result equations similar to equations (6) are set up which show that, for the squeeze-film damper, the direct damping terms are equal and of the same sign as for the journal bearing under static load; the cross-damping terms are equal but of opposite sign; the direct stiffness terms are twice the values and of the same sign, and the cross-stiffness terms are twice the values and of opposite sign. The effect of adding a centering spring of stiffness k is to increase each direct stiffness term by k.

Provided that we can assume that a rotating oil film exists in a squeeze-film damper, which is similar in nature to the stationary oil film in a journal bearing, then we can again replace the static eccentricity ratio vector ε_0 of the latter by a rotating eccentricity ratio vector ε_0 for the squeeze-film damper, with the proviso that all cross-coefficients are of opposite sign and that all displacement coefficients (a) are of double magnitude.

There is some doubt as to the degree to which cavitation in a squeeze-film damper resembles cavitation in a journal bearing [5]. This is likely to depend on external factors such as supply pressure and loading and is the subject of much interest. The correspondence between an uncavitated squeeze-film and an uncavitated journal bearing oil film

should, however, be complete. Displacement and velocity coefficients are available for the latter in the literature; see, e.g., reference [6]. For a squeeze-film which is half cavitated the coefficients of equations (20) can, subject to the above reservations, be suitably modified. They have also been derived by White [7], using a different approach.

We can illustrate the importance of the squeeze-film coefficients in again determining the static displacement of the circular orbit resulting from the application of an external static load.

3.1. EFFECT OF STATIC LOAD

With reference again to Figure 5, $\delta P'_r$ and $\delta P'_s$ are defined as in equations (11) except that a_{rr}, b_{rr}, etc., take on their new values and k is to be added both to a_{rr} and to a_{ss}. Thus,

$$m[\ddot{s} - s\omega^2 + 2\dot{r}\omega] = -(a_{ss} + k)s - b_{ss}\dot{s} - a_{sr}r - b_{sr}\dot{r} - W\cos\omega t,$$

$$m[\ddot{r} - r\omega^2 - 2\dot{s}\omega] = -(a_{rr} + k)r - b_{rr}\dot{r} - a_{rs}s - b_{rs}\dot{s} - W\sin\omega t. \tag{24}$$

Solving for the complementary functions again gives an indication of the stability of the system for a given orbit radius ε_0 and predicts the tendency or otherwise to jump to a different orbit radius.

Solving equations (24) for their particular integrals and putting $r = y\sin\omega t + x\cos\omega t$ gives equations identical in form to equations (13), where this time,

$$a_1 = b_{rr}b_{ss}\omega^2 - (a_{ss} + k - 2m\omega^2)(a_{rr} + k - 2m\omega^2) - (b_{sr} + 2m\omega)(b_{rs} - 2m\omega)\omega^2 + a_{sr}a_{rs},$$

$$b_1 = -b_{ss}(a_{rr} + k - 2m\omega^2) - b_{rr}(a_{ss} + k - 2m\omega^2) + a_{rs}(b_{sr} + 2m\omega) + a_{sr}(b_{rs} - 2m\omega),$$

$$c_1 = \omega b_{rs} + a_{ss} + k - 4m\omega^2, \qquad d_1 = \omega b_{ss} - a_{rs}. \tag{25}$$

The linear coefficients a_{rr}, b_{rr}, etc., are functions of ε_0, the radius of the circular orbit. ε_0 is the response, dependent upon the dynamic force provided by unbalance, together with the parameters of the squeeze-film damper.

3.2. RESPONSE DUE TO UNBALANCE

In Figure 6 is shown, in diagrammatic form, the outer race of a rolling-element bearing within the oil container (the bearing), under the action of a restoring force $kc\varepsilon$ arising from the equivalent stiffness k of a centering spring. Vibration results from a dynamic force P_c due to some cause, such as unbalance. The amplitude of orbital motion depends upon $kc\varepsilon$, P_c, P'_1 and P'_2, the last two forces arising hydrodynamically from the squeeze-film, similar to those in Figure 3(b). The equations governing the concentric motion of the shaft centre are then

$$P_c\cos(\omega t - \alpha) + P'_1 - kc\varepsilon_0 = -mc\varepsilon_0\omega^2, \qquad P_c\sin(\omega t - \alpha) - P'_2 = 0, \tag{26}$$

where ε_0 is the eccentricity ratio resulting from unbalance. In equations (26) the squeeze-film forces, P'_1 and P'_2, can be shown from reference [6], to be given, for concentric motion, by

$$P'_1 = 0, \qquad P'_2 = [\pi\mu Rl^3/c^2(1 - \varepsilon_0^2)^{3/2}]\varepsilon_0\omega. \tag{27}$$

These relate to a full uncavitated oil film. The assumption of concentric motion of the rotor centre precludes the prediction of subharmonic vibrations, which have been found in some squeeze-film applications [8]. However, the speed ranges over which such vibrations appear are fairly restricted and predictable, and separate attention could be focused on them using a more comprehensive form of equations (27).

Equations (26) may be made non-dimensional by dividing by $mc\omega^2$ to give

$$Q_c \cos(\omega t - \alpha) = -\varepsilon_0(1-\bar{k}), \qquad Q_c \sin(\omega t - \alpha) = (\pi\mu R/m\omega)(l/c)^3[\varepsilon_0/(1-\varepsilon_0^2)^{3/2}], \tag{28}$$

where $\bar{k} = k/m\omega^2 = (\omega/\omega_n)^{-2}$ and $Q_c = P_c/mc\omega^2$.

If P_c arises due to mass unbalance mu, then $P_c = mu\omega^2$ and $Q_c = u/c$. By putting $\beta = (\mu R/m\omega)(l/c)^3$, equations (28) may be rewritten to give

$$(u/c)\cos(\omega t - \alpha) = (\bar{k}-1)\varepsilon_0, \qquad (u/c)\sin(\omega t - \alpha) = \pi\beta\varepsilon_0/(1-\varepsilon_0^2)^{3/2}. \tag{29}$$

Hence, after some manipulation, we obtain

$$\left(\frac{u}{c}\right)^2 \frac{(1-\varepsilon_0^2)^3}{\varepsilon_0^2}\left(\frac{\omega}{\omega_n}\right)^4 = A^2\left(\frac{\omega}{\omega_n}\right)^2 + \left[1-\left(\frac{\omega}{\omega_n}\right)^2\right]^2(1-\varepsilon_0^2)^3, \tag{30}$$

where $A = (\pi\mu R/\sqrt{km})(l/c)^3$ and $\omega_n = \sqrt{k/m}$.

Now suppose that the supply pressure is insufficient to maintain a positive pressure in areas of the squeeze-film where the boundary surfaces are instantaneously separating. For the sake of simplicity assume that as a result the squeeze-film becomes half cavitated. It may then be shown from equations (8) that P_2' is halved and that P_1' is no longer zero, being given by

$$P_1' = (-2\mu R l^3\omega/c^2)[\varepsilon_0^2/(1-\varepsilon_0^2)^2].$$

Hence, for circular concentric whirl, we have the following equations which correspond to equations (29) for the uncavitated case:

$$(u/c)\cos(\omega t - \alpha) = (\bar{k}-1)\varepsilon_0 + 2\beta\varepsilon_0^2/(1-\varepsilon_0^2)^2,$$
$$(u/c)\sin(\omega t - \alpha) = (\pi\beta/2)\varepsilon_0/(1-\varepsilon_0^2)^{3/2}, \tag{31}$$

in which $\beta = A(\bar{k})^{1/2}\pi$. Hence

$$\left(\frac{u}{c}\right)^2 = \frac{A^2\varepsilon_0^2\bar{k}}{(1-\varepsilon_0^2)^3}\left[\frac{1}{4} + \frac{4\varepsilon_0^2}{\pi^2(1-\varepsilon_0^2)}\right] + \varepsilon_0^2(\bar{k}-1)^2 + \frac{4\varepsilon_0^3 A\bar{k}^{1/2}}{\pi(1-\varepsilon_0^2)^2}(\bar{k}-1). \tag{32}$$

Mohan and Hahn [9] have shown how a half-cavitated squeeze-film gives rise to response curves displaying the classical hardening-stiffness form, with the consequent prediction of non-linear jump phenomena.

Let us now find y and x (equations (13)) for a case where $k = 0$ and where the squeeze-film is half cavitated, and compare the orbits and their positions with the corresponding orbits and positions obtained by solving the full non-linear equations (7) in which $\omega = 0$. Although this case is subject to the reservations expressed earlier regarding the cavitation zone, it will again be a demanding test of the efficacy of the linear treatment. Other squeeze-films are unlikely to be significantly more non-linear than the half film and the presence of a centralizing spring stiffness would serve to moderate the effect of the squeeze-film non-linearity in the total system. For such a squeeze-film we find that equations (25) reduce to

$$a_1 = -(a_{ss} - 2m\omega^2)(a_{rr} + a_{ss}), \qquad b_1 = (a_{rs}/\omega)(a_{rr} + a_{ss}), \qquad c_1 = 2a_{ss} - 4m\omega^2,$$
$$d_1 = -2a_{rs}.$$

Hence

$$-y/c = \bar{W}(1-\varepsilon_0^2)^3/\beta\varepsilon_0(3+\varepsilon_0^2), \qquad x/c = 0. \tag{33}$$

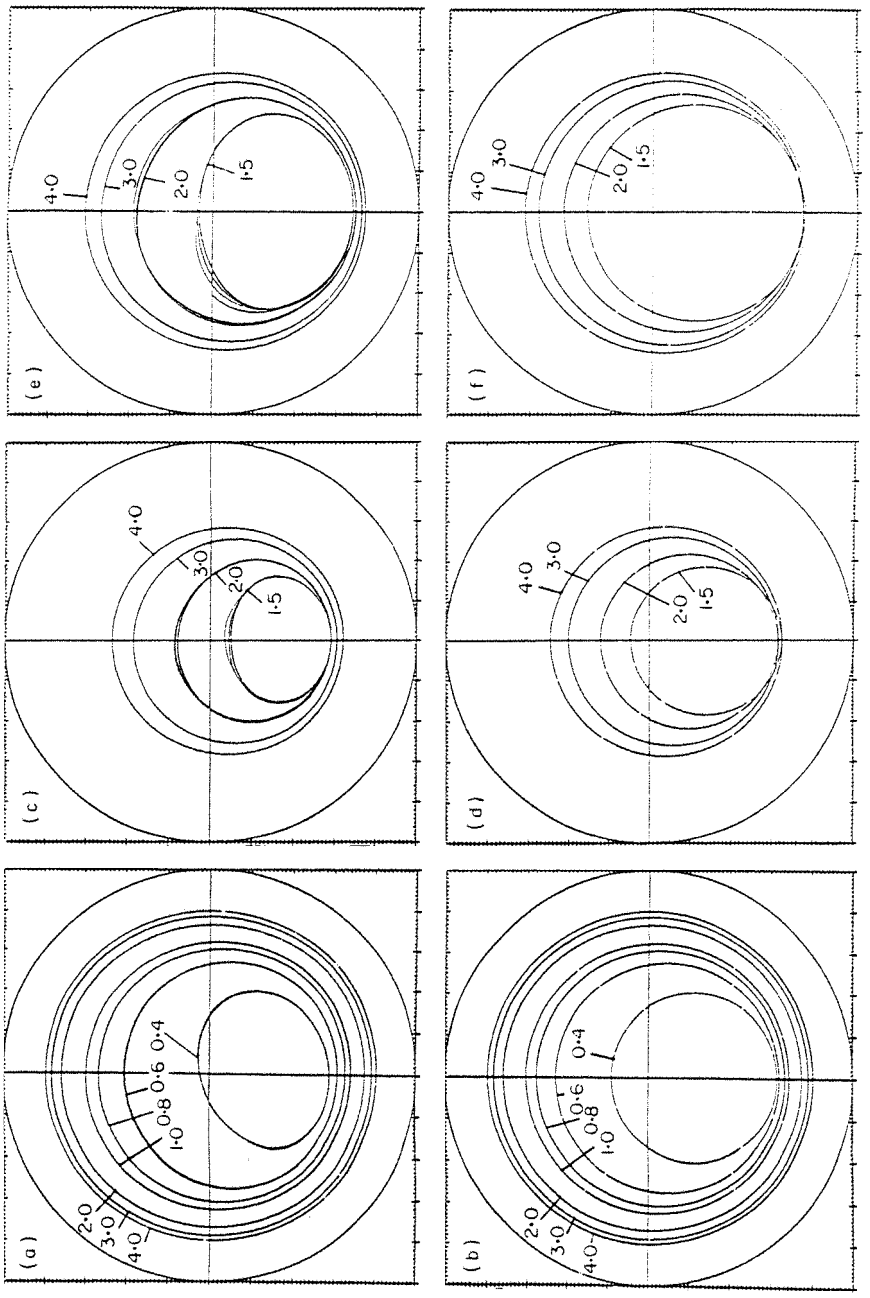

Figure 8. Squeeze-film damper orbits. (a) Non-linear, $\beta = 0{\cdot}4$, $\bar{W} = 0{\cdot}2$; (b) linear, $\beta = 0{\cdot}4$, $\bar{W} = 0{\cdot}2$; (c) non-linear, $\beta = 2{\cdot}0$, $\bar{W} = 1{\cdot}0$; (d) linear, $\beta = 2{\cdot}0$, $\bar{W} = 1{\cdot}0$; (e) non-linear, $\beta = 1{\cdot}0$, $\bar{W} = 1{\cdot}0$; (f) linear, $\beta = 1{\cdot}0$, $\bar{W} = 1{\cdot}0$.

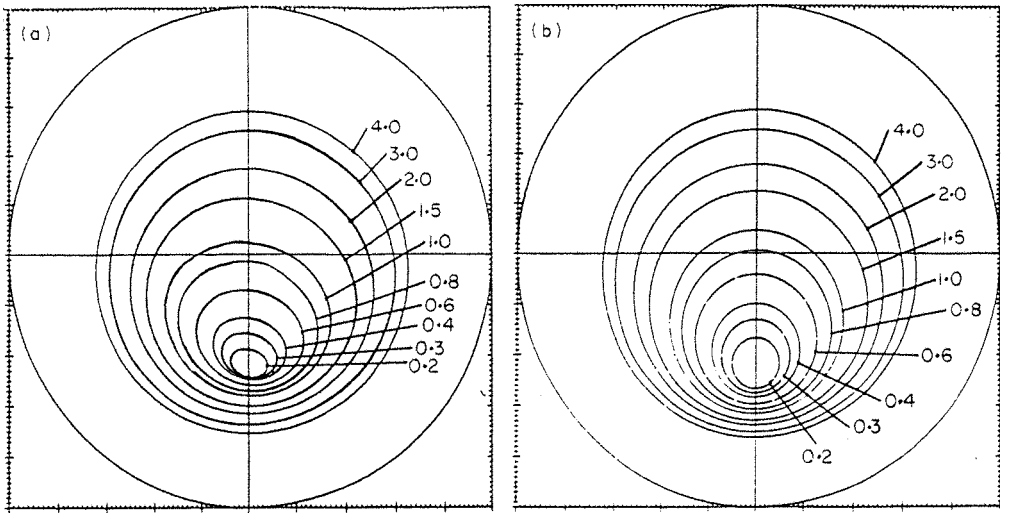

Figure 9. Squeeze-film isolator orbits. (a) Non-linear, $\beta = 1{\cdot}0$, $\bar{W} = 1{\cdot}0$, $\bar{k} = 2{\cdot}0$; (b) linear, $\beta = 1{\cdot}0$, $\bar{W} = 1{\cdot}0$, $\bar{k} = 2{\cdot}0$.

A set of non-dimensional parameters governing equations (33) is, by reference to equations (32), again $\bar{W}$, u/c and $\bar{W}/\beta$. Figures 8(a)-(f) show comparisons between damper orbits relevant to the range of damper and load conditions with those obtained by solving the full non-linear equations (7), in which $\omega = 0$.

The comparisons serve to show that the linear treatment gives a rapid means of estimating the vibration orbits and their dispositions for moderate values of mean damper deflection. As for the journal bearing it may be assumed that, provided that the circular journal-centre orbit circumscribes the bearing centre, then it gives a reliable indication of the size and position fo the true non-linear orbit, for moderate values of $\bar{W}/\beta$.

The presence of a retainer spring will reduce the significance of $\bar{W}/\beta$, as Figure 9(a) shows. This figure relates to orbits of journal-centre motion for the same values of β and $\bar{W}$ as were employed in Figure 8(e), but with the addition of a parallel spring, which for zero u/c, would cause the journal to take up an eccentricity ratio of 0·5 as a result of a gravity load. This implies that the value of $\bar{k}$ for this case is 2·0. The journal-centre orbits obtained by the corresponding linear treatment are shown in Figure 9(b). The improvement in the comparisons with the non-linear orbits is apparent.

4. CONCLUSIONS

The purpose of this paper is to show that for a journal bearing there exists a correspondence between the linear oil-film coefficients referred to stationary co-ordinates for perturbation from a static equilibrium position and coefficients referred to rotating co-ordinates for perturbation from a circular concentric orbit. A similar correspondence is shown to exist with the coefficients referred to rotating co-ordinates for the oil film of a squeeze-film damper.

Journal-bearing coefficients referred to stationary co-ordinates have been used to predict relatively small orbits of the unbalance response of heavy rotors such as those used in large power turbines. Similar coefficients are used here to estimate rapidly the dispositions of relatively large vibration orbits, certainly those circling the bearing centre, resulting from unbalance forces superimposed upon moderate static loads, whether they relate to journal bearings or to squeeze-film dampers. Comparisons of the sizes and dispositions

of such orbits are shown to be satisfactory when compared with orbits obtained by solving the full non-linear equations of motion.

Fluid inertia forces may be considered in a similar way and inertia coefficients used in corresponding force equations incorporating the same displacement and velocity coefficients considered in this paper. However, in the vast majority of cases, their effect, will be relatively minor, since rotor mass will dominate over any added mass effect of the fluid.

ACKNOWLEDGMENTS

The authors acknowledge the financial support provided by the Science & Engineering Research Council and Rolls-Royce plc, to carry out research into the vibration of aero engine assemblies, of which this work forms a part.

REFERENCES

1. R. HOLMES 1960 *Journal of Mechanical Engineering Science* **2** (4), 337–341. The vibration of a rigid shaft on short sleeve bearings.
2. R. HOLMES 1977 *Journal of Mechanical Enginnering Science* **19** (6), 271–277. The damping characteristics of vibration isolators used in gas turbines.
3. G. CAPRIZ 1963 *Annale Scuola Normale Superiore* **17**, 31. Sulle vibrazioni della aste rotanti.
4. J. A. COLE and C. J. HUGHES 1957 *Proceedings of the Lubrication and Wear Conference (Institution of Mechanical Engineers)* 147–149. Visual study of film extent in dynamically-loaded complete journal bearings.
5. H. MARSH 1974 *Proceedings of the 1st Leeds–Lyon Symposium on Tribology, September*, 91–95. Cavitation in dynamically loaded journal bearings.
6. R. HOLMES 1963 *Proceedings of the Institution of Mechanial Engineers* **177** (11), 291–308. Oil-whirl characteristics of a rigid rotor in 360° journal bearings.
7. D. C. WHITE 1972 *Conference on Vibrations in Rotating Systems, February (Institution of Mechanical Express)*, 213–229. The dynamics of a rigid rotor supported in squeeze film bearings.
8. J. L. NIKOLAJSEN and R. HOLMES 1979 *Journal of Mechanical Engineering Science* **21** (4), 247–252. Investigations of squeeze-film isolators for the vibration control of a flexible rotor.
9. S. MOHAN and E. J. HAHN 1974 *Transactions of the American Society of Mechanical Engineers, Engineering for Industry*, 976–982. Design of squeeze-film damper supports for rigid rotors.

APPENDIX: NOTATION

a_{rs}, etc.,	displacement coefficients
A	$=(\pi\mu R/\sqrt{km})(l/c)^3$
b_{rs}, etc.,	velocity coefficients
c	radial clearance
D	bearing diameter
e	eccentricity of journal in bearing
$F_{1,2}$	functions in oil-film forces
$g_{1,2,3,}$	functions in oil-film forces
h	oil-film thickness
$h_{1,2}$	functions in oil-film forces
k	stiffness of centering spring per land
l	bearing or squeeze-film land length
m	mass per bearing land or per squeeze-film land
p	oil-film pressure
$P_{1,2,c}$	oil-film forces or external force
Q_c	$=P_c/mc\omega^2$
r	radial co-ordinate
R	$=D/2$ bearing radius

s	transverse co-ordinate
t	time
u	displacement of mass centre from axis of rotation
W	external static load
x	stationary co-ordinate
y	stationary co-ordinate
z	axial co-ordinate
α	attitude angle
$\dot{\alpha}_s$	angular velocity perturbation
β	$=(\mu R/m\omega)(l/c)^3$
γ	$=\mu R(l/c)^3$
ε	$=e/c$, eccentricity ratio
ε_0	static or rotating eccentricity ratio vector
μ	lubricant viscosity
λ	$=\mu l R^3/\pi c^2$
θ	circumferential co-ordinate
ω	shaft or journal angular velocity
ω_n	$=\sqrt{k/m}$
C_B	bearing centre
C_j	dynamic journal centre

APPENDIX 7

Numerical Stability of The Harmonic Balance Method

Harmonic Balance enables a full non-linear SFD model to be approximated by linear Fourier coefficients. Applied generally the method is capable of deriving quasi-linear stiffness and damping coefficients for as full a Fourier Series as is required. Thus, as well as the synchronous response, the non-synchronous response of an assembly might be investigated.

The non-linear horizontal, or x displacement can be written as a Fourier Series in the form:

$$x(t) = Ao + \sum_{(J=1)}^{J} (A_J.\cos(jwt/N) + B_J.\sin(jwt/N)) \qquad .....\{A7.1\}$$

and similarly in the vertical, or y direction. J is the total number of equally spaced frequencies of interest and A_J and B_J are the linear Fourier displacement coefficients. N is an integer which is smaller than J and A_N and B_N are the synchronous components of the displacement response. The non-linear force can also be approximated using linear coefficients such that

$$fx(t) = fo + k.x + c.\dot{x} + \sum_{(J\neq N)}^{J} (a_J.\cos(jwt/N) + b_J.\sin(jwt/N)) \qquad .....\{A7.2\}$$

where fo is a static force, k is a synchronous stiffness coefficient, c is a synchronous damping coefficient and a_J and b_J are nonsynchronous force coefficients.

Therefore, providing that a non-linear force function, fx can be described and integrated with respect to (w.t), a set of linear force coefficients can be derived from a set of initial amplitude coefficient estimates. The force coefficients can then be used within a linear dynamic model of the system to calculate a revised set of amplitude coefficients. If the revised amplitude coefficients are similar to the initial estimates to within a prescribed convergence tolerance, or maximum error, then these coefficients represent an acceptable linear approximation of the response. If the comparison of the revised amplitude coefficients with the initial estimates is not within the maximum error then these revised coefficients can be reinserted to calculate a new non-linear force, fx and a new set of linear force coefficients derived. Thus a further set of amplitude coefficients may be calculated using the force

coefficients in the linear model and the convergence check carried out once more. This iteration is repeated until convergence is achieved and the process is illustrated by the flow diagram of Fig 11.5.

This simple iteration can be described generally by the formula

$$X_{(n+1)} = H\{X_{(n)}\} \qquad .....\{A7.3\}$$

Consider first the synchronous response of a SFD. The iteration formula, {A7.3} generates an iteration which is stable for a π film model of a SFD whose journal has no static load, no linear support stiffness and a reasonably high bearing parameter, β (refer to [76]). If a linear support stiffness is included, then the iteration is not stable at, or very close to resonance due to the phase, ie the phase between the unbalance and displacement is 90°. In this instance the amplitude is determined exclusively by the damping provided by the SFD. Remote from the resonance peak, in the absence of bistable solutions, the response is dictated primarily by the stiffness of the linear support. Such limitations on the modelling of the SFD response using the simple harmonic balance method severely restrict its application.

It is not surprising that convergence problems arise. Even when only considering the synchronous response, the iteration is being carried out on six interdependent displacement coefficients. The iteration algorithm described by equation {A7.3} can be referred to as a direct iteration [77]. Consider, for the sake of simplicity, that only one variable, or coefficient is involved in the iteration, then the convergence of equation {A7.3} is determined by the gradient and form of the relationship of equation, as shown in Fig A7.1. Figs A7.1a,b illustrate two cases where convergence is assured, whereas, Figs A7.1c,d illustrate situations where convergence does not take place. In these instances a geometric transformation of the curve about the line of gradient unity will encourage convergence (as shown by the chained curve in Fig A7.1c).

For the case of a number of interdependent variables a different iteration curve or relationship will exist for each variable at each step of the iteration. The convergence path of one variable will therefore not be along a number of points between the unity gradient line and one iteration function as in Fig A7.1a, for example, but will be along a number of points between the unity gradient line and a number of iteration functions, which have the potential of changing significantly between subsequent iterations. The inadequacy of the harmonic

balance iteration of equation {A7.3} in this application is due to such numerical instabilities.

Although Xu [54] did not describe this shortfall, it was encountered during the analysis resulting in the paper, [54]. To attempt to overcome the instability Xu made a simple adjustment to the iteration method. A similar alteration was made, independently of Xu [54], by Levesley [77] after encountering the same difficulties. The stability of the method was improved by altering the iteration, equation {A7.3}, to the form shown below

$$X_{(n+1)} = H\{(X_{(n)} + X_{(n-1)})/2\} \qquad \text{.....\{A7.4\}}$$

Equation {A7.4} represents an iteration which updates the displacement vector, X with the mean of the two previous displacement vectors. This technique resulted in stable iterations for a wider range of SFD parameters and the results compare well with those from the Runge-Kutta method [76].

In conclusion, the beneficial qualities of the harmonic balance method include the ability of the method to incorporate a non-analytical model of the squeeze-film. In particular, the Simpson's integration of the pressure map within the film, as used by the Runge-Kutta method, can be incorporated if required, allowing variation of the oil cavitation and supply pressures. Also the harmonic balance method does not rely on stored tables of pre-calculated data, as in the quasi-linear approach of Dogan [72]. The drawback of the harmonic balance method, as with many algorithms, is the stability of the convergence. For SFDs with no static load or parallel spring support, ie as for a vertical rotor, the method converges to a solution very quickly, displaying all the required qualities of speed and accuracy required by industry. The unfortunate effect of static load and support stiffness on iterative stability and the distinct benefits of introducing stability to the iteration algorithm have been discussed [77].

BIBLIOGRAPHY

1 REYNOLDS, O. On the theory of lubrication and its application to Mr. Beauchamp Tower's experiments, including an experimental determination of the viscosity of olive oil. Phil. Trans. R. Soc., 1886, 177, 157-234.

2 DOWSON, D. Osbourne Reynolds centenary (1886-1986). Proc. Instn. Mech. Engrs., 1987, 210, 75-96.

3 PINKUS, O. and STERNLICHT, B. Theory of hydrodynamic lubrication. 1961 (McGraw-Hill, New York).

4 VANCE, J.M. Rotordynamics of turbomachinery. 1988 (John Wiley & Sons Inc., New York).

5 DEN HARTOG, J.P. Mechanical vibrations. 1956 (McGraw-Hill, NewYork).

6 TIMOSHENKO, S., YOUNG, D.H. and WEAVER, J.R. Vibration problems in engineering. Fourth edition. 1974 (Wiley, New York).

7 SIMANDIRI, S. and HAHN, E.J. Experimental evaluation of the predicted behaviour of squeeze-film-bearing-supported rigid rotors. Instn. Mech. Engrs., J. Mech. Engrg. Science, Feb 1976, 109-117.

8 TSE, S.T., MORSE, I.E. and HINKLE, R.T. Mechanical vibrations; theory and applications. Second Edition, 1978 (Allyn and Bacon, Inc., Boston).

9 MAGNUS, K. Vibrations. 1965 (Blackie & Son Ltd., London).

10 STOKER, J.J. Nonlinear vibrations. 1950 (Interscience, New York).

11 BLAQUIERE, A. Nonlinear system analysis. 1966 (Academic Press, New York).

12 UEDA, Y. Explosions of strange attractors exhibited by duffing's equation. Annals of the New York Academy of Sciences, 1980, 357, 422-433.

13 SZEMPLINSKA-STUPNICKA, W. Secondary resonances and approximate models of routes to chaotic motion in non-linear oscillators. J Sound and Vibration, 1987, 113, 155-172.

14 NAYFEH, A.H. The response of single degree of freedom systems with quadratic and cubic non-linearities to a subharmonic excitation. J Sound and Vibration, 1983, 89, 457-470.

Bibliography 1

15 PLAUT, R.H. and HSIEH, J.C. Non-linear structural vibrations involving a time delay in damping. J Sound and Vibration, 1987, 113, 497-510.

16 NEWLAND, D.E. An introduction to random vibrations and spectral analysis. Second edition. 1984 (Longman, New York).

17 RANDALL, R.B. Frequency analysis. Second edition. 1977 (Bruel and Kjaer, Denmark).

18 TOMLINSON, G.R. Attacking the problem of non-linearity in modal testing and analysis. Chartered Mech. Engineer, 1988, January, 34-37.

19 MITCHELL, J.R., HOLMES, R. and BYRNE, J. Oil whirl of a rigid rotor in 360 degree journal bearings: further characteristics. Proc. Instn. Mech. Engrs., 1965-6, 180, Pt 1, No. 25, 593-609.

20 COOPER, S. Preliminary investigation of oil films for the control of vibration. Instn. Mech. Engrs., Lubrication and Wear Conv., 1963, 305-315.

21 KULINA, M., MULLEN, J., NATESH, M. and SALTZMAN, H. A new concept for critical speed control. Soc Automotive Engrs., National Aeronautic Meeting, New York, 1967, 670347.

22 HOLMES, R. The control of engine vibration using squeeze film dampers. Trans. ASME, J. Engrg. for Power, 105, 1983, 525-529.

23 HOLMES, R. and DOGAN, M. Investigation of a rotor bearing assembly incorporating a squeeze-film damper bearing. J. Mech. Engrg. Science, 24, 1982, 129-137.

24 DEDE, M.M. and HOLMES, R. On prediction and experimental assessment of engine-bearing performance. Tribology International, 17, 1984, 251-257.

25 MALANOSKI, S.B. Case histories in which subsynchronous or synchronous vibration amplitudes have been minimized after employing custom designed damper bearings. Mechanical Technology Incorporated, New York, April 1979.

26 EHRICH, D. and CHILDS, D. Self-excited vibration in high-performance turbomachinery. Mechanical Engineering, May 1984, 66-79.

Bibliography 2

27 FIROOZIAN, R. and STANWAY, R. Modelling and control of turbomachinery vibrations. Trans ASME, J Vibration, Acoustics, Stress and Reliability in Design, 1988, 110, 521-527.

28 BURROWS, C.R., SAHINKAYA, M.N. and TURKAY, O.S. An adaptive squeeze-film bearing. Trans. ASME, J. Tribology, 1984, 106, 145-151.

29 FLEMING, P. Dual clearance squeeze film damper for high load conditions. Trans. ASME, J. Tribology, 1985, 107, 274-279.

30 WHITE, D.C. Squeeze film journal bearings. PhD Thesis, University of Cambridge, 1970.

31 BOOKER, J.F. A table of the journal-bearing integral. Trans. ASME, J. Basic Engng, 1965, 533-535.

32 RAMLI, M.D., ELLIS, J. and ROBERTS, J.B. On the computation of inertial coefficients in squeeze-film bearings. Proc. Instn Mech. Engrs., 1987, 210, 125-131.

33 SMITH, D.M. Journal bearing dynamic characteristics-effect of inertia of lubricant. Proc. Instn Mech. Engrs., 1964-5, 179, Part 3J, 37-44.

34 ROBERTS, J.B., HOLMES, R. and MASON P.J. Estimation of squeeze-film damping and inertial coefficients from experimental free-decay data. Proc. Instn Mech. Engrs., 1986, 200, 123-133.

35 MOHAN, S. and HAHN, E.J. Design of squeeze film damper supports for rigid rotors. Trans. ASME, J. Engrg for Industry, 1974, 976-982.

36 CAPRIZ, G. Communications. Proc. Instn Mech. Engrs., 1965-1966, 180, Pt.1, 607-609.

37 GUNTER, E.J., BARRETT, L.E. and ALLAIRE, P.E. Design of nonlinear squeeze-film dampers for aircraft engines. Trans. ASME, J. Lubric. Technol., 1977, 57-64.

38 FEDER, E., BANSAL, P.N. and BLANCO, A. Investigation of squeeze film damper forces produced by circular orbits. Trans. ASME, J. Engrg for Power, 1978, 100, 15-21.

39 CARNAHAN, B., LUTHER, H.A. and WILKES J.O. Applied numerical methods. 1969 (Wiley & Sons Inc., New York).

Bibliography 3

40 BERT,C.W. and STRICKLIN, J.D. Comparative evaluation of six different numerical integration methods for non-linear dynamic systems. J Sound and Vibration, 127, No.2, 1988,221-229.

41 HOLMES, R. Research note: the non-linear performance of squeeze-film bearings. J. Mech. Engrg Science, 1972, 14, No.1, 74-77.

42 HUMES, B. and HOLMES, R. The role of subatmospheric film pressures in the vibration performance of squeeze-film bearings, J. Mech. Engrg Science, 1978, 20, No.5, 283-289.

43 CRAVEN, A.H. and HOLMES, R. The vibration of engine crankshafts - a fast numerical solution. International J. for Numerical Methods in Engrg, 1972, 5, 17-24.

44 GUILHEN, P.M., BERTHIER, P., FERRARIS, G. and LALANNE, M. Instability and unbalance response of dissymmetric rotor-bearing systems. Trans ASME, J Vibration, Acoustics, Stress and Reliability in Design, 1988, 110, 288-294.

45 GREENHILL, L.M. and NELSON, H.D. Iterative determination of squeeze film damper eccentricity for flexible rotor systems. Trans. ASME, J. Mech. Design, 1982, 104, 334-338.

46 TAYLOR, D.L. and KUMAR, B.R.K. Closed-form, steady-state solution for the unbalance response of a rigid rotor in squeeze film damper. Trans. ASME, J. Engrg for Power, 1983, 105, 551-559.

47 HOLMES, R. The damping characteristics of vibration isolators used in gas turbines. J. Mech. Engrg Science, 1977, 19, No.6, 271-277.

48 HOLMES, R. and SYKES, J.E.H. Large-amplitude vibrations in rotor assemblies. J. Sound and Vibration, 1989, 133(2), 337-351.

49 BURROWS, C.R., SAHINKAYA, M.N. and KUCUK, N.C. Modelling of oil-film forces in squeeze-film bearings. Trans. ASME, J. Tribology, 1986, 108, 262-269.

50 STANWAY, R., BURROWS, C.R. and HOLMES, R. Discrete-time modelling of a squeeze-film bearing. J. Mech. Engrg Science, 1979, 21, 419-427.

51 STANWAY, R., FIROOZIAN, R. and MOTTERSHEAD, J.E. Estimation of the linearized damping coefficients of a squeeze-film vibration isolator. Proc. Instn. Mech. Engrs., 1987, 201, No.C3, 181-191.

52 SZERI, A.Z., RAIMONDI, A.A. and GIRON-DUARTE, A. Linear force coefficients for squeeze-film dampers. Trans. ASME, J. Lubric. Technol., 1983, 105, 326-334.

53 CHEN, S. and XU, J. Equivalent linearization of a nonlinear element with respect to subharmonic motions. Northwestern Polytechnical University, People's Republic of China.

54 XU, J. An application of equivalent linearization to the unbalance response calculation of rotor-SFDB systems. Northwestern Polytechnical University, People's Republic of China.

55 FENG, N.S. and HAHN, E.J. Effects of gas entrainment on squeeze film damper performance. Trans. ASME, J. Tribology, 1987, 109, 149-154.

56 HAYWARD, A.T.J. The viscosity of bubbly oil. National Engineering Laboratory, 1961, Fluids Report No.99.

57 HEWITT, G.F. and HALL-YALOR, N.S. Annular two-phase flow. First Ed., 1970.

58 FENG, N.S. and HAHN, E.J. Inlet pressure and cavitation boundary effects on the orbit jump phenomenon in squeeze film damper operation. Proc. Instn. Mech. Engrs., 1989, 203, 209-217.

59 NIKOLAJSEN, J.L. and HOLMES, R. Investigation of squeeze-film isolators for the vibration control of a flexible rotor. J. Mech. Engrg Science, 1979, 21, No.4, 247-252.

60 DYER, D. and REASON, B.R. A study of tensile stresses in a journal-bearing oil film. J. Mech. Engrg Science, 1976, 18, No.1, 46-52.

61 WALTON, J.F., WALOWIT, J.A., ZORI, E.S. and SCHRAND, J. Experimental observation of cavitating squeeze-film dampers. Trans. ASME, J. Tribology, 1987, 109, 290-295.

62 ZEIDAN, F.Y. and VANCE, J.M. Cavitation effects on the pressure distribution of a squeeze film damper bearing. Dept. Mech. Engrg, Texas A&M University, Texas 77843.

63 BOTMAN, M. and SAMAHA, M.A. Experiments on the dynamic behaviour of a supercritical rotor. Trans. ASME, J. Mech. Design, 1982, 104, 364-369.

64 COOKSON, R.A., FENG, X.H. and KOSSA, S.S. The effect of journal misalignment on the oil-film forces generated in a squeeze film damper. Trans. ASME, J. Engrg Power, 1983, 105, 560-564.

65 HOLMES, R. and DEDE, M.M. Non-linear phenomena in aero-engine rotor vibration. Proc. Instn. Mech. Engrs., 1989, 203, 25-34.

66 NAYFEH, A.H. Combination tones in the response of single degree of freedom systems with quadratic and cubic non-linearities. J. Sound and Vibration, 1984, 92, 379-386.

67 NEILSON, R.D and BARR, A.D.S Dynamics of a rigid rotor mounted on discontinuously non-linear elastic supports. Proc. Instn. Mech. Engrs., 1988, 202, No. C5, 369-376.

68 BLACK, H.F. Interaction of a whirling rotor with a vibrating stator across a clearance annulus. J. Mech. Engrg Science, 1968, 10, No. 1, 1-12.

69 SIMANDIRI, S. and HAHN, E.J. Effect of pressurization on the vibration isolation capability of squeeze film bearings. Trans AMSE, J Engrg for Industry, 1976, 109-117.

70 SMALLEY, A.J., DARLOW, M.S. and MEHTA, R.K. The dynamic characteristics of o-rings. ASME Paper No. 77-DET-27.

71 XU, J. The transient dynamic performance of a rotor-SFDB system during passage through resonance. Theory of Lub. and Bearing Inst., Xi'an Jiaotong University, Xi'an, China.

72 DOGAN, M. Investigation of an aero-engine squeeze-film damper. DPhil Thesis, University of Sussex, 1983.

73 THOMPSON, J.M.T. Instabilities and catastrophes in science and engineering. 1982 (Wiley, Chichester).

74 REIF, Z.F. The effect of static deflection on the harmonic resonance of a system with a hardening non-linear spring. Aero J of Royal Aeronautical Soc, Jan 1970, 74, 59-62.

75 MICKENS, R.E. Comments on the method of harmonic balance. J. Sound and Vibration, 1984, 94(3), 456-460.

76 CONTE, S.D. and DE BOOR, C. Elementary numerical analysis, an algorithmic approach. Second Edition, 1972 (McGraw-Hill Kogakusha, Tokyo).

77 LEVESLEY, M.L. Transfer thesis. Department of Mechanical Engineering, University of Southampton, March 1990, Report No ME/90/04.

78 SYKES, J.E.H. and HOLMES, R. Study of sealed squeeze-film dampers and their representation in linear form. Department of Mechanical Engineering, University of Southampton, March 1990, Report No ME/90/03.

The following published papers were included in the bound thesis. These have not been digitised due to copyright restrictions, but the links are provided.

https://doi.org/10.1016/0022-460x(89)90930-9